

THE ROLE OF ENVIRONMENTAL PARAMETERS IN THE INTERACTIONS OF
AQUEOUS ELECTROLYTES WITH GRAPHENE SOLID STATE DEVICES

THE ROLE OF ENVIRONMENTAL PARAMETERS IN THE INTERACTIONS OF
AQUEOUS ELECTROLYTES WITH GRAPHENE SOLID STATE DEVICES

By SHAYAN ANGIZI, B.SC., M.Sc.

A Thesis Submitted to the School of Graduate Studies in Partial Fulfilment of the
Requirement of the Degree of Doctor of Philosophy in Chemistry

McMaster University ©
Copyright by Shayan Angizi, September 2022

Ph.D. Thesis – S. Angizi; McMaster University - Chemistry

McMaster University, DOCTOR OF PHILOSOPHY (2022), Hamilton, Ontario, Canada
(Chemistry)

TITLE: The Role of Environmental Parameters in The Interactions of Aqueous Electrolytes
with Graphene Solid State Devices

AUTHOR: Shayan Angizi, M.Sc. (McMaster University)

SUPERVISOR: Professor Peter Kruse

NUMBER OF PAGES: xxiii, 188

Lay Abstract

This thesis aims to investigate the interfacial interactions between graphene-based water quality devices and aqueous electrolytes to enhance the functionality of graphene derivatives in aqueous environments. The study focuses on the mechanisms through which graphene devices respond to changes in electrolyte parameters such as pH, oxidation-reduction potential (ORP), dissolved oxygen (DO) and ionic strength. In order to investigate the possible interference of these environmental parameters with the detection of analytes in water, multiple graphene devices (such as chemiresistive and Schottky diodes) were fabricated to better understand how graphene perceives aqueous electrolytes. This thesis explores four groups of interfacial interactions: electrostatic gating effect, surface charge transfer, substitutional doping, and ion trapping, and strives to manufacture sensitive water quality sensors based on graphene.

Abstract

Since the discovery of thermodynamically stable monolayer graphene, it has succeeded in overtaking a number of conventional materials in chemical sensing applications due to its exceptional chemical and electrical properties. In addition to being electrically conductive, graphene also has a large surface area which facilitates faster electronic interaction with analytes. In spite of graphene's inherent potential for chemical sensing, its application to aqueous electrolytes has been limited by an incomplete understanding of its interactions with the electrolytes' environmental parameters. This thesis focuses on mechanisms through which graphene-based solid-state sensors (i.e., chemiresistors, Schottky diodes) respond to changes in aqueous electrolytes. Multiple environmental parameters, including pH, ionic strength, oxidation-reduction potential, as well as a target analyte (free chlorine), were chosen to examine their impacts on the performance of devices.

To begin, graphene's pH response was explored, showing that its pH sensitivity is strongly defect-dependent. The graphene defectivity was determined with the aid of Raman spectroscopy and X-ray photoelectron spectroscopy (XPS). As revealed by measurements of the oxygen-to-carbon ratio (O/C) in XPS and the D-band/G-band intensity ratio (I_D/I_G) in Raman, graphene responds to pH in two main defectivity regions. In a low defect region, the graphene surface was shown to mainly interact with corresponding ions (i.e., H_3O^+ and OH^-) through an electrostatic gating effect. However, in the high defect region, the response is dominated by protonation-deprotonation of oxygen-based functional groups. Therefore, the modulation of defectivity resulted in the change in pH responsivity. According to this result, we demonstrated that thermally reduced graphene oxide could be highly pH-sensitive to the pH range of 3-10 by dominating the defect induced pH response.

Aside from pH, the impacts of changes in ionic strength, DO, and ORP of the electrolytes were investigated. We demonstrate that graphene chemiresistive devices can be used to investigate deviations in experimental screening lengths from the theoretical Debye length. We also

present an overview of ion arrangements in the proximity of graphene, emphasizing the importance of DO in the Stern layer.

Lastly, the development of an ultra-sensitive water quality sensor was shown by utilizing monolayer graphene in Schottky diodes. For the case study, free chlorine, a primary disinfectant of water, was chosen as the target analyte. Schottky diodes are demonstrated to offer sensitivity and LOD values competitive with current literature when environmental parameters are taken into account. I believe that this thesis provides a deeper understanding of graphene's applicability in aqueous media and opens new research avenues in graphene/aqueous interfacial interactions.

Acknowledgments

I am grateful to my beloved wife and my little angel, Avery Rosha, for being with me through all ups and downs and making my life a small piece of heaven.

I thank my parents, Sheida and Mehdi, for helping me be who I am now, and my brother for all his wisdom and support throughout my life.

I would like to thank my previous supervisor, Professor A. Simchi, for providing me with the opportunity to pursue advanced scientific research. I thank my former colleague, Professor MH. Shaeri, for giving me the courage to dive into the sea of science and facing unpredictables; may he rest in peace.

I am grateful to Professor Kruse for guiding me through all these years of Ph.D. study and giving me the opportunity and freedom to become an independent researcher and thinker. He provided me with many amazing ideas and suggestions for my papers and reports, and I am grateful to him for being so patient with my transition from an “engineer” to a “scientist”.

I thank Prof. P. Ravi Selvaganaphathy and Prof. Gillian Goward for serving as my supervisory committee and providing me with suggestions, critics, and interest in my research.

I would like to thank Dr. Mark C. Biesinger, from Surface Science Western, Dr. Shahram Tavakkoli and Doris Stevanovic from the Centre for Emerging Technology and Devices (CEDT) at McMaster University, and Dr. Alex Adronov for their help and support.

Lastly, I would like to thank my friends Md. Ali Akbar, Lea Hong, Eugene Yat Chun Yu, Johnson Dalmieda, Maryam Darestani-Farahani, Mehraneh Tavakkoli, and Vinay Patel for their fruitful discussions and assistance in performing experiments.

Table of Contents

Chapter 1	Introduction	1
1.1	Motivation	1
1.2	Structure of this thesis	2
1.3	References	3
Chapter 2	Graphene/Aqueous electrolyte Interfacial Interaction	2
2.1	Graphene	5
2.1.1	Synthesis	6
2.1.2	Nanomorphology and Derivatives	8
2.1.3	Properties	9
2.1.3.1	Number of Layers (thickness)	10
2.1.3.2	Edge termination	11
2.1.3.3	Defectivity	12
2.2	Graphene based Chemical Sensors	16
2.2.1	Chemiresistors	16
2.2.2	Field Effect Transistors	17
2.2.3	Schottky Diodes	20
2.2.3.1	Junction Formation	20
2.2.3.2	Calculating the Schottky junction's parameters	22
2.2.3.3	Sensing application	23
2.3	Graphene versus water	25
2.3.1	Wettability of graphene	25
2.3.1.1	Substrate	27
2.3.1.2	Topography and roughness	29
2.3.1.3	Defectivity	30
2.3.1.4	Number of Layers (thickness)	31
2.4	Interfacial Interactions	31
2.4.1	Electrostatic Gating Effect	31
2.4.2	Surface Charge Transfer	37
2.4.2.1	pH	39
2.4.2.2	ORP	40
2.4.2.3	Dissolved gases	42
2.4.3	Substitutional Doping	43

2.4.4 Trapped ions/molecules	44
2.5 Conclusion	45
2.6 References	45
Chapter 3 Defect Engineering of Graphene to Modulate pH response of Graphene Devices	65
3.1 Abstract	66
3.2 Introduction	66
3.3 Materials and Experimental Design	68
3.4 Results and Discussions	69
3.4.1 Relation of Surface Defect Density with pH	69
3.4.2 Surface Dominant Sensing Mechanism	71
3.4.3 Defect Dominant Sensing Mechanism	74
3.5 Conclusion	78
3.6 References	79
3.7 Supporting Information	82
Chapter 4 Defect Density-Dependent pH response of Graphene Derivatives: Towards the Development of pH sensitive Graphene Oxide Devices	97
4.1 Abstract	98
4.2 Introduction	98
4.3 Materials and Methods	99
4.3.1 Single-Layer Graphene Transfer Processes	99
4.3.2 Synthesis of FLG and Sensor Fabrication	100
4.3.3 GO Preparation and Sensor Fabrication	101
4.3.4 Characterization	101
4.4 Results and Discussions	101
4.4.1 pH Response of Bare Graphene	101
4.4.2 Selective Functionalization of Graphene	104
4.4.3 pH Response of GO and Its Application towards the Development of GO-Based pH Sensors	108
4.5 Conclusion	110
4.6 References	111
4.7 Supporting Information	114

Chapter 5	Graphene Versus Concentrated Electrolytes: An Experimental Study to Explore the Role of the Electrochemical Double Layer	122
5.1	Abstract	122
5.2	Introduction	122
5.3	Results and Discussions	125
5.4	Conclusion	135
5.5	References	136
5.6	Supporting Information	139
Chapter 6	Graphene-Silicon Schottky Devices for Operation in Aqueous Environments: Device Performance and Sensing Application	149
6.1	Abstract	150
6.2	Introduction	150
6.3	Device Fabrication	151
6.4	Results and Discussions	151
6.4.1	Device Performance	151
6.4.2	Impact of Environmental Parameters	153
6.4.2.1	Effect of Solution Conductivity and Ionic Strength	153
6.4.2.2	Effect of pH	155
6.4.2.3	Effect of Oxidation-Reduction-Potential (ORP)	155
6.4.3	Application as a Sensor by Introducing Selectivity Through Chemical Functionalization	156
6.4.4	Interference Studies	159
6.4.5	Comparison with Chemiresistive Platforms	160
6.5	Conclusion	161
6.6	References	161
6.7	Supporting Information	164
Chapter 7	Conclusions and Outlook	181

List of Figures

Chapter 2 Graphene/Aqueous Electrolyte Interfacial Interactions

Figure 2.1	Synthesis methods of graphene	7
Figure 2.2	Graphene derivatives	9
Figure 2.3	A) zigzag, b) Armchair and c) arbitrary edge configuration of graphene. Two possible graphene layer sequences of d) Bernal and e) Rhombohedral	12
Figure 2.4	High resolution electron microscopy images of a) Stone Wales, b) single vacancy. and c) one-dimensional defects in graphene d) Schematic of graphene sheets containing oxygen-based functional groups on the plane and edge. e) example of covalent functionalization of graphene planes and edges using azomethine yilde. f) An example of non-covalent functionalization of graphene using aryne cycloaddition reactions	14
Figure 2.5	Devices configuration of a) chemiresistive, b) backgated FET, and c) SGFET exposed to an aqueous solution. d) The schematic of a SFGET operating in aqueous environment using Pt gate electrode, e) The shift in neutrality point of graphene upon exposure to various pH, measured in the static mode of FET	20
Figure 2.6	a) Energy band diagram of graphene and n-type Si after junction formation, b) shift in graphene fermi energy depending on the doping processes.	22
Figure 2.7	a) Schematic of graphene/n-Si Schottky devices, change in b) series resistance and c) ideality factor and SBH of Schottky junction by exposure to molecules with different electron accepting ability. d) The reverse biased response of UV-illuminated G/n-Si junction to BSA	25
Figure 2.8	Three phases contact lines of water droplet on solid with the corresponding forces	26
Figure 2.9	Arrangement of ions in at the graphene/electrolyte interface on a) hydrophobic and b) hydrophilic substrates, c) Dependence of WCA in graphene device on the doping state of graphene	29
Figure 2.10	Theoretical models on EDL and their corresponding ion arrangement: 1) Helmholtz, 2) Gouy-Chapman Stern, 3) Grahame's theories.	33

Figure 2.11	A comprehensive equivalent circuit explaining the EDL structure in graphene devices, b) Deviation of experimental decay length from theoretically measured Debye length	37
Figure 2.12	A schematic of defect induced pH response of graphene caused by oxygen based functional groups	40
Figure 2.13	Charge transfer by proton injection/extraction mechanism	45
Chapter 3	Defect Engineering of Graphene to Modulate pH Response of Graphene Devices	
Figure 3.1	(a) Schematic illustration and real image of a chemiresistive sensor consisting of a glass substrate, pencil-drawn rectangles as contacts, FLG as the active layer, copper tape for contacts and parafilm as a dielectric. SEM images of the drop-casted FLG on the glass substrate in different magnifications of (b) 1 μm and (c) 100 nm.	67
Figure 3.2	(a) Raman Spectra of sonicated FLG for 6 h, 12 h, and 18 h revealing the change in defect density level. Chemiresistive sensing performance of sonicated samples: (b) 6 h, (c) 12 h, and (d) 18 h of sonication. (e) Calibration curves of the corresponding sensors and (f) plot of change in sensitivity by variation of I_D/I_G .	69
Figure 3.3	Sensing calibration curves and schematic representation of N_2 -annealed sensors (a,b) 1 h, (c,d) 4 h, and (e,f) 8 h, respectively.	70
Figure 3.4	(a) Raman Spectra of the N_2/H_2 - annealed samples, (b) variation of I_{2D}/I_G ratio by annealing duration, (c) plot of I_D/I_G versus annealing duration, (d) plot of I_D/I_G vs I_D/I_G representing the stage of defect density.	72
Figure 3.5	Sensor performance, calibration curves, and schematic illustration of (a–c) 1 h, (d–f) 4 h, (g–i) 6 h, and (j–l) 8 h N_2/H_2 annealed sensors, respectively. Schematic models of surface charge modulation due to the presence of double layer at graphene/solution interfaces for (m) acidic solution, (n) basic solution.	73
Figure 3.6	UV–visible spectra of the pyrene derivatives functionalized FLG at different pH values (a) Py- NH_2 /FLG, (b) Py- OH /FLG, (c) PyCHO/FLG, and (d) Py-COOH/FLG.	75
Figure 3.7	The sensing performance of PD functionalized sensors. a) Py- NH_2 /FLG b) Py-CHO/FLG c) Py-COOH/FLG d) Py- OH /FLG e) Schematic representation of defect-induced	76

mechanism by functional groups at different pH values. The red dots represent the double layer.

Figure 3.8	Relationship of graphene's pH sensitivity with surface defect density. The inset shows the experimentally obtained data for blank, annealed, and sonicated samples.	76
Figure 3.9	FTIR spectrum of 6h sonicated FLG that shows the presence of various oxygen based functional groups on the surface/edge.	83
Figure 3.10	Raman of N ₂ -annealed samples for 1h, 4h, and 8h	84
Figure 3.11	Graphene chemiresistive response of N ₂ annealed samples a) 1h, b) 4h, and c) 8h	85
Figure 3.12	Examples of deconvoluted Raman spectra for (a) blank samples, and (b) 1 h, (c) 4 h, (d) 6 h and (e) 8 h N ₂ /H ₂ -annealed samples.	86
Figure 3.13	Visual depiction of 1-aminopyrene adsorbed onto an 8x8 graphene flake. Visualized using Avogadro.	90
Figure 3.14	Schematic illustration of directional excitation in pyrene molecules	91
Figure 3.15	Absorption spectra of pyrene derivatives in pH 3-8	93
Figure 3.16	Absorption spectra of FLG in pH range of 3 to 8	94
Figure 3.17	Calibration curves of PD functionalized graphene: a) Py-NH ₂ /FLG b) Py-CHO/FLG c) Py-OH/FLG d) Py-COOH/FLG	95
Figure 3.18	Plot of ID/IG ratio for pyrene derivative functionalized FLG compared to 8h N ₂ /H ₂ annealed sample	96
Chapter 4 Defect Density-Dependent pH Response of Graphene Derivatives: Towards the Development of pH-Sensitive Graphene Oxide Devices		
Figure 4.1	Sensor fabrication steps: (a) Cleaning and pre-patterning with pencil-drawn contacts, (b) airbrushing FLG, and (c) attachment of Cu tape and dielectrics. (d) SEM image of the FLG airbrushed on the surface, (e) the I-V curve of the fabricated chemiresistive sensor indicating the ohmic device (sensor resistance was ~10 kΩ).	100

- Figure 4.2 XPS high-resolution spectra of (a) O 1s and (b) C 1s of SLG, (c) pH response of SLG between pH 5.5–8 (the inset shows the corresponding calibration curve) with $I_o = 1524$ nA, and (d) schematics illustration of the formation of EDL on graphene in acidic solution and its electrostatic gating charging. 102
- Figure 4.3 XPS high-resolution spectra of (a) O 1s and (b) C 1s of FLG, (c) pH response of FLG to pH 5.5–9 ($I_o = 1788$ nA), (d) Raman of FLG deconvoluted to the main graphene characteristics of D, G, D', and 2D (inset shows the deconvoluted Raman spectrum of SLG), and (e) schematic illustration of defect-induced pH response of FLG through protonation/deprotonation of carboxyl, hydroxyl, and amine groups. 103
- Figure 4.4 Sensing performance of 8 h annealed FLG functionalized by (a) 0.3 mM ($I_o = 1274$ nA), (b) 0.15 mM ($I_o = 1980$ nA), (c) 0.1 mM ($I_o = 2052$ nA), and (d) 0.05 mM ($I_o = 1812$ nA) of Py-COOH; (e) the calibration bar graph of the sensors demonstrating the highest pH response at around -COOH pKa (3.1). The error bars represent average \pm standard deviation of the last two minutes of the chemiresistive response (3 samples each). 106
- Figure 4.5 Variation of FLG pH sensitivity as a function of (a) carboxyl, (b) amine, and (c) hydroxyl defect densities. The error bars represent the average \pm standard deviation of the last two minutes of the chemiresistive response (3 samples each). 107
- Figure 4.6 Sensing performance of 8 h annealed FLG functionalized by (a) 1.4 mM ($I_o = 2035$ nA), (b) 0.7 mM ($I_o = 2775$ nA), (c) 0.35 mM ($I_o = 2330$ nA), and (d) 0.1 mM ($I_o = 1927$ nA) of Py-NH₂. (e) The graph represents the calibration curve of the Py-NH₂-functionalized sensors. The sensing performance of 8 h annealed FLG functionalized with (f) 1.6 mM ($I_o = 385$ nA), (g) 0.8 mM ($I_o = 1220$ nA), and (h) 0.4 mM ($I_o = 764$ nA) of Py-OH. (i) The calibration bar graph of the sensors demonstrating the maximum pH response at pH around -OH pKa (8.7). The error bars represent the average \pm standard deviation of the last two minutes of the chemiresistive response (3 samples each). 107
- Figure 4.7 The GO sensor fabrication: (1) Bare GO; (2) Bare GO exposed to the aqueous solution for 30 min; (3) Bare GO exposed to the aqueous solution for 6 min; (4) The GO chemiresistor without water exposure; (5) GO annealed for 6 h and (6) 26 h; (7) The 24 h annealed GO-based chemiresistor. (b) Deconvoluted Raman spectrum of 24 h-GO represents the presence of (from left to right): D, D*, G, D', 2D, 2D', D + G, and an ID/IG ratio of 1.3. (c) The pH response and (d) 109

calibration curve of 24 h-GO ($I_0 = 242$ nA). The solution conductivity response of (e) FLG ($I_0 = 2870$ nA) and (f) 24 h-GO-based devices ($I_0 = 1050$ nA).

Figure 4.8	XPS survey spectra of a) SLG, b) FLG	114
Figure 4.9	Raman spectra of FLG before and after exposure to pH	115
Figure 4.10	Raman spectrum of 8h annealed FLG	116
Figure 4.11	pH response of 8h annealed FLG	117
Figure 4.12	Calibration curve of the pH response of 8h annealed FLG	119
Figure 4.13	The Lorentzian deconvolution of GO Raman spectrum	121

Chapter 5 Graphene versus Concentrated Electrolytes: An Experimental Study to Explore the Role of the Electrochemical Double Layer

Figure 5.1	a) Raman spectra of FLG (black), FLG exposed to NaCl solution (Blue), and FLG-drop cast 0.1 M NaCl (red), b) chemiresistive response of FLG to the addition of NaCl in 0 ppm DO solution. e) chemiresistive response and f) calibration curve of FLG to the addition of NaCl in the presence of DO (7 ppm).	127
Figure 5.2	Chemiresistive response of graphene to variation of DO between 0 (N ₂ purged) and 11 ppm (air purged) in a) 1 mM NaCl, b) 10 mM NaCl, c) 100 mM NaCl solutions, d) schematic illustration of EDL at graphene/electrolyte interface focusing on the role of DO.	131
Figure 5.3	a) Graph of change in sensor response as a function of theoretical Debye screening length (blue) for two sections of ideal (black) and non-ideal (red) solutions. Chemiresistive sensing response of FLG to c) LiCl, d) NaCl, and e) KCl. (The insets show the corresponding calibration curves).	134
Figure 5.4	Change in the ionic conductivity of the a) LiCl, b) NaCl, and c) KCl solution as a function of concentration.	141
Figure 5.5	Variation of dissolved oxygen in a solution equilibrating with air upon purging N ₂ and air	142
Figure 5.6	Voltage-dependent response graphene chemiresistive device in a) 10 mV, b) 50 mV, c) 100 mV, and d) 500 mV applied potential, d) signal-to-noise ratio of the sensors operate at each voltage with the $n=6$.	143
Figure 5.7	Change in theoretical Debye screening length of the solution as a function of NaCl concentration	144

Figure 5.8	pH response of graphene to pH 3-5 before and after the exposure to highly concentrated NaCl solution (0-600 mM).	144
Figure 5.9	Nyquist plots of FLG chemiresistive sensor in 50 mM NaCl in 0 and 7 ppm dissolved O ₂ .	145
Figure 5.10	The linear slopes of chemiresistive response as a function of screening length for a) low range and b) high concentration regions.	145
Figure 5.11	Defect density-dependent EDL response of graphene surface exposed to NaCl solution for a) graphene, reduced GO for b) 12 h, c) 9h, and d) 6h under N ₂ /H ₂ environment at 350 °C	146

Chapter 6 Graphene-Silicon Schottky Devices For Operation in Aqueous Environments: Device Performance and Sensing Application

Figure 6.1	a-f) Device fabrication process, g) schematic illustration of the proposed platform indicating the thickness and lateral dimensions.	152
Figure 6.2	a) Raman spectrum of monolayer graphene transferred on SiO ₂ . XPS high-resolution spectra of b) O1s and c) C 1s for transferred graphene. FESEM images of transferred graphene on d) SiO ₂ and e) interface of Si and SiO ₂ indicating the continuity of the film, f) J-V curves of the G/n-Si device.	153
Figure 6.3	a) Variation of G/n-Si R _s by exposure to various concentrations of NaCl (the inset shows changes in FSBH with solution conductivity, i.e., ionic strength), b) The schematic illustration of the EDL and charge doping of the graphene surface by the inner Helmholtz layer. The variation of c) R _s and d) ϕ_{SB} as a function of Debye length shows the impact of changes in the EDL on surface characteristics, e) The schematic representation of EDL at high ionic strength. An increase of ionic strength reduces the screening length (Debye length).	154
Figure 6.4	a) J-V curves of a G/n-Si Schottky diode upon exposure to pH 3-8 (inset illustrates the corresponding semi-logarithmic graph), b) change in series resistance and ϕ_{SB} (inset) of the device as the results of pH.	155
Figure 6.5	a) J-V curves of G/n-Si exposed to various concentrations of free chlorine. b) obtained device response by the change in resistance upon increasing the free chlorine concentration (inset shows the change in ϕ_{SB}), c) Graph represents the change in solution conductivity by addition of free chlorine at different NaCl background concentrations, d) change in ORP	157

- response of G/n-Si junction (blank) as a function of the ionic strength of the solution.
- Figure 6.6 a) Raman spectra of 1-aminopyrene (bottom) and 1-aminopyrene doped graphene (top), extracted b) R_s and c) in φ_{SB} variation of devices at given free chlorine concentrations, Cl 2p high-resolution XPS spectra of AP/G/n-Si d) before and e) after exposure to free chlorine. N 1s high-resolution XPS spectra of AP/G/n-Si f) before and g) after exposure to free chlorine 158
- Figure 6.7 Schematic illustration of the mechanism by which the electronic band structures of G/n-Si are modulated upon addition of free chlorine on a) blank and b) AP-doped sensors. The electronic structure highlights the conduction band (E_c), valence band (E_v), and Fermi energy (E_f) of the n-Si in contact with graphene. The position of E_f (purple dashed line) represents the p-doped nature of the graphene. FM , FS ; φ , and χ are indicative of graphene work function, Si work function, the built-in potential of the junction, and electron affinity of Si, respectively. 159
- Figure 6.8 Anionic interference (on the left side of dashed line) study by addition of 2.5 ppm HPO_4^{2-} , 250 ppm SO_4^{2-} , 25 ppm NO_3^- , 43.5 ppm Cl^- , 11.2 ppm HCO_3^- , and 0.5 ppm free chlorine (the inset on shows the relative sensor response of anions to free chlorine response). b) cations interference test (on the right side of the dashed line) by addition of 4.2 ppm K^+ , 7.1 ppm Mg^+ , and 12.3 ppm Ca^+ (inset shows the relative sensor response of cations to free chlorine response), b) oxidant interference study at pH 5.6 by addition of 1.34 μM of each oxidant (0.5 ppm $HOCl = 9.53 \mu M$) 160
- Figure 6.9 Raman spectrum of Graphene before PMMA removal. 166
- Figure 6.10 The plot of solution conductivity ($mS.cm^{-1}$) of an aqueous solution upon addition of NaCl. 168
- Figure 6.11 Change in pH of the solution upon addition of free chlorine 169
- Figure 6.12 a) plot of oxidation reduction potential of the solution by addition of free chlorine b) change in the device series resistance with increasing the ORP values. 169
- Figure 6.13 a) $dV/dLnJ$ vs. J graphs for the blank device at forward bias, demonstrating the validity of the used circuit model, b) the H vs. J graphs of the blank device, revealing the linearity of the fitted lines with less than 10% offset from the model. 170
- Figure 6.14 J-V curves of AP-G/Si upon exposure to free chlorine concentrations 170

Figure 6.15	J-V curves of a) G/n-Si and b) AP/G/n-Si devices before and after exposure to water (the insets show the corresponding semi-logarithmic J-V curves)	171
Figure 6.16	a) $dV/d\ln J$ vs. J graphs for AP/G/n-Si at forward bias, demonstrating the validity of the used circuit model, b) the H vs. J graphs of AP/G/n-Si device, revealing the linearity of the fitted lines with less than 10% offset from the model.	171
Figure 6.17	Blank and AP doped device performances upon addition of NaCl at different concentrations.	172
Figure 6.18	Variation of rectification factors for blank (black-top) and doped (red-bottom) devices at different free chlorine concentrations.	173
Figure 6.19	J-V curves of AP-doped device upon variation of pH from 3 to 8 (the insets represent the corresponding semilogarithmic curves).	173
Figure 6.20	UV-vis absorption spectra of 1-aminopyrene molecules at pH 3-8.	175
Figure 6.21	Change in R_s and Φ_{SB} (inset) of the 1-aminopyrene doped devices upon exposure to pH 3-8.	176
Figure 6.22	Real-time chemiresistive measurements of a) blank b) AP-doped sensors upon exposure to free chlorine, c) calibration curves of the sensors.	177
Figure 6.23	Comparison of blank and AP-doped G/n-Si Schottky diode and chemiresistive responses to free chlorine under same conditions.	177

List of Tables

Chapter 3 Defect Engineering of Graphene to Modulate pH Response of Graphene Devices

Table 3.1	Solubility Information of PDs	68
Table 3.2	HOMO-LUMO energies of Py-NH ₂ , Py-OH, and Py-COOH in Solution and adsorbed onto a 8×8 graphene sheet	74
Table 3.3	Summary of information derived from deconvoluted Raman spectra	89
Table 3.4	Adsorption energies and distances of Py-NH ₂ , Py-OH, and Py-COOH in both protonated and deprotonated forms.	90
Table 3.5	Calculated UV-Vis peak positions (oscillator strength in brackets)	92
Table 3.6	Calculated UV-Vis triplet state positions	92

Chapter 4 Defect Density-Dependent pH Response of Graphene Derivatives: Towards the Development of pH-Sensitive Graphene Oxide Devices

Table 4.1	Summary of the oxygen-containing groups obtained from XPS spectra of SLG and FLG	104
Table 4.2	Summary of information on pyrene concentrations and their corresponding relative surface coverage obtained from literature.	118
Table 4.3	Average ± standard deviation of Py-COOH functionalized sensors to pH range 3-8 (3 sensors each)	119
Table 4.4	Average ± standard deviation of maximum response of pyrene derivative functionalized sensors as a function of surface density (3 sensors each)	120
Table 4.5	Average ± standard deviation of Py-NH ₂ functionalized sensors to pH range 3-8 (3 sensors each)	120
Table 4.6	Average ± standard deviation of Py-OH functionalized sensors to pH range 3-9 (3 sensors each)	120

Chapter 6 Graphene-Silicon Schottky Devices For Operation in Aqueous Environments: Device Performance and Sensing Application

Table 6.1	Comparison of solid-state free chlorine sensors in literature with this work	160
-----------	--	-----

List of All Abbreviations and Symbols

2D	two dimensional
A*	Richardson's constant
AFM	Atomic Force Microscopy
APS	Ammonium Persulfate
BSA	Bovine Serum Albumin
C _{ads}	Adsorption Capacitance
C _B	Bulk Solution Capacitance
C _H	Helmholtz Capacitance
CH ₃ COOH	Acetic Acid
CNT	Carbon Nano Tube
CPE	Constant Phase Element
DFT	Density Functional Theory
DH	Debye-Hückel
DI	Deionized
DO	Dissolved Oxygen
EA	Electron Acceptor
E _C	Conduction Band Energy
ED	Electron Donor
EDL	Electrochemical Double Layer
E _f	Fermi Energy
EIS	Electrochemical Impedance Spectroscopy
E _o	Vacuum Energy
E _V	Valence Band Energy
FE	Field Emission

FET	Field Effect Transistor
FLG	Few-Layer Graphene
G	Graphene
GNR	Graphene Nano Ribbon
GO	Graphene Oxide
H ₂ O ₂	Hydrogen Peroxide
HCl	Hydrochloric Acid
HCO ₃ ⁻	Bicarbonate
HOCl	Hypo chloric Acid
HOPG	Highly Ordered Pyrolytic Graphite
I	Ionic Strength
I _D	D-band intensity
IEFPCM	Integral Equation Formalism Polarizable Continuum Model
I _G	G-band intensity
IHL	Inner Helmholtz Layer
IPA	Isopropanol
KCl	Potassium Chloride
KMnO ₄	Potassium Permanganate
LiCl	Lithium Chloride
LOD	Limit of Detection
M	Metal
NaCl	Sodium Chloride
NH ₃	Ammonium
NO	Nitrogen monoxide
NO ₂	Nitrogen dioxide

OCI ⁻	Hypochlorite
OCP	Open Circuit Potential
OH ⁻	Hydroxide ion
OHL	Outer Helmholtz Layer
ORP	Oxidation Reduction Potential
PCAT	Phenyl-Capped Aniline Tetramer
PD	Pyrene Derivative
PDMS	Polydimethylsiloxane
PMMA	Poly methyl methacrylate
PTFE	Polytetrafluoroethylene
Py	Pyrene
r-GO	reduced Graphene Oxide
R _{int}	Interface resistance
S	Semiconductor
SCL	Strongly Correlated liquid
SEM	Scanning Electron Microscopy
SFG	Sum Frequency Generation
SFM	Surface Force Measurement
SGFET	Solution Gated Field Effect Transistor
SGFET	Solution Gated-Field effect Transistor
Si	Silicon
SiO ₂	Silicon dioxide
SLG	Single Layer Graphene
SO ₄ ²⁻	Sulfate ion
TE	Thermionic Emission

TFE	Thermionic Field Emission
UV-Vis	Ultraviolet-Visible
V_{bi}	Built-in potential
V_G	Gate Voltage
WCA	Water Contact Angle
WHO	World Health Organization
XPS	X-ray Photoelectron Spectroscopy
Z	ion charge
η	ideality factor
Φ_G	Graphene Work Function
Φ_S	Semiconductor Work Function
Φ_{SB}	Schottky Barrier Height
χ	Semiconductor Affinity

Declaration of Academic Achievements

Chapter 3 is based on the article published in the *Langmuir* (Angizi, S., Yu, E.Y.C., Dalmieda, J., Saha, D., Selvaganapathy, P.R. and Kruse, P., 2021. *Langmuir*, 37(41), pp.12163-12178). Shayan Angizi and Peter Kruse designed the study. E.Y.C.Y. performed the pH experiments. S.A. performed the pH experiments, Raman characterization and both UV-Visible and FTIR spectroscopies. J.D. performed the simulation and theoretical studies. D.S. helped in analyzing the Raman spectra and deconvolution processes of the peaks. P.R.S. revised the manuscript and improved the discussions pertaining to sensing mechanisms.

Chapter 4 is based on the article published in *Nanomaterials* (Angizi, S., Huang, X., Hong, L., Akbar, M.A., Selvaganapathy, P.R. and Kruse, P., 2022. *Nanomaterials*, 12(11), p.1801). The author's contribution to this paper is as follows: S.A. and P.K. designed the experiments. S.A. operated the pH experiments, analyzed the data and wrote the original draft of the manuscript. X.H. operated the pH experiments and annealing processes of graphene oxide. L.H. performed pH experiments, helped with data analysis, and Raman measurements and developed a reproducible sensor fabrication method. M.A.A. prepared the setup and contributed to the discussions of pH in the water without the presence of buffer solution as well as operating UV-Visible measurements. P.R.S revised the manuscript and contributed to the discussions.

Chapter 5 is based on a draft prepared for submission. The author's contribution to this chapter is as follows. S.A. and P.K. designed the study. S.A. performed the ionic strength experiments, data analysis, and Raman characterizations and wrote the original draft of the manuscript. L.H. also performed the experiments and data analysis. X.H. helped set up the dissolved oxygen setup and L.H. operated the experiments.

Chapter 6 is based on the article published in *Carbon* (Angizi, S., Selvaganapathy, P.R. and Kruse, P., 2022. *Carbon*, 194, pp.140-153.) The author's contribution is as follows. S.A. and P.K. designed the study. S.A. performed the device fabrications, experiments, and

characterization and wrote the original draft of the manuscript. P.R.S. revised the manuscript and contributed to the development of the discussion.

Chapter 1 Introduction

1.1 Motivation

The rising importance of graphene has made it a pivotal part of future technology, particularly chemical devices, from chemical sensing platforms¹ to energy devices². Applications of graphene as sensing materials mainly rely on its unique electronic properties, exceptional conductivity, ambipolar characteristics together with the (ultra) large specific surface area and modifiable surface chemistry^{3,4}. Accordingly, graphene has become an irreplaceable part of solid-state gas⁵, water quality⁶, and bio sensing technologies⁷. Most applications of graphene involve the presence of aqueous electrolytes, which are comprised not only of water molecules, but also ions, dissolved molecules, gases, and other chemicals. However, despite graphene's inherent potential, interpretation of graphene interaction with aqueous electrolytes has remained a challenge. It is mainly because an aqueous electrolyte brings a multi-dimensional interacting environment to graphene: i) graphene may interact with water molecules, determined by its surface hydrophobicity⁸; ii) the arrangement of the ions at the graphene/electrolyte interface, known as electrochemical double layer (EDL), may alter the properties of graphene⁹; iii) dissolved gases and molecules in the solutions may cause surface charge transfer¹⁰. As a result of this interacting environment, it is often difficult to interpret how graphene responds to changes in aqueous electrolytes. Moreover, the type and strength of graphene interactions with aqueous electrolytes depends on its physical characteristics such as thickness, lateral size, defectivity¹¹. Additionally, solution parameters, including pH, oxidation-reduction potential (ORP), and ionic strength can add to this system's complexity¹². The motivation behind this thesis is to explore how graphene solid-state sensors respond to changes in pH, ORP, and ionic strength of solutions. Chemiresistive and Schottky diode devices having graphene transducer were utilized to trace the interactions through changes in the output signal.

1.2 Structure of this Thesis

Chapter 2 begins by explaining the fundamentals of graphene's crystallography, properties, and synthesis processes. Then, special attention is given to reviewing the graphene's defects and derivatives. The chapter then continues by discussing the working principles of three most used device configurations of chemiresistors, Schottky diodes, and Field Effect Transistors (FETs). Afterwards, possible interfacial interactions between graphene and aqueous solutions are discussed, categorizing the interactions into four sections of i) electrostatic gating effect; ii) surface charge transfer, iii) substitutional doping, and iv) ion trapping. In each mechanism, the focus is given to explaining the chemistry of reactions followed by the literature review.

In chapter 3, the pH responsivity of graphene is shown to be caused by two simultaneous mechanisms: electrostatic gating, and defects in the graphene material. We showed that charge transfer caused by the electrostatic mechanism results in opposite charge doping of the protonation-deprotonation of oxygen-containing functional groups. Accordingly, adjusting graphene defectivity could result in the modulation of graphene pH sensitivity. The plot of sensitivity in pH response as a function of defectivity (measured by Raman spectroscopy) was presented, illustrating the regions in which each sensing mechanisms are dominant.

In chapter 4, we showed that modulating the defect density as well as the type of the defect on graphene is an approach to developing highly pH-sensitive graphene derivatives. We utilized pyrene-based molecules containing graphene's functional groups to selectively module graphene's pH responsive sites. It is shown that the density and types of pH responsive sites (i.e., carboxyl, hydroxyl, amine, etc.) influence its sensitivity. Moreover, multiple graphene derivatives, including single-layer graphene, few-layer graphene, and graphene oxide, were characterized by XPS and Raman spectroscopy, and tested against pH. As a result, a slightly reduced GO (thermally reduced in N_2/H_2) was developed that is sensitive to pH changes from 3-10 (up to 180% change in current).

In chapter 5, the impact of the ionic strength of electrolytes on the performance of graphene chemiresistors is explored. The alkaline chloride salts are used to adjust the ionic strength. Then, the relationships among ionic strength, theoretical Debye length and sensor response are obtained. The results reveal the deviation from the ideal behavior predicted by the Debye-Hückel theory occurs at low concentrations (50 mM for NaCl and 10-20 mM for KCl) in graphene compared to commonly used substrates SiO₂ (500-600 mM). The crucial role of dissolved oxygen (DO) in the EDL of graphene is also explored, demonstrating that the higher ionic strength results in a larger graphene sensitivity to DO. This study aims to present a more thorough understanding of how ions are arranged in EDL and how that affects graphene properties through changes in experimental decay length.

In chapter 6, more advanced devices such as graphene/silicon Schottky junctions are constructed to provide a deeper interpretation of the interactions. The formation of a potential barrier against electron flow and the exponential dependence of junction resistance on change in barrier energy provide an ultra-sensitive platform for interactions. In light of this, the study focused on the detection of free chlorine as the model system since its addition simultaneously alters the pH and ORP of the solution. The junction was also exposed to the change in pH, ORP, temperature, and ionic strength, and descriptive explanations for the change in graphene properties are reported. Lastly, the functionalization of graphene with external molecules (1-aminopyrene) is explored to improve the sensitivity toward free chlorine detection, resulting in a limit of detection (LOD) and sensitivity values of 59 nM and 0.53 μM^{-1} , respectively.

Finally, chapter 7 summarizes the main findings of each research study, focusing on their contributions to the science. Also, some of the possible future projects are introduced to reveal a pathway for future researchers to follow.

1.3 References

- (1) Yavari, F.; Koratkar, N. Graphene-Based Chemical Sensors. *J. Phys. Chem. Lett.* **2012**, 3 (13), 1746–1753. <https://doi.org/10.1021/jz300358t>.

- (2) Zang, X. Graphene-Based Flexible Energy Storage Devices. In *Graphene*; Elsevier, 2018; pp 175–199. <https://doi.org/10.1016/B978-0-12-812651-6.00007-0>.
- (3) Guo, S.; Dong, S. Graphene and Its Derivative-Based Sensing Materials for Analytical Devices. *J. Mater. Chem.* **2011**, *21* (46), 18503. <https://doi.org/10.1039/c1jm13228h>.
- (4) Varghese, S.; Varghese, S.; Swaminathan, S.; Singh, K.; Mittal, V. Two-Dimensional Materials for Sensing: Graphene and Beyond. *Electronics* **2015**, *4* (3), 651–687. <https://doi.org/10.3390/electronics4030651>.
- (5) Choi, J. H.; Lee, J.; Byeon, M.; Hong, T. E.; Park, H.; Lee, C. Y. Graphene-Based Gas Sensors with High Sensitivity and Minimal Sensor-to-Sensor Variation. *ACS Appl. Nano Mater.* **2020**, *3* (3), 2257–2265. <https://doi.org/10.1021/acsnm.9b02378>.
- (6) Zubiarraín-Laserna, A.; Kruse, P. Review—Graphene-Based Water Quality Sensors. *J. Electrochem. Soc.* **2020**, *167* (3), 037539. <https://doi.org/10.1149/1945-7111/ab67a5>.
- (7) Peña-Bahamonde, J.; Nguyen, H. N.; Fanourakis, S. K.; Rodrigues, D. F. Recent Advances in Graphene-Based Biosensor Technology with Applications in Life Sciences. *J. Nanobiotechnology* **2018**, *16* (1), 75. <https://doi.org/10.1186/s12951-018-0400-z>.
- (8) Melios, C.; Giusca, C. E.; Panchal, V.; Kazakova, O. Water on Graphene: Review of Recent Progress. *2D Mater.* **2018**, *5* (2), 022001. <https://doi.org/10.1088/2053-1583/aa9ea9>.
- (9) Jurado, L. A.; Espinosa-Marzal, R. M. Insight into the Electrical Double Layer of an Ionic Liquid on Graphene. *Sci. Rep.* **2017**, *7* (1), 4225. <https://doi.org/10.1038/s41598-017-04576-x>.
- (10) Leonardi, S. G.; Aloisio, D.; Latino, M.; Donato, N.; Neri, G. Dissolved Oxygen Sensor Based on Reduced Graphene Oxide; 2014; pp 89–93. https://doi.org/10.1007/978-3-319-00684-0_17.
- (11) Pak, A. J.; Paek, E.; Hwang, G. S. Impact of Graphene Edges on Enhancing the Performance of Electrochemical Double Layer Capacitors. *J. Phys. Chem. C* **2014**, *118* (38), 21770–21777. <https://doi.org/10.1021/jp504458z>.
- (12) Angizi, S.; Selvaganapathy, P. R.; Kruse, P. Graphene-Silicon Schottky Devices for Operation in Aqueous Environments: Device Performance and Sensing Application. *Carbon N. Y.* **2022**, *194*, 140–153. <https://doi.org/10.1016/j.carbon.2022.03.052>.
- (13) Angizi, S.; Yu, E. Y. C.; Dalmieda, J.; Saha, D.; Selvaganapathy, P. R.; Kruse, P. Defect Engineering of Graphene to Modulate PH Response of Graphene Devices. *Langmuir* **2021**, *37* (41), 12163–12178. <https://doi.org/10.1021/acs.langmuir.1c02088>.

Chapter 2 Graphene/Aqueous Electrolyte Interfacial Interactions

This chapter focuses on investigating the interfacial interactions between graphene derivatives and aqueous electrolytes. For this purpose, the properties of graphene are initially reviewed, particularly physical characteristics that influence surface chemistry. In addition, the relationship between graphene properties and its synthesis approach is described, emphasizing the importance of surface pre-treatment. Next, the working principles and fundamentals of two-terminal graphene-based solid state sensing devices are described. It is elucidated how the device configuration can influence electrical output signal. Every section begins with a literature review that examines the limitations of practical application and understanding of the performance of graphene-based devices in aqueous solutions. Then, interfacial interactions between graphene and electrolytes are discussed, revealing four charge transfer mechanisms of electrostatic gating effect, surface charge transfer, substitutional doping, and ion trapping. The final section focuses on the future possibilities for better interpretation of electrolyte interactions with aqueous media.

2.1 Graphene

Graphene refers to a monolayer of carbon atoms bonded through sp^2 hybridized networks. Such structure (with lateral sizes above 20 nm) was believed to be thermodynamically unstable till 2004 when Andre Geim and Konstantin Novoselov successfully isolated a monolayer of carbon atoms through a scotch tap exfoliation process¹. In a graphene lattice, the sp^2 hybridization is made by $2s$, $2p_x$, and $2p_y$ orbitals, forming three bonds per carbon atom. The nature of the bonds is considered purely covalent and due to the existing $2p_z$ electrons, a pi-electron cloud exists above the surface^{2,3}. This electron cloud is made by two π electrons in each hexagon resulting in superior conductivity of graphene, making graphitic films a candidate for applications in which the electrical transducer material is required. Accordingly, many chemical or electrical properties of graphene heavily depend on the symmetry of the electron clouds in the lattice^{4,5}.

2.1.1 Synthesis

A graphene film can be synthesized in two ways: top-down and bottom-up (Figure 2.1). In a top-down method, graphite precursors are broken down into smaller flakes and undergoes two size reduction events: i) exfoliation, and ii) lateral size reduction^{6,7}. The former means that the stacked graphene layers in graphite structure are diverged by dominating the applied forces to π - π interactions between two adjacent layers⁸. These forces are often provided by external sources. Examples of such exfoliation are liquid exfoliation (e.g., sonication processes⁹, ball milling¹⁰, etc.), where the solvent's chemical and mechanical interactions with the edges of graphite sheets cause the lattice expansion and exfoliation. In a sonication process, the applied sonic forces through the solvent yield the local temperature to increase and intensify the solvent/graphite interactions¹¹. Similarly, the explosion of solvent bubbles generated by the sonication applies both normal and shear forces to the graphite lattice, leading to a reduction in lateral size and thickness, respectively⁸. According to the method of synthesis, the symmetry of graphene's electron cloud, number of layers, and lateral dimension differ significantly. Notably, even though the exfoliation product may contain defects, it is cost-effective and could be scaled up. One issue with liquid exfoliation of graphene is the use of toxic solvents such as Dimethylformamide (DMF)¹², Dimethyl sulfoxide (DMSO), or N-Methyl-2-pyrrolidone (NMP)¹³. In fact, overcoming the π - π interactions requires solvents with surface tension larger than the surface energy of graphene to facilitate intercalation processes¹⁴. Nevertheless, recent examinations have employed solvent chemistry to utilize greener alternatives such as water, isopropanol, ethanol, or acetone¹⁵⁻¹⁷.

The bottom-up processes include the reactions in which sp^2 networks of carbon-carbon bonds are assembled gradually to build graphene sheets¹⁸. Chemical Vapor Deposition (CVD) and Physical Vapor Deposition (PVD) are the most commonly used approaches for the bottom-up synthesis of graphene. However, other liquid-based syntheses, such as solvothermal or

hydrothermal methods, have recently been developed to synthesize GQDs or GNPs^{19,20}. Comparing graphene properties produced by top-down and bottom-up approaches commences with the film quality. The former usually results in smaller flakes unsystematically shaped via a procedure with many external chemical species (defect). While in the latter, the reaction kinetics are directed, and optimization of parameters leads to an exceptionally smooth, large area, atomically thin graphene with a well-defined electronic structure²¹.

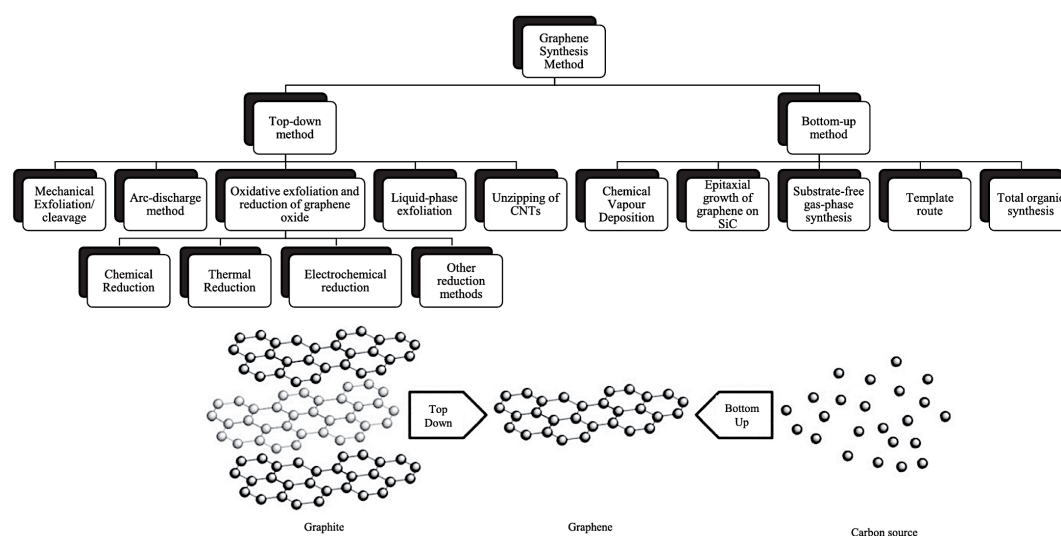


Figure 2.1. Synthesis methods of graphene ²². Reprinted with permission from Elsevier © Copyright 2018.

The synthesis process of monolayer graphene is CVD technique in which gaseous precursors are introduced to the preheated substrate surface, mainly Cu and Ni. The produced graphene layer should be transferred to the desired substrate for subsequent applications²³. Since the quality of the graphene strongly depend on the transfer method, various techniques such as wet²⁴, dry²⁵, Electrochemical delamination²⁶, roll-to-roll²⁷, and support-free transfer methods²⁸ have been developed. Although the processing details of each method are different, they will contain at least a few of the following steps: i) Formation of a layer of flexible polymers such as polymethyl methacrylate (PMMA) or Polyvinyl alcohol (PVA) on graphene film; ii) etching the substrate and obtaining floating graphene in the etching solutions; iii) rinsing graphene sheets to eliminate the excess solvents and chemical species; iv) transferring to the desired

substrate followed by heat treatment. In the first step, a thin layer of PMMA or PVA is spin-coated on graphene to form a transparent flexible support layer for when the substrates are etched off^{29,30}. For etching the substrate, ammonium persulfate and iron (III) chloride solutions have been the most used etchants for Cu and Ni, respectively³¹. For Cu, binary solutions (H₂O₂: HCl, 1:2) or other mixtures such as HCl: H₂O₂:CuSO₄:5H₂O (50 mL:50 mL:10 g) have also been utilized. In practice, however, they are not commonly used due to complications associated with subsequent contamination removal^{31,32}.

2.1.2 Nanomorphology and Derivatives

To this moment, a variety of graphene-based nanomaterials have been introduced. The most standard (and thermodynamically stable) ones are as follows: single layer graphene (SLG), few-layer graphene (FLG), Graphene nanosheets (GNSs), graphene oxide (GO), reduced GO, graphene nanoribbons (GNNRs), and graphene quantum dots (GQDs)³³. A complete demonstration of graphene derivatives can be found in Figure 2.2 The term SLG refers to a one-atom-thick sheet of graphene. Since the thickness is atomically thin, the surface chemistry is significantly stimulated by the surroundings, particularly the substrate. The provided surface area by monolayer graphene can be as high as 2640 m²/g, much higher than carbon nanotubes

(100-1000 m²/g) or even carbon black (850-900 m²/g). Also, monolayer graphene is low in defect and is used to devise (ultra) sensitive chemical sensors due to its surface sensitivity³⁴.

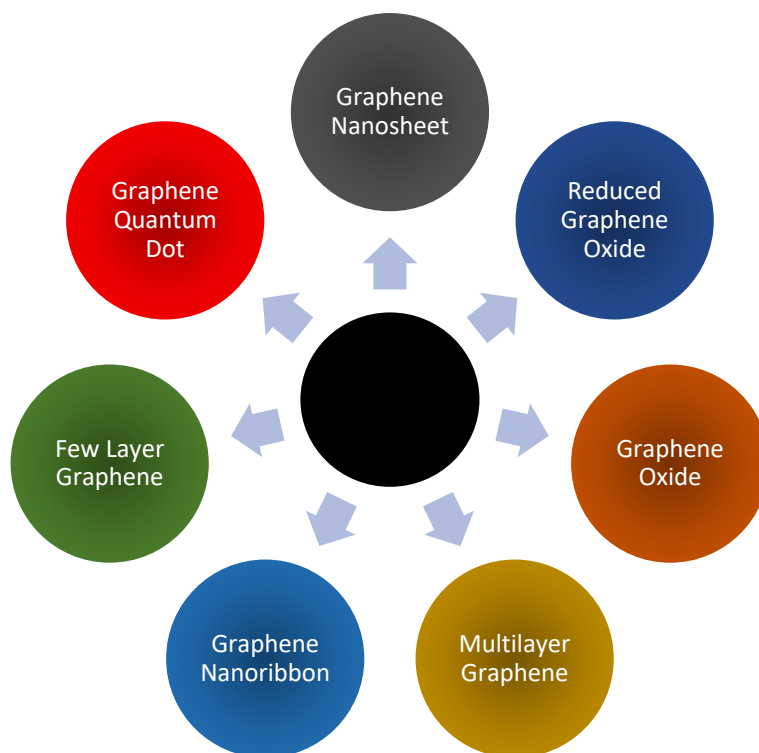


Figure 2.2. Graphene derivatives.

2.1.3 Properties

Graphene's unique optoelectronic properties have become the center of its popularity, in addition to its synthesis and physical characteristics. The conjugation of p electrons in graphene generates π (valence) and π^* (conduction) bands. In defect-free graphene, the Fermi energy is defined where the valence (HOMO) and conduction (LUMO) collide³⁵. According to the tight-binding model resolved for honeycomb lattices, the graphene Bravais lattice involves two atoms of A and B in a repeating order. In the momentum space called Brillouin Zone (BZ), there are still six points (two non-equivalent sets of three points) named K and K', acting as the neutrality or Dirac points of the graphene^{36,37}.

Moreover, the linear dispersion of electrons in graphene leads to a zero effective mass at the Dirac point. Graphene's unique band structure can also be explained in more detail by considering it a zero-band-gap semiconductor³⁸. Considering the Fermi energy at the charge

neutrality point of pristine graphene, any shift in the Fermi energy causes it to cross over the Dirac point, into the conduction or valence layers. This means that depending on the chemistry of graphene, both p-doped and n-doped graphene are possible, carrying the hole and electrons as majority carriers, respectively³⁹. In other words, graphene is ambipolar and can be electrically doped through chemical absorption or electric fields to tune the charge carriers between electrons and holes⁴⁰. This phenomenon is essential in graphene sensing applications since a single interaction with the target analyte can be detected by the change in the current density of graphene, depending on its p- or n- doping. The graphene ballistic transport mechanism is another reason for its extensive functionality as a transducer in the presence of external media⁴¹. This property determines the electron's ability to travel across the film (order of sub-micrometer) without facing electric resistivity caused by external adsorbates or topographical disturbance.

2.1.3.1 Number of Layers (thickness)

The graphene's electronic properties depend on multiple parameters, including the number of layers, edge configuration, and defectivity. Varying the number of layers impacts the electronic structures so that SLG is deemed a zero-bandgap semiconductor while graphite with $n=\infty$ is a semi-metal with nearly 40 meV overlap of conduction and valence bands⁴¹. Therefore, based on the thickness, graphene is categorized as follows: monolayer ($n=1$), bi-layer ($n=2$), and multi layers ($2 < n < 10$). Based on recent publications, the band overlap of graphene with $n=11$ is only 10% different from that of graphite⁴². Also, the thinner film may contain higher degrees of unwanted chemical species in a liquid exfoliation process. Since the presence of external chemicals causes disturbing symmetry of electron clouds, the exfoliation process deteriorates the overall conductance^{42,43}. The surface current generated by the adsorbates can also be affected by the thickness of the graphene. The surface current in a thin graphene sheet dominates the carriers moving across the film. Upon increasing the thickness, however, the bulk current is added to the overall current; therefore, the ratio of the surface to bulk current

decreases significantly. This observation was verified by a reduction in the graphene-based sensor's surface sensitivity to analytes by increasing the thickness⁴⁴. This balance between conductivity enhancement and preserving the surface current is the key challenge in selecting thickness for graphene application.

2.1.3.2 Edge termination

The edge configuration of graphene is also a determining factor in graphene's properties. The edges could have either zigzag (Figure 2.3.a), armchairs (Figure 2.3.b), or arbitrary configurations (Figure 2.3.c). Based on the tight bonding approaches, the zigzag edges show the edge-band near the Fermi level due to the delocalized orbitals caused by the presence of dangling bonds. In contrast, the armchair edge configuration in GNRs shows semiconductive characteristics and is strongly sensitive to the width of the sheet. Moreover, due to high edge formation energies in graphene (10 eV nm^{-1}), the edges are prone to interact actively with the surroundings⁴⁵. These interactions can be amplified by edge stresses, commonly found after high-intensity fabrication methods of graphene (i.e., probe sonication or ball milling). Understanding the edge configuration and its impact on the properties becomes a complex topic when the number of layers increases. Stable crystallographic configurations of graphene layers can be either ABA (Bernal – Figure 2.3.d) or ABC (Rhombohedral - Figure 2.3.e). Although nearly 80% of the graphite powder in nature is found in Bernal configurations, introducing chemical species during the synthesis may disrupt the arrangement of layers and edges⁴⁶.

Therefore, the edge chemistry of graphene should be monitored for a deeper understanding of its electronic properties and chemical reactivity.

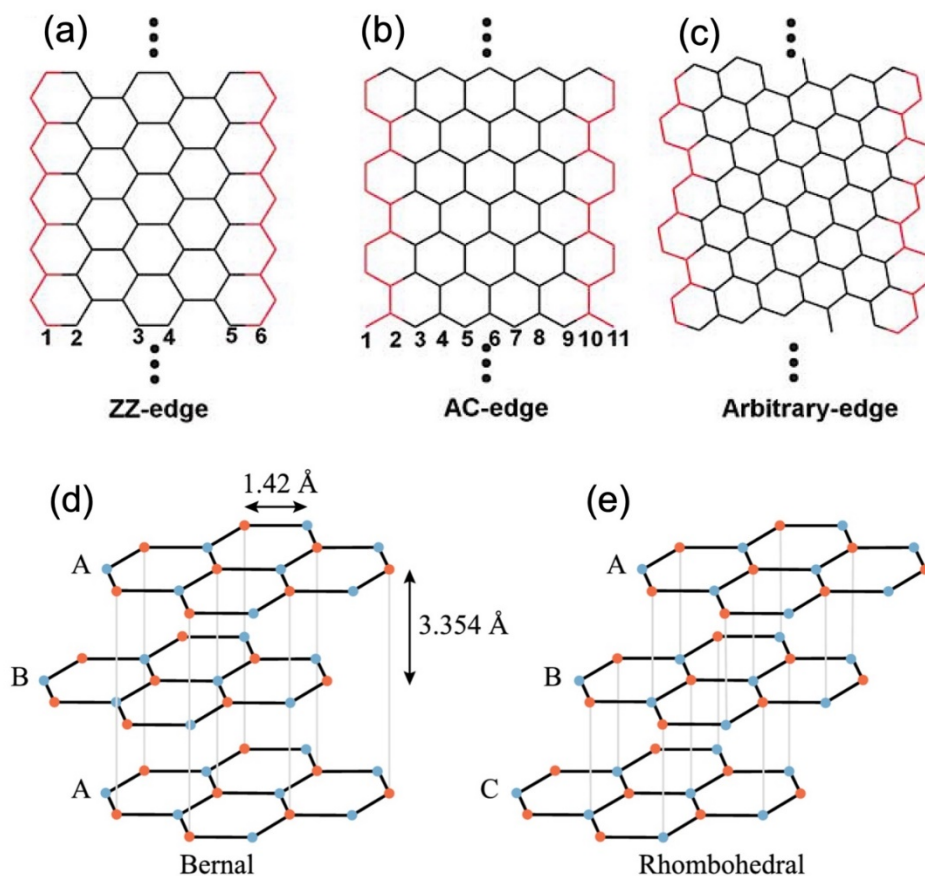


Figure 2.3. a) zigzag, b) Armchair and c) arbitrary edge configuration of graphene⁴⁵. Reprinted with permission from Royal Society of Chemistry (RSC), © Copyright 2013. Two possible graphene layer sequences of d) Bernal and e) Rhombohedral⁴⁶. Reprinted with permission from IOP, © Copyright 2020.

2.1.3.3 Defectivity

The defectivity of graphene is also a vital parameter determining the performance of graphene devices. The term 'defect' refers to the presence of non- sp^2 networks of carbon atoms. The infinite symmetry of the graphene lattice is disrupted when hybridization is altered⁴⁷. These defects could be point defects, one-dimensional defects, dopants, or functional groups. While point defects could be produced during exfoliation or post-heating steps, they are more often created through bottom-up reactions when precursor reactions are not stoichiometric⁴⁸. The

most expected point defects in monolayer and multi-layer graphene are as follows: Stone-Wales, single vacancies, multiple vacancies, and edge defects⁴⁹. The Stone-Wales defects are triggered by the existence of non-hexagonal rings that do not require removed or added atoms to the structure. The stress applied to the graphene sheets causes hexagons to be repositioned to two pentagons and two heptagons through the rotation of C-C bonds⁴⁹. Stone Wales defects are not easily made due to high formation energy ($E_f = 5$ eV) and are difficult to identify through spectroscopic measurements. Accordingly, high-resolution electron microscopies are usually employed to detect these atomic dislocations in graphene lattice⁵⁰ (Figure 2.4.a). The single vacancy defects are caused by missing one lattice atom. Notably, single vacancies could create up to three in-plane dangling bonds, enhancing the surface energy of graphene⁵⁰ (Figure 2.4.b). Multiple vacancies, also called double vacancy defects, are created when two atoms are missing, initiating a complex defect configuration. Remarkably, the odd numbers of bonds are ascertained to be energetically favored. Therefore, the double vacancy configuration may be adjusted to preserve one or three dangling bonds. This will later enhance the surface energy and, subsequently, the chemical reactivity of graphene film considerably.

Another point defect is the one-dimensional defects observed in numerous experimental studies on graphene (Figure 2.4.c)⁵¹. This defect is shaped when two graphene domains with different crystal orientations meet at the interface. These tilt boundaries could either be dangling bond-free (hexagon) or produce pairs of pentagons at the junction. These boundaries, in addition to other point defects, could be utilized for many subsequent surface treatments due to readily available bonds and controllable grain sizes of graphene⁵¹. A change in the edge termination of graphene sheets due to the removal of one or more carbon atoms is called an edge defect. Thus, the armchair edge can be converted to a zigzag upon removing one atom. In contrast, removing one atom from zigzag termination leads to forming (open) pentagons. The chemical/physical adsorption of atoms to the edge to saturate the dangling bonds could also vary the lattice parameters, enhancing the disorder level of graphene⁵².

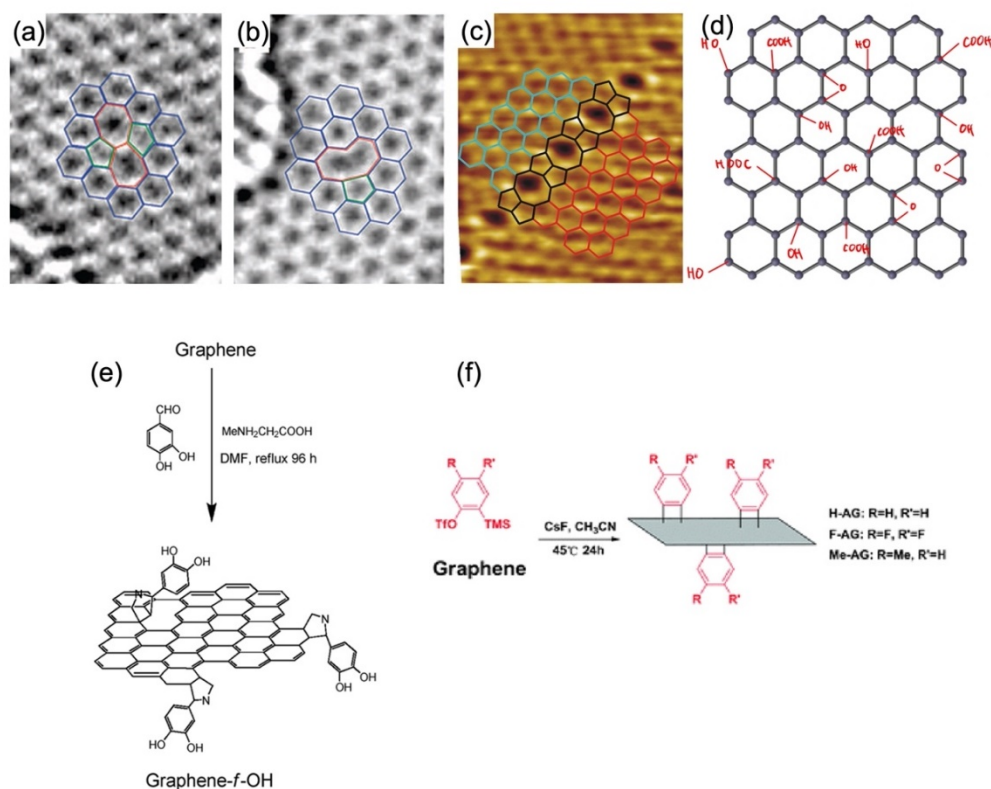


Figure 2.4. High resolution electron microscopy images of a) Stone Wales, b) single vacancy⁵⁰. Reprinted with permission from American Chemical Society (ACS), © Copyright 2008, and c) one-dimensional defects in graphene⁵¹. Reprinted with permission from Springer Nature, © Copyright 2010. d) Schematic of graphene sheets containing oxygen-based functional groups on the plane and edge. e) example of covalent functionalization of graphene planes and edges using azomethine ylide⁵³. Reprinted with permission from Royal Society of Chemistry (RSC), © Copyright 2010. f) An example of non-covalent functionalization of graphene using aryne cycloaddition reactions⁵⁴. Reprinted with permission from Royal Society of Chemistry (RSC), © Copyright 2010.

The chemical or physical interactions of foreign atoms with graphene mainly result in doping. Dopants could replace or displace carbon atoms in the hexagonal rings and form other point defects⁵⁵. Inspired by doping processing in semiconductor research, dopants can modulate the majority carriers in graphene. The most common dopant of graphene is oxygen, which can replace carbon and leave behind one single vacancy per ring⁵⁶. However, due to the atomic radii difference between oxygen and carbon, the lattice expansion causes topographical distortion, affecting carrier mobility⁵⁶. As discussed in the properties of graphene, shifting the Fermi level away from the Dirac point causes a change in the balance of electrons and holes. By

introducing the oxygen dopants, the graphene is hole-doped due to larger electronegativity values than carbon, leading to lowering the Fermi energy⁵⁶. Studies have revealed that a small amount of oxygen (O/C~0.01) is nearly unavoidable in graphene; therefore, graphene derivatives are considered intrinsically p-doped⁵⁷. Hence, CVD-grown SLG transferred on SiO₂ may still show a carbon-to-oxygen atomic percent ratio of 0.01-0.02. Nevertheless, besides oxygen, graphene has been reported to be doped by many other atoms such as alkaline metals⁵⁸, alkaline earth metals⁵⁹, transition metals⁵⁹, halogens⁶⁰. In addition, graphene hybridization with external molecules or functional groups has also been considered a defect. The formation of various oxygen-based functional groups such as carboxyl (–COOH), hydroxyl (–OH), ether (–O–), carbonyl (–C=O), aldehyde (–CHO) and ester (–COO–) has frequently been reported upon oxidation of graphene during the synthesis or transfer processes (Figure 2.4.d). In fact, by increasing the oxygen content above a certain level, graphene enters the GO region. In GO, oxygen content can be as high as 40%, creating semiconductive characteristics⁶¹. Other common functional groups of graphene are amine and amide, mainly based on nitrogen⁶¹. Besides, graphene has also been frequently functionalized with external molecules via covalent (Figure 2.4.e) or non-covalent interactions (Figure 2.4.f). On one side, π electrons provide a fertile surface for molecules to bind through π - π or Lewis acid-base interactions^{54,62}. On the other side, direct covalent binding with carbon atoms converts the sp^2 hybridization to sp^3 , altering the defectivity level. Notably, the nature of π -complexes could vary classified as follows based on the condition: cation- π interaction, anion- π , H- π interaction, π - π interaction, and nonpolar interaction of gas- π ⁶².

2.2 Graphene-Based Chemical Sensors

In order to understand the interfacial interactions between aqueous electrolytes and graphene, it is necessary to understand the working principle of devices. These devices are made of graphene derivatives (i.e., monolayer, few-layer graphene, graphene oxide) as electrical

conductors and often operated at an applied potential. Below, three main categories of graphene-based solid-state devices have been discussed, focusing on the advantages and shortcomings of their operations in aqueous electrolytes.

2.2.1 Chemiresistors

Chemiresistive devices are solid-state platforms in which the transducing material is located between two contacts and applied potential to the contacts generates a current across the film⁶³.

The design of a chemiresistor is depicted in Figure 2.5.a Chemiresistors follow Ohm's law, meaning the voltage-current relationship is linear. After exposing the active film to the analyte and possible interactions, the change in the current (or resistance) is recorded over time⁶³.

Therefore, graphene resistance may increase or decrease depending on the type of interaction. This should be noted that no current passing through the solution or the bulk of the active layer contributes to the chemiresistive measurements. Also, a significant portion of the device resistance results from contact resistance⁶⁴.

Chemiresistors are relatively simple to fabricate, straightforward to use, and cost-effective. There are numerous reports on the gas sensing application of graphene chemiresistors for detecting NO_x ⁶⁵, H_2 ⁶⁶, CH_4 ⁶⁷, and NH_3 ⁶⁸. This extensive use of graphene for gas sensing relies on the simplicity of prediction of the direct interactions between analyte and graphene. For example, the chemiresistive resistance increases upon the interaction of electron-withdrawing groups such as NO_x with graphene⁶⁵. However, once the chemiresistor is placed in an aqueous electrolyte, in addition to the analyte, parameters such as pH, ORP, and ionic strength will interfere with the detection mechanism⁶⁹. This issue can be addressed by the interpretation of interfacial interactions and enhancing the sensitivity toward the target using surface modification. In 2017, it was demonstrated that noncovalent functionalization of a graphite film by phenyl capped polyaniline tetramer (PCAT), as a molecular switch, can enhance the graphene sensitivity towards water oxidants (i.e., free chlorine, HOCl/OCl^-)^{70,71}. Accordingly,

oxidizing the PCAT increases the sensor selectivity and sensitivity, giving the quantification range of 0.1-12 ppm. Our recent study also demonstrated that the SLG functionalized with 1-amino pyrene could result in LOD and sensitivity of 16.1 ppb and 51 ppm⁻¹, respectively, for free chlorine detection⁶⁹. The mechanism for such sensitive detection was proposed as chloramination of amine groups and covalent bonding. The enhanced sensitivity was revealed due to chloramination of amine groups, directly detecting both HOCl and OCl⁻ species⁶⁹.

Graphene chemiresistors have also been used to detect ions in water. Modifying reduced graphene oxide (r-GO) with a PASE linker was shown to enhance nucleophilic substitution reaction upon interacting with Hg²⁺⁷². The mercury ions hole-dopes the surface through direct charge transfer and reduce the resistance over time⁷². Graphene modification by self-assembling Au nanoparticles on 1-pyrenemethylamine was another method for detecting Cr (VI)⁷³. The subsequent noncovalent modification with 1,4 dithiothreitol could also facilitate disulfide bond formation and produce Cr³⁺⁷³. In 2021, Dalmieda et al.⁷⁴ revealed that surface treatment of FLG with bathocuproine could create a selective surface for detecting silver ions (Ag⁺) in water. The authors demonstrated a pH treatment for resting the sensors with nearly 100% recovery in Ag⁺ response⁷⁴.

2.2.2 Field Effect Transistors

Graphene-based Field effect transistors (GFETs) consist of a graphene conductive channel between two terminals named drain and source. The third terminal, called the gate electrode, is either located at the back of the substrate (Figure 2.5.b), or far in the solution (Figure 2.5.c)^{75,76}. The voltage applied between the drain and source generates a current across the graphene, while the applied voltage between the gate and source modulates the electric field produced by the gate electrode⁷⁷. The drain and source electrodes are often covered by an insulator to avoid bypassing the current to the solution. By applying a gate voltage (V_G), an electric field is generated perpendicular to the graphene surface and influences the current⁷⁷.

Since graphene demonstrates ambipolar charge characteristics, modulation of V_G results in a change in Fermi energy. The voltage in which graphene's neutrality point is obtained is usually called V_{Dirac} . Accordingly, if $V_G < V_{Dirac}$, graphene becomes a hole conductor while $V_G > V_{Dirac}$ results in electrons as the majority carriers⁷⁸. The current passing through graphene modulated by V_g can be obtained by Eq. 1⁷⁸:

$$I_{ds} = \frac{W}{L} \mu C_i |V_g - V_{Dirac}| V_{ds} \quad (1)$$

where I_{ds} is the current between drain and source terminals; W is the width, L is the length of the graphene channel; μ is the mobility of the charge carrier, and C_i is the total capacitance generated by the gate⁷⁸. In solution-gated FETs (SGFET), graphene interaction with aqueous solution forms parallel layers of ions in the vicinity of the surface. This ion arrangement is strongly affected by the V_G . The negative V_G accumulates positive charges near the electrode leading to an instantaneous configuration of counter ions at the graphene surface⁷⁹. This means the concept of EDL becomes important as the total capacitance (C_i) is defined by EDL capacitance (C_{EDL}) and graphene quantum capacitance (C_Q). The C_i of an SGFET is expressed by Eq. 2⁷⁸:

$$\frac{1}{C_i} = \frac{1}{C_{EDL}} + \frac{1}{C_Q} \quad (2)$$

Quantum capacitance varies with thickness, and its contribution to total capacitance decreases as thickness increases. In addition, SFGETs are more sensitive than other FET configurations because EDL screening lengths are usually smaller than gate dielectric thicknesses. As a result, SFGETs could be a viable candidate for sensitive water quality monitoring⁶³.

It is noteworthy to mention that the static mode characterization of SGFET (I_{SD} vs V_G at a constant V_{SD}) results in the plot of charge neutrality point as a function of the analyte concentration⁸⁰. Upon interacting with the surroundings, this graph shows whether graphene is electron-doped or hole-doped. For example, in the study of graphene pH sensitivity using an SFGET made by Pt gate electrodes (Figure 2.5.d), authors revealed that increasing the pH

induces electrons in the graphene⁸¹. As seen in Figure 2.5.e, the minimum conductivity shifts to a larger V_G , demonstrating the graphene has been n-doped. The mechanism for such a phenomenon was demonstrated as follows: in basic solutions, a deprotonated form of OH^- ($-\text{O}^-$) ions negatively charge the surface. Therefore, in summary, the static mode represents the graphene doping state before and during the interactions. The shift of minimum conductivity to larger V_G is interpreted as n-doping, while the red shift represents the hole doping⁸¹.

The dynamic mode characterization of SGFET results in the plot of change in current or resistance as a function of time during the interaction with the analyte. According to the literature, the static mode is required to investigate the doping state of graphene prior to, during, and after the exposure to analytes, while the dynamic mode is used for real-time monitoring⁸².

Apart from pH, SGFETs have been widely used for other aspects of water quality sensing, including interpretation of ionic strength⁸³, ion detection⁸⁴, and disinfectant detection⁸⁰. This means SGFETs provide a profound understanding of the device's operation upon interaction with the environment.

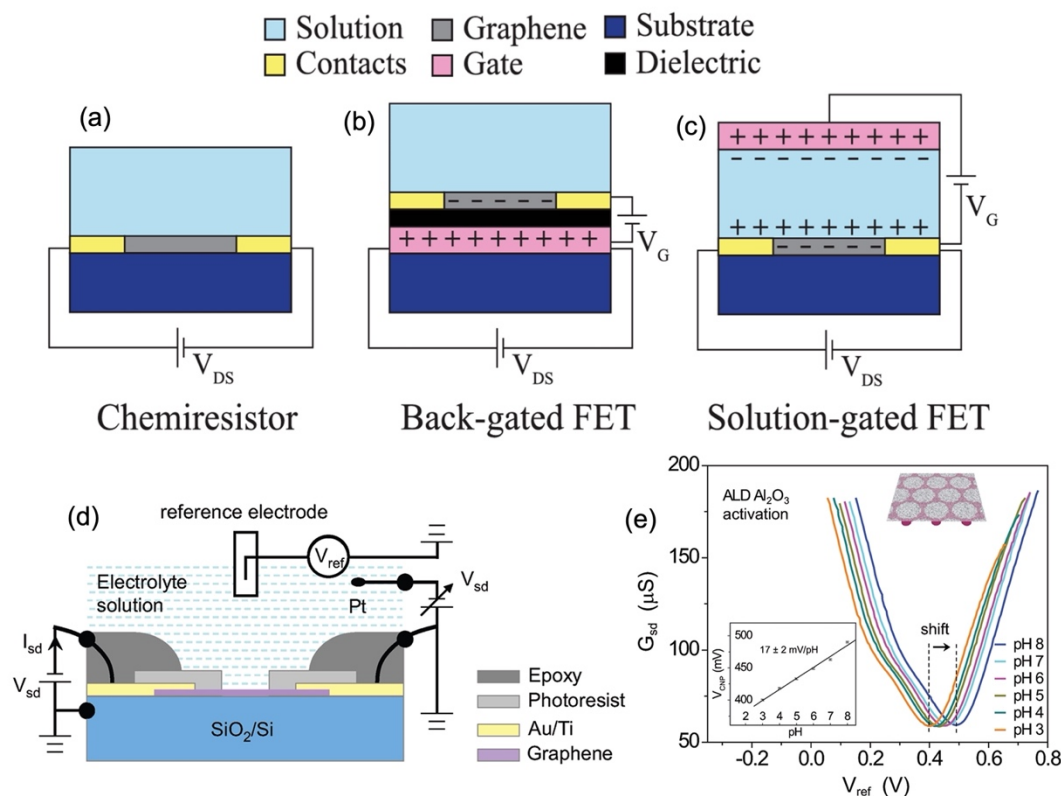


Figure 2.5. Devices configuration of a) chemiresistive, b) backgated FET, and c) SGFET exposed to an aqueous solution⁴⁶. Reprinted with permission from IOP, © Copyright 2020. d) The schematic of a SFGET operating in aqueous environment using Pt gate electrode, e) The shift in neutrality point of graphene upon exposure to various pH, measured in the static mode of FET⁸¹. Reprinted with permission from American Chemical Society (ACS), © Copyright 2011.

2.2.3 Schottky Diodes

2.2.3.1 Junction formation

Schottky diodes are another class of devices that can be exploited to explore the change in the electronic properties of graphene during interactions. The notion of diode denotes a non-linear dependence of current on voltage⁸⁵. Generally, the direct interaction of a metal and a semiconductor can lead to two behaviors: 1) non-rectification and 2) rectification. The former is when the current depends on the applied potential linearly. The latter, however, is called Schottky junction and makes electrons flow in one biasing direction and blocks the current in the opposite voltage direction. Based on the semiconductor studies, the interface between a metal (M) and semiconductor (S) can be either ohmic or Schottky, depending on the doping

level of the semiconductor⁸⁶. Since the discussion here is about graphene, the M is replaced by graphene (G).

Two key parameters of ϕ_s and ϕ_G indicate the work functions of semiconductor and graphene, respectively, which in this case $\phi_s < \phi_G$ ⁸⁷. The work function is theoretically defined as the minimum thermodynamic energy required to eject one electron from a ground state. The other parameter that needs to be explained is the electron affinity of the semiconductor (χ), which implies the amount of energy released or spent to add one electron to the conduction band of a gas phase particle and form an anion⁸⁷.

Upon the formation of the junction, electrons begin to flow from the semiconductor to graphene to align the Fermi energy levels on two sides of junctions due to thermal equilibrium in electron concentrations⁸⁸. Accordingly, the depletion of electrons in semiconductors generates an area without a mobile carrier occupied by positively charged immobile ions (Figure 2.6.a, positive and negative signs at the junction). The distribution of density of states in the proximity of the Dirac point in graphene does not allow the generation of conventional 'depletion regions'; however, the Coulombic interactions of positive ions (in semiconductor) attract electrons on graphene at the junction, creating an electric field, E ⁸⁸. This electric field acts as a barrier against the electron flow, named the built-in potential (V_{bi}). Also, discontinuity in the allowed energy state creates a potential barrier at the junction interface, named Schottky barrier (Φ_{SB}). This barrier is against the flow of electrons from G to S and acts similar to V_{bi} for the flow from S to G⁸⁹.

Considering the dependence of Φ_{SB} on the Fermi energy of the graphene, a small shift in this energy causes the electron to pass by the potential barriers and results in a significant current change. Figure 2.6.b shows that for the proposed system, electron doping reduces the Φ_{SB} by increasing the Fermi energy, while the barrier is strengthened upon hole-hole-doping.

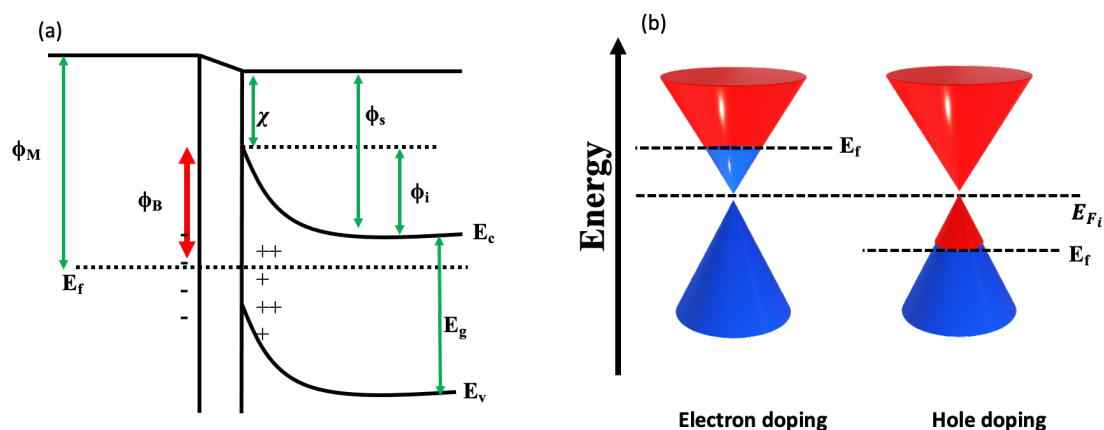


Figure 2.6. a) Energy band diagram of graphene and n-type Si after junction formation, b) shift in graphene Fermi energy depending on the doping processes.

According to Figure 2.6.a, Φ_{SB} for an ideal junction can be postulated by Schottky-Mott's equation (Eq. 3)⁸⁷:

$$\Phi_{SB} = \phi_M - \chi \quad (3)$$

2.2.3.2 Calculating Schottky Junction's parameters

Understanding the junction properties can be done through the extraction of multiple parameters by which the impact of surface reactions on the junction can be explored.

Considering the Thermionic emission equation obtained from (Eq. 5)⁸⁷:

$$J = J_s \left[\exp\left(\frac{q(V_D - (R_s I))}{\eta k_B T}\right) - 1 \right] \quad (5)$$

by isolating V, equation 6 will be produced⁸⁶:

$$V = \frac{\eta k_B T}{q} \ln\left(\frac{J}{J_s}\right) + J A R_s \quad (6)$$

by differentiation equation 6, we can obtain^{85,86,88}

$$\frac{dV}{dJ} = \frac{\eta k_B T}{q} \cdot \frac{1}{J} + A R_s \quad (7)$$

Therefore, plotting $\frac{dV}{dJ}$ vs. $\frac{1}{J}$ will lead to a linear dependence with slope and Y intercepts of ideality factor and series resistance, respectively. The ideality factor shows how close the junction is to operating in ideal conditions ($\eta=1$). The larger η represents larger current leakage

and inefficient electron TE transport process. To obtain Φ_{SB} , isolation of V from thermionic theory will result in:

$$V = JAR_s + \eta\Phi_{SB} + \frac{\eta k_B T}{q} \ln\left(\frac{J}{A^* T^2}\right) \quad (8)$$

and by defining the new term of H (J)⁶⁹:

$$H(J) \equiv V - \frac{\eta k_B T}{q} \ln\left(\frac{J}{A^* T^2}\right) \quad (9)$$

$$H(J) \equiv R_s AJ + \eta\Phi_{SB} \quad (10)$$

Accordingly, plotting H vs. J will result in a linear dependence having the slope and Y-intercepts of $A \times R_s$ (area \times series resistance) and $\eta \times \Phi_{SB}$ respectively⁶⁹.

The temperature dependence experiment of the device is also commonly done to calculate the voltage-independent Φ_B at 0 V as well as the “actual” value of Richardson’s constant. According to the literature, Φ_{SB} increases as temperature increases, therefore, saturation current decreases. This is due to the presence of carriers with sufficient thermal energy to jump over Φ_{SB} and reduce the width of the depletion region⁹⁰.

To calculate Φ_B and Richardson constant, the plot of $\ln\left(\frac{I_0}{T^2}\right)$ vs $\frac{1000}{T}$ is a straight line with the slope and Y-intercept of Φ_{SB} and A^* , respectively⁹⁰.

$$\ln\left(\frac{I_0}{T^2}\right) = \ln(AA^*) - \frac{\Phi_{SB}}{k} \cdot \frac{1}{T} \quad (11)$$

2.2.3.3 Sensing application

The ultra-sensitive nature of the junction to graphene properties provides a platform to explore graphene-aqueous electrolyte interactions. Traditionally, Schottky diodes have extensively been utilized for gas detection^{91,92}. But lately, their applications in aqueous electrolytes or detection of bio-analytes have grown. The study done by Kim et al. in 2013⁹³, demonstrated that G/n-Si junction properties are sensitive to the addition of liquid electron acceptor (EA) and donor (ED) molecules such as nitrobenzene, chlorobenzene, benzene, and anisole (Figure 2.7.a). They revealed that the η decreases upon exposure to EA while Φ_{SB} it increases from

0.79 to 80 eV (nitrobenzene)⁹³. (Figures 2.7.b and c). In contrast, strong EDs such as anisole decreased Φ_{SB} from 0.75 to 0.73 eV for the p-type Si). The mechanism for such behavior was explained by adjusting the Fermi energy of graphene upon exposure to molecules. By p-doping the graphene (exposing to EAs), the Fermi energy is lowered; therefore, the junction band bending increases⁹³. In 2019, Noroozi and Abdi⁹⁴ demonstrated the use of G/n-Si junction for the sensitive detection of BSA under UV exposure. The showed addition of this bioanalyte decreases the reserve bias current (Figure 2.7.d), leading to the high sensitivity of 0.5 A M^{-1} , LOD of 0.25 nM, and wide detection range of (100 nM to 100 μM)⁹⁴. In the recent study published by our research group⁶⁹, G/n-Si was operated in the aqueous electrolyte to explore the role of pH, ORP, ionic strength in graphene interaction with electrolytes. The device was then functionalized using 1-aminopyrene and used as a free chlorine sensor. Once the device is placed in aqueous electrolytes, the arrangement of the ion at the surface (EDL) affects electron transport by adjusting the Schottky barrier. The device showed that increasing the ionic strength from nearly $0.055 \mu\text{S}\cdot\text{cm}^{-1}$ (ultra-pure water) to $0.83 \text{ mS}\cdot\text{cm}^{-1}$ (8.55 mM NaCl) increased the R_s of the junction up to 257%⁶⁹. This significant increase in the resistance implies the critical role of electrolyte ions' capacitive charging in determining graphene's properties. The pH response of the G/n-Si junction was also determined: nearly 20% change in R_s of the junction by varying the pH between 3-8. This was shown for the interference correction caused by the pH detecting HOCl/OCl^- . The AP functionalized G/n-Si showed a linear range of 0.01-0.7 ppm, LOD of 3.1 ppb (59 nM) and a sensitivity of 10.2 ppm^{-1} , 5 times more sensitive than a chemiresistive platform with the same materials⁶⁹.

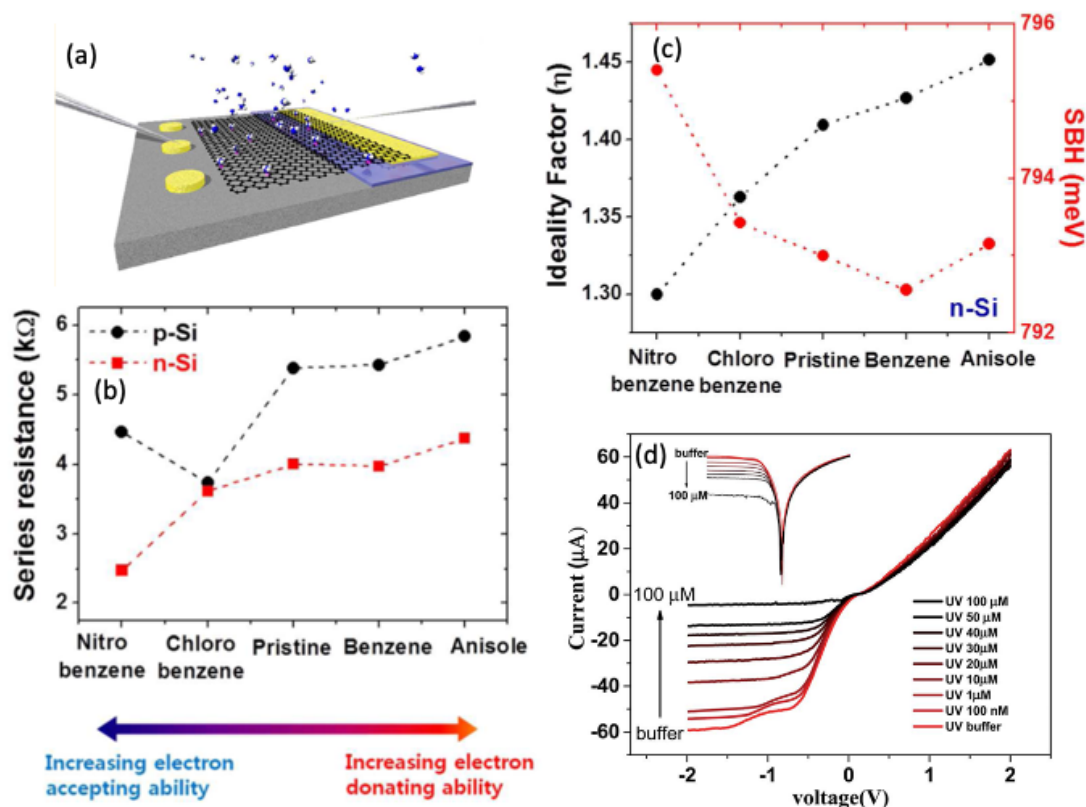


Figure 2.7. a) Schematic of graphene/n-Si Schottky devices, change in b) series resistance and c) ideality factor and SBH of Schottky junction by exposure to molecules with different electron accepting ability⁹³. Reprinted with permission from American Chemical Society (ACS), © Copyright 2013. D) The reverse biased response of UV-illuminated G/n-Si junction to BSA⁹⁴. Reprinted with permission from Royal Society of Chemistry (RSC) © Copyright 2019.

2.3 Graphene versus Water

2.3.1 Wettability of graphene

The wettability of graphene derivatives has been a controversial topic over the last decades. Defect-free SLG is an ideal model for studying surface hydrophobicity due to the long-ordered arrangement of the atoms and electron clouds⁹⁵. Nevertheless, since its substrate greatly influences its properties, it is not practical⁹⁵. In contrast, graphene's higher thickness provides less substrate-dependent influences; however, it is often accompanied by disordered lattices or defects. An ideal graphene was initially believed to be hydrophobic because of its highly symmetrical π -electron cloud as well as the non-polarity of the covalent bond. Therefore, various theoretical and experimental studies revealed contact angles of bare graphene could be in the realistic range of 95-100°^{96,97}. However, recent studies argue that the observed

hydrophobicity could originate from the instantaneously formed adsorbates (e.g., adventitious carbon) on graphene^{96,98}. In this section, we discuss factors affecting graphene's wettability in aqueous media, focusing on their impact on graphene applications.

Based on the water contact angle (WCA) measurements, graphene wettability can be categorized into four groups: super-hydrophobic ($150^\circ < \theta < 180^\circ$), hydrophobic ($90^\circ < \theta < 150^\circ$), hydrophilic ($10^\circ < \theta < 90^\circ$) and super-hydrophilic ($0^\circ < \theta < 10^\circ$). This angle is defined as a tangent angle at the liquid-gas interface (Figure 2.8) and can be calculated as follows²:

$$\cos\theta_Y = \frac{\gamma_{SV} - \gamma_{SL}}{\gamma_{LV}} \quad (12)$$

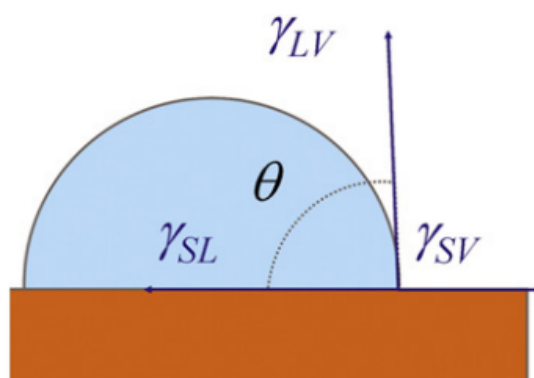


Figure 2.8. Three phases contact lines of water droplet on solid with the corresponding forces⁹⁹. Reprinted with permission from Elsevier, © Copyright 2009.

where, γ_{SV} , and γ_{SL} are the interfacial energies between liquid-vapor, solid-vapor, and solid-liquid, respectively. This angle and graphene /electrolyte interactions depend on three concepts 1) surface tension, 2) surface energy, and 3) surface interactions⁹⁹.

The surface tension of a surface is directly associated with the liquid surface. In fact, the surface tension (γ_{LV}) is due to the difference in the number of water molecules at the surface compared to the bulk. Accordingly, γ_{LV} is described as “the attractive forces between neighbouring molecules in a liquid’s surface layer which then causes the layer to behave as an elastic sheet.”

⁹⁹ Although the surface tension of water is high (72 mN/m), the shape of the water molecule

encountering the graphene surface will depend on the graphene surface energy as well as chemistry⁹⁶.

Surface energy is associated with the surface atoms' excess energy compared to the bulk material as they are not involved in chemical bonds¹⁰⁰. In fact, the surface free energy of material changes with the surface area, thickness, and the presence of adsorbates through the passivation of surface unterminated atoms. In an ideal condition where graphene and water molecules do not interact (i.e., superhydrophobicity), the surface tension and surface free energy become almost identical¹⁰⁰. However, the presence of local charges in the graphene lattice intensifies the graphene/water interactions; therefore, the two terms are not interchangeable. The literature shows graphene surfaces have smaller surface energy than wet surfaces¹⁰⁰. Also, in atomically thin graphene, the surface energy becomes excessively high as no bulk atom is present, and they all are surface atoms. Accordingly, it is expected to have lower wettability with the solvents having low surface tension.

Surface interaction also involves the possibility of graphene interacting with ions, molecules, and other chemical species in water⁹⁶. Since graphene interfacial interactions depend on surface chemistry, the parameters affecting these interactions can be classified as thickness, substrate, roughness or microtopography, defectivity, and edge termination.

2.3.1.1 Substrate

Graphene is transparent to wetting, particularly in thin structures, which means that the configuration of molecules and ions at the electrolyte/graphene interface depends on the substrate's hydrophobicity/hydrophilicity. As seen in Figures 2.9.a and b, exposing graphene transferred onto polytetrafluoroethylene (PTFE) and SiO₂, representing hydrophobic and hydrophilic surfaces, respectively, changes the arrangement of ions in EDL¹⁰¹. Therefore, WCA can vary from 95° to 70° in SiO₂ and PTFE, respectively. It should be noted that the first layer of ions is filled with positive ions due to the negative zeta potential of the graphene

surface caused by electronegative oxygen atoms. This indicates the sharper drop in the surface potential to the solution potential for hydrophilic surfaces¹⁰¹.

Moreover, the substrate could also influence the electronic properties of the graphene, and so its wettability. Researchers found that graphene is more receptive to covalent functionalization when transferred onto hydrophobic substrates such as SiO₂ and Al₂O₃ compared to an alkyl-terminated monolayer. In fact, interactions between graphene and oxygen-terminated substrates have been shown to lower graphene's average Fermi energy position, compared with h-BN and alkyl-terminated monolayers.¹⁰² This substrate dependent properties are important since the theoretical studies have revealed that doping states of graphene adjust the configuration of a water molecule. According to Hong et al.,⁹⁶ n-doped graphene (by substrate or gate-field) attracts the water dipole through hydrogen sides, resulting in a WCA of 78° (Figure 2.9.c). For p-doped graphene (60°), however, the oxygen atoms are closer to the surface, and due to the electronegativity difference, the Coulombic interactions are stronger. Therefore, the WCA can be lower than neutral graphene (88°) (Figure 2.9.c). It should be noted that the scenario is altered when graphene chemistry is changed by adding dopants or chemical functionalization⁹⁶.

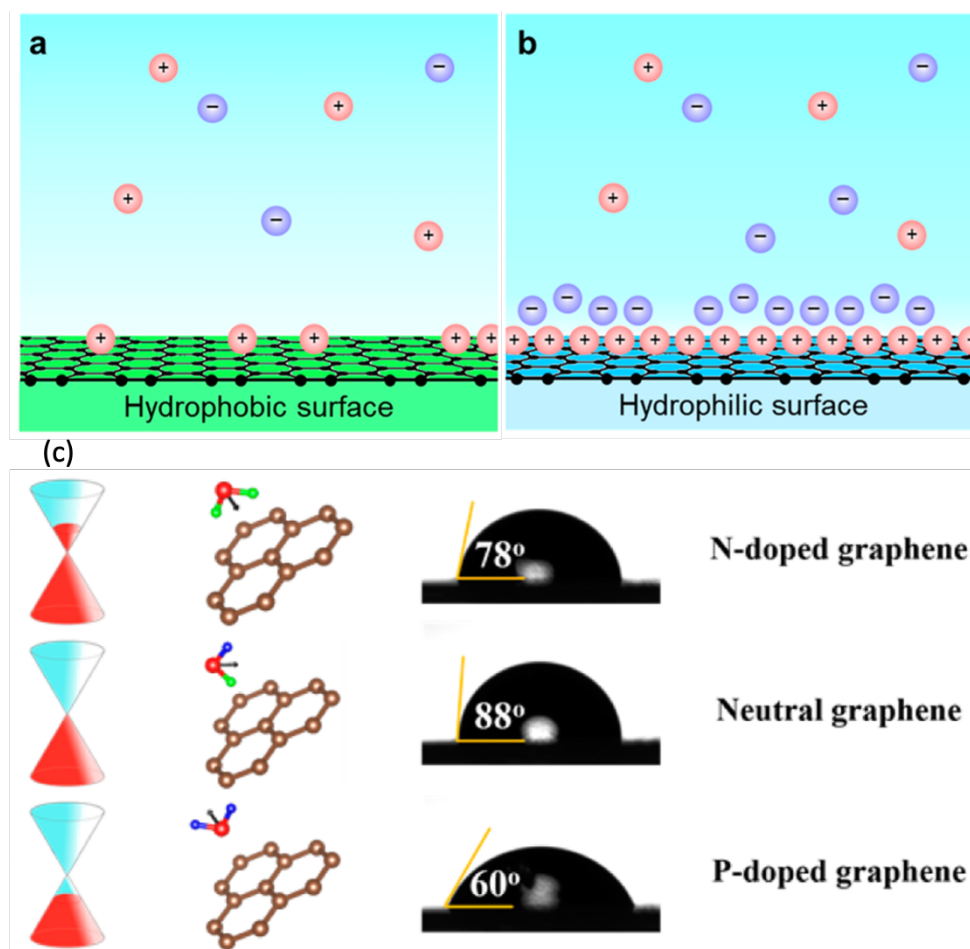


Figure 2.9. Arrangement of ions in at the graphene/electrolyte interface on a) hydrophobic and b) hydrophilic substrates¹⁰¹. Reprinted with permission from American Chemical Society (ACS), © Copyright 2019. c) Dependence of WCA in graphene device on the doping state of graphene on hydrophilic substrates (SiO₂)⁹⁶. Reprinted with permission from American Chemical Society (ACS), © Copyright 2016.

2.3.1.2 Topography and roughness

The surface topography and roughness of graphene films determine their wettability. Topography can be classified into two main types: macro and micro topographies. In the macro, the orientation of the graphene flakes deposited on the surface will create a nonuniform surface that is often not reproducible. Such morphology happens mostly when top-down synthesis methods are used, and the deposition technique (e.g., drop casting or airbrushing) forms a layer of products with the desired thickness. The micro-topographical issue often comes with bottom-up deposition methods whereby the atom-by-atom formation of the film could result in

microscale roughness. In both cases, surface roughness could influence graphene aqueous electrolyte contact angle through two simultaneous phenomena:

- 1) An air gap between the graphene and water.
- 2) Disruption in the arrangement of the ions.

Surface hydrophobicity is enhanced when air is present in the roughness of the surface or between flakes since the air-water contact angle is 180° .¹⁰³ This means more significant surface roughness may cause the graphene to repel water more, reducing graphene/aqueous solution interactions¹⁰⁴. However, higher roughness leads to larger edge exposure to the solution at the same time. Since the edges have a larger affinity than the plane for interaction with surroundings due to the dangling bonds, the WCA should be determined by the balance of these two phenomena. Moreover, the density of water molecules in droplets is altered when the solid surface is nonuniform. The water surface tension rises at sharp humps or downs, reducing the WCA with graphene. Therefore, the balance of trapped air, surface tension changes, and edge exposure would determine graphene water interactions.

2.3.1.3 Defectivity

According to studies on the change in WCA by the electric field, it was shown that p-doping through applying positive gate potential with respect to graphene on SiO₂ decreases the WCA⁹⁶. However, in all these experiments, the chemistry of graphene and bonds is preserved intact. A valid concern is, therefore, what happens to the surface if the chemistry changes. We can address this issue by looking at the impact of dopants and functional groups on graphene devices. Generally, upon the addition of oxygen atoms (as the most common dopant), carbon networks lose one electron per bond with oxygen; therefore, the balance of electrons and holes is disrupted. Due to this, the majority of carriers become holes⁵⁶. The WCA, however, is determined by the charges that electrolytes are subjected to, meaning the oxygen atoms provide non-bonding electrons, making the surface potential negative. This can be intensified by the

presence of the oxygen-based functional group. Comparing the zeta potential of FLG (-10 to +20 mV) and GO (-40 to -30) in neutral pH and their corresponding WCA demonstrates that higher surface charges will lead to larger hydrophilicity¹⁰³. The surface hydrophobicity increases upon functionalizing with large chain organic molecules, or groups containing -F, -CH₃^{64,81} etc.

2.3.1.4 Number of Layers (thickness)

It has been well-studied that graphene wettability is thickness dependent. Excluding the role of substrate here, it is increasing the thickness from one-atomic layer to two causes the increase in hydrophobicity¹⁰⁵. This was shown due to a change in the friction forces applied to the AFM tip caused by the arrangement of water molecules. Also, it was demonstrated that larger friction forces of 1L graphene might lead to out-of-plane puckering. Also, higher thicknesses of more than 11 layers refer to the structures like graphite, which is hydrophilic ($\theta < 80^\circ$). This means the WCA must increase from 1 to 2 and decrease from 2 to higher thicknesses. Thickness could also affect the substrate's impact on graphene's properties. Accordingly, thicker film results in receiving a lower effect of the substrate¹⁰⁵.

2.4 Interfacial Interactions

2.4.1 Electrostatic Gating Effect

To investigate capacitive charge transfer into graphene, it is imperative to understand the fundamentals of EDL. As a general rule, EDLs are composed of multiple parallel layers of ions and molecules arranged at the interface between solids and electrolytes. The composition of these layers has been extensively studied over the last few decades, resulting in the development of multiple theoretical models. The first reported model on the structure of EDL belongs to Helmholtz¹⁰⁶, where the polarized electrodes attract all counter ions to its surface (Figure 2.10-1). Helmholtz's theory is based on a typical capacitor with two oppositely charged

plates and a dielectric in between. For such capacitor, the total capacitance is expressed by^{106,107}:

$$C_H = \frac{\epsilon_0 \epsilon_r}{d} A \quad (13)$$

In this equation, ϵ_0 and ϵ_r are the permittivity values in vacuum and solution, respectively; A is the surface area of the electrodes¹⁰⁶. Although the calculation of EDL's capacitance seems simple using the abovementioned equation, accurate measurement of ϵ_r has been a challenge. The spectroscopic measurements have successfully determined the bulk solution's ϵ_r ; however, findings have revealed that the attraction of mobile charges to the graphene/electrolyte surface creates a concentration gradient. Therefore, thermodynamically unfavorable ions de-mixing (accumulation) results in different values of ϵ_r ^{108,109}. Moreover, Helmholtz's theory considers the distance between two plates as the radius of solvated ions, meaning the coordination numbers of the ions determine the thickness of the dielectric. Notably, the charge screening (image charges) outside of the solution is due to the polarization effect caused by the sudden change in the dielectric properties across the graphene/solution interface¹¹⁰.

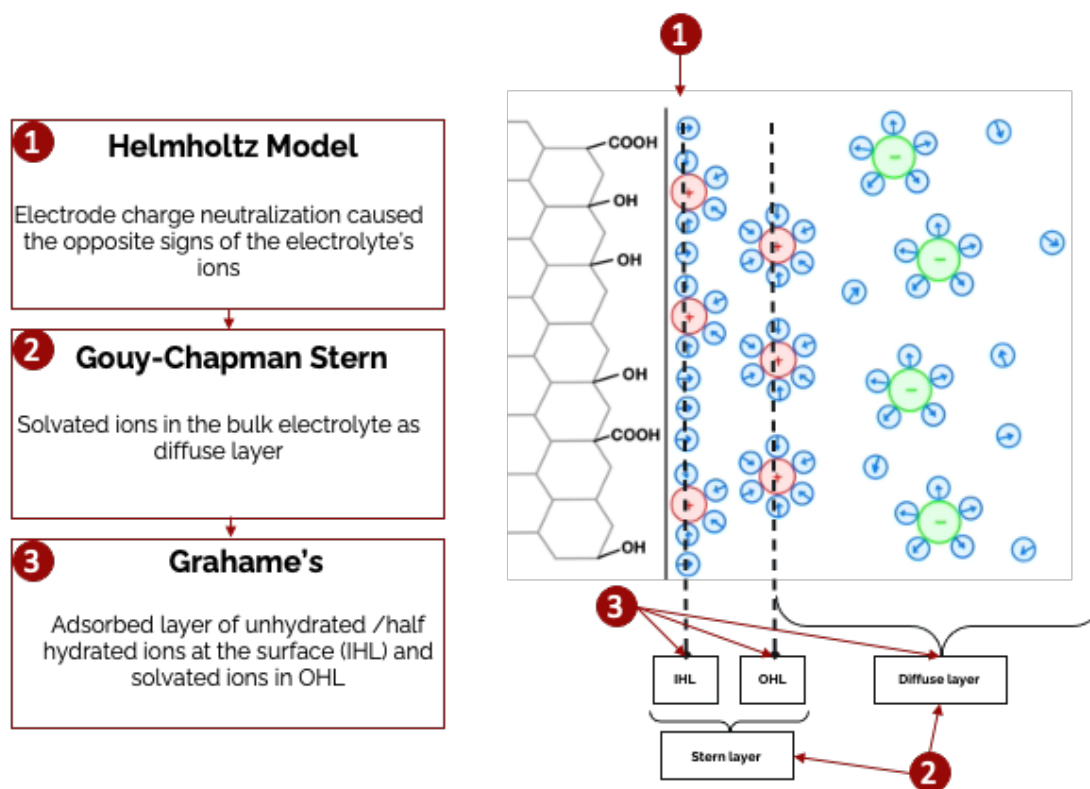


Figure 2.10. Theoretical models on EDL and their corresponding ion arrangement: 1) Helmholtz, 2) Gouy-Chapman Stern, 3) Grahame's theories.

Gouy and Chapman later improved the Helmholtz theory by introducing the concept of the diffuse layer¹¹¹. According to this theory, the ion's movement from/into Helmholtz layers occurred by the applied potential result in the EDL capacitance (Figure 2.10-2). The combination of the diffuse layer and the Helmholtz layer was later modelled by Stern¹⁰⁷, demonstrating that the total capacitance depends on the arrangement of the ions in the Helmholtz layer, and the movement of the ions in the Diffuse layers as follows¹⁰⁷:

$$\frac{1}{C_{EDL}} = \frac{1}{C_{Helmholtz}} + \frac{1}{C_{Diffuse}} \quad (14)$$

The composition of EDL was later completed by introducing three distinct layers of Inner Helmholtz Layer (IHL), Outer Helmholtz Layer (OHL), and the diffuse layer (Figure 2.10-3). The IHL and OHL could be classified as the Stern layer, where the ions are present close to the solid/electrolyte interface. In IHL, the hydrated ions and solvent molecules are adsorbed to the interface and are responsible for the charge screening through the field effect on the graphene⁶⁹.

In contrast, the OHL is formed by the solvated ions and ions farther in the solution and does not participate in charge transfer processes. There has been mixed information on the conformation and composition of OHL. According to electrochemical studies, the OHL is filled with ions having the same charge as IHL due to the attraction forces of polarized electrode¹⁰⁷. Yet, numerous research has suggested that OHL is filled with oppositely charged ions compared to IHL. This could originate from the Coulombic attraction of IHL ions and forming a layer of counterions¹¹². Notably, this phenomenon often occurs when no current passes through the solution, and the device is operated at open circuit potential (OCP).

Multiple theories and EIS equivalent circuits have been developed so far to explore the capacitive charging of EDL in graphene devices. Perhaps, the most efficient equivalent circuit is presented by Ref¹⁰⁷ where the total capacitance of EDL is due to ions adsorption (C_{ads}), Helmholtz Layer (C_{H}), and bulk capacitance (C_{B}). This should be noted that C_{ads} and C_{H} represent the capacitance caused by ions in the IHL; however, the C_{ads} exclusively indicates the presence of unhydrated adsorbed ions on the graphene surface¹⁰⁷. As seen in Figure 2.11.a, the equivalent circuit confirms the existence of bulk resistance (R_{bulk}), solution resistance (R_{s}), and interfacial resistance (R_{int}). Therefore, the presence of adsorbed ions on the surface causes a change in interfacial resistances parallel to EDL capacitance. Moreover, the screening length of the EDL on a solid surface determines the strength of the electrostatic gate field. The Debye-Hückel (D-H) theory explains that the screening length of ions in the vicinity of the surface depends on the ionic strength of the solution and can be calculated as follows¹¹³:

$$\lambda_D = \sqrt{\frac{\epsilon_0 \epsilon_r K T}{2 I e^2}} \quad (15)$$

where K , T , I , and e are Boltzmann's constant, temperature, ionic strength, and charge of electrons. The limitation of this theory is the dilution of the solution. This screening length can be used to predict the electric fields and show where the solid's surface potential drops to the solution potential¹¹³.

The EDL response of graphene becomes essential when it encounters the change in various parameters of aqueous electrolytes, particularly pH and ionic strength. The pH response of defect-free graphene is due to the capacitive screening field of hydronium (H_3O^+) or hydroxide (OH^-) ions in the solution⁶⁴. According to the literature, reducing the pH increases the H_3O^+ in the vicinity of the graphene surface (Stern Layer) and immobilizes the electrons to the surface. Therefore, the n-doping of the surface increases the device's resistance. In contrast, more basic solutions result in the presence of OH^- ions at interface; therefore, capacitive p-doping of graphene^{64,112}. Notably, the formation of the EDL and its electrostatically transferred charges by H_3O^+ or OH^- have all been shown to be fully non-faradaic. This observation has been reported for various devices, including FETs, chemiresistive devices, and Schottky junctions. One crucial point to consider is that EDL interaction of H_3O^+ or OH^- with graphene is dominant over other interactions if only the graphene defectivity is below a specific value. This means that, upon increasing the defectivity through the formation of oxygen-containing functional groups, other alternative pathways such as protonation-deprotonation of functional groups will compete with EDL interactions^{64,114}. The surface roughness or edge termination have also been shown effective in local charging the surface through an ion trapping mechanism¹¹². Since the CVD-grown SLG-based devices offer such low defects with well-defined edge terminations, their EDL response is incredibly dominant. Nevertheless, they may not be ideal for investigating the role of EDL in high electrostatic fields as SLG could be prone to cross the neutrality point (Dirac point)¹¹⁴.

The ionic strength of the solution also affects the graphene properties through electrostatic forces. Generally, addition of a soluble salt enhances the ionic strength ($I = \frac{1}{2} \sum c_i z^2$) and reduces the Debye screening length¹¹⁵. Thus, it is expected to observe the impact of the added salts graphene mainly through electrostatic forces. One excellent example is NaCl, where its dissolution in water generates non-redox active ions; therefore, other ion-graphene interactions

can be excluded from the discussion¹¹⁶. By introducing NaCl and formation of Na⁺ and Cl⁻ hydrated ions, the Stern Layer on graphene is dominated by the Na⁺ ions. Accordingly, the Stern Layer of a non-modified graphene should always have positive ions¹¹⁷. Nevertheless, recent research studies have shown graphene affinity towards OH⁻, Cl⁻, and SO₄²⁻ ions¹¹⁰. Depending on the ions, they could be adsorbed on graphene as fully hydrated, half-hydrated, or even non-hydrated. Our example, Na⁺, does not undergo underpotential deposition; therefore, it preserves its solvation spheres and water molecules will be sandwiched between ions and graphene⁶⁹. This hypothesis is that exposure of graphene to aqueous electrolytes changes the intensity of peaks associated with O–H stretching (3000–3600 cm⁻¹)¹¹⁰. Sum generation frequency studies (SFG) show that symmetry disruption at the interface causes a sharp peak at around 3600 cm⁻¹, almost independent of the salt concentration. Therefore, water molecules in the proximity of graphene enhance the dangling O–H stretch vibration intensities, independent of the salt concentration¹¹⁰. Nevertheless, the majority of the water molecules below in IHL are randomly distributed, and their orientations do not follow the bulk solution. This abrupt change in orientation from bulk to the surface suppresses the O–H stretch vibration peaks of hydrogen bonded water molecules¹¹⁰.

The other central consideration is the inconsistency in theoretical and experimental screening lengths of the aqueous electrolytes at high concentrations. Generally, in a dilute solution, ions are separated with no ion-ion interactions; therefore, the dielectric constant can be measured uniformly throughout the electrolyte¹¹⁵. This means D-H theory can predict the screening length within its range. In concentrated electrolytes, Surface Force Measurement (SFM) studies revealed that the decay length of the EDL forces is measured much larger than predicted values in D-H (Figure 2.11.b)¹¹³. When a large number of ions are attracted to graphene, the non-electrostatic interactions of water-cations with surface π bonds could result in the surface charge reversal, depending on the charge, size, and affinity of the cations¹¹⁸. These non-

electrostatic interactions overcompensate surface charge in the two-dimensional “strongly correlated liquid (SCL)” at the surface. Using the term SCL instead of IHL gives the impression of an immobile layer of ions; therefore, using the streaming current (S_{str}) versus SCL is a powerful way to elucidate the mechanism¹¹⁸. Van der Heyden et al.¹¹⁸ stated by using S_{str} , concentrations up to 0.15 monovalent ions (K^+) do not show charge reversal through suppressing the charge inversion up to neutralization point. However, the reversal was observed up to 400 mM for divalent cations. Later, in 2019, Gaddam and Ducker¹¹³ reported for the first time the charge inversion of silica surface by addition of high concentration monovalent ions of Li^+ , Na^+ , K^+ , and Cs^+ (~ 1 M). Although these reports demonstrate the cause for difference in theoretical and experimental Debye screening lengths, the charge reversal on graphene has yet to be explored¹¹³.

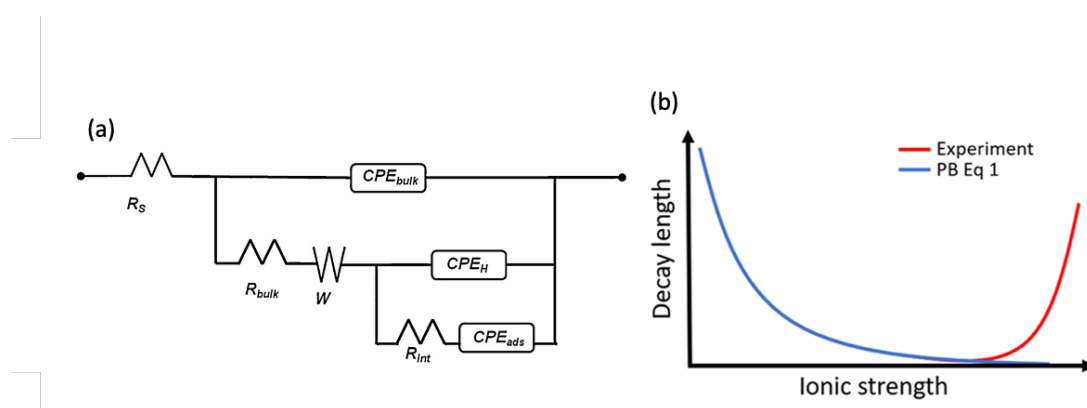


Figure 2.11. a) A comprehensive equivalent circuit explaining the EDL structure in graphene devices¹⁰⁷. Reprinted with permission from Elsevier, © Copyright 2014. b) Deviation of experimental decay length from theoretically measured Debye length¹¹³. Reprinted with permission from American Chemical Society, © Copyright 2019.

2.4.2 Surface Charge transfer

Direct charge transfer in graphene has been known for nearly a decade. The charge transfer occurs through doping graphene with external chemical species and can be classified as electrical doping (also known as the gate effect) or chemical doping¹¹⁹. The electrical doping is covered in section 2.4.1, that the presence of solution ions/molecules in the vicinity of

graphene alters its electronic characteristics through capacitive charging. In this section, the chemical doping of graphene by aqueous electrolytes will be reviewed.

The surface charge transfer, commonly seen in graphene/aqueous electrolyte interactions, occurs during the adsorption of adsorbates on the graphene surface. The nature of forces attracting adsorbates to graphene depends on the chemistry of graphene and adsorbates. However, the most demonstrated interactions are i) non-covalent (Coulombic interactions, van der Waals forces, hydrogen bonding, protonation/deprotonation of acid-bases) and ii) covalent bonds. In either case, the adsorbate interactions could p-dope or n-dope the graphene^{39,120}. That is why surface charge transfer (a.k.a. adsorbate-induced doping) does not alter the graphene network and can be reversible. Furthermore, the positions of the dopant's HOMO and LUMO with respect to the Fermi level can be utilized to explore the significance and direction of the transferred charges. Accordingly, graphene is charged by the dopant (a donor) if the dopant's HOMO $> E_f$. In contrast, if $E_f < \text{LUMO}$, the dopant (acceptor) is charged by graphene¹²¹.

The charge transfer caused by gaseous adsorbates is relatively well understood. However, the concept becomes complex as adsorbates are attracted to graphene in the presence of water. In fact, local charges on the surface caused by defects generates preferable sites for the adsorbates to be drawn towards the surface. The complexity of interpretation for surface charge transfer to/from graphene in water can be summarized as follows:

1. Ions are solvated, and the solvation spheres vary by the ions' chemical affinity for water molecules.
2. The co-presence of multiple ions and species at the surface makes the output signal complicated to understand.
3. Graphene adsorbate interactions are strongly dependent on graphene's hydrophobicity.
4. Adsorbates could transfer charge by electrostatic gating effect or trapped ions mechanisms.

5. Solution parameters, including pH, temperature, and ORP, also determine the extent of ions' adsorption on the surface.

As examined in section 2.4.1, studies have revealed that ion accumulation will emerge in the proximity of graphene electrodes at zero potential or gate voltage. Therefore, graphene's functional groups and edge termination together with electrolyte parameters play a role in determining the adsorbate-induced charge transfer.

2.4.2.1 pH

The non-faradic interactions of H_3O^+ and OH^- on graphene were reported as one of the electrolytes' capacitive charging effects. However, pH-responsive oxygen-containing functional groups contribute to the chemical doping of pH. In 2021, it was reported that a reduction in pH (below 4) in the presence of graphene triggers the protonation of carboxyl groups⁶⁴. In fact, at neutral pH, carboxyl groups are in the deprotonated forms ($-\text{COO}^-$) and carry negative charges. By reducing pH below its $\text{pK}_a=3.75$, $-\text{COO}^-$ is protonated as $-\text{COOH}$ and the surface is p-doped⁶⁴. Similar phenomena happen in the presence of amine groups with the pK_a of 4.12, meaning the reduction in pH protonates NH_2 to NH_3^+ . Comprehensive studies showed that the hydroxyl ($-\text{OH}$) group with $\text{pK}_a=8.47$ and carboxyl and amine at low pH ranges dominate the interactions with graphene (Figure 2.12). However, it should be noted that the electrostatic response of H_3O^+ and its protonation/deprotonation will have opposite signs. If reduction in pH n-dopes graphene by screening the electrons, it causes protonation of COO^- to COOH and p-dopes the graphene^{64,122,123}. Hence, controlling the concentration of pH-sensitive functional groups could result in pH-insensitive graphene by balancing the gating effect and defect-induced responses.

The pH response of other carbon-based nanomaterials such as CNTs¹²⁴ also follows the same mechanism. In highly defective graphene derivatives such as GO, however, the capacitive charge transfer is heavily suppressed by the acid-base protonation of the functional groups. It's

been shown that enhanced stability of GO-based sensors could result in 180% total change in currents of the graphene by changing the pH from 3-9¹¹⁴. Therefore, GO could potentially be integrated into next-generation biological devices where simultaneous pH measurement is required.

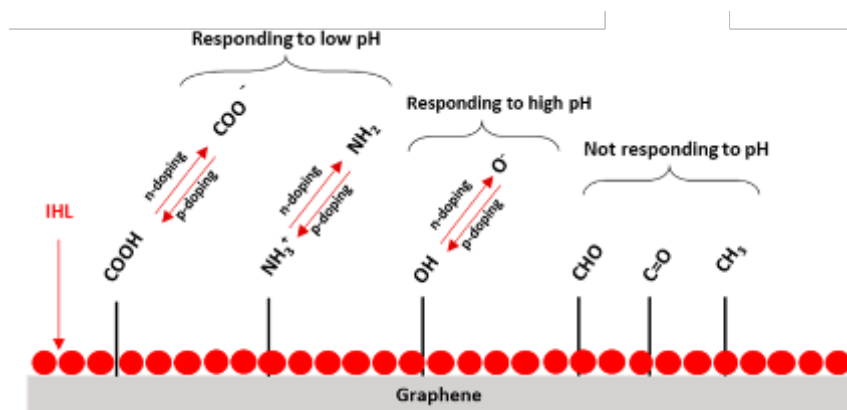


Figure 2.12. A schematic of defect induced pH response of graphene caused by oxygen based functional groups⁶⁴. Reprinted with permission from American Chemical Society (ACS), © Copyright 2021.

2.4.2.2 ORP

The ORP of an aqueous electrolyte is a measure of its oxidizing potential. A natural water's ORP is generally determined by its DO content⁶³. However, the ORP is often artificially increased in order to prevent pathogen growth in the water. Among the many factors that affect the ORP values of electrolytes, disinfectants and are one of most effective. Other parameters such as pH, ionic strength and temperature can also influence the ORP value of an electrolyte; however, they often cause only minor changes. A solution's ORP value can be measured by the difference between the build-up charge on a platinum working electrode caused by losing electrons to oxidants or taking electrons from a reductant, and a reference electrode. Therefore, based on the Nernst equation, it can be expressed as Eq. 16¹²⁵:

$$E_{mv} = E_o - 2.3026 \frac{RT}{nF} \log \frac{[reducer]^r}{[oxidizer]^o} \quad (16)$$

Where E_{mv} and E_o are the redox potential and standard redox potential, respectively, R is the gas constant, T is the temperature, n is the number of transferred electrons, F is the Faraday

constant, and r and o are the coefficients of the reducer and oxidizer in the balanced reaction, respectively.¹²⁵

For water disinfection purposes, hypochlorite (OCl^-), hydrogen peroxide (H_2O_2), peracetic acid (CH_3COOH), or potassium permanganate (KMnO_4) are commonly added to water⁶³. These disinfectants act as oxidizing agents, preventing the growth of pathogens and bacteria⁴⁴. Therefore, it is anticipated that operating graphene devices in real conditions (sea, river, pools etc.), causes graphene oxidation by these molecules/ions. Also, oxidant detection using conventional titration methods such as iodometric or amperometric, or chemiluminescence, and electrochemical methods are not suitable for the continuous monitoring of the concentration⁶³. Hence, understanding how graphene devices perceive the oxidants could assist in the development of practical devices. In these devices, the charge transfer that occurs by surface/edge adsorption of molecules is modulated by the ORP of the solution. Recent studies on hypochlorite detection by using graphene devices have shown the LODs of 7 ppb for bare graphene¹²⁶. It means the bare surface of graphene offers sufficient charge transfer to be detected among other ions. Yet, selectivity is an issue when multiple disinfectants are co-present in the solution (e.g., KMnO_4 and HOCl). To be more specific, by addition of hypochlorite to water, depending on the pH, three components of OCl^- , HOCl , and Cl_2 can be present¹²⁷. In fact, equilibrium among these three components is pH dependent so that Cl_2 , HOCl and OCl^- are stable in low (below 4), mid (5-7), and high (above 7) pH values, respectively¹²⁷. These three together are often referred to as ‘free chlorine’. Graphene interaction with free chlorine is also pH dependent. Both HOCl and OCl^- within the Stern layer act as electron-withdrawing groups on the surface, p-doping the graphene. While the nature of the interaction is believed to be a Coulombic interaction between negatively charged OCl^- and electron-deficient sites in the surface (point defects) or carbon atoms attached to oxygen sites, the attraction forces of HOCl remain controversial⁶⁹. ORP of a solution is also adjusted with

the pH, meaning the increase in pH could result in increasing the ORP. As the solution becomes more acidic, the relative oxidation ability of the solution rises. Nonetheless, there are numerous instances in which addition of molecule can alter the ORP and pH in the same way; for example, the addition of hypochlorite (a weak base) increases the pH, while the solution's ORP is enhanced.¹²⁷

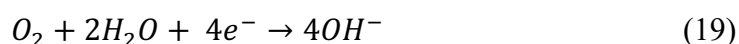
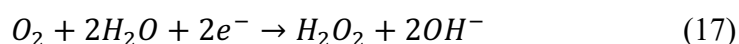
2.4.2.3 *Dissolved gases*

DO concentration could also affect the ORP of the solution. DO, defined as molecular oxygen within water, is a crucial indicator of water quality and its concentration is crucial for the preservation of aquatic life. Creatures like crabs or oysters need DO (1- 6 mg/L), while shallow water fish require a larger concentration of 4-15 mg/L¹¹⁹. Also, DO is produced by aeration of water through wind, photosynthesis of phytoplankton, algae etc¹¹⁹. This information is vital since the operation of graphene in aqueous electrolytes will be accompanied by the presence of DO. Also, DO is an electron-withdrawing group. Although the mechanisms have not been fully explained yet, two approaches could be predicted:

- 1- Direct adsorption of DO on graphene surface through Coulombic interactions between DO lone pairs and electron-deficient sites of graphene lattice (i.e., carbon bonded to electronegative atoms such as oxygen, point defects, armchair configured edges). In this case, the non-covalent interaction of DO with carbon positively charges the graphene and, therefore, p-dopes the surface.
- 2- Presence of DO in the vicinity of graphene in the OHL. Graphene with negative surface charges often attracts the first layer of positive ions in IHL. By introducing DO in IHL, it can neutralize the electrostatic effects of the positive charges. Hence, the surface is p-doped

Thus far, a few literatures have studied the direct measurement of DO using graphene derivatives¹²⁸. For example, laser-induced graphene decorated with Platinum nanoparticles

was shown to operate in an extended linear dynamic range of 30-400 μM with a response time of 2s¹²⁸. In another report, reduced- GO decorated with silver nanoparticles significantly enhanced DO detection, offering a LOD and sensitivity of 0.031 μM and 0.205 $\mu\text{A}/\mu\text{M}$, respectively¹²⁹. In these catalytic detections of DO, a two-step reduction of DO to OH^- involving four electrons (Eq. 17 and Eq. 18) will be simplified to a one-step reduction process (Eq. 19). Accordingly, the response time decreases, and the sensitivity is raised significantly.



2.4.3 Substitutional doping

Substitutional doping is characterized by replacing one or more types of atoms with carbon in a graphene lattice. These foreign atoms possess different numbers of valence electrons and alter the lattice symmetry of graphene. The doping processes often require high energy from temperature, pressure, or substantial chemical affinity between precursor and graphene¹²⁰. During liquid exfoliation processes, particularly tip sonication or wet-ball milling, the graphene surface is activated by local temperature and forces. The ‘surface activation’ happens through three main steps: i) formation of defects, ii) altering edge configuration, and 3) size reduction. The first two stages have already been reviewed in sections 2.1.3.2 and 2.1.3.3. The size reduction enhances the specific surface area of the graphene; therefore, the accessible surface for the chemical reaction increases. There are numerous studies on the substitutional doping of graphene with alkaline metals^{58,130–132}, alkaline earth metals^{133,134}, transition metals^{135–138}, semi-metals^{139–141}, and non-metals^{142–145} indicates the importance of this phenomenon. For graphene devices working in an aqueous solution, the substitutional doping becomes more complex compared to the gaseous phases. The sophistication originates from three main objects:

- 1- An immobile ion (IHL) layer at the graphene/electrolyte interface prevents ion/molecular mobility towards substitutional doping.
- 2- The difference in solubility of the dopant in graphene and electrolyte might act as an energy barrier for the doping
- 3- Ions are solvated in aqueous electrolytes; therefore, substitutional doping should be done by overcoming solvation spheres and (underpotential) deposition. Hence, the substitutional doping of alkaline and alkaline earth metals in electrolytes is unlikely to happen.

2.4.4 Trapped Ions/Molecules

This mechanism has recently been introduced as one of the plausible approaches that graphene deals with electrolytes. Inspired by the term trapped, the ions or molecules present in electrolytes could be trapped within the sheets of graphene or in graph boundaries^{64,112}. The former configuration is found when a percolation network of graphene sheets is used. The gaps between the sheets vary depending on the size, thickness, orientation, and substrate of the graphene sheet. The local charge is induced upon physically trapping the molecule/ions in those gaps, shifting the graphene electronic properties⁶⁴. The latter configuration could even be a single layer of graphene possessing grain boundaries. Boundaries on graphene could be formed due to its conformal deposition on the substrates with the grains. In fact, fine-grained Cu substrates bring a larger area of disordered boundaries. Therefore, carbon atoms deposited in that area will also be disorderly shaped, generating a large density of vacancies¹¹². These vacancies are the entrance gates for ion diffusion. It has been shown the H_3O^+ trapping into graphene films could p-dope the surface (Figure 2.13), meaning it acts as adsorbate-induced charge transfer, but it is physically entangled with the surface. The surface adsorption of Na^+ through porosities has also shown to be the same, but n-doping the surface through hydrating water molecules¹⁴⁶.

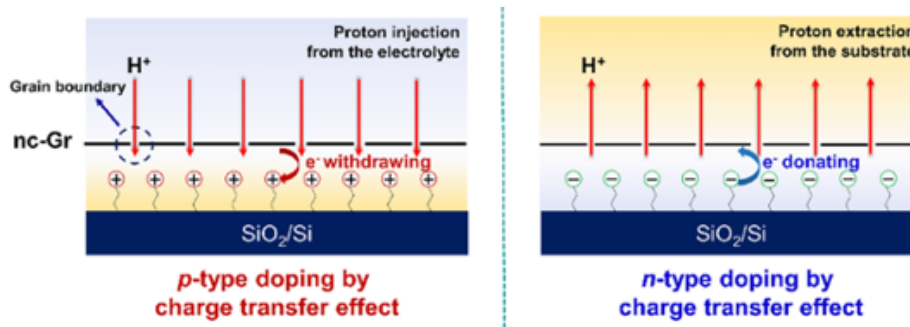


Figure 2.13. Charge transfer by proton injection/extraction mechanism¹¹². Reprinted with permission from American Chemical Society (ACS), © Copyright 2021.

2.5 Conclusion

In this chapter, the most recent findings on the interfacial interactions between graphene devices and aqueous electrolytes are discussed in four categories: electrostatic gating, surface charge transfer, substitutional doping, and ion/molecule trapping. In this study, it is demonstrated that the arrangement of ions in the electrolyte near the graphene surface can modulate the output signal through electrostatic gating. Also, graphene wettability dictates graphene/water interactions, and parameters such as substrate, defectivity, thickness, and topography influence the way graphene interacts with water. Besides, the concept of surface charge transfer was explored by considering the presence of immobile ions of the surface. This chapter aims to familiarize the reader with important concepts governing the graphene-water interface and to review the fundamentals for better understanding the operation principles of graphene devices in aqueous media.

2.6 References

- (1) Novoselov, K. S.; Geim, A. K.; Morozov, S. V.; Jiang, D.; Zhang, Y.; Dubonos, S. V.; Grigorieva, I. V.; Firsov, A. A. Electric Field Effect in Atomically Thin Carbon Films. *Science* **2004**, *306* (5696), 666–669. <https://doi.org/10.1126/science.1102896>.
- (2) Novoselov, K. S.; Mishchenko, A.; Carvalho, A.; Castro Neto, A. H. 2D Materials and van Der Waals Heterostructures. *Science* **2016**, *353* (6298). <https://doi.org/10.1126/science.aac9439>.

- (3) Zhang, F.; Yang, K.; Liu, G.; Chen, Y.; Wang, M.; Li, S.; Li, R. Recent Advances on Graphene: Synthesis, Properties and Applications. *Composites Part A: Applied Science and Manufacturing* **2022**, *160*, 107051. <https://doi.org/10.1016/j.compositesa.2022.107051>.
- (4) Geim, A. K.; Novoselov, K. S. The Rise of Graphene. *Nature Materials* **2007**, *6* (3), 183–191. <https://doi.org/10.1038/nmat1849>.
- (5) Zeng, M.; Xiao, Y.; Liu, J.; Lu, W.; Fu, L. Controllable Fabrication of Nanostructured Graphene Towards Electronics. *Advanced Electronic Materials* **2016**, *2* (4), 1500456. <https://doi.org/10.1002/aelm.201500456>.
- (6) Buzaglo, M.; Ruse, E.; Levy, I.; Nadiv, R.; Reuveni, G.; Shtein, M.; Regev, O. Top-Down, Scalable Graphene Sheets Production: It Is All about the Precipitate. *Chemistry of Materials* **2017**, *29* (23), 9998–10006. <https://doi.org/10.1021/acs.chemmater.7b03428>.
- (7) Kumar, N.; Salehiyan, R.; Chauke, V.; Joseph Botlhoko, O.; Setshedi, K.; Scriba, M.; Masukume, M.; Sinha Ray, S. Top-down Synthesis of Graphene: A Comprehensive Review. *FlatChem* **2021**, *27*, 100224. <https://doi.org/10.1016/j.flatc.2021.100224>.
- (8) Li, Z.; Young, R. J.; Backes, C.; Zhao, W.; Zhang, X.; Zhukov, A. A.; Tillotson, E.; Conlan, A. P.; Ding, F.; Haigh, S. J.; Novoselov, K. S.; Coleman, J. N. Mechanisms of Liquid-Phase Exfoliation for the Production of Graphene. *ACS Nano* **2020**, *14* (9), 10976–10985. <https://doi.org/10.1021/acsnano.0c03916>.
- (9) Ciesielski, A.; Samori, P. Grapheneviasonication Assisted Liquid-Phase Exfoliation. *Chem. Soc. Rev.* **2014**, *43* (1), 381–398. <https://doi.org/10.1039/C3CS60217F>.
- (10) León, V.; Quintana, M.; Herrero, M. A.; Fierro, J. L. G.; Hoz, A. de la; Prato, M.; Vázquez, E. Few-Layer Graphenes from Ball-Milling of Graphite with Melamine. *Chemical Communications* **2011**, *47* (39), 10936. <https://doi.org/10.1039/c1cc14595a>.

- (11) Turner, P.; Hodnett, M.; Dorey, R.; Carey, J. D. Controlled Sonication as a Route to In-Situ Graphene Flake Size Control. *Scientific Reports* **2019**, *9* (1), 8710. <https://doi.org/10.1038/s41598-019-45059-5>.
- (12) Keeley, G. P.; O'Neill, A.; Holzinger, M.; Cosnier, S.; Coleman, J. N.; Duesberg, G. S. DMF-Exfoliated Graphene for Electrochemical NADH Detection. *Physical Chemistry Chemical Physics* **2011**, *13* (17), 7747. <https://doi.org/10.1039/c1cp20060g>.
- (13) Shih, Y.-W.; Tseng, G.-W.; Hsieh, C.-Y.; Li, Y.-Y.; Sakoda, A. Graphene Quantum Dots Derived from Platelet Graphite Nanofibers by Liquid-Phase Exfoliation. *Acta Materialia* **2014**, *78*, 314–319. <https://doi.org/10.1016/j.actamat.2014.06.027>.
- (14) Yeon, C.; Yun, S. J.; Lee, K.-S.; Lim, J. W. High-Yield Graphene Exfoliation Using Sodium Dodecyl Sulfate Accompanied by Alcohols as Surface-Tension-Reducing Agents in Aqueous Solution. *Carbon* **2015**, *83*, 136–143. <https://doi.org/10.1016/j.carbon.2014.11.035>.
- (15) Yi, M.; Shen, Z.; Zhang, X.; Ma, S. Achieving Concentrated Graphene Dispersions in Water/Acetone Mixtures by the Strategy of Tailoring Hansen Solubility Parameters. *Journal of Physics D: Applied Physics* **2013**, *46* (2), 025301. <https://doi.org/10.1088/0022-3727/46/2/025301>.
- (16) Liu, W.-W.; Xia, B.-Y.; Wang, X.-X.; Wang, J.-N. Exfoliation and Dispersion of Graphene in Ethanol-Water Mixtures. *Frontiers of Materials Science* **2012**, *6* (2), 176–182. <https://doi.org/10.1007/s11706-012-0166-4>.
- (17) Halim, U.; Zheng, C. R.; Chen, Y.; Lin, Z.; Jiang, S.; Cheng, R.; Huang, Y.; Duan, X. A Rational Design of Cosolvent Exfoliation of Layered Materials by Directly Probing Liquid–Solid Interaction. *Nature Communications* **2013**, *4* (1), 2213. <https://doi.org/10.1038/ncomms3213>.
- (18) Yavari, F.; Koratkar, N. Graphene-Based Chemical Sensors. *The Journal of Physical Chemistry Letters* **2012**, *3* (13), 1746–1753. <https://doi.org/10.1021/jz300358t>.

- (19) Zhang, F.; Zhang, R.; Feng, J.; Ci, L.; Xiong, S.; Yang, J.; Qian, Y.; Li, L. One-Pot Solvothermal Synthesis of Graphene Wrapped Rice-like Ferrous Carbonate Nanoparticles as Anode Materials for High Energy Lithium-Ion Batteries. *Nanoscale* **2015**, *7* (1), 232–239. <https://doi.org/10.1039/C4NR05671J>.
- (20) Facure, M. H. M.; Schneider, R.; Mercante, L. A.; Correa, D. S. Rational Hydrothermal Synthesis of Graphene Quantum Dots with Optimized Luminescent Properties for Sensing Applications. *Materials Today Chemistry* **2022**, *23*, 100755. <https://doi.org/10.1016/j.mtchem.2021.100755>.
- (21) Tour, J. M. Top-Down versus Bottom-Up Fabrication of Graphene-Based Electronics. *Chemistry of Materials* **2014**, *26* (1), 163–171. <https://doi.org/10.1021/cm402179h>.
- (22) Lee, X. J.; Hiew, B. Y. Z.; Lai, K. C.; Lee, L. Y.; Gan, S.; Thangalazhy-Gopakumar, S.; Rigby, S. Review on Graphene and Its Derivatives: Synthesis Methods and Potential Industrial Implementation. *Journal of the Taiwan Institute of Chemical Engineers* **2019**, *98*, 163–180. <https://doi.org/10.1016/j.jtice.2018.10.028>.
- (23) Lin, L.; Deng, B.; Sun, J.; Peng, H.; Liu, Z. Bridging the Gap between Reality and Ideal in Chemical Vapor Deposition Growth of Graphene. *Chemical Reviews* **2018**, *118* (18), 9281–9343. <https://doi.org/10.1021/acs.chemrev.8b00325>.
- (24) Kim, S.; Shin, S.; Kim, T.; Du, H.; Song, M.; Lee, C.; Kim, K.; Cho, S.; Seo, D. H.; Seo, S. Robust Graphene Wet Transfer Process through Low Molecular Weight Polymethylmethacrylate. *Carbon* **2016**, *98*, 352–357. <https://doi.org/10.1016/j.carbon.2015.11.027>.
- (25) Cunge, G.; Ferrah, D.; Petit-Etienne, C.; Davydova, A.; Okuno, H.; Kalita, D.; Bouchiat, V.; Renault, O. Dry Efficient Cleaning of Poly-Methyl-Methacrylate Residues from Graphene with High-Density H₂ and H₂-N₂ Plasmas. *Journal of Applied Physics* **2015**, *118* (12), 123302. <https://doi.org/10.1063/1.4931370>.

- (26) Wang, Y.; Zheng, Y.; Xu, X.; Dubuisson, E.; Bao, Q.; Lu, J.; Loh, K. P. Electrochemical Delamination of CVD-Grown Graphene Film: Toward the Recyclable Use of Copper Catalyst. *ACS Nano* **2011**, *5* (12), 9927–9933. <https://doi.org/10.1021/nn203700w>.
- (27) Hong, N.; Kireev, D.; Zhao, Q.; Chen, D.; Akinwande, D.; Li, W. Roll-to-Roll Dry Transfer of Large-Scale Graphene. *Advanced Materials* **2022**, *34* (3), 2106615. <https://doi.org/10.1002/adma.202106615>.
- (28) Wang, B.; Huang, M.; Tao, L.; Lee, S. H.; Jang, A. R.; Li, B. W.; Shin, H. S.; Akinwande, D.; Ruoff, R. S. Support-Free Transfer of Ultrasoother Graphene Films Facilitated by Self-Assembled Monolayers for Electronic Devices and Patterns. *ACS Nano* **2016**, *10* (1), 1404–1410. <https://doi.org/10.1021/acsnano.5b06842>.
- (29) Ullah, S.; Yang, X.; Ta, H. Q.; Hasan, M.; Bachmatiuk, A.; Tokarska, K.; Trzebicka, B.; Fu, L.; Rummeli, M. H. Graphene Transfer Methods: A Review. *Nano Research* **2021**, *14* (11), 3756–3772. <https://doi.org/10.1007/s12274-021-3345-8>.
- (30) Ma, L. P.; Ren, W.; Cheng, H. M. Transfer Methods of Graphene from Metal Substrates: A Review. *Small Methods* **2019**, *3* (7), 1900049. <https://doi.org/10.1002/smt.201900049>.
- (31) Wang, M.; Yang, E. H.; Vajtai, R.; Kono, J.; Ajayan, P. M. Effects of Etchants in the Transfer of Chemical Vapor Deposited Graphene. *Journal of Applied Physics* **2018**, *123* (19), 195103. <https://doi.org/10.1063/1.5009253>.
- (32) Chen, M.; Haddon, R. C.; Yan, R.; Bekyarova, E. Advances in Transferring Chemical Vapour Deposition Graphene: A Review. *Materials Horizons* **2017**, *4* (6), 1054–1063. <https://doi.org/10.1039/c7mh00485k>.
- (33) Madurani, K. A.; Suprpto, S.; Machrita, N. I.; Bahar, S. L.; Illiya, W.; Kurniawan, F. Progress in Graphene Synthesis and Its Application: History, Challenge and the Future Outlook for Research and Industry. *ECS Journal of Solid State Science and Technology* **2020**, *9* (9), 093013. <https://doi.org/10.1149/2162-8777/abbb6f>.

- (34) Zhu, Y.; Murali, S.; Cai, W.; Li, X.; Suk, J. W.; Potts, J. R.; Ruoff, R. S. Graphene and Graphene Oxide: Synthesis, Properties, and Applications. *Advanced Materials* **2010**, *22* (35), 3906–3924. <https://doi.org/10.1002/adma.201001068>.
- (35) Wang, J.; Mu, X.; Sun, M.; Mu, T. Optoelectronic Properties and Applications of Graphene-Based Hybrid Nanomaterials and van Der Waals Heterostructures. *Applied Materials Today* **2019**, *16*, 1–20. <https://doi.org/10.1016/j.apmt.2019.03.006>.
- (36) Yang, G.; Li, L.; Lee, W. B.; Ng, M. C. Structure of Graphene and Its Disorders: A Review. *Science and Technology of Advanced Materials* **2018**, *19* (1), 613–648. <https://doi.org/10.1080/14686996.2018.1494493>.
- (37) Zhan, D.; Yan, J.; Lai, L.; Ni, Z.; Liu, L.; Shen, Z. Engineering the Electronic Structure of Graphene. *Advanced Materials* **2012**, *24* (30), 4055–4069. <https://doi.org/10.1002/adma.201200011>.
- (38) Lherbier, A.; Blase, X.; Niquet, Y. M.; Triozon, F.; Roche, S. Charge Transport in Chemically Doped 2D Graphene. *Physical Review Letters* **2008**, *101* (3), 036808. <https://doi.org/10.1103/PhysRevLett.101.036808>.
- (39) Pinto, H.; Markevich, A. Electronic and Electrochemical Doping of Graphene by Surface Adsorbates. *Beilstein Journal of Nanotechnology* **2014**, *5* (1), 1842–1848. <https://doi.org/10.3762/bjnano.5.195>.
- (40) Novoselov, K. S.; Geim, A. K.; Morozov, S. V.; Jiang, D.; Katsnelson, M. I.; Grigorieva, I. V.; Dubonos, S. V.; Firsov, A. A. Two-Dimensional Gas of Massless Dirac Fermions in Graphene. *Nature* **2005**, *438* (7065), 197–200. <https://doi.org/10.1038/nature04233>.
- (41) Geim, A. K. Graphene: Status and Prospects. *Science* **2009**, *324* (5934), 1530–1534. <https://doi.org/10.1126/science.1158877>.

- (42) Partoens, B.; Peeters, F. M. From Graphene to Graphite: Electronic Structure around the K Point. *Physical Review B - Condensed Matter and Materials Physics* **2006**, *74* (7), 075404. <https://doi.org/10.1103/PhysRevB.74.075404>.
- (43) Eda, G.; Mattevi, C.; Yamaguchi, H.; Kim, H.; Chhowalla, M. Insulator to Semimetal Transition in Graphene Oxide. *Journal of Physical Chemistry C* **2009**, *113* (35), 15768–15771. <https://doi.org/10.1021/jp9051402>.
- (44) Zubiarrain-Laserna, A.; Angizi, S.; Akbar, M. A.; Divigalpitiya, R.; Selvaganapathy, P. R.; Kruse, P. Detection of Free Chlorine in Water Using Graphene-like Carbon Based Chemiresistive Sensors. *RSC Advances* **2022**, *12* (4), 2485–2496. <https://doi.org/10.1039/D1RA08264G>.
- (45) Zhang, X.; Xin, J.; Ding, F. The Edges of Graphene. *Nanoscale* **2013**, *5* (7), 2556–2569. <https://doi.org/10.1039/c3nr34009k>.
- (46) Zubiarrain-Laserna, A.; Kruse, P. Review—Graphene-Based Water Quality Sensors. *Journal of The Electrochemical Society* **2020**, *167* (3), 037539. <https://doi.org/10.1149/1945-7111/ab67a5>.
- (47) Feicht, P.; Eigler, S. Defects in Graphene Oxide as Structural Motifs. *ChemNanoMat* **2018**, *4* (3), 244–252. <https://doi.org/10.1002/cnma.201700357>.
- (48) Liu, L.; Qing, M.; Wang, Y.; Chen, S. Defects in Graphene: Generation, Healing, and Their Effects on the Properties of Graphene: A Review. *Journal of Materials Science and Technology* **2015**, *31* (6), 599–606. <https://doi.org/10.1016/j.jmst.2014.11.019>.
- (49) Tian, W.; Li, W.; Yu, W.; Liu, X. A Review on Lattice Defects in Graphene: Types Generation Effects and Regulation. *Micromachines* **2017**, *8* (5), 163. <https://doi.org/10.3390/mi8050163>.

- (50) Meyer, J. C.; Kisielowski, C.; Erni, R.; Rossell, M. D.; Crommie, M. F.; Zettl, A. Direct Imaging of Lattice Atoms and Topological Defects in Graphene Membranes. *Nano Letters* **2008**, *8* (11), 3582–3586. <https://doi.org/10.1021/nl801386m>.
- (51) Lahiri, J.; Lin, Y.; Bozkurt, P.; Oleynik, I. I.; Batzill, M. An Extended Defect in Graphene as a Metallic Wire. *Nature Nanotechnology* **2010**, *5* (5), 326–329. <https://doi.org/10.1038/nnano.2010.53>.
- (52) Girit, Ç. Ö.; Meyer, J. C.; Erni, R.; Rossell, M. D.; Kisielowski, C.; Yang, L.; Park, C. H.; Crommie, M. F.; Cohen, M. L.; Louie, S. G.; Zettl, A. Graphene at the Edge: Stability and Dynamics. *Science* **2009**, *323* (5922), 1705–1708. <https://doi.org/10.1126/science.1166999>.
- (53) Georgakilas, V.; Bourlinos, A. B.; Zboril, R.; Steriotis, T. A.; Dallas, P.; Stubos, A. K.; Trapalis, C. Organic Functionalisation of Graphenes. *Chemical Communications* **2010**, *46* (10), 1766. <https://doi.org/10.1039/b922081j>.
- (54) Zhong, X.; Jin, J.; Li, S.; Niu, Z.; Hu, W.; Li, R.; Ma, J. Aryne Cycloaddition: Highly Efficient Chemical Modification of Graphene. *Chemical Communications* **2010**, *46* (39), 7340. <https://doi.org/10.1039/c0cc02389b>.
- (55) Terrones, H.; Lv, R.; Terrones, M.; Dresselhaus, M. S. The Role of Defects and Doping in 2D Graphene Sheets and 1D Nanoribbons. *Reports on Progress in Physics* **2012**, *75* (6), 062501. <https://doi.org/10.1088/0034-4885/75/6/062501>.
- (56) Zhu, X.; Liu, K.; Lu, Z.; Xu, Y.; Qi, S.; Zhang, G. Effect of Oxygen Atoms on Graphene: Adsorption and Doping. *Physica E: Low-dimensional Systems and Nanostructures* **2020**, *117*, 113827. <https://doi.org/10.1016/j.physe.2019.113827>.
- (57) Li, T.; Yarmoff, J. A. Defect-Induced Oxygen Adsorption on Graphene Films. *Surface Science* **2018**, *675*, 70–77. <https://doi.org/10.1016/j.susc.2018.05.001>.
- (58) Yamada, T.; Okigawa, Y.; Hasegawa, M. Potassium-Doped n-Type Bilayer Graphene. *Applied Physics Letters* **2018**, *112* (4), 043105. <https://doi.org/10.1063/1.5012808>.

- (59) Xu, X.; Li, W.; Wang, X.; Dou, S.-X. Superconducting Properties of Graphene Doped Magnesium Diboride. In *Applications of High-Tc Superconductivity*; InTech, 2011. <https://doi.org/10.5772/17117>.
- (60) Guo, J.; Zhang, J.; Zhao, H.; Fang, Y.; Ming, K.; Huang, H.; Chen, J.; Wang, X. Fluorine-Doped Graphene with an Outstanding Electrocatalytic Performance for Efficient Oxygen Reduction Reaction in Alkaline Solution. *Royal Society Open Science* **2018**, 5 (10), 180925. <https://doi.org/10.1098/rsos.180925>.
- (61) Kudus, M. H. A.; Zakaria, M. R.; Akil, H. Md.; Ullah, F.; Javed, F. Oxidation of Graphene via a Simplified Hummers' Method for Graphene-Diamine Colloid Production. *Journal of King Saud University - Science* **2020**, 32 (1), 910–913. <https://doi.org/10.1016/j.jksus.2019.05.002>.
- (62) Georgakilas, V.; Otyepka, M.; Bourlinos, A. B.; Chandra, V.; Kim, N.; Kemp, K. C.; Hobza, P.; Zboril, R.; Kim, K. S. Functionalization of Graphene: Covalent and Non-Covalent Approaches, Derivatives and Applications. *Chemical Reviews* **2012**, 112 (11), 6156–6214. <https://doi.org/10.1021/cr3000412>.
- (63) Kruse, P. Review on Water Quality Sensors. *Journal of Physics D: Applied Physics* **2018**, 51 (20), 203002. <https://doi.org/10.1088/1361-6463/aabb93>.
- (64) Angizi, S.; Yu, E.; Dalmieda, J.; Saha, D.; Selvaganapathy, P. R.; Kruse, P. Defect Engineering of Graphene to Modulate PH Response of Graphene Devices. *Langmuir* **37** (41), 12163–12178. <https://doi.org/10.1021/acs.langmuir.1c02088>.
- (65) Yang, L.; Zheng, G.; Cao, Y.; Meng, C.; Li, Y.; Ji, H.; Chen, X.; Niu, G.; Yan, J.; Xue, Y.; Cheng, H. Moisture-Resistant, Stretchable NO_x Gas Sensors Based on Laser-Induced Graphene for Environmental Monitoring and Breath Analysis. *Microsystems & Nanoengineering* **2022**, 8 (1), 78. <https://doi.org/10.1038/s41378-022-00414-x>.

- (66) Eom, T. H.; Kim, T.; Jang, H. W. Hydrogen Sensing of Graphene-Based Chemoresistive Gas Sensor Enabled by Surface Decoration. *JOURNAL OF SENSOR SCIENCE AND TECHNOLOGY* **2020**, *29* (6), 382–387. <https://doi.org/10.46670/JSST.2020.29.6.382>.
- (67) Wu, Z.; Chen, X.; Zhu, S.; Zhou, Z.; Yao, Y.; Quan, W.; Liu, B. Room Temperature Methane Sensor Based on Graphene Nanosheets/Polyaniline Nanocomposite Thin Film. *IEEE Sensors Journal* **2013**, *13* (2), 777–782. <https://doi.org/10.1109/JSEN.2012.2227597>.
- (68) Mackin, C.; Schroeder, V.; Zurutuza, A.; Su, C.; Kong, J.; Swager, T. M.; Palacios, T. Chemiresistive Graphene Sensors for Ammonia Detection. *ACS Applied Materials & Interfaces* **2018**, *10* (18), 16169–16176. <https://doi.org/10.1021/acsami.8b00853>.
- (69) Angizi, S.; Selvaganapathy, P. R.; Kruse, P. Graphene-Silicon Schottky Devices for Operation in Aqueous Environments: Device Performance and Sensing Application. *Carbon* **2022**, *194*, 140–153. <https://doi.org/10.1016/j.carbon.2022.03.052>.
- (70) Mohtasebi, A.; Broomfield, A. D.; Chowdhury, T.; Selvaganapathy, P. R.; Kruse, P. Reagent-Free Quantification of Aqueous Free Chlorine via Electrical Readout of Colorimetrically Functionalized Pencil Lines. *ACS Appl Mater Interfaces* **2017**, *9* (24), 20748–20761. <https://doi.org/10.1021/acsami.7b03968>.
- (71) Hoque, E.; Hsu, L. H. H.; Aryasomayajula, A.; Selvaganapathy, P. R.; Kruse, P. Pencil-Drawn Chemiresistive Sensor for Free Chlorine in Water. *IEEE Sens Lett* **2017**, *1* (4), 1–4. <https://doi.org/10.1109/LSENS.2017.2722958>.
- (72) Sudibya, H. G.; He, Q.; Zhang, H.; Chen, P. Electrical Detection of Metal Ions Using Field-Effect Transistors Based on Micropatterned Reduced Graphene Oxide Films. *ACS Nano* **2011**, *5* (3), 1990–1994. <https://doi.org/10.1021/nn103043v>.
- (73) Tan, F.; Cong, L.; Jiang, X.; Wang, Y.; Quan, X.; Chen, J.; Mulchandani, A. Highly Sensitive Detection of Cr(VI) by Reduced Graphene Oxide Chemiresistor and 1,4-Dithiothreitol

- Functionalized Au Nanoparticles. *Sensors and Actuators B: Chemical* **2017**, *247*, 265–272.
<https://doi.org/10.1016/j.snb.2017.02.163>.
- (74) Dalmieda, J.; Zubiarrain-Laserna, A.; Ganepola, D.; Selvaganapathy, P. R.; Kruse, P. Chemiresistive Detection of Silver Ions in Aqueous Media. *Sensors and Actuators B: Chemical* **2021**, *328*, 129023. <https://doi.org/10.1016/j.snb.2020.129023>.
- (75) Reddy, D.; Register, L. F.; Carpenter, G. D.; Banerjee, S. K. Graphene Field-Effect Transistors. *Journal of Physics D: Applied Physics* **2011**, *44* (31), 313001.
<https://doi.org/10.1088/0022-3727/44/31/313001>.
- (76) Schwierz, F. Graphene Transistors. *Nature Nanotechnology* **2010**, *5* (7), 487–496.
<https://doi.org/10.1038/nnano.2010.89>.
- (77) Krsihna, B. V.; Ravi, S.; Prakash, M. D. Recent Developments in Graphene Based Field Effect Transistors. *Materials Today: Proceedings* **2021**, *45*, 1524–1528.
<https://doi.org/10.1016/j.matpr.2020.07.678>.
- (78) Béraud, A.; Sauvage, M.; Bazán, C. M.; Tie, M.; Bencherif, A.; Bouilly, D. Graphene Field-Effect Transistors as Bioanalytical Sensors: Design, Operation and Performance. *The Analyst* **2021**, *146* (2), 403–428. <https://doi.org/10.1039/D0AN01661F>.
- (79) Fu, W.; Jiang, L.; van Geest, E. P.; Lima, L. M. C.; Schneider, G. F. Sensing at the Surface of Graphene Field-Effect Transistors. *Advanced Materials* **2017**, *29* (6), 1603610.
<https://doi.org/10.1002/adma.201603610>.
- (80) He, Q.; Wu, S.; Yin, Z.; Zhang, H. Graphene-Based Electronic Sensors. *Chemical Science* **2012**, *3* (6), 1764. <https://doi.org/10.1039/c2sc20205k>.
- (81) Fu, W.; Nef, C.; Knopfmacher, O.; Tarasov, A.; Weiss, M.; Calame, M.; Schönenberger, C. Graphene Transistors Are Insensitive to PH Changes in Solution. *Nano Letters* **2011**, *11* (9), 3597–3600. <https://doi.org/10.1021/nl201332c>.

- (82) Novodchuk, I.; Bajcsy, M.; Yavuz, M. Graphene-Based Field Effect Transistor Biosensors for Breast Cancer Detection: A Review on Biosensing Strategies. *Carbon* **2021**, *172*, 431–453. <https://doi.org/10.1016/j.carbon.2020.10.048>.
- (83) Wu, G.; Tang, X.; Lin, Z.; Meyyappan, M.; Lai, K. W. C. The Effect of Ionic Strength on the Sensing Performance of Liquid-Gated Biosensors. In *2017 IEEE 17th International Conference on Nanotechnology (IEEE-NANO)*; IEEE, 2017; pp 242–245. <https://doi.org/10.1109/NANO.2017.8117313>.
- (84) Chee, L. H.; Kumar, P.; Kang, C. H.; Burhanudin, Z. A. DNA/AuNP-Graphene Back-Gated Field Effect Transistor as a Biosensor for Lead (II) Ion Detection. In *2017 IEEE Regional Symposium on Micro and Nanoelectronics (RSM)*; IEEE, 2017; pp 127–130. <https://doi.org/10.1109/RSM.2017.8069165>.
- (85) Chen, C.-C.; Aykol, M.; Chang, C.-C.; Levi, A. F. J.; Cronin, S. B. Graphene-Silicon Schottky Diodes. *Nano Letters* **2011**, *11* (5), 1863–1867. <https://doi.org/10.1021/nl104364c>.
- (86) Sinha, D.; Lee, J. U. Ideal Graphene/Silicon Schottky Junction Diodes. *Nano Letters* **2014**, *14* (8), 4660–4664. <https://doi.org/10.1021/nl501735k>.
- (87) Di Bartolomeo, A. Graphene Schottky Diodes: An Experimental Review of the Rectifying Graphene/Semiconductor Heterojunction. *Physics Reports* **2016**, *606*, 1–58. <https://doi.org/10.1016/j.physrep.2015.10.003>.
- (88) Song, L.; Yu, X.; Yang, D. A Review on Graphene-Silicon Schottky Junction Interface. *Journal of Alloys and Compounds* **2019**, *806*, 63–70. <https://doi.org/10.1016/j.jallcom.2019.07.259>.
- (89) Kong, X.; Zhang, L.; Liu, B.; Gao, H.; Zhang, Y.; Yan, H.; Song, X. Graphene/Si Schottky Solar Cells: A Review of Recent Advances and Prospects. *RSC Advances* **2019**, *9* (2), 863–877. <https://doi.org/10.1039/C8RA08035F>.

- (90) Korucu, D.; Turut, A. Temperature Dependence of Schottky Diode Characteristics Prepared with Photolithography Technique. *International Journal of Electronics* **2014**, *101* (11), 1595–1606. <https://doi.org/10.1080/00207217.2014.888774>.
- (91) Fattah, A.; Khatami, S. Selective H₂S Gas Sensing with a Graphene/n-Si Schottky Diode. *IEEE Sensors Journal* **2014**, *14* (11), 4104–4108. <https://doi.org/10.1109/JSEN.2014.2334064>.
- (92) Singh, A.; Uddin, Md. A.; Sudarshan, T.; Koley, G. Gas Sensing by Graphene/Silicon Hetrostructure. In *2013 IEEE SENSORS*; IEEE, 2013; pp 1–4. <https://doi.org/10.1109/ICSENS.2013.6688450>.
- (93) Kim, H.-Y.; Lee, K.; McEvoy, N.; Yim, C.; Duesberg, G. S. Chemically Modulated Graphene Diodes. *Nano Letters* **2013**, *13* (5), 2182–2188. <https://doi.org/10.1021/nl400674k>.
- (94) Noroozi, A. A.; Abdi, Y. A Graphene/Si Schottky Diode for the Highly Sensitive Detection of Protein. *RSC Advances* **2019**, *9* (34), 19613–19619. <https://doi.org/10.1039/C9RA03765A>.
- (95) Chi, X.; Zhang, J.; Nshimiyimana, J. P.; Hu, X.; Wu, P.; Liu, S.; Liu, J.; Chu, W.; Sun, L. Wettability of Monolayer Graphene/Single-Walled Carbon Nanotube Hybrid Films. *RSC Adv.* **2017**, *7* (76), 48184–48188. <https://doi.org/10.1039/C7RA09934G>.
- (96) Hong, G.; Han, Y.; Schutzius, T. M.; Wang, Y.; Pan, Y.; Hu, M.; Jie, J.; Sharma, C. S.; Müller, U.; Poulidakos, D. On the Mechanism of Hydrophilicity of Graphene. *Nano Letters* **2016**, *16* (7), 4447–4453. <https://doi.org/10.1021/acs.nanolett.6b01594>.
- (97) Taherian, F.; Marcon, V.; van der Vegt, N. F. A.; Leroy, F. What Is the Contact Angle of Water on Graphene? *Langmuir* **2013**, *29* (5), 1457–1465. <https://doi.org/10.1021/la304645w>.
- (98) Kozbial, A.; Li, Z.; Conaway, C.; McGinley, R.; Dhingra, S.; Vahdat, V.; Zhou, F.; D’Urso, B.; Liu, H.; Li, L. Study on the Surface Energy of Graphene by Contact Angle Measurements. *Langmuir* **2014**, *30* (28), 8598–8606. <https://doi.org/10.1021/la5018328>.

- (99) Shirtcliffe, N. J.; McHale, G.; Atherton, S.; Newton, M. I. An Introduction to Superhydrophobicity. *Advances in Colloid and Interface Science* **2010**, *161* (1–2), 124–138. <https://doi.org/10.1016/j.cis.2009.11.001>.
- (100) Melios, C.; Giusca, C. E.; Panchal, V.; Kazakova, O. Water on Graphene: Review of Recent Progress. *2D Materials* **2018**, *5* (2), 022001. <https://doi.org/10.1088/2053-1583/aa9ea9>.
- (101) Kwon, S. S.; Choi, J.; Heiranian, M.; Kim, Y.; Chang, W. J.; Knapp, P. M.; Wang, M. C.; Kim, J. M.; Aluru, N. R.; Park, W. Il; Nam, S. Electrical Double Layer of Supported Atomically Thin Materials. *Nano Letters* **2019**, *19* (7), 4588–4593. <https://doi.org/10.1021/acs.nanolett.9b01563>.
- (102) Wang, Q. H.; Jin, Z.; Kim, K. K.; Hilmer, A. J.; Paulus, G. L. C.; Shih, C.-J.; Ham, M.-H.; Sanchez-Yamagishi, J. D.; Watanabe, K.; Taniguchi, T.; Kong, J.; Jarillo-Herrero, P.; Strano, M. S. Understanding and Controlling the Substrate Effect on Graphene Electron-Transfer Chemistry via Reactivity Imprint Lithography. *Nat Chem* **2012**, *4* (9), 724–732. <https://doi.org/10.1038/nchem.1421>.
- (103) Raj, R.; Maroo, S. C.; Wang, E. N. Wettability of Graphene. *Nano Letters* **2013**, *13* (4), 1509–1515. <https://doi.org/10.1021/nl304647t>.
- (104) Yu, Y.; Zhao, Z.-H.; Zheng, Q.-S. Mechanical and Superhydrophobic Stabilities of Two-Scale Surface Structure of Lotus Leaves. *Langmuir* **2007**, *23* (15), 8212–8216. <https://doi.org/10.1021/la7003485>.
- (105) Munz, M.; Giusca, C. E.; Myers-Ward, R. L.; Gaskill, D. K.; Kazakova, O. Thickness-Dependent Hydrophobicity of Epitaxial Graphene. *ACS Nano* **2015**, *9* (8), 8401–8411. <https://doi.org/10.1021/acs.nano.5b03220>.
- (106) Helmholtz, H. Ueber Einige Gesetze Der Vertheilung Elektrischer Ströme in Körperlichen Leitern Mit Anwendung Auf Die Thierisch-Elektrischen Versuche. *Annalen der Physik und Chemie* **1853**, *165* (6), 211–233. <https://doi.org/10.1002/andp.18531650603>.

- (107) Kang, J.; Wen, J.; Jayaram, S. H.; Yu, A.; Wang, X. Development of an Equivalent Circuit Model for Electrochemical Double Layer Capacitors (EDLCs) with Distinct Electrolytes. *Electrochimica Acta* **2014**, *115*, 587–598. <https://doi.org/10.1016/j.electacta.2013.11.002>.
- (108) De Ninno, A.; Nikollari, E.; Missori, M.; Frezza, F. Dielectric Permittivity of Aqueous Solutions of Electrolytes Probed by THz Time-Domain and FTIR Spectroscopy. *Physics Letters A* **2020**, *384* (34), 126865. <https://doi.org/10.1016/j.physleta.2020.126865>.
- (109) Morikawa, K.; Kazoe, Y.; Mawatari, K.; Tsukahara, T.; Kitamori, T. Dielectric Constant of Liquids Confined in the Extended Nanospace Measured by a Streaming Potential Method. *Analytical Chemistry* **2015**, *87* (3), 1475–1479. <https://doi.org/10.1021/ac504141j>.
- (110) Yang, S.; Zhao, X.; Lu, Y.-H.; Barnard, E. S.; Yang, P.; Baskin, A.; Lawson, J. W.; Prendergast, D.; Salmeron, M. Nature of the Electrical Double Layer on Suspended Graphene Electrodes. *Journal of the American Chemical Society* **2022**, *144* (29), 13327–13333. <https://doi.org/10.1021/jacs.2c03344>.
- (111) Chapman, D. L. LI. A Contribution to the Theory of Electrocapillarity. *The London, Edinburgh, and Dublin Philosophical Magazine and Journal of Science* **1913**, *25* (148), 475–481. <https://doi.org/10.1080/14786440408634187>.
- (112) Jung, S.-H.; Seo, Y.-M.; Gu, T.; Jang, W.; Kang, S.-G.; Hyeon, Y.; Hyun, S.-H.; Lee, J.-H.; Whang, D. Super-Nernstian PH Sensor Based on Anomalous Charge Transfer Doping of Defect-Engineered Graphene. *Nano Letters* **2021**, *21* (1), 34–42. <https://doi.org/10.1021/acs.nanolett.0c02259>.
- (113) Gaddam, P.; Ducker, W. Electrostatic Screening Length in Concentrated Salt Solutions. *Langmuir* **2019**, *35* (17), 5719–5727. <https://doi.org/10.1021/acs.langmuir.9b00375>.
- (114) Angizi, S.; Huang, X.; Hong, L.; Akbar, M. A.; Selvaganapathy, P. R.; Kruse, P. Defect Density-Dependent PH Response of Graphene Derivatives: Towards the Development of PH-

Sensitive Graphene Oxide Devices. *Nanomaterials* **2022**, *12* (11), 1801.

<https://doi.org/10.3390/nano12111801>.

- (115) Kontogeorgis, G. M.; Maribo-Mogensen, B.; Thomsen, K. The Debye-Hückel Theory and Its Importance in Modeling Electrolyte Solutions. *Fluid Phase Equilibria* **2018**, *462*, 130–152. <https://doi.org/10.1016/j.fluid.2018.01.004>.
- (116) Lee, C. K.; Seo, J. G.; Kim, H. J.; Hong, S. J.; Song, G.; Ahn, C.; Lee, D. J.; Song, S. H. Versatile and Tunable Electrical Properties of Doped Nonoxidized Graphene Using Alkali Metal Chlorides. *ACS Applied Materials & Interfaces* **2019**, *11* (45), 42520–42527. <https://doi.org/10.1021/acsami.9b15480>.
- (117) Kwon, K. C.; Choi, K. S.; Kim, B. J.; Lee, J.-L.; Kim, S. Y. Work-Function Decrease of Graphene Sheet Using Alkali Metal Carbonates. *The Journal of Physical Chemistry C* **2012**, *116* (50), 26586–26591. <https://doi.org/10.1021/jp3069927>.
- (118) van der Heyden, F. H. J.; Stein, D.; Besteman, K.; Lemay, S. G.; Dekker, C. Charge Inversion at High Ionic Strength Studied by Streaming Currents. *Physical Review Letters* **2006**, *96* (22), 224502. <https://doi.org/10.1103/PhysRevLett.96.224502>.
- (119) Koesharyani, I.; Gardenia, L.; Widowati, Z.; Khumaira, K.; Rustianti, D. *Dissolved oxygen: Fundamentals of environmental measurements*. Jurnal Riset Akuakultur. <https://www.fondriest.com/environmental-measurements/parameters/water-quality/dissolved-oxygen/> %3E.
- (120) Liu, H.; Liu, Y.; Zhu, D. Chemical Doping of Graphene. *Journal of Materials Chemistry* **2011**, *21* (10), 3335–3345. <https://doi.org/10.1039/c0jm02922j>.
- (121) Gierz, I.; Riedl, C.; Starke, U.; Ast, C. R.; Kern, K. Atomic Hole Doping of Graphene. *Nano Letters* **2008**, *8* (12), 4603–4607. <https://doi.org/10.1021/nl802996s>.

- (122) Kim, D. H.; Park, W. H.; Oh, H. G.; Jeon, D. C.; Lim, J. M.; Song, K. S. Two-Channel Graphene PH Sensor Using Semi-Ionic Fluorinated Graphene Reference Electrode. *Sensors* **2020**, *20* (15), 4184. <https://doi.org/10.3390/s20154184>.
- (123) Salvo, P.; Melai, B.; Calisi, N.; Paoletti, C.; Bellagambi, F.; Kirchhain, A.; Trivella, M. G.; Fuoco, R.; Di Francesco, F. Graphene-Based Devices for Measuring PH. *Sensors and Actuators B: Chemical* **2018**, *256*, 976–991. <https://doi.org/10.1016/j.snb.2017.10.037>.
- (124) Gou, P.; Kraut, N. D.; Feigel, I. M.; Bai, H.; Morgan, G. J.; Chen, Y.; Tang, Y.; Bocan, K.; Stachel, J.; Berger, L.; Mickle, M.; Sejdić, E.; Star, A. Carbon Nanotube Chemiresistor for Wireless PH Sensing. *Scientific Reports* **2015**, *4* (1), 4468. <https://doi.org/10.1038/srep04468>.
- (125) Chang, C.-N.; Cheng, H.-B.; Chao, A. C. Applying the Nernst Equation To Simulate Redox Potential Variations for Biological Nitrification and Denitrification Processes. *Environmental Science & Technology* **2004**, *38* (6), 1807–1812. <https://doi.org/10.1021/es021088e>.
- (126) Xiong, C.; Zhang, T.; Wang, D.; Lin, Y.; Qu, H.; Chen, W.; Luo, L.; Wang, Y.; Zheng, L.; Fu, L. Highly Sensitive Solution-Gated Graphene Transistor Based Sensor for Continuous and Real-Time Detection of Free Chlorine. *Analytica Chimica Acta* **2018**, *1033*, 65–72. <https://doi.org/10.1016/j.aca.2018.06.041>.
- (127) Sharif, O. Towards Identifying Disinfectants and Quantifying Disinfectant Levels in Water, McMaster University, 2017.
- (128) Faruk Hossain, M.; McCracken, S.; Slaughter, G. Electrochemical Laser Induced Graphene-Based Oxygen Sensor. *Journal of Electroanalytical Chemistry* **2021**, *899*, 115690. <https://doi.org/10.1016/j.jelechem.2021.115690>.
- (129) Fu, L.; Zheng, Y.; Fu, Z.; Wang, A.; Cai, W. Dissolved Oxygen Detection by Galvanic Displacement-Induced Graphene/Silver Nanocomposite. *Bulletin of Materials Science* **2015**, *38* (3), 611–616. <https://doi.org/10.1007/s12034-015-0900-5>.

- (130) Denis, P. A. Chemical Reactivity of Lithium Doped Monolayer and Bilayer Graphene. *Journal of Physical Chemistry C* **2011**, *115* (27), 13392–13398.
<https://doi.org/10.1021/jp203547b>.
- (131) Kwon, K. C.; Choi, K. S.; Kim, C.; Kim, S. Y. Role of Metal Cations in Alkali Metal Chloride Doped Graphene. *The Journal of Physical Chemistry C* **2014**, *118* (15), 8187–8193.
<https://doi.org/10.1021/jp500646e>.
- (132) Watcharinyanon, S.; Virojanadara, C.; Johansson, L. I. Rb and Cs Deposition on Epitaxial Graphene Grown on 6H-SiC(0001). *Surface Science* **2011**, *605* (21–22), 1918–1922.
<https://doi.org/10.1016/j.susc.2011.07.007>.
- (133) Chen, C.; Zhang, J.; Zhang, B.; Ming Duan, H. Hydrogen Adsorption of Mg-Doped Graphene Oxide: A First-Principles Study. *The Journal of Physical Chemistry C* **2013**, *117* (9), 4337–4344. <https://doi.org/10.1021/jp308271b>.
- (134) Chapman, J.; Su, Y.; Howard, C. A.; Kundys, D.; Grigorenko, A. N.; Guinea, F.; Geim, A. K.; Grigorieva, I. V.; Nair, R. R. Superconductivity in Ca-Doped Graphene Laminates. *Scientific Reports* **2016**, *6* (1), 23254. <https://doi.org/10.1038/srep23254>.
- (135) Du, Z.; Chen, X.; Hu, W.; Chuang, C.; Xie, S.; Hu, A.; Yan, W.; Kong, X.; Wu, X.; Ji, H.; Wan, L.-J. Cobalt in Nitrogen-Doped Graphene as Single-Atom Catalyst for High-Sulfur Content Lithium–Sulfur Batteries. *Journal of the American Chemical Society* **2019**, *141* (9), 3977–3985. <https://doi.org/10.1021/jacs.8b12973>.
- (136) Jiang, L.; Chen, Z.; Cui, Q.; Xu, S.; Hou, X.; Tang, F. Density Functional Theory Research on the Adsorption Properties of Ti-Doped Graphene for Acetone and Other Gases. *Materials Science in Semiconductor Processing* **2022**, *138*, 106252.
<https://doi.org/10.1016/j.mssp.2021.106252>.
- (137) Lin, P.-C.; Villarreal, R.; Achilli, S.; Bana, H.; Nair, M. N.; Tejeda, A.; Verguts, K.; De Gendt, S.; Auge, M.; Hofsässs, H.; De Feyter, S.; Di Santo, G.; Petaccia, L.; Brems, S.;

- Fratesi, G.; Pereira, L. M. C. Doping Graphene with Substitutional Mn. *ACS Nano* **2021**, *15* (3), 5449–5458. <https://doi.org/10.1021/acsnano.1c00139>.
- (138) Cortés-Arriagada, D.; Villegas-Escobar, N.; Ortega, D. E. Fe-Doped Graphene Nanosheet as an Adsorption Platform of Harmful Gas Molecules (CO, CO₂, SO₂ and H₂S), and the Co-Adsorption in O₂ Environments. *Applied Surface Science* **2018**, *427*, 227–236. <https://doi.org/10.1016/j.apsusc.2017.08.216>.
- (139) Chen, Y.; Liu, Y.; Wang, H.; Zhao, J.; Cai, Q.; Wang, X.; Ding, Y. Silicon-Doped Graphene: An Effective and Metal-Free Catalyst for NO Reduction to N₂ O? *ACS Applied Materials & Interfaces* **2013**, *5* (13), 5994–6000. <https://doi.org/10.1021/am400563g>.
- (140) Gecim, G.; Ozekmekci, M.; Fellah, M. F. Ga and Ge-Doped Graphene Structures: A DFT Study of Sensor Applications for Methanol. *Computational and Theoretical Chemistry* **2020**, *1180*, 112828. <https://doi.org/10.1016/j.comptc.2020.112828>.
- (141) Sahoo, M.; Sreena, K. P.; Vinayan, B. P.; Ramaprabhu, S. Green Synthesis of Boron Doped Graphene and Its Application as High Performance Anode Material in Li Ion Battery. *Materials Research Bulletin* **2015**, *61*, 383–390. <https://doi.org/10.1016/j.materresbull.2014.10.049>.
- (142) Wang, L.; Li, Y.; Wang, Y.; Kong, W.; Lu, Q.; Liu, X.; Zhang, D.; Qu, L. Chlorine-Doped Graphene Quantum Dots with Enhanced Anti- and Pro-Oxidant Properties. *ACS Applied Materials & Interfaces* **2019**, *11* (24), 21822–21829. <https://doi.org/10.1021/acscami.9b03194>.
- (143) Huang, S.; Li, Y.; Feng, Y.; An, H.; Long, P.; Qin, C.; Feng, W. Nitrogen and Fluorine Co-Doped Graphene as a High-Performance Anode Material for Lithium-Ion Batteries. *Journal of Materials Chemistry A* **2015**, *3* (46), 23095–23105. <https://doi.org/10.1039/C5TA06012E>.
- (144) Albero, J.; Vidal, A.; Migani, A.; Concepción, P.; Blancafort, L.; García, H. Phosphorus-Doped Graphene as a Metal-Free Material for Thermochemical Water Reforming at

Unusually Mild Conditions. *ACS Sustainable Chemistry & Engineering* **2019**, 7 (1), 838–846. <https://doi.org/10.1021/acssuschemeng.8b04462>.

- (145) Shao, Y.; Zhang, S.; Engelhard, M. H.; Li, G.; Shao, G.; Wang, Y.; Liu, J.; Aksay, I. A.; Lin, Y. Nitrogen-Doped Graphene and Its Electrochemical Applications. *Journal of Materials Chemistry* **2010**, 20 (35), 7491. <https://doi.org/10.1039/c0jm00782j>.
- (146) Sun, X.; Wang, Z.; Fu, Y. Q. Adsorption and Diffusion of Sodium on Graphene with Grain Boundaries. *Carbon N Y* **2017**, 116, 415–421. <https://doi.org/10.1016/j.carbon.2017.01.024>.

Chapter 3 Defect Engineering of Graphene to Modulate pH Response of Graphene Devices

This chapter shows the defect-dependent pH response of graphene, focusing on the pH sensing mechanisms. With varying defects of graphene in the aqueous electrolyte, two categories of graphene interactions were identified: capacitive charge screening and direct charge transfer. The former was dominant when the defectivity level was below a specific range ($I_D/I_G=0.35$, measured by Raman spectroscopy). While the latter becomes dominant above the ratio, demonstrating that the protonation/deprotonation of pH-sensitive oxygen-containing functional groups controls the generated current through the surface. Two countervailing mechanisms balance out at the crossover point ($I_D/I_G = 0.35$), creating a pH-insensitive graphene device. To understand the defect-induced pH response of graphene, selective functionalization using pyrene derivatives was utilized to uncover the dominant acid-base interactions of carboxyl and amine groups at low pH and hydroxyl groups at high pH.

Reprinted with permission from Langmuir, 2021, 37, 41, 12163–12178, Shayan Angizi, Eugene Yat Chun Yu, Johnson Dalmieda, Dipankar Saha, P. Ravi Selvaganapathy, and Peter Kruse. DOI: 10.1021/acs.Langmuir.1c02088© 2021 America Chemical Society

Defect Engineering of Graphene to Modulate pH Response of Graphene Devices

Shayan Angizi, Eugene Yat Chun Yu, Johnson Dalmieda, Dipankar Saha, P. Ravi Selvaganapathy, and Peter Kruse*

 Cite This: *Langmuir* 2021, 37, 12163–12178

 Read Online

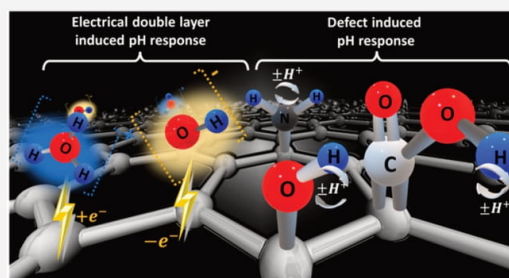
ACCESS |

 Metrics & More

 Article Recommendations

 Supporting Information

ABSTRACT: Graphene-based pH sensors are a robust, durable, sensitive, and scalable approach for the sensitive detection of pH in various environments. However, the mechanisms through which graphene responds to pH variations are not well-understood yet. This study provides a new look into the surface science of graphene-based pH sensors to address the existing gaps and inconsistencies among the literature concerning sensing response, the role of defects, and surface/solution interactions. Herein, we demonstrate the dependence of the sensing response on the defect density level of graphene, measured by Raman spectroscopy. At the crossover point ($I_D/I_G = 0.35$), two countervailing mechanisms balance each other out, separating two regions where either a surface defect induced (negative slope) or a double layer induced (positive slope) response dominates. For ratios above 0.35, the pH-dependent induction of charges at surface functional groups (both pH-sensitive and nonsensitive groups) dominates the device response. Below a ratio of 0.35, the response is dominated by the modulation of charge carriers in the graphene due to the electric double layer formed from the interaction between the graphene surface and the electrolyte solution. Selective functionalization of the surface was utilized to uncover the dominant acid–base interactions of carboxyl and amine groups at low pH while hydroxyl groups control the high pH range sensitivity. The overall pH-sensing characteristics of the graphene will be determined by the balance of these two mechanisms.



1. INTRODUCTION

The pH of aqueous solutions plays a major role in the control of chemical and biological processes, and it needs to be carefully regulated for many chemical equilibria such as redox reactions, complex formation, and solubility.¹ The pH of drinking water can influence corrosion processes (including the dissolution of lead from pipes) and the effectiveness of disinfectants. Hence, the pH of drinking water is typically regulated to between 6.5 and 9.0 based on standards reported by the World Health Organization (WHO).² In the laboratory and for commercial applications, pH is commonly measured potentiometrically with porous glass electrodes^{3,4} or using colorimetric indicators either in solution⁵ or immobilized on paper strips.⁶ Colorimetric methods consume reagents while electrodes for potentiometric methods require frequent maintenance, and often, special conditions are required to preserve the electrodes,^{7–9} limiting their utility for online monitoring applications. Graphene-based solid-state devices have been explored as alternatives.¹⁰ The advent of graphene in 2004¹¹ was followed by a wave of research on two-dimensional materials,^{12–15} which revealed their inherent potential in many different sensing applications,^{16–18} including solid state pH sensors.^{19,20} Graphene is a honeycomb structure

with sp^2 -hybridized carbon atoms covalently bonded in-plane, while weak van der Waals interactions in the out-of-plane direction result in stacking of adjacent layers.^{21,22} Apart from the excellent mechanical strength, chemical and thermal stability, and high thermal conductivity of graphene, its superior electrical conductivity and unique optoelectronic properties, ultrahigh carrier mobility, and cone-shaped band diagram have made it a unique electronic material. In particular, the electronic structure of these atomically thin layers at the Dirac points where π and π^* states are touching is amenable to chemical and physical modification.^{23–25} Therefore, the ultrasensitivity of atomic layers of graphene to external chemical species has inspired the development of graphene-based sensing platforms.

To overcome the current challenges and increase the sensitivity of pH electrodes, many efforts have been devoted

Received: August 5, 2021
Revised: September 23, 2021
Published: October 8, 2021



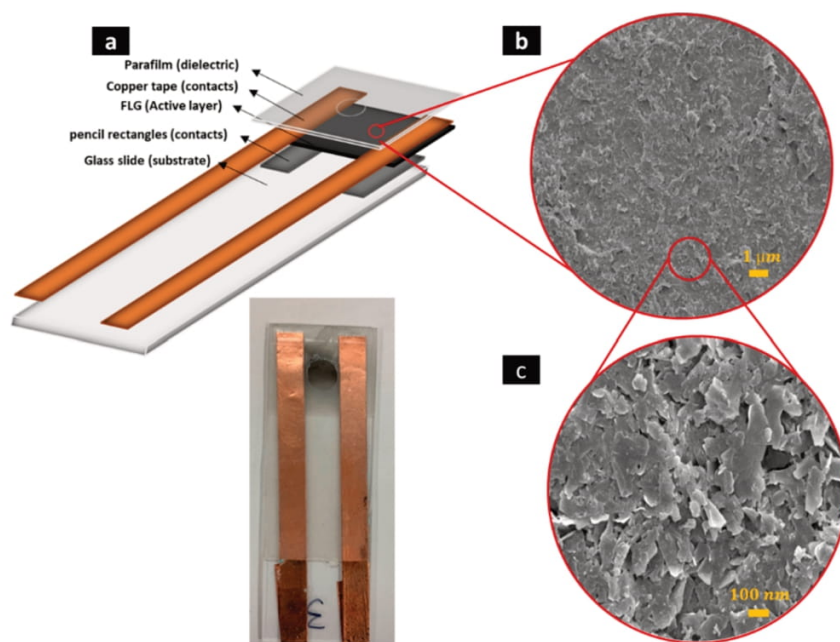


Figure 1. (a) Schematic illustration and real image of a chemiresistive sensor consisting of a glass substrate, pencil-drawn rectangles as contacts, FLG as the active layer, copper tape for contacts and parafilm as a dielectric. SEM images of the drop-casted FLG on the glass substrate in different magnifications of (b) 1 μm and (c) 100 nm.

to the integration of graphene as active layer. Considering the (theoretically) hydrophobic nature of graphene, its surface interactions with ions and aqueous solutions should be extremely limited.²⁶ However, it has been shown that the presence of local charges caused by defects (vacancies, dopants, and functional groups) provides local hydrophilic sites.^{27–29} In 2011, a chemiresistive pH sensor based on single-layer graphene was demonstrated, giving a linear relationship between the pH value and the change in sensor resistance. The reported slope was 2 $\text{k}\Omega/\text{pH}$, and the experiment was done with pH resolutions of 0.97 and 0.33 pH in acid and alkali solutions. The pH resolution is defined as the ratio of the maximum standard deviation of multiple experiments over the sensitivity of the sensors. They observed that with increasing pH the overall resistance of the sensor decreases.³⁰ The proposed mechanism is direct nonfaradaic adsorption of hydronium (H_3O^+) and hydroxide (OH^-) ions onto the surface of graphene so that charge transfer is blocked across the graphene/solution interface. As a result of the formation of the electric double-layer (EDL), the inner Helmholtz layer is dominated by adsorbed H_3O^+ ; this induces negative image charges in the graphene, effectively acting as an n-dopant. In contrast, if OH^- dominated the inner Helmholtz layer, positive charges would be induced in the graphene, leading to p-doping. The structure of the EDL can be further examined by adding a gate electrode to modulate its thickness.^{30–32} In the solution-gate field-effect transistor (SGFET), the channel conductivity is controlled by applying a gate potential across the dielectric (electrolyte).³³ With the assumption that only direct interaction of ions with the surface causes pH sensitivity, a negative gate voltage increases OH^- ion concentration in the inner Helmholtz layer and results in an increased conductivity of the channel. In contrast, a positive gate voltage causes the accumulation of H_3O^+ ions and reduces the channel

conductivity. In other words, as the pH increases, the Dirac point moves toward a more positive potential, resulting in p-doping of graphene. In 2013, Maily-Giacchetti et al. reported a substrate independent pH sensitivity of SGFET. Accordingly, neither remaining residues from the graphene transfer process nor the nature of the substrate underneath graphene could affect the pH sensitivity (21 mV/pH).³⁴ Moreover, the electrostatic gating effect induced by adsorption of H_3O^+ or OH^- ions (capacitive charging of the EDL) at the graphene surface was found to be the main mechanism responsible for the pH sensing.^{35,36} One common aspect among all these studies is a focus on maintaining the graphene surface “clean”. This means that impacts of surface abnormalities such as functional groups on the pH sensing mechanism are either neglected or kept aside. For that purpose, a monolayer of organic compounds such as aryl halides can repel the water from the surface and minimize the interfacial interactions. This condition simulates the “ideal” graphene film where a hydrophobic surface repels the water. Even though the role of grain boundaries and surface defects has been debated, the actual sensing mechanism has not been conclusively revealed.^{32,37,38} There has also been some discussion on the influence of defects on other carbon-based nanomaterials such as carbon nanotubes (CNTs).^{39–41} Carboxylic acid groups have been shown to be active pH-sensitive sites on CNTs due to their ability to be deprotonated at higher pH.⁴² However, no discussions on surface modulation mechanisms, other groups, or defect density were presented. Moreover, this resulted in a current vs pH trend that is an opposite of the previously discussed mechanism, which has not been explained.

Here, we investigate the pH sensitivity of few-layer graphene (FLG) through modulation of its defect density. We show that the chemiresistive sensor response results from the balance of two simultaneous mechanisms of the graphene–solution

Table 1. Solubility Information of PDs

PDs	Self-Assembly Solvent	Functional groups	Concentration	ref
1-hydroxypyrene	Acetonitrile	Hydroxyl (–OH)	1.6 mM	45
1-aminopyrene	Ethanol	Amine (–NH ₂)	1.4 mM	45
1-pyrenecarboxaldehyde	Acetonitrile	Aldehyde (–CHO)	1.2 mM	45,48
1-Pyrenecarboxylic acid	Ethanol	Carboxyl (–COOH)	0.3 mM	45,49

interface as well as the acid–base interactions of functional groups. An experimental crossover point at a certain defect density determines which of the mechanisms dominates. To selectively examine the surface interactions, the impact of annealing duration on the sensing performance of FLG-chemiresistive sensors was investigated. The defect dominant mechanism was further elucidated by controlled functionalization of the FLG surface using pyrene derivatives (PDs) resembling the presence of selected functional groups. We show that pH-sensitive functional groups can act as active sites where their protonation or deprotonation as a result of changing pH values varies the sensor response. pH-insensitive groups may enhance the surface hydrophilicity and either escalate surface–solution interactions or diminish the response due to acid–base interactions. Lastly, the dominance of either mechanism will determine the overall pH response of a graphene device.

2. MATERIALS AND EXPERIMENTAL DESIGN

2.1. Materials. Graphite powder (99.99%) was purchased from Sigma-Aldrich. Pre-cleaned frosted-end microscopic glass slides and Parafilm “M” were purchased from VWR. 1-amino pyrene (Py-NH₂), 1-hydroxy pyrene (Py-OH), 1-carboxyaldehyde pyrene (Py-CHO), and pyrene carboxylic acid (Py-COOH) were purchased from Sigma-Aldrich and used without further purification. Isopropanol (HPLC grade, 99.99%) was purchased from Fisher Scientific. Ultrapure water used for the experiments (18.2 MΩ·cm) was obtained from a Millipore Simplicity UV water purifier system. Sodium hydroxide (99%) and hydrochloric acid (37.2%) were purchased from Caledon Laboratories Ltd. and used to adjust the pH in the experiments.

2.2. Sensor Fabrication and Experimental Procedure. The chemiresistive sensor design has previously been reported in ref 43 and 44. Briefly, 40 mg of graphite powder is added to 15 mL of a mixture of H₂O/IPA 1:1.45 (v/v). Then, the mixture is sonicated for 6 h in a bath sonicator (Elmasonic P60H ultrasonic cleaner, 100% power; sweep mode) at 37 kHz and 30 °C. After this, the FLG suspension is centrifuged at 14000 rpm (13140 × g) for 5 min in an Eppendorf MiniSpin Plus microcentrifuge, and the supernatant is separated. Then the product is again centrifuged at 14000 rpm (13140 × g) for 15 min, keeping the sedimented flakes for sensor fabrication.

To prepare the chemiresistive sensors, glass slides were rinsed with acetone, water, and methanol to clean the surface from pre-existing contaminants. Then two rectangles were drawn using a 9B pencil to provide uniform contacts with the subsequent active layer. As-prepared FLG is then drop-casted on the surface to form an active layer with an average resistance of ~20 kΩ. When an annealing process was required, the FLG films were annealed in a tube furnace (a three-heat zone Lindberg Thermodyne 21100) at 500 °C (15 °C/min heating ramp, overnight cooling) under a flow of either N₂(g) or N₂(g)/H₂(g) for the required time. Later, the copper tape was attached to both sides of the FLG film followed by masking with prepatterned Parafilm as dielectric (Figure 1a). The masking of the sensors with a dielectric (here Parafilm) is an essential part of sensor fabrication, preventing the exposure of the copper contacts to water. For this purpose, a piece of Parafilm was cut to the size of the glass slide width (~2 cm × 3 cm). Then the center of the film was punched to form a circular hole with a diameter of ~1 cm. Then samples were preheated to 70 °C (slightly above the Parafilm's glass transition

temperature ~60 °C). At this point, by the gentle application of uniform pressure, all desired areas are covered by a thin uniform layer of parafilm (Figure 1a). Scanning electron microscopy (SEM) images of the FLG network on the glass slides are shown in Figure 1b,c at different magnifications.

At the start of each experiment, the sensors were immersed into a fresh solution of 200 ppm (3.42 mM) NaCl in DI water; they were left overnight to establish an equilibrium at the sensor-solution interface and minimize the impact of momentary changes on sensor response. All experiments were done using 200 ppm of NaCl (3.42 mM) in DI water to avoid interference from changes in the ionic strength of the solution on the FLG surface responses. The experiments were then carried out the next day by adjusting the pH with 0.1 M HCl and NaOH and recording the sensor responses. The acid or base were added gradually to reach the desired pH (between 3 and 8) and the sensors were kept at each pH for 30–35 min. It should be noted that due to the drift of the current in each step, the sensor responses were calculated using the last 60 points of each step. Hence, we assumed 30–40 min as the responsivity of the sensors to pH values. The observed noise has several distinct origins. The contact area between the chemiresistive film and the copper tape is a source of several nA of baseline noise. Larger jumps are introduced into the data due to electromagnetic interferences from the stirrer and mechanical events (turbulences, variations in the meniscus) due to the agitation of the solution. However, stirring is essential to achieve a uniform and defined pH in the entire analyte bowl (containing a pH electrode and multiple sensors for reproducibility).

2.3. Doping. In order to dope the surface of FLG with PDs, sensors were dipped into saturated solutions overnight. A discussion on surface passivation of graphene with PDs has been reported elsewhere.⁴⁵ To reach at least about 90% surface coverage by a monolayer of PDs and to avoid the formation of dimers or trimers, surfaces of the sensors were rinsed with a compatible solvent.^{46,47} Table 1 shows the specific information on the PDs and corresponding solvents used in this work.

2.4. Theoretical Calculations. Bulk density functional theory (DFT) calculations were done using Gaussian09 software using the Becke 3-parameter Lee–Yang–Parr (B3LYP) functional and the 6-31G++(d,p) basis set. The pK_a values were calculated using the thermodynamic cycles as described in the literature.⁵⁰ The solvation method used for the pyrenes was the integral equation formalism polarizable continuum model (IEFPCM) with the exception of 1-aminopyrene, where the solvation model based on density (SMD) was used.⁵¹ Surface adsorption calculations were done using MOPAC software with parametrization method 6 and hydrogen correction (PM6-DH2). Structures were visualized using Avogadro software.

2.5. Characterization. A Renishaw inVia Raman spectrometer was employed to characterize the samples in the range of 200–3500 cm⁻¹ with a spectral resolution of 2 cm⁻¹. A 514 nm laser was focused through a 50× objective lens and an aperture for a spot size of about 1.5 μm. The laser power was limited to 1% to avoid sample damage. Raman spectra for each sample were taken from two different spots per sample and three samples per condition. The deconvolution of Raman spectra was done using the Gaussian 7010 function with manual baseline correction. The SEM images were taken by a JEOL JSM7000F microscope at 20 kV. Chemiresistive sensing measurements were carried out using a four-channel eDAQ EPU452 Quad Multifunction isoPod. The channel type for chemiresistive sensing was set to biosensor, with an applied voltage of 10 mV. A pH electrode (purchased from eDAQ Inc.) was calibrated with pH 4 and pH 7 calibration solutions before the experiments.

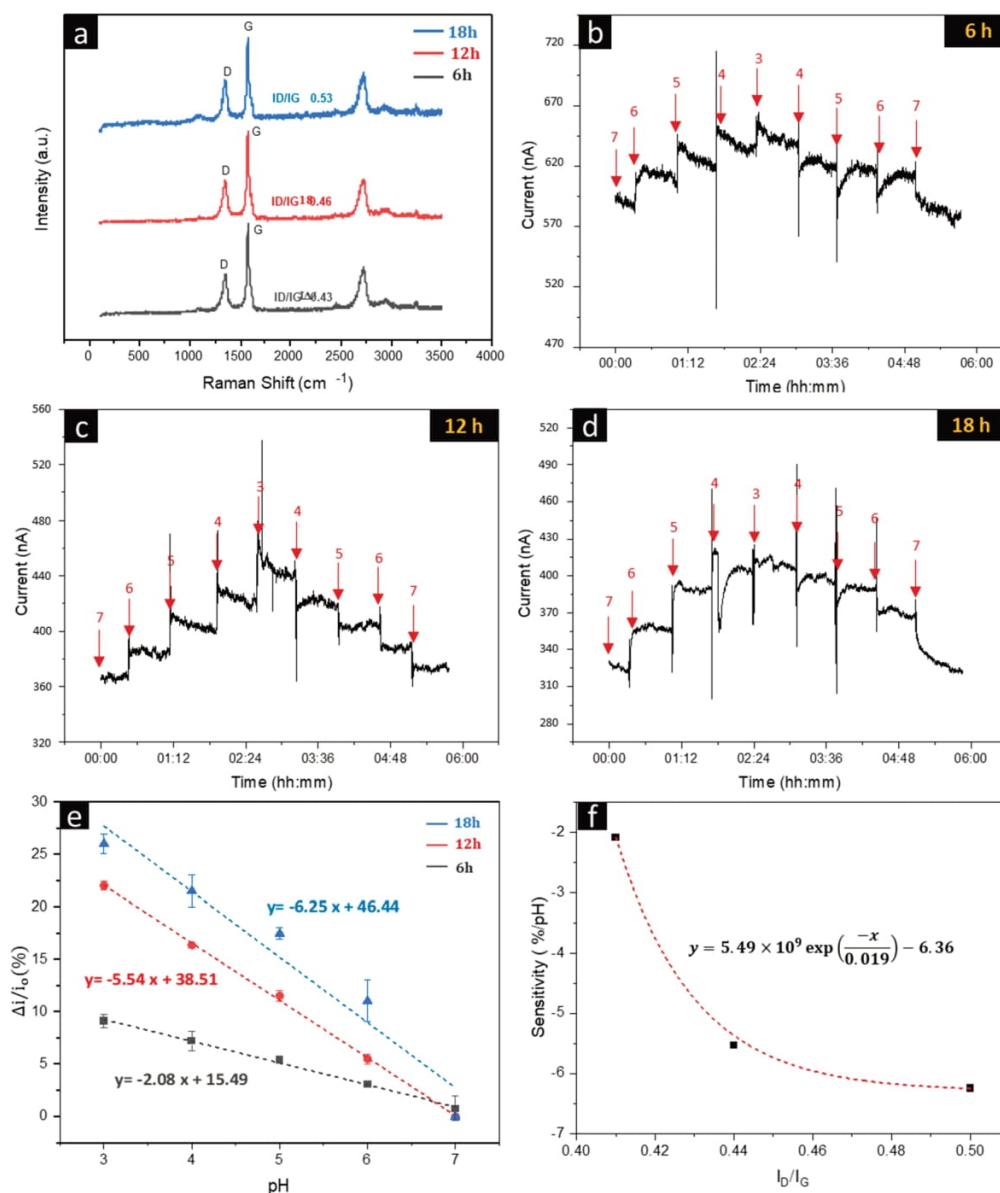


Figure 2. (a) Raman Spectra of sonicated FLG for 6 h, 12 h, and 18 h revealing the change in defect density level. Chemiresistive sensing performance of sonicated samples: (b) 6 h, (c) 12 h, and (d) 18 h of sonication. (e) Calibration curves of the corresponding sensors and (f) plot of change in sensitivity by variation of I_D/I_G .

3. RESULTS AND DISCUSSION

3.1. Relation of Surface Defect Density with pH.

Sonication is one of the most facile liquid phase exfoliation techniques and can produce nanosized materials on a large scale. Since the exfoliation mechanisms during the sonication often involve chemical interaction of materials with solution, the presence of local chemical contaminant species in the product is unavoidable.⁵² Therefore, interpretation of the surface chemistry to understand the impact of sonication duration on both defect density and pH sensitivity of the sensors is critical. The exfoliation of graphite to create FLG disturbs the symmetry of the infinite lattice geometry of graphene due to the formation of point defects, dopants,

functional groups, and sp^3 hybridized regions.⁵³ So far, despite extensive research on the surface characteristics of graphene, their qualitative and quantitative relations with its pH sensitivity are not well understood. Raman spectra of FLG sonicated for 6, 12, and 18 h in an IPA/H₂O 55:45 v/v solvent mixture are shown in Figure 2a. The G peak at 1531 cm^{-1} is assigned to the in-plane stretching vibrations of the sp^2 hybridized lattice originating from the Raman active E_{2g} phonon mode at the Γ point of its Brillouin zone (BZ).⁵⁴ The D band at 1357 cm^{-1} results from the disruption of the infinite symmetry of the carbon atoms. This peak is often used as a measure of defect density in graphene through vacancies, grain boundaries, dopants, or the presence of sp^3 hybrid-

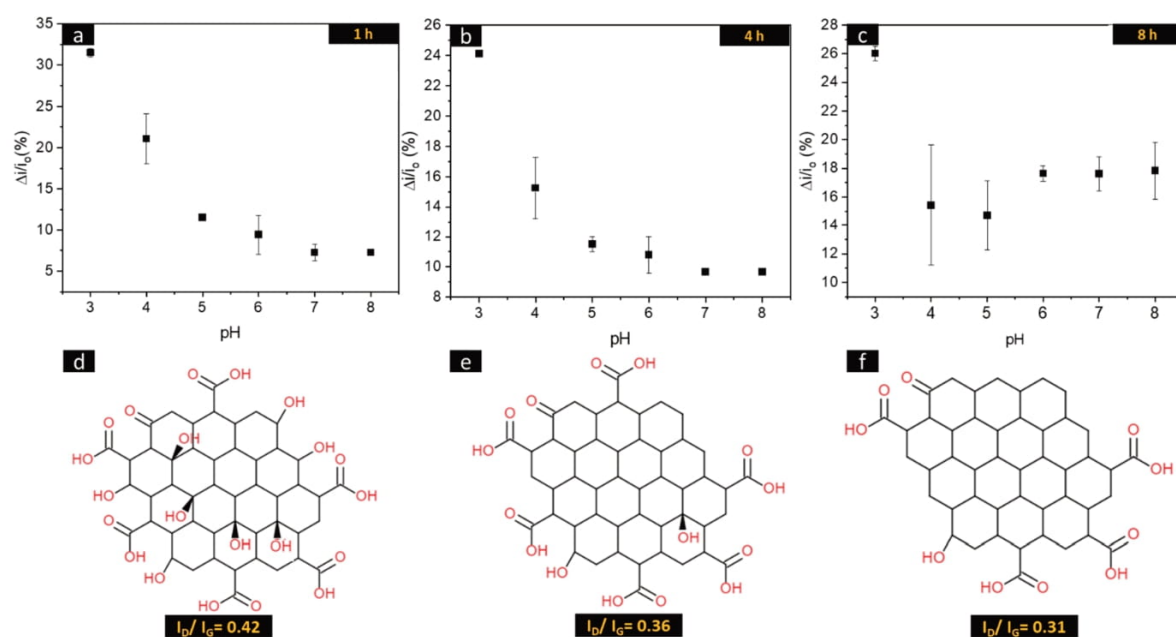


Figure 3. Sensing calibration curves and schematic representation of N_2 -annealed sensors (a,b) 1 h, (c,d) 4 h, and (e,f) 8 h, respectively.

izations.^{55,56} Therefore, the ratio of I_D/I_G can be employed to predict the level of surface “soundness”.^{57–59} As noticed in Figure 2a, the ratio of I_D/I_G rises as the sonication time increases, indicating that the products are becoming more defective. The sonication process leads to the formation of surface and/or edge functionalization and the creation of local polarities on the surface. These local sites increase the hydrophilicity of the flakes, rendering a more stable suspension. In the FTIR spectrum of a 6 h-sonicated sample (Figure S1), the peaks at 1067.5 and 1007.1 cm^{-1} (1000–1300 cm^{-1}) result from C–O stretching of alcohols and phenols. The peak at 1312.2 cm^{-1} (1250–1350 cm^{-1}) is due to C–O stretching of alkoxy groups.⁶⁰ The peak at 1711.9 cm^{-1} (1680–1720 cm^{-1}) corresponds to C=O stretching derived from either aldehydes or ketones. Two very small peaks at 2920.6 and 3007.1 cm^{-1} can be assigned to C–H stretching, representing $-\text{CH}_2$ and $-\text{CH}_3$ groups of the surface, respectively.^{59,61} Lastly, the broad peak at 3510 cm^{-1} (2500–3500 cm^{-1}) can be assigned to the O–H stretching of carboxylic acid groups.⁶² These results reveal that the surface is partially covered with oxygen-based functional groups, even after sonication for only 6 h.

The information obtained from FTIR spectra reveals the presence of functional groups. It is important to consider how the FLG responds to pH changes as the defect density of the surface increases. In order to address this question, Figure 2b,c illustrates the sensing performance of sensors made from 6, 12, and 18 h sonicated FLG upon exposure to aqueous solutions of various pH. The 6 h (Figure 2b), 12 h (Figure 2c), and 18 h (Figure 2d) sonicated sensors display an upward change in current upon a decrease in pH value and vice versa. This trend is opposite of the published behavior for low defect monolayer graphene³⁰ but it is in good agreement with the reported results for COOH functionalized CNTs.⁴² Notably, the sensors are responding to all pH values throughout the cycle. The sensitivity of the sensors is found to increase with

sonication time, confirming that the pH sensitivity is a function of surface defect density (Figure 2e). Not only does the 18 h sonicated sensor have a higher sensitivity, but also it shows higher responses at each pH compared to 6 and 12 h. The relationship of sensor sensitivity and FLG I_D/I_G ratio is shown in Figure 2f. As predicted, a higher I_D/I_G ratio (higher defect density) leads to greater sensitivity. However, this increase is not linear and increasing the I_D/I_G ratio from 0.41 to 0.44 results in ~ 2.5 times higher sensitivity. In contrast, the increase of I_D/I_G from 0.44 to 0.5 improves the sensitivity only slightly (~ 1.1 times higher). This demonstrates that introducing defects at lower defect densities will severely alter graphene’s pH sensitivity while its impact will diminish when the I_D/I_G ratio is already high. We found the exponential decay function fitting to the curve as

$$\%/\text{pH} = 5.49 \times 10^9 \exp\left(-\frac{\left(\frac{I_D}{I_G}\right)}{0.019}\right) - 6.36$$

Since the calibration curve has a negative slope, an increase in the I_D/I_G ratio gives rise to a more negative sensitivity (higher absolute value). While the exact curve shape cannot be derived with absolute certainty from the three data points in Figure 2f, several conclusions can be drawn: First, the Y-intercept is -6.36 , a number close to the slope of the 18 h sonicated calibration curve, meaning the sensitivity should not change considerably for any sonication times beyond 18 h. Second, by solving the equation for sensitivity ≈ 0 , an I_D/I_G ratio of 0.35 ± 0.02 is obtained. A sensitivity value of ≈ 0 refers to a flat calibration curve, rendering the device useless for pH sensing, although it may be desirable for sensing other parameters without pH interference. The value of 0.35 is only an approximation extrapolated from the above fit. It will also vary with device geometry and preparation procedures. In our case, however, it is consistent with data from molecularly

modified films, as discussed in the following sections. Importantly, it divides the range of pH sensitivity parameters into two regions: one with negative slopes and one with positive slopes. Below $I_D/I_G = 0.35$, the slopes of the calibration curves become positive while ratios above $I_D/I_G = 0.35$ result in negative slopes of the calibration curves. This implies two separate dominant regions for the different sensing mechanisms, although the precise value of this crossover point varies by experimental conditions. The high range I_D/I_G represents dominance of the defect-dominant sensing mechanism while below $I_D/I_G = 0.35$, the prevalent pH sensing mechanism will be solution/surface interactions. To evaluate this hypothesis, a series of surface annealing experiments was designed, while measuring the sensing performance of the sensors.

3.2. Surface Dominant Sensing Mechanism. **3.2.1. N_2 -Annealing.** For the purpose of identifying the sensing mechanisms and minimizing defect density of the surface, separate batches of sensors were annealed either under N_2 or under N_2/H_2 (95%/5%). The former is shown to be ineffective in surface reduction, and thermal dissociation of functional groups occurs. However, the latter is known as an effective method to reduce the surface.⁶³ The sensors were initially annealed for 1, 4, and 8 h under pure N_2 at 500 °C. Raman spectra of the N_2 -annealed samples revealed that the average I_D/I_G ratio drops from initially 0.46 to 0.31 upon annealing for 8 h. In fact, no substantial drop in I_D/I_G ratio was observed after 4 h annealing. Therefore, 8 h was assumed to suffice for achieving close to the minimum I_D/I_G ratio obtainable by N_2 -annealing (SI, Figure S2). Since the furnace environment does not contain a reducing agent, existing functional groups should be thermally removed, meaning that thermal energy provides the necessary dissociation energy of the groups from the surface. Figure 3 illustrates the sensing performances of N_2 -annealed sensors. As observed in Figures 3a and S3a, 1 h N_2 -annealed sensors reveal higher responses at lower pH values and low responses at high pH values. This trend is intensified as annealing increases. This difference can be seen in the calibration curves of the samples. A comparison of Figure S3c with Figure 2b (the linear behavior of 6 h sonicated sample) shows that the sensor is responding only to low pH, exhibiting a close to exponential relationship. This behavior originates from a transition in the sensing mechanism due to thermal reduction (the mechanism will be discussed in the section Defect Dominant Sensing Mechanism). A comparison of the sensor responses for 4 h (Figures 3b and S3b) and 8 h N_2 -annealed (Figures 3c and S3c) reveals that the longer annealing duration lowers the sensitivity to higher pH values. Notably, the reverse variation of current with pH at lower pH can be still seen after 8 h of N_2 -annealing, demonstrating an ineffective surface reduction and the presence of residual surface defects. As mentioned, the slope of the calibration curve is still negative between pH 3 and 5 for the 8 h N_2 -annealed sample but turns positive for higher pH values (Figure 3c). This means that a higher pH leads to higher surface conductance, exactly opposite of the previously observed pattern. This can be reconfirmed by comparing the I_D/I_G ratio of the 8 h N_2 -annealed sample (0.31) with our predicted crossover point (0.35).

As discussed above, the existence of alcohols, ketones, aldehydes, and carboxylic acids on the FLG surface is expected due to sonication. The mechanism of thermal reduction of the functional groups strongly depends on the annealing environ-

ment. Since the N_2 (g) environment lacks a reducing agent, the functional groups should be thermally removed. It has been reported that thermal annealing at below 150 °C causes only a 3% mass loss of graphene due to small amounts of H_2O (g) being desorbed from the graphene surface. With annealing at temperatures around 150–300 °C, however, hydroxyl groups and minor amounts of epoxy and carbonyl groups are removed. The thermal removal of –OH groups thus requires a lower energy compared to other existing functional groups and a short anneal at a temperature of around 500 °C can effectively remove them. However, only a few of the carboxyl groups undergo reduction since that requires temperatures at or above 500 °C. In our case, the annealing temperature is limited to 500 °C (due to the softening of the glass slides at 550 °C) and the annealing process requires more time. As the N_2 -annealing duration increases, more –COOH groups will leave the surface (see Figure 3d–f). The high TGA mass loss for graphene oxide at temperatures between 500 and 1000 °C is reported to be due to desorption of CO_2 (g) and H_2 (g) from oxygen-containing functional groups. Therefore, carboxyl group removal occurs through direct conversion of –COOH to CO_2 (g) and H_2 (g). This is consistent with the pH-response of the N_2 -annealed sample. The pK_a of hydroxyl, aldehyde/ketone, and carboxyl groups directly attached to FLG are reported as 8.9, 35.2 and 3.4, respectively.⁴⁵ It means the protonation or deprotonation of these groups occurs at pH values around their pK_a . Aldehydes and ketones do not contribute to the pH response since their pK_a fall outside the range of 1–14.⁴⁸ However, –COOH groups at low pH and –OH groups at high pH values may respond to pH variations. For sonicated samples (Figure 2b–d) responses were observed over the entire pH range due to contributions from all active functional groups. The responses for annealed samples, however, are largely attenuated at high pH values while decreasing the pH from 4 to 3 increases the current due to the presence of –COOH on the surface ($pK_a \sim 3.4$). It should be noted that all experiments were done in DI water with 200 ppm of NaCl (3.4 mM) in order to eliminate the impact of ionic strength changes on the sensing responses. When DI water is left to equilibrate with the atmosphere (~400 ppm of CO_2), the dissolved CO_2 (g) forms carbonic acid (a weak acid) and lowers the pH down to ~5.5.⁶⁴ Therefore, moving down from pH 5.5 to 3, the current increases gradually due to the protonation of $-COO^-$ to COOH (Figure S3a–c). Since the protonation of $-COO^-$ p-dopes the FLG, the concentration of majority carriers in the chemiresistive film increases and therefore with it the current. When going back to higher pH, a sharp drop in current from 3 to 4 is observed followed by a gradual decrease in current from pH 4 to 5, meaning that the surface becomes less sensitive to higher pH (Figure 3a,b). As the pH rises, noticeable deprotonation of the –OH groups starts to occur at around pH 8.5. Deprotonation of hydroxyl groups will n-dope the surface and therefore, a drop in current is expected. However, no sharp peak or response was observed due to successful reduction of OH groups. This explains the behavior of 8 h N_2 -annealed samples shown in Figure 3c: inefficient annealing of the surface where the density of OH groups at high pH is extremely low while carboxyl groups are responding at low pH. In fact, both sensing mechanisms are observed in the same graph, low pH responses due to defects and high pH response due to changes in the EDL. Large error bars at pH 4 of the calibration curves may be due to nonuniformity of surface reduction.

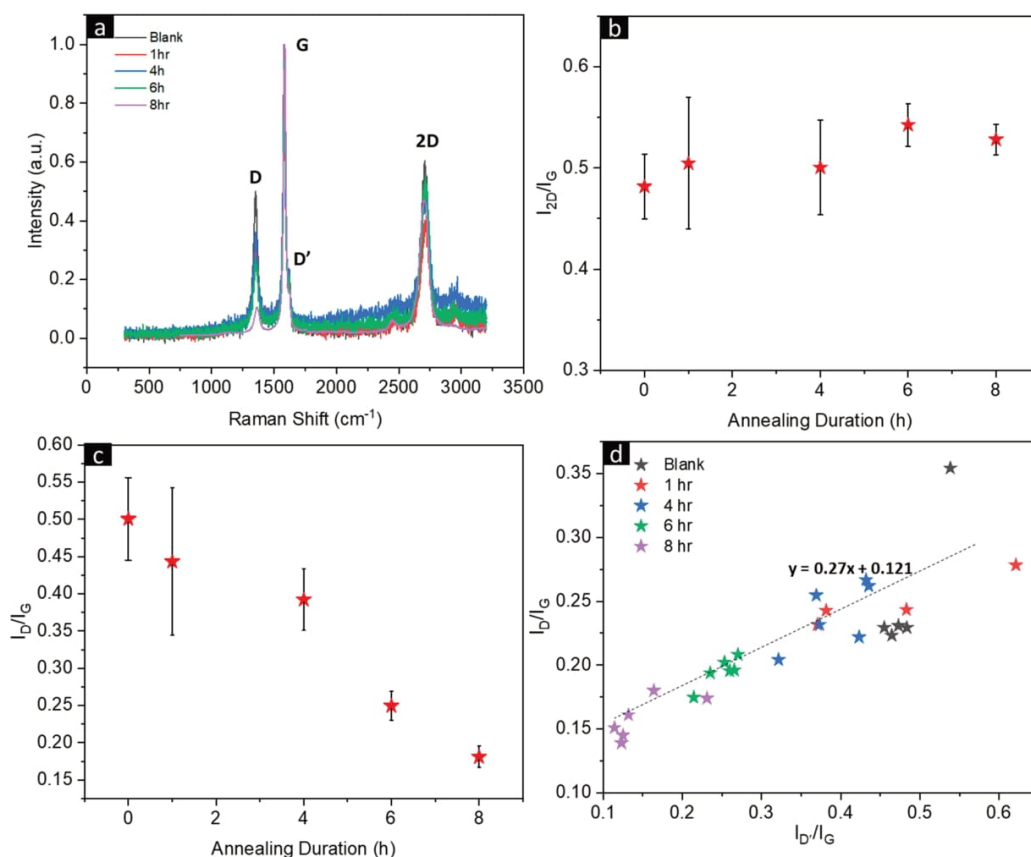


Figure 4. (a) Raman Spectra of the N_2/H_2 -annealed samples, (b) variation of I_{2D}/I_G ratio by annealing duration, (c) plot of I_D/I_G versus annealing duration, (d) plot of I_D/I_G vs $I_{D'}/I_G$ representing the stage of defect density.

3.2.2. N_2/H_2 Annealing. To ensure the effectiveness of the annealing and reduction of the surface, samples were annealed under 5% H_2 gas in N_2 . The I_D/I_G ratio in the Raman spectra of the samples (Figure 4a) was found to decrease with longer annealing times, from 0.51 for not annealed to 0.17 for 8 h annealed, confirming the successful reduction of the surface in a more effective approach than that with N_2 (Figure 4b). Higher annealing durations were also found to result in a more uniform distribution of the I_{2D}/I_G ratio in samples (lower error bars) due to a more uniform surface. The double-resonant 2D band of graphene is strongly sensitive to the dynamics of the photoexcited electron–hole pairs. The presence of defects reduces the carrier lifetime, resulting in the reduction of I_{2D} .⁶⁵ Since structural defects are the recombination centers of the photogenerated carriers, a higher uniformity of I_{2D}/I_G signifies that the symmetry of the graphene lattice has been restored due to a reduction in defect density (Figure 4c). The symmetry of the 2D peak has been reported to also be affected by different parameters such as thickness or defects. For a “defect-free” monolayer graphene, the 2D band will be highly symmetrical while higher thicknesses or defect levels generate shoulders or smaller peaks.⁶⁶ Examples of deconvoluted Raman spectra for each condition are shown in the SI, Figure S4). The extremely low ratio of these two peak intensities shows the improved symmetry in the 2D band (this is

confirmed by comparison of Figure 4a with as prepared FLG shown in Figure 1a).

Moreover, the annealing duration also will affect the intensities of the D and D' peaks. The D' band originates from intravalley one-phonon Raman processes in defective graphene, and its intensity varies with the defect density level of the graphene. Recent reports have revealed that upon increase of the defect density, the $I_{D'}/I_G$ ratio increases initially and then starts to decrease.⁶⁵ Since the D' sits on the shoulder of the G peak, the data should be baseline corrected and deconvoluted for accuracy. However, the additional dependency on defect concentration (n_d) makes their interpretation more complex. A plot of $I_{D'}$ vs I_D ($I_{D'}/I_G$ vs I_D/I_G) for different time durations yields a slope of 0.27 (Figure 4d). In vastly defective structures of graphene (resembling graphene oxide), slopes of 13.5, 7, and 3.5 have been interpreted to indicate the presence of sp^3 hybridization, vacancy defects and boundary-like defects in graphite, respectively.⁶⁵ Although our reported number is far below these reported data points, it is in good agreement with theoretical findings for on-site defects ($I_D/I_{D'} \approx 1.3$).⁶⁷ These on-site defects, which include both vacancy-like defects and hopping defects, are often caused by the distortion of the graphene lattice due to the presence of sp^3 -hybridized abnormalities. Therefore, for lower defect densities, they often are used to demonstrate the surface defect density.

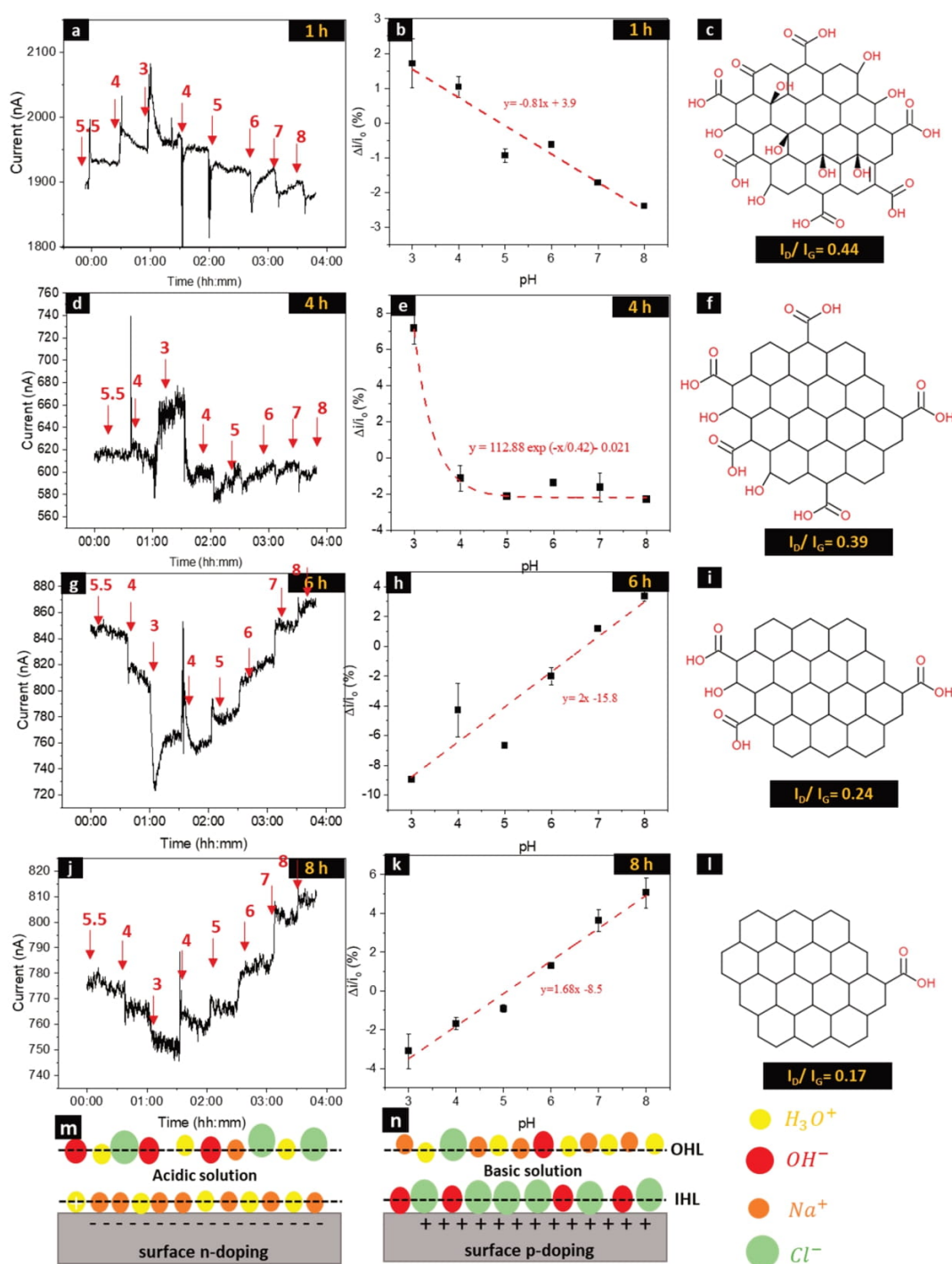


Figure 5. Sensor performance, calibration curves, and schematic illustration of (a–c) 1 h, (d–f) 4 h, (g–i) 6 h, and (j–l) 8 h N_2/H_2 annealed sensors, respectively. Schematic models of surface charge modulation due to the presence of double layer at graphene/solution interfaces for (m) acidic solution, (n) basic solution.

This indicates that the structure possesses significantly fewer sp^3 hybridized sites caused by oxygen-based functional groups.

Considering that the N_2/H_2 -annealing environment includes H_2 as a reducing agent, we expect to observe a higher decrease

in surface defect density due to both thermal removal and hydrogen-based surface reduction of functional groups. This time, since the reduction of alcohols occurs in one step (primary alcohol \rightarrow hydrocarbon + water), it is expected that

they will be either reduced or gradually degraded at high temperatures.⁶⁸ In contrast, the reduction of carboxyl groups occurs in three steps of (carboxyl \rightarrow aldehyde \rightarrow primary alcohol \rightarrow hydrocarbon + water) and requires a higher amount of energy to be reduced.^{68,69} These reducing steps require the presence of H_2 (or another reducing agent). Figure 5 shows the sensing characteristics of the N_2/H_2 -annealed sensors. The 1 h N_2/H_2 -annealed sensor responds to all pH steps (Figure 5a); however, the magnitude of the responses decreases at higher pH levels (calibration curve in Figure 5b). At this annealing time, the I_D/I_G ratio was calculated to be ~ 0.44 , meaning that the given time is not sufficient for surface reduction and a lot of defects still remain (Figure 5c). For the 4 h N_2/H_2 -annealed sensor (Figure 5d,e), upon approaching pH 3, a noticeable jump in current is observed. This could be explained by the presence of carboxyl active sites that are being protonated (deprotonated) upon decrease (increase) in pH. The presence of $-COOH$ after 4 h annealing is illustrated in Figure 5f. The same trend was already observed in 8 h N_2 -annealed samples before, shown in Figure 3c. Moreover, this considerable response in the low pH range followed by pH-insensitivity of the sensor at higher pH changes the common linear calibration curves to exponential forms. Therefore, sensitivity can no longer be assumed to be constant for different pH values (Figure 5d). The important point is the difference in bonding configurations of $-OH$ and $-COOH$ on the graphene surface. Considering that the oxygen in $-OH$ is directly attached to one of the carbon atoms in graphene's plane, the protonation or deprotonation causes the direct charge transfer to the surface. On the other side, even though reduction of the $-COOH$ may result in a resupply of $-OH$ during annealing, this time $-OH$ is attached to an out-of-plane carbon atom, preventing direct charge transfer to the surface. In the case of 6 h N_2/H_2 -annealing of FLG (Figure 5g), an opposite sensing behavior was observed, an indication that there was a change in the dominant pH sensing mechanism of the graphene. Although the presence of the sharp jump in current at pH 3–4 is indicative of the presence of carboxyl groups (shown in Figure 5i), the functional groups are not the dominant sensing pathway anymore (see the corresponding calibration curve in Figure 5h). This is further confirmed by 8 h N_2/H_2 -annealed samples (Figure 5j) showing an identical behavior as pH varies, resulting in a linear calibration curve with a positive slope of 0.016 (Figure 5k). At this point, the surface contains fewer defects so that the double layer induced sensing mechanism dominates over the surface defect response (Figure 5l). This behavior can be explained through EDL formation and charge screening at the film–solution interface. In general, upon decrease of pH, the concentration of $H_3O^+_{aq}$ in solution increases exponentially, also impacting the composition of the EDL. Consequently, the inner Helmholtz plane formed by $H_3O^+_{aq}$ near the surface screens the negative charges on the surface and n-dopes it. Therefore, current in p-doped graphene drops upon reduction in pH level.³⁰ In contrast, the basic solution induces the OH^-_{aq} to the inner Helmholtz plane which results in p-doping of the surface. Figure 5m,n illustrate the formation of a double layer on the surface of graphene. At low defect densities, this mechanism is dominant and therefore charge-transfer doping through acid–base interactions of defects will be heavily suppressed by the EDL-induced mechanism.

One other factor to consider is the presence of Na^+_{aq} and Cl^-_{aq} in the solution. The increase in ionic strength of the

solution through the addition of salt results in a more compact EDL due to an increase in the concentration of potential determining ions (PDI) and floating counterions. Hence, solution ionic strength can severely impact the surface sensing mechanisms. We chose a moderately low concentration of NaCl (3.42 mM) to minimize the impact of acid and base addition (when varying the pH) on the solution ionic strength while retaining the sensor responses. The addition of 200 ppm of NaCl releases 3.42 mM each of Na^+_{aq} and Cl^-_{aq} ions. Considering that pH 3 corresponds to 1 mM $H_3O^+_{aq}$, the ratio of $H_3O^+_{aq}$ to Na^+_{aq} in the bulk and presumably on the surface is 1:3. Since the ionic radii of $H_3O^+_{aq}$ and Na^+_{aq} are nearly the same, for a particular surface area, the probability of locating $H_3O^+_{aq}$ to Na^+_{aq} is 1:3.4. It should also be noted that the hydration spheres of the ions introduce H_2O molecules as a dielectric between the charges of the double layer and the surface. The ratio of $H_3O^+_{aq}$ to Na^+_{aq} will drop significantly at higher pH values and therefore, increasing the ionic strength lessens the ratio of charge doping ions to PDI. Although the sensitivity can be maximized by minimizing the ionic strength, the impact of solution ionic strength on sensor response cannot be neglected.

3.3. Defect Dominant Sensing Mechanism. To explore the role of functional groups, PDs were employed to replicate the selective surface-functionalization of FLG. This models the scenario that the FLG surface is largely passivated by the anchoring of pyrene rings, exposing the functional group tails of the molecules to the solution. Since the common functional groups of the graphene through liquid exfoliation techniques are carboxyl ($-COOH$), hydroxyl ($-OH$), aldehyde ($-CHO$), and amine ($-NH_2$), the PDs of Py-COOH, Py-OH, Py-CHO, and Py-NH₂ were chosen. To facilitate the π - π stacking interactions of the pyrene rings with defect-free regions of graphene, sensors were thermally N_2/H_2 -annealed for 8 h prior to functionalization. The π - π stacking of the PDs will facilitate the charge transfer interactions of the attached functional groups with the graphene surface.⁷⁰ Although the absence of any steric hindrances allows observing the direct impact of changes in PD on graphene's conductivity, the lower degree of delocalization may lead to higher surface resistances.^{45,71} The impact of the interactions with the graphene surface on the delocalized π -electron clouds in pyrene will result in a change in pK_a of the functional groups in the PDs compared to the free molecules. The HOMO–LUMO gaps of PDs were calculated (Table 2) before and after

Table 2. HOMO-LUMO Energies of Py-NH₂, Py-OH, and Py-COOH Acid in Solution and Adsorbed onto an 8 × 8 Graphene Sheet

	Py-NH ₂	Py-OH	Py-COOH
Bulk HOMO	-5.841 eV	-5.488 eV	-5.955 eV
Bulk LUMO	-2.092 eV	-1.825 eV	-2.532 eV
Surface HOMO	-7.835 eV	-6.485 eV	-6.467 eV
Surface LUMO	-4.995 eV	-3.575 eV	-3.608 eV

adsorption onto an 8 × 8 graphene flake, showing a decrease in both HOMO and LUMO energies, indicative of stabilization upon adsorption to the 8 × 8 graphene flake. These decreases would also indicate a change in the pK_a toward more neutral conditions; in other words, the 1-aminopyrene would experience an increase in its pK_a (going from $-NH_3^+$ to NH_2) and the 1-hydroxypyrene and the Py-COOH acid would

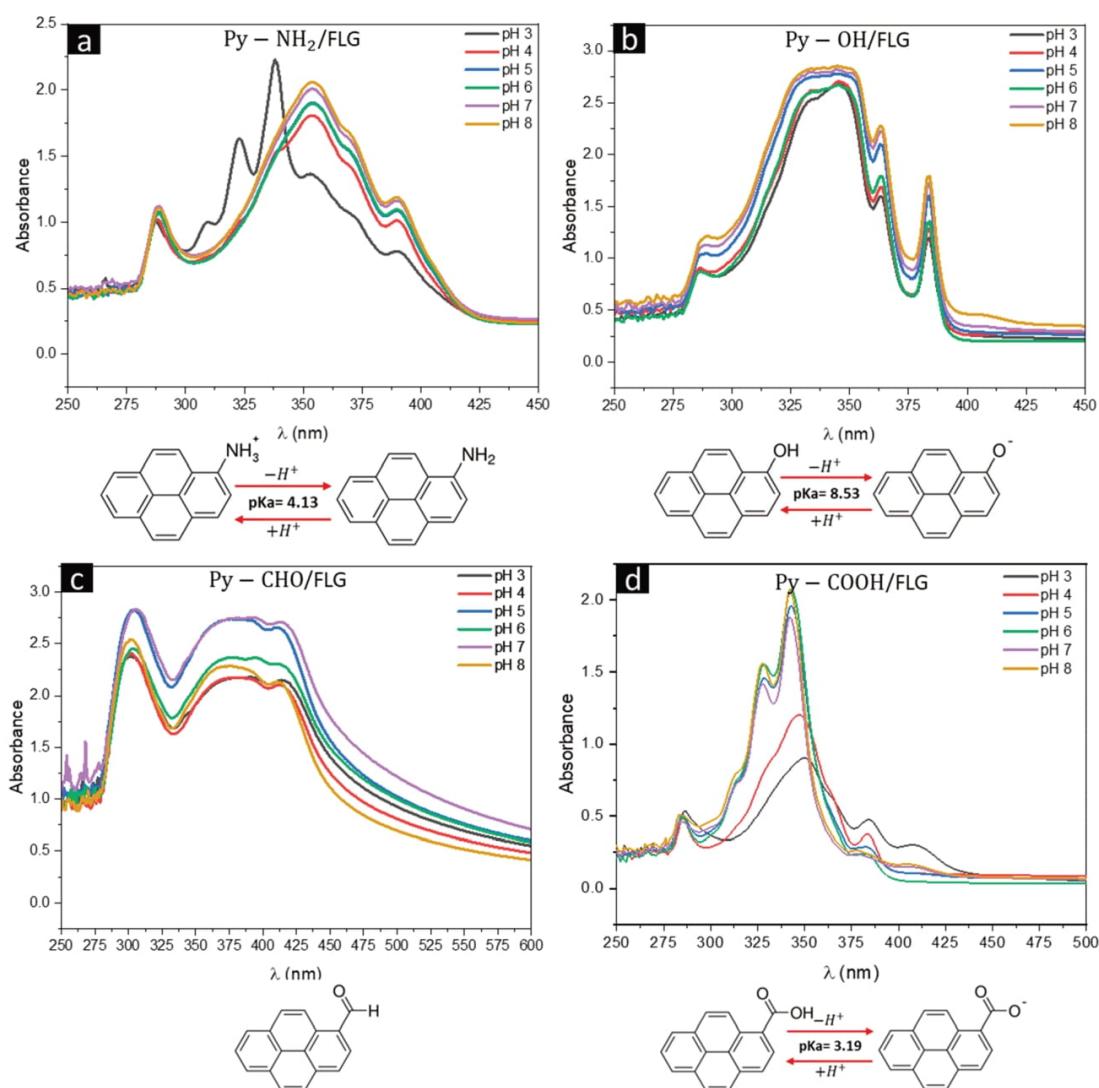


Figure 6. UV-visible spectra of the pyrene derivatives functionalized FLG at different pH values (a) Py-NH₂/FLG, (b) Py-OH/FLG, (c) Py-CHO/FLG, and (d) Py-COOH/FLG.

see a decrease in its pK_a (going from $-\text{COO}^-$ and $-\text{O}^-$ to $-\text{COOH}$ and $-\text{OH}$).

The effect that the pH of the solution has on the adsorption strength of the pyrene derivatives is also made apparent through their adsorption energies and distances (Table S2). Figure S5 shows that the Py-NH₂ molecule is adsorbed parallel to the graphene fragment such that the lone pair of the nitrogen is facing out of the plane, making it more accessible to protonation. This is also similar to what is seen in Py-OH and Py-COOH. When adsorption energies are looked at, a clear trend is seen based on whether the substituent is electron donating or withdrawing. For example, the $-\text{NH}_2$ group is known to be electron donating, hence the π -system of 1-aminopyrene will have significant overlap with that of graphene. However, $-\text{NH}_3^+$ is electron withdrawing, which will reduce the amount of overlap between these orbitals. This is reflected through the increase in adsorption energy going

from -125.92 kcal/mol to -11.68 kcal/mol after protonation occurs. Similarly, $-\text{OH}$ is an electron donating group which increases in activation strength when deprotonated, which can be seen through the decrease in adsorption energy from -159.55 kcal/mol to -247.81 kcal/mol. Conversely, $-\text{COOH}$ is an electron withdrawing group which, upon deprotonation, becomes an electron donating group. This is also reflected in the decrease in adsorption energy for Py-COOH after deprotonation going from -214.13 kcal/mol to -258.50 kcal/mol. On the basis of adsorption distance, the only trend seen is that charged species will be separated further from the surface than neutral species.

UV-visible spectra of the pyrene molecules/FLG at different pH help us to understand the impact of pH on each PD (Figure 8). This resembles the presence of various functional groups on the FLG and should be reflected in the sensor data. Py-NH₂, like other derivatives, is inherently

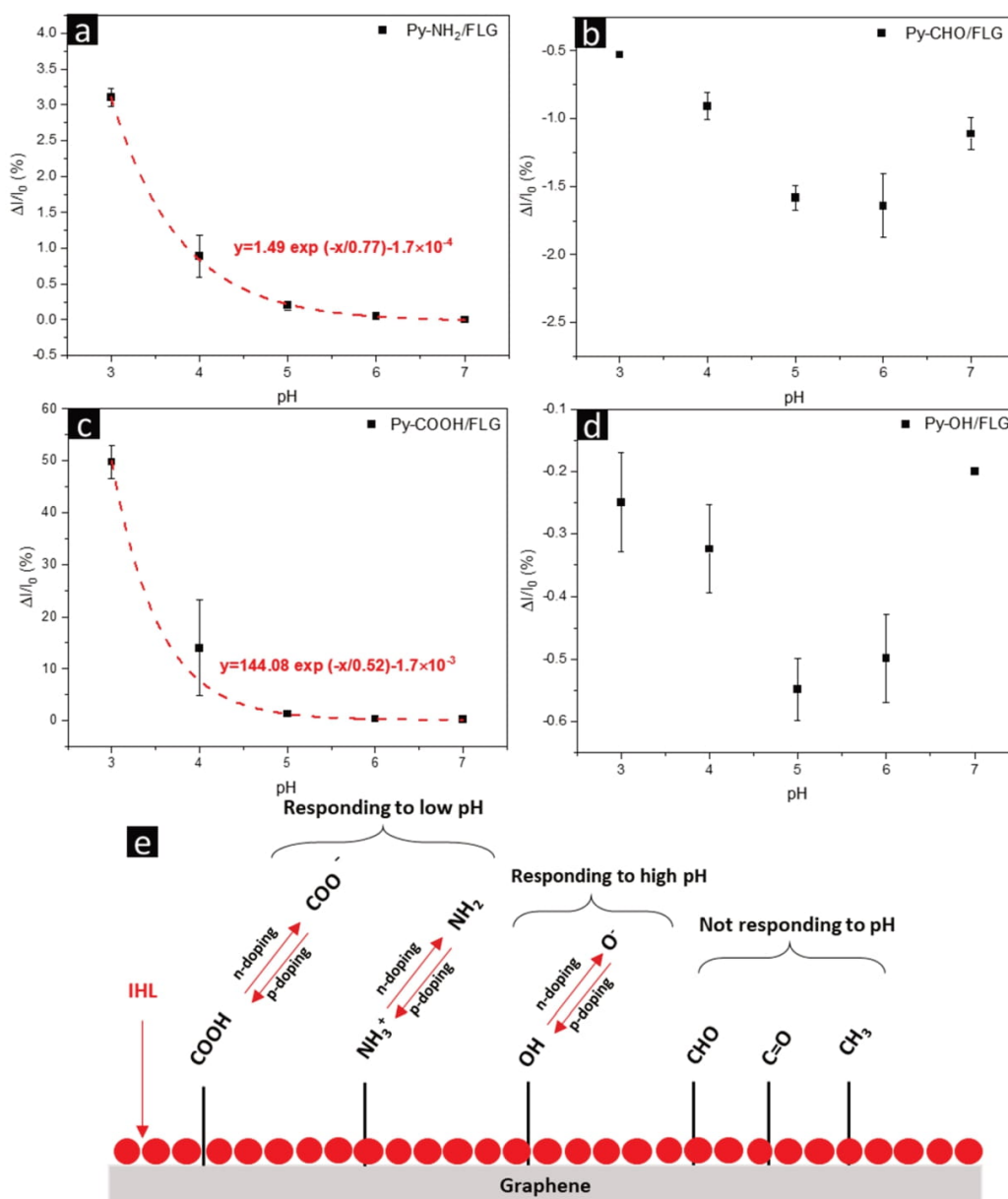


Figure 7. Sensing performance of PD functionalized sensors. a) Py-NH₂/FLG b) Py-CHO/FLG c) Py-COOH/FLG d) Py-OH/FLG e) Schematic representation of defect-induced mechanism by functional groups at different pH values. The red dots represent the double layer.

aromatic (presence of the pyrenyl group) and can interact with the sp^2 hybridization of graphene via π - π interaction. It has been shown that the anchoring of Py-NH₂ on the graphene surface is thermodynamically highly favorable and considered an irreversible process.⁷² The UV-vis spectrum of Py-NH₂ shows three main absorption peaks at around 288, 353, and 390 nm (Figure 6a). Due to overlap of the 288 nm peak of Py-NH₂ with a graphene absorption feature at 279 nm, the presence of both features in Py-NH₂/FLG cannot be unambiguously resolved. The spectrum at pH 3 is distinct from those at higher pH values, with new peaks at 338, 323, and 309 nm arising from the presence of the protonated form

of the molecule. This is confirmed by computational studies on both protonated and deprotonated states of Py-NH₂ (Figure S4). As observed, the peaks at ~288 and 353 nm are due to the absorption mechanism of the -NH₂ sites. Upon protonation of -NH₂ to -NH₃⁺ by decreasing the pH to around pK_a (4.19), the intensity of the peak at 353 nm decreases due to the loss of nonbonding orbitals while a new peak arises at 338 nm due to singlet state absorption of -NH₃⁺. Two other new peaks, one at 309 nm and one at 323 nm also arise corresponding to the triplet states induced by protonation of -NH₂.

Figure 6b illustrates the absorption spectra of Py-OH/FLG at different pH levels. The characteristic peaks at 285, 345,

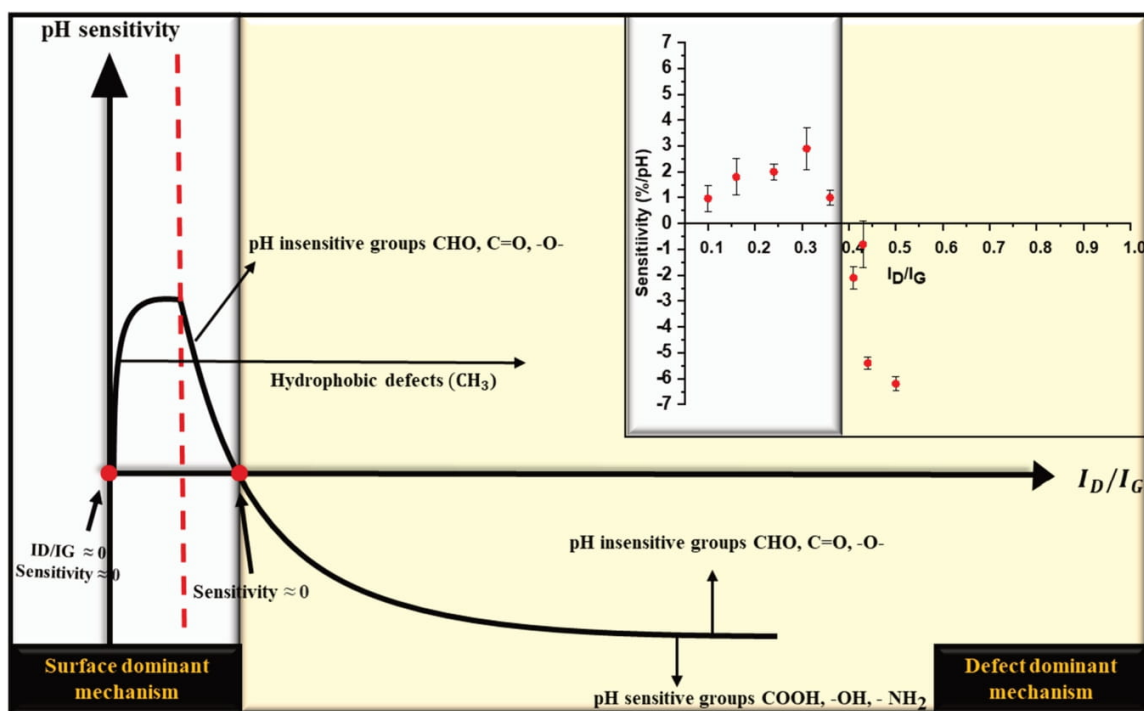


Figure 8. Relationship of graphene's pH sensitivity with surface defect density. The inset shows the experimentally obtained data for blank, annealed, and sonicated sample.

363, and 383 nm have already been reported for Py-OH.⁷³ The peaks at higher energy levels originate primarily from excitation along the long (a , a_1) direction while the lower energies are due to the excitation along the short (b , b_1) direction (see SI, Figure S6). The peak broadening at 345 nm is a result of Py-OH deprotonation at $pK_a = 8.5$, generating a shoulder at 290 nm. The red-shift in peak positions of Py-OH (shown in SI, Figure S6) compared to FLG/Py-OH is due to the absorption of Py-OH on the FLG surface, suppressing the π to π^* transitions of PDs. Moreover, enhancement of π -conjugation decreases the required energy for the transition, resulting in a red shift.⁷³ The absorption edge of FLG at 285–290 nm^{74,75} overlaps with the molecular peak at 279 nm (computational) or 285 nm (experimental). Nevertheless, the spectra confirm that in the pH range of 3 to 8, Py-OH does not participate in any acid–base interactions. Figure 6c validates the same trend for Py-CHO. The positions and widths of the peaks have remained unchanged upon increasing the pH from 3 to 8, consistent with the calculated pK_a for Py-CHO on FLG of 40.66.⁴⁸

Figure 6d shows how the absorption spectra of FLG/Py-COOH vary by changing the pH level. The peaks at 281 and 353 are known fingerprints of Py-COOH.⁴⁹ Therefore, the appearance of these peaks along with π to π^* transitions of FLG confirms the absorption of Py-COOH onto FLG. Approaching a pH of ~ 3 and passing the pK_a causes the 353 nm peak to blue-shift (red line is pH 4, and the black line is pH 3). Moreover, the disappearance and appearance of peaks at 325 and 417 nm, respectively, are the other signs of the emergence of $-\text{COO}^-$ with increasing pH for Py-COOH⁴⁹ (Tables S3 and S4). Absorption spectra of pyrene molecules

and FLG independently at various pH are displayed in the SI, Figures S7 and S8, respectively.

Figure S9 displays the sensing performance of PD functionalized sensors. The significant jump in I_D/I_G ratios of annealed samples after functionalization with PD further confirms the successful surface passivation (see SI, Figure S10). Annealing was done in order to enhance the direct π – π interactions of pyrene with defect free areas on the surface of FLG. Therefore, the control sensor (annealed) retains a similar characteristic as displayed in Figure 5g,h. Starting with Py-NH₂/FLG (Figure 7a) and considering our calculated pK_a of 4.19, the current increases when the pH value is lowered to 4 or 3 due to p-doping as a result of protonation of $-\text{NH}_2$ to $-\text{NH}_3^+$. The change in current for each pH step increases as the pK_a is approached (Figure 7a), an inverse behavior compared to the 8 h N₂/H₂-annealed sensors (the I_D/I_G ratio of NH₂/FLG of ~ 0.79 is higher than the crossover point of 0.35). Lower responses of the Py-NH₂ sensor compared to its bare counterpart are due to the surface density of amino groups (one amine group per molecule), shown in Figure 7a. A sensor fabricated by adsorption of Py-CHO onto a FLG film is (nearly) insensitive to variations in pH (Figures S9b), giving a maximum current change of 1% over the tested range. The sharp jump in current at around pH 3 and 4 could be due to some remaining carboxyl groups of the surface after annealing (calibration curve shown in Figure 7b). While the double-layer-induced mechanism is dominant for an 8 h N₂/H₂-annealed sensor, it is not necessarily defect-free. Even though the functional group's responses will be suppressed below the crossover point, adsorption of Py-CHO increases the defect density. Thus, after exceeding the crossover ratio, defects will be the dominant mechanism. Hence, the remaining acid

groups may also respond. This hypothesis was also tested with Py-COOH. Since the starting pH of the experiment is set to 5.5 (higher than its pK_a), the carboxyl groups are initially deprotonated ($-\text{COO}^-$). With the pH value being lowered to 3, protonation occurs so that the surface is hole-doped again, resulting in a significant current change at pH 3 for Py-COOH/FLG (Figure 7c, close to 41%; see also SI, Figure S9c for raw data representation). This indicates that either the majority of $-\text{COOH}$ groups are effectively protonated below the pK_a , or that their density is high due to the combination of Py-COOH and pre-existing surface defects. In summary, low range pH sensitivity is mainly due to acid–base interactions of amine and carboxyl groups. The high range responses are due to $-\text{OH}$ groups becoming deprotonated and leaving $-\text{O}^-$ groups on the surface. Since the negatively charged polarities will n-dope the FLG, the conductance of the film decreases. Therefore, we can conclude that during the increase in pH, the initial drop in conductance is caused by the deprotonation of amine or carboxyl groups, followed by a gradual decrease in conductivity due to deprotonation of $-\text{OH}$ groups at around 8.5 (Figure S9d). However, since the experiment is limited to a pH range of 3–8, the Py-OH sensor shows no response (maximum response of 0.55% shown in Figure 7d). As illustrated in Figure 7e, carboxyl and amine groups are responsible for the response at low pH while hydroxyl groups govern the response at high pH. Since the EDL is always present at the surface even at high defect densities, it is important to always consider the specific balance between the two mechanisms.

The overall relationship between the pH response of FLG and its defect density (represented by the I_D/I_G ratio) is illustrated in Figure 8, accounting for both mechanisms. The left and right regions of the graph represent dominance of the double layer induced response and dominance of the surface defect response, respectively. In the right region, increasing the defect density initially leads to a higher sensitivity (negative values, i.e., negative slope of the calibration curve) until it saturates at a specific defect density. After this point, introducing more defects will not considerably affect the sensitivity. With surface reduction to I_D/I_G around the crossover point (here it is at $I_D/I_G = 0.35$), the curve enters the region of low defect density at the left of the graph, where the double layer induced mechanism dominates. With a continued reduction of the I_D/I_G ratio, the slope of the calibration curves will become more positive. However, since a defect-free (or at least very low defect) graphene surface is hydrophobic, the sensitivity will start to drop significantly as we approach zero. At this point, graphene repels the water completely and no interactions can occur.^{76–78} It is important to consider how this graph is adapted through different functionalization, fabrication processes and defect density levels. For instance, addition of fluorobenzene on graphene increases the I_D/I_G ratio, but it enhances the hydrophobicity at the same time, leading to extremely low pH sensitivity.³⁷ Another example is an increase in the quantity pH insensitive groups such as $-\text{CHO}$ by which both defect density level and hydrophilicity rise.

The experimentally derived data of I_D/I_G versus pH sensitivity for all sonicated and annealed sensors are plotted in Figure 8 (inset). Starting at $I_D/I_G = 0$, as discussed above, the hydrophobicity of the graphene surface is dominant and no interactions can occur, leading to a sensitivity of zero. With the addition of nonpolar defects such as CH_3 , the minimum defect

density required to achieve zero sensitivity increases. Therefore, zero sensitivity can be obtained even at higher I_D/I_G ratios, as seen in the results of ref 37 that fluorobenzene-functionalized graphene (simulated superhydrophobic graphene) has the sensitivity of ~ 0 mV/pH. With an increase in the defect density using polar functional groups, however, the hydrophilicity of the graphene enhances, escalating the graphene/solution interactions. That causes an increase in pH-sensitivity (greater positive value) in higher I_D/I_G ratios since the double layer induced response is dominant (up to a point shown by the red dashed line in Figure 8). However, a further increase in the density of pH-sensitive functional groups (such as $-\text{COOH}$, $-\text{OH}$ or NH_2) enhances the surface defect induced response, counteracting the double layer induced response. With a continual increase of I_D/I_G , the pH-sensitivity decreases to a crossover point (here $I_D/I_G = 0.35$) where the two sensing mechanisms balance each other out and lead to a zero pH sensitivity of the graphene. Enhancement of defect density beyond the crossover point at 0.35 (which is specific to our experimental approach and will vary by condition) leads to the dominance of surface defect induced responses (negative slope). At this point, addition of pH-sensitive groups such as $-\text{COOH}$, $-\text{NH}_2$ and $-\text{OH}$ makes the slope more negative and pH sensitivity increases significantly. With continued increase of the defect density, the slope becomes more negative in value up to a point of saturation beyond which the addition of defects no longer changes the overall sensitivity.

4. CONCLUSION

We have demonstrated that there are two competing ways in which a graphene surface responds to changes in pH. The mechanism that prevails depends on the nature and density of surface functionalities (or defects). Careful consideration of the role of surface defects can console inconsistencies in the current literature regarding the variation of graphene surface resistance as a function of pH. Below a certain defect density (here $I_D/I_G = 0.35$) of a graphene surface in contact with an aqueous electrolyte, it is primarily the formation of an EDL at the graphene/solution interface that controls modulation of the charge carrier density in the graphene. Increasing the solution acidity causes the incorporation of positively charged hydronium ions into the inner Helmholtz plane, screening the negative charges on the surface. In a basic solution, the higher density of hydroxide ions results in hole-doping of the surface. Therefore, the current through the FLG network increases with increasing pH. At defect densities above a certain crossover point (here $I_D/I_G = 0.35$), the existing defects and functional groups at the graphene surface will start to dominate control over the charge carrier density. Protonation and deprotonation of pH-sensitive groups on the surface such as carboxyl, hydroxyl, and amines will be the major sensing pathways. In contrast, nonpolar, pH-insensitive groups enhance the surface hydrophobicity, reducing the pH response. Thermal annealing can be used to control the slope of the calibration curves through the reduction of the surface defect density. When the duration of effective thermal annealing and successful reduction of surface is increased, the slope of the calibration curves will shift from negative to positive.

Commercial stand-alone pH meters are most commonly based on an ion-selective electrode in a potentiometric (2 electrode) configuration together with a reference electrode. Potentials are measured with about 1 mV resolution at a sensitivity of around 60 mV/pH. For a chemiresistive sensor of

our design to have an equivalent resolution (given a maximum sensitivity of 6%/pH from Figure 2f at a current of around 500 nA, i.e., 30 nA/pH), it would require the current measurement to be accurate to 0.5 nA. While not impossible, this is a lot more difficult to accomplish under field conditions than a voltage measurement to 1 mV. Changes in the geometry of the sensing element can bring improvements, but ultimately, this work does not aim to introduce a new generation of stand-alone pH meters; it rather aims to provide helpful insights into the surface science of graphene-based devices in contact with aqueous media, such as pH, water quality, or biological sensors. While the pH response of a dedicated pH sensor (or a pH-sensitive smart material) should be maximized, in many applications, it is undesirable for the device performance to be a function of pH. This means that pH sensitivity can be easily adjusted (increased or decreased) compared to previously reported graphene-based sensors only by controlling the defect densities. We have addressed inconsistencies among literature reports of pH sensing behavior of graphene devices by quantifying the role of defects in balancing countervailing response mechanisms.

■ ASSOCIATED CONTENT

Supporting Information

The Supporting Information is available free of charge at <https://pubs.acs.org/doi/10.1021/acs.langmuir.1c02088>.

Detailed information on sensor fabrication, FTIR spectrum, deconvoluted Raman spectra and sensor calibration curves (PDF)

■ AUTHOR INFORMATION

Corresponding Author

Peter Kruse – Department of Chemistry and Chemical Biology, McMaster University, Hamilton, Ontario L8S 4M1, Canada; orcid.org/0000-0003-4051-4375; Email: pkruise@mcmaster.ca

Authors

Shayan Angizi – Department of Chemistry and Chemical Biology, McMaster University, Hamilton, Ontario L8S 4M1, Canada; orcid.org/0000-0002-5345-4271

Eugene Yat Chun Yu – Department of Chemistry and Chemical Biology, McMaster University, Hamilton, Ontario L8S 4M1, Canada

Johnson Dalmieda – Department of Chemistry and Chemical Biology, McMaster University, Hamilton, Ontario L8S 4M1, Canada

Dipankar Saha – Department of Chemistry and Chemical Biology, McMaster University, Hamilton, Ontario L8S 4M1, Canada; orcid.org/0000-0002-6268-2807

P. Ravi Selvaganapathy – Department of Mechanical Engineering, McMaster University, Hamilton L8S 4M1, Canada; orcid.org/0000-0003-2041-7180

Complete contact information is available at: <https://pubs.acs.org/doi/10.1021/acs.langmuir.1c02088>

Notes

The authors declare no competing financial interest.

■ ACKNOWLEDGMENTS

Authors are thankful to Dr. Ross Anthony, Dr. Shahram Tavakoli and Doris Stevanovic from the Centre for Emerging

Device Technologies (CEDT), McMaster University for help with annealing furnaces; Dr. Alex Adronov for granting access to spectroscopic analyses (Raman and FTIR); Chris Butcher in the Center for Canadian Electron Microscopy (CCEM) for help with SEM. The authors acknowledge financial support from the Natural Sciences and Engineering Research Council of Canada (NSERC) through the Discovery Grant Program and a Collaborative Research and Development Grant, by 3M Canada, by the Ontario Centers of Excellence, as well as by a Canada First Research Excellence Fund project “Global Water Futures.”

■ REFERENCES

- (1) Salvo, P.; Melai, B.; Calisi, N.; Paoletti, C.; Bellagambi, F.; Kirchhain, A.; Trivella, M. G.; Fuoco, R.; Di Francesco, F. Graphene-Based Devices for Measuring PH. *Sens. Actuators, B* **2018**, *256*, 976–991.
- (2) World Health Organization (WHO) and the United Nations Children's Fund (UNICEF). *Progress on Drinking Water, Sanitation and Hygiene: 2017 Update and SDG Baseline*; Geneva, 2017.
- (3) Salis, A.; Pinna, M. C.; Bilaničová, D.; Monduzzi, M.; Lo Nostro, P.; Ninham, B. W. Specific Anion Effects on Glass Electrode Ph Measurements of Buffer Solutions: Bulk and Surface Phenomena. *J. Phys. Chem. B* **2006**, *110* (6), 2949–2956.
- (4) Cheng, K. L. pH Glass Electrode and Its Mechanism. *ACS Symp. Ser.* **1989**, *64110* (390), 286–302.
- (5) Wencel, D.; Abel, T.; McDonagh, C. Optical Chemical pH Sensors. *Anal. Chem.* **2014**, *86* (1), 15–29.
- (6) Monaghan, M. T.; Brogan, K.; Lockington, D.; Rotchford, A. P.; Ramaesh, K. Variability in Measuring pH Using Litmus Paper and the Relevance in Ocular Chemical Injury. *Eye* **2020**, *34* (11), 2133–2134.
- (7) Avolio, R.; Grozdanov, A.; Avella, M.; Barton, J.; Cocca, M.; De Falco, F.; Dimitrov, A. T.; Errico, M. E.; Fanjul-Bolado, P.; Gentile, G.; Paunovic, P.; Ribotti, A.; Magni, P. Review of pH Sensing Materials from Macro- to Nano-Scale: Recent Developments and Examples of Seawater Applications. *Crit. Rev. Environ. Sci. Technol.* **2020**, *0* (0), 1–43.
- (8) Toumazou, C.; Shepherd, L. M.; Reed, S. C.; Chen, G. I.; Patel, A.; Garner, D. M.; Wang, C. J. A.; Ou, C. P.; Amin-Desai, K.; Athanasiou, P.; Bai, H.; Brizido, I. M. Q.; Caldwell, B.; Coomber-Alford, D.; Georgiou, P.; Jordan, K. S.; Joyce, J. C.; La Mura, M.; Morley, D.; Sathyavrudhan, S.; Temelso, S.; Thomas, R. E.; Zhang, L. Simultaneous DNA Amplification and Detection Using a pH-Sensing Semiconductor System. *Nat. Methods* **2013**, *10* (7), 641–646.
- (9) Ghoneim, M. T.; Nguyen, A.; Dereje, N.; Huang, J.; Moore, G. C.; Murzynowski, P. J.; Dagdeviren, C. Recent Progress in Electrochemical pH-Sensing Materials and Configurations for Biomedical Applications. *Chem. Rev.* **2019**, *119* (8), 5248–5297.
- (10) Catania, F.; Marras, E.; Giorcelli, M.; Jagdale, P.; Lavagna, L.; Tagliaferro, A.; Bartoli, M. A Review on Recent Advancements of Graphene and Graphene-Related Materials in Biological Applications. *Appl. Sci.* **2021**, *11* (2), 1–21.
- (11) Novoselov, K. S. Electric Field Effect in Atomically Thin Carbon Films. *Science (Washington, DC, U. S.)* **2004**, *306* (5696), 666–669.
- (12) Angizi, S.; Khalaj, M.; Alem, S. A. A.; Pakdel, A.; Willander, M.; Hatamie, A.; Simchi, A. Review—Towards the Two-Dimensional Hexagonal Boron Nitride (2D h-BN) Electrochemical Sensing Platforms. *J. Electrochem. Soc.* **2020**, *167* (12), 126513.
- (13) Angizi, S.; Akbar, M. A.; Darestani-Farahani, M.; Kruse, P. Review—Two-Dimensional Boron Carbon Nitride: A Comprehensive Review. *ECS J. Solid State Sci. Technol.* **2020**, *9* (8), 083004.
- (14) Angizi, S.; Shayeganfar, F.; Azar, M. H.; Simchi, A. Surface/Edge Functionalized Boron Nitride Quantum Dots: Spectroscopic Fingerprint of Bandgap Modification by Chemical Functionalization. *Ceram. Int.* **2020**, *46* (1), 978–985.
- (15) Angizi, S.; Khalaj, M.; Alem, S. A. A.; Pakdel, A.; Willander, M.; Hatamie, A.; Simchi, A. Review - Towards the Two-Dimensional

- Hexagonal Boron Nitride (2D h-BN) Electrochemical Sensing Platforms. *J. Electrochem. Soc.* **2020**, *167* (12), 126513.
- (16) Lee, C. W.; Suh, J. M.; Jang, H. W. Chemical Sensors Based on Two-Dimensional (2D) Materials for Selective Detection of Ions and Molecules in Liquid. *Front. Chem.* **2019**, *7*, 1–21.
- (17) Rezvani, E.; Hatamie, A.; Berahman, M.; Simchi, M.; Angizi, S.; Rahmati, R.; Kennedy, J.; Simchi, A. Synthesis, First-Principle Simulation, and Application of Three-Dimensional Ceria Nanoparticles/Graphene Nanocomposite for Non-Enzymatic Hydrogen Peroxide Detection. *J. Electrochem. Soc.* **2019**, *166* (5), H3167–H3174.
- (18) Hatamie, A.; Rahmati, R.; Rezvani, E.; Angizi, S.; Simchi, A. Yttrium Hexacyanoferrate Microflowers on Freestanding Three-Dimensional Graphene Substrates for Ascorbic Acid Detection. *ACS Appl. Nano Mater.* **2019**, *2* (4), 2212–2221.
- (19) Salvo, P.; Calisi, N.; Melai, B.; Cortigiani, B.; Mannini, M.; Caneschi, A.; Lorenzetti, G.; Paoletti, C.; Lomonaco, T.; Paolicchi, A.; Scatagliini, I.; Dini, V.; Romanelli, M.; Fuoco, R.; Di Francesco, F. Temperature and pH Sensors Based on Graphenic Materials. *Biosens. Bioelectron.* **2017**, *91*, 870–877.
- (20) Fang, M.; Long, J.; Zhao, W.; Wang, L.; Chen, G. pH-Responsive Chitosan-Mediated Graphene Dispersions. *Langmuir* **2010**, *26* (22), 16771–16774.
- (21) Zubiarrain-Laserna, A.; Kruse, P. Review—Graphene-Based Water Quality Sensors. *J. Electrochem. Soc.* **2020**, *167* (3), 037539.
- (22) Wang, Y.; Zhang, L.; Zhang, Z.; Sun, P.; Chen, H. High-Sensitivity Wearable and Flexible Humidity Sensor Based on Graphene Oxide/Non-Woven Fabric for Respiration Monitoring. *Langmuir* **2020**, *36* (32), 9443–9448.
- (23) Yavari, F.; Koratkar, N. Graphene-Based Chemical Sensors. *J. Phys. Chem. Lett.* **2012**, *3* (13), 1746–1753.
- (24) Singh, E.; Meyyappan, M.; Nalwa, H. S. Flexible Graphene-Based Wearable Gas and Chemical Sensors. *ACS Appl. Mater. Interfaces* **2017**, *9* (40), 34544–34586.
- (25) Kaiser, D.; Tang, Z.; Küllmer, M.; Neumann, C.; Winter, A.; Kahle, R.; Georgi, L.; Weimann, T.; Siegmann, M.; Gräfe, S.; Centeno, A.; Zurutuza, A.; Turchanin, A. pH Sensors Based on Amino-Terminated Carbon Nanomembrane and Single-Layer Graphene van Der Waals Heterostructures. *Appl. Phys. Rev.* **2021**, *8* (3), 031410.
- (26) Kostarelos, K.; Novoselov, K. S. Graphene Devices for Life. *Nat. Nanotechnol.* **2014**, *9* (10), 744–745.
- (27) Snapp, P.; Kim, J. M.; Cho, C.; Leem, J.; Haque, M. F.; Nam, S. W. Interaction of 2D Materials with Liquids: Wettability, Electrochemical Properties, Friction, and Emerging Directions. *NPG Asia Mater.* **2020**, *12* (1), 1–16.
- (28) Schneider, G. F.; Xu, Q.; Hage, S.; Luik, S.; Spoor, J. N. H.; Malladi, S.; Zandbergen, H.; Dekker, C. Tailoring the Hydrophobicity of Graphene for Its Use as Nanopores for DNA Translocation. *Nat. Commun.* **2013**, *4*, 1–7.
- (29) Belyaeva, L. A.; van Deursen, P. M. G.; Barbetsea, K. I.; Schneider, G. F. Hydrophilicity of Graphene in Water through Transparency to Polar and Dispersive Interactions. *Adv. Mater.* **2018**, *30* (6), 1703274.
- (30) Lei, N.; Li, P.; Xue, W.; Xu, J. Simple Graphene Chemiresistors as pH Sensors: Fabrication and Characterization. *Meas. Sci. Technol.* **2011**, *22* (10), 107002.
- (31) Sha, R.; Komori, K.; Badhulika, S.; Amperometric, P. H. Amperometric pH Sensor Based on Graphene-Polyaniline Composite. *IEEE Sens. J.* **2017**, *17* (16), 5038–5043.
- (32) Jung, S. H.; Seo, Y. M.; Gu, T.; Jang, W.; Kang, S. G.; Hyeon, Y.; Hyun, S. H.; Lee, J. H.; Whang, D. Super-Nernstian pH Sensor Based on Anomalous Charge Transfer Doping of Defect-Engineered Graphene. *Nano Lett.* **2021**, *21* (1), 34–42.
- (33) Zeng, Z.; Wei, W.; Li, B.; Gao, M.; Yu, Z. G.; Chim, W. K.; Zhu, C. CVD Polycrystalline Graphene as Sensing Film of Extended-Gate ISFET for Low-Drift pH Sensor. *J. Electrochem. Soc.* **2021**, *168* (6), 067520.
- (34) Maily-Giacchetti, B.; Hsu, A.; Wang, H.; Vinciguerra, V.; Pappalardo, F.; Occhipinti, L.; Guidetti, E.; Coffa, S.; Kong, J.; Palacios, T. pH Sensing Properties of Graphene Solution-Gated Field-Effect Transistors. *J. Appl. Phys.* **2013**, *114* (8), 084505.
- (35) Kim, D. H.; Park, W. H.; Oh, H. G.; Jeon, D. C.; Lim, J. M.; Song, K. S. Two-Channel Graphene pH Sensor Using Semi-Ionic Fluorinated Graphene Reference Electrode. *Sensors* **2020**, *20* (15), 1–11.
- (36) Panteli, C.; Georgiou, P.; Fobelets, K. Reduced Drift of CMOS ISFET pH Sensors Using Graphene Sheets. *IEEE Sens. J.* **2021**, *21* (13), 14609–14618.
- (37) Fu, W.; Nef, C.; Knopfmacher, O.; Tarasov, A.; Weiss, M.; Calame, M.; Schönenberger, C. Graphene Transistors Are Insensitive to pH Changes in Solution. *Nano Lett.* **2011**, *11* (9), 3597–3600.
- (38) Angizi, S.; Hatamie, A.; Ghanbari, H.; Simchi, A. Mechanochemical Green Synthesis of Exfoliated Edge-Functionalized Boron Nitride Quantum Dots: Application to Vitamin C Sensing through Hybridization with Gold Electrodes. *ACS Appl. Mater. Interfaces* **2018**, *10* (34), 28819–28827.
- (39) Gou, P.; Kraut, N. D.; Feigel, I. M.; Bai, H.; Morgan, G. J.; Chen, Y.; Tang, Y.; Bocan, K.; Stachel, J.; Berger, L.; Mickle, M.; SejdíC, E.; Star, A. Carbon Nanotube Chemiresistor for Wireless pH Sensing. *Sci. Rep.* **2015**, *4*, 1–6.
- (40) Takeda, S.; Nakamura, M.; Ishii, A.; Subagyo, A.; Hosoi, H.; Sueoka, K.; Mukasa, K. A pH Sensor Based on Electric Properties of Nanotubes on a Glass Substrate. *Nanoscale Res. Lett.* **2007**, *2* (4), 207–212.
- (41) Goh, G. L.; Agarwala, S.; Tan, Y. J.; Yeong, W. Y. A Low Cost and Flexible Carbon Nanotube pH Sensor Fabricated Using Aerosol Jet Technology for Live Cell Applications. *Sens. Actuators, B* **2018**, *260*, 227–235.
- (42) Li, P.; Martin, C. M.; Yeung, K. K.; Xue, W. Dielectrophoresis Aligned Single-Walled Carbon Nanotubes as pH Sensors. *Biosensors* **2011**, *1* (1), 23–35.
- (43) Saha, D.; Selvaganapathy, P. R.; Kruse, P. Peroxide-Induced Tuning of the Conductivity of Nanometer-Thick MoS₂ Films for Solid-State Sensors. *ACS Appl. Nano Mater.* **2020**, *3* (11), 10864–10877.
- (44) Dalmieda, J.; Zubiarrain-Laserna, A.; Ganepola, D.; Selvaganapathy, P. R.; Kruse, P. Chemiresistive Detection of Silver Ions in Aqueous Media. *Sens. Actuators, B* **2021**, *328*, 129023.
- (45) Zhen, X. V.; Swanson, E. G.; Nelson, J. T.; Zhang, Y.; Su, Q.; Koester, S. J.; Bühlmann, P. Noncovalent Monolayer Modification of Graphene Using Pyrene and Cyclodextrin Receptors for Chemical Sensing. *ACS Appl. Nano Mater.* **2018**, *1* (6), 2718–2726.
- (46) Negrito, M.; Elinski, M. B.; Hawthorne, N.; Pedley, M. P.; Han, M.; Sheldon, M.; Espinosa-Marzal, R. M.; Batteas, J. D. Using Patterned Self-Assembled Monolayers to Tune Graphene–Substrate Interactions. *Langmuir* **2021**, *37* (33), 9996–10005.
- (47) Golbek, T. W.; Faase, R. A.; Rasmussen, M. H.; Tykwinski, R. R.; Stryker, J. M.; Ivar Andersen, S.; Baio, J. E.; Weidner, T. Model Asphaltenes Adsorbed onto Methyl- and COOH-Terminated SAMs on Gold. *Langmuir* **2021**, *37* (32), 9785–9792.
- (48) Sahoo, G. P.; Das, D.; Sheet, P. S.; Beg, H.; Salgado-Morán, G.; Misra, A. Morphology Directing Synthesis of 1-Pyrene Carboxaldehyde Microstructures and Their Photo Physical Properties. *RSC Adv.* **2014**, *4* (21), 10903–10911.
- (49) An, X.; Simmons, T.; Shah, R.; Wolfe, C.; Lewis, K. M.; Washington, M.; Nayak, S. K.; Talapatra, S.; Kar, S. Stable Aqueous Dispersions of Noncovalently Functionalized Graphene from Graphite and Their Multifunctional High-Performance Applications. *Nano Lett.* **2010**, *10* (11), 4295–4301.
- (50) Pliego, J. R. Thermodynamic Cycles and the Calculation of pK_a. *Chem. Phys. Lett.* **2003**, *367* (1–2), 145–149.
- (51) Lian, P.; Johnston, R. C.; Parks, J. M.; Smith, J. C. Quantum Chemical Calculation of pK_as of Environmentally Relevant Functional Groups: Carboxylic Acids, Amines, and Thiols in Aqueous Solution. *J. Phys. Chem. A* **2018**, *122* (17), 4366–4374.

- (52) Turner, P.; Hodnett, M.; Dorey, R.; Carey, J. D. Controlled Sonication as a Route to In-Situ Graphene Flake Size Control. *Sci. Rep.* **2019**, *9* (1), 1–8.
- (53) Kim, J.; Kwon, S.; Cho, D.-H.; Kang, B.; Kwon, H.; Kim, Y.; Park, S. O.; Jung, G. Y.; Shin, E.; Kim, W.-G.; Lee, H.; Ryu, G. H.; Choi, M.; Kim, T. H.; Oh, J.; Park, S.; Kwak, S. K.; Yoon, S. W.; Byun, D.; Lee, Z.; Lee, C. Direct Exfoliation and Dispersion of Two-Dimensional Materials in Pure Water via Temperature Control. *Nat. Commun.* **2015**, *6* (1), 8294.
- (54) Ferrari, A. C.; Basko, D. M. Raman Spectroscopy as a Versatile Tool for Studying the Properties of Graphene. *Nat. Nanotechnol.* **2013**, *8* (4), 235–246.
- (55) Lim, C. X.; Hoh, H. Y.; Ang, P. K.; Loh, K. P. Direct Voltammetric Detection of DNA and pH Sensing on Epitaxial Graphene: An Insight into the Role of Oxygenated Defects. *Anal. Chem.* **2010**, *82* (17), 7387–7393.
- (56) Araujo, P. T.; Terrones, M.; Dresselhaus, M. S. Defects and Impurities in Graphene-like Materials. *Mater. Today* **2012**, *15* (3), 98–109.
- (57) Jorio, A.; Ferreira, E. H. M.; Moutinho, M. V. O.; Stavale, F.; Achete, C. A.; Capaz, R. B. Measuring Disorder in Graphene with the G and D Bands. *Phys. Status Solidi B* **2010**, *247* (11–12), 2980–2982.
- (58) Dresselhaus, M. S.; Jorio, A.; Souza Filho, A. G.; Saito, R. Defect Characterization in Graphene and Carbon Nanotubes Using Raman Spectroscopy. *Philos. Trans. R. Soc., A* **2010**, *368* (1932), 5355–5377.
- (59) Caçado, L. G.; Jorio, A.; Ferreira, E. H. M.; Stavale, F.; Achete, C. A.; Capaz, R. B.; Moutinho, M. V. O.; Lombardo, A.; Kulmala, T. S.; Ferrari, A. C. Quantifying Defects in Graphene via Raman Spectroscopy at Different Excitation Energies. *Nano Lett.* **2011**, *11* (8), 3190–3196.
- (60) Khalili, D. Graphene Oxide : A Promising Carbocatalyst for the Regioselective Thiocyanation of Aromatic Amines, Phenols, Anisols and Enolizable Ketones by Hydrogen Peroxide/KSCN in Water Department of Chemistry, College of Sciences, Shiraz University, Shiraz 7. *Mater. Sci. Res. India* **2017**, *14* (1), 19–30.
- (61) Ranjan, P.; Agrawal, S.; Sinha, A.; Rao, T. R.; Balakrishnan, J.; Thakur, A. D. A Low-Cost Non-Explosive Synthesis of Graphene Oxide for Scalable Applications. *Sci. Rep.* **2018**, *8* (1), 1–13.
- (62) Luceño-Sánchez, J. A.; Maties, G.; Gonzalez-Arellano, C.; Diez-Pascual, A. M. Synthesis and Characterization of Graphene Oxide Derivatives via Functionalization Reaction with Hexamethylene Diisocyanate. *Nanomaterials* **2018**, *8* (11), 870–6.
- (63) Huh, S. H. Thermal Reduction of Graphene Oxide. In *Physics and Applications of Graphene: Experiments*; Mikhailov, S., Ed.; Condensed Matter Physics, 2011; pp 73–90. DOI: 10.5772/590.
- (64) Beiron, J.; Normann, F.; Kristoferson, L.; Strömberg, L.; Gardarsdóttir, S. Ó.; Johnsson, F. Enhancement of CO₂ Absorption in Water through pH Control and Carbonic Anhydrase-A Technical Assessment. *Ind. Eng. Chem. Res.* **2019**, *58* (31), 14275–14283.
- (65) Eckmann, A.; Felten, A.; Mishchenko, A.; Britnell, L.; Krupke, R.; Novoselov, K. S.; Casiraghi, C. Probing the Nature of Defects in Graphene by Raman Spectroscopy. *Nano Lett.* **2012**, *12* (8), 3925–3930.
- (66) Roscher, S.; Hoffmann, R.; Ambacher, O. Determination of the Graphene-Graphite Ratio of Graphene Powder by Raman 2D Band Symmetry Analysis. *Anal. Methods* **2019**, *11* (9), 1180–1191.
- (67) Venezuela, P.; Lazzeri, M.; Mauri, F. Theory of Double-Resonant Raman Spectra in Graphene: Intensity and Line Shape of Defect-Induced and Two-Phonon Bands. *Phys. Rev. B: Condens. Matter Mater. Phys.* **2011**, *84* (3), 1–25.
- (68) Jin, M.; Jiao, N.; Zhang, C. X.; Xiao, H. P.; Zhang, K. W.; Sun, L. Z. Reduction Mechanism of Hydroxyl Group from Graphene Oxide with and without -NH₂ Agent. *Phys. B* **2015**, *477*, 70–74.
- (69) Sengupta, I.; Chakraborty, S.; Talukdar, M.; Pal, S. K.; Chakraborty, S. Thermal Reduction of Graphene Oxide: How Temperature Influences Purity. *J. Mater. Res.* **2018**, *33* (23), 4113–4122.
- (70) Lv, S. S.; Bian, L.; Qiu, J. X.; Zhang, X. T.; Gao, M. J.; He, X. C.; Ma, X. F.; Li, G. Surface Modification of Graphene Oxide with Pyrene Derivatives and Their Photo-Switching Behaviors. *Mater. Sci. Forum* **2017**, *898*, 1739–1748.
- (71) Chen, T.; Li, M.; Liu, J. π - π Stacking Interaction: A Nondestructive and Facile Means in Material Engineering for Bioapplications. *Cryst. Growth Des.* **2018**, *18* (5), 2765–2783.
- (72) Luo, L. Q.; Zhang, Z.; Ding, Y. P.; Deng, D. M.; Zhu, X. L.; Wang, Z. X. Label-Free Electrochemical Impedance Genosensor Based on 1-Aminopyrene/Graphene Hybrids. *Nanoscale* **2013**, *5* (13), 5833–5840.
- (73) Milosavljevic, B. H.; Thomas, J. K. The Photophysics of 1-Hydroxypyrene, the Acidity of Its Singlet Excited State, and the Nature of Its Photoionization Process in Polar Media. *Photochem. Photobiol. Sci.* **2002**, *1* (2), 100–104.
- (74) Wang, N.; Xu, Q.; Xu, S.; Qi, Y.; Chen, M.; Li, H.; Han, B. High-Efficiency Exfoliation of Layered Materials into 2D Nanosheets in Switchable CO₂/Surfactant/H₂O System. *Sci. Rep.* **2015**, *5* (June), 1–9.
- (75) Ojrzyńska, M.; Wroblewska, A.; Judek, J.; Malolepszy, A.; Duzynska, A.; Zdrojek, M. Study of Optical Properties of Graphene Flakes and Its Derivatives in Aqueous Solutions. *Opt. Express* **2020**, *28* (5), 7274.
- (76) Rafiee, J.; Mi, X.; Gullapalli, H.; Thomas, A. V.; Yavari, F.; Shi, Y.; Ajayan, P. M.; Koratkar, N. A. Wetting Transparency of Graphene. *Nat. Mater.* **2012**, *11* (3), 217–222.
- (77) Li, Z.; Wang, Y.; Kozbial, A.; Shenoy, G.; Zhou, F.; McGinley, R.; Ireland, P.; Morganstein, B.; Kunkel, A.; Surwade, S. P.; Li, L.; Liu, H. Effect of Airborne Contaminants on the Wettability of Supported Graphene and Graphite. *Nat. Mater.* **2013**, *12* (10), 925–931.
- (78) Zhang, X.; Wan, S.; Pu, J.; Wang, L.; Liu, X. Highly Hydrophobic and Adhesive Performance of Graphene Films. *J. Mater. Chem.* **2011**, *21* (33), 12251–12258.

Supporting Information

Defect engineering of graphene to modulate the pH
response of graphene devices

*Shayan Angizi¹, Eugene Yat Chun Yu¹, Johnson Dalmieda¹, Dipankar Saha¹, P. Ravi
Selvaganapathy², Peter Kruse^{1,*}*

¹ Department of Chemistry and Chemical Biology, McMaster University, Hamilton, Ontario L8S
4M1 Canada

² Department of Mechanical Engineering, McMaster University, Hamilton, L8S 4M1, Canada

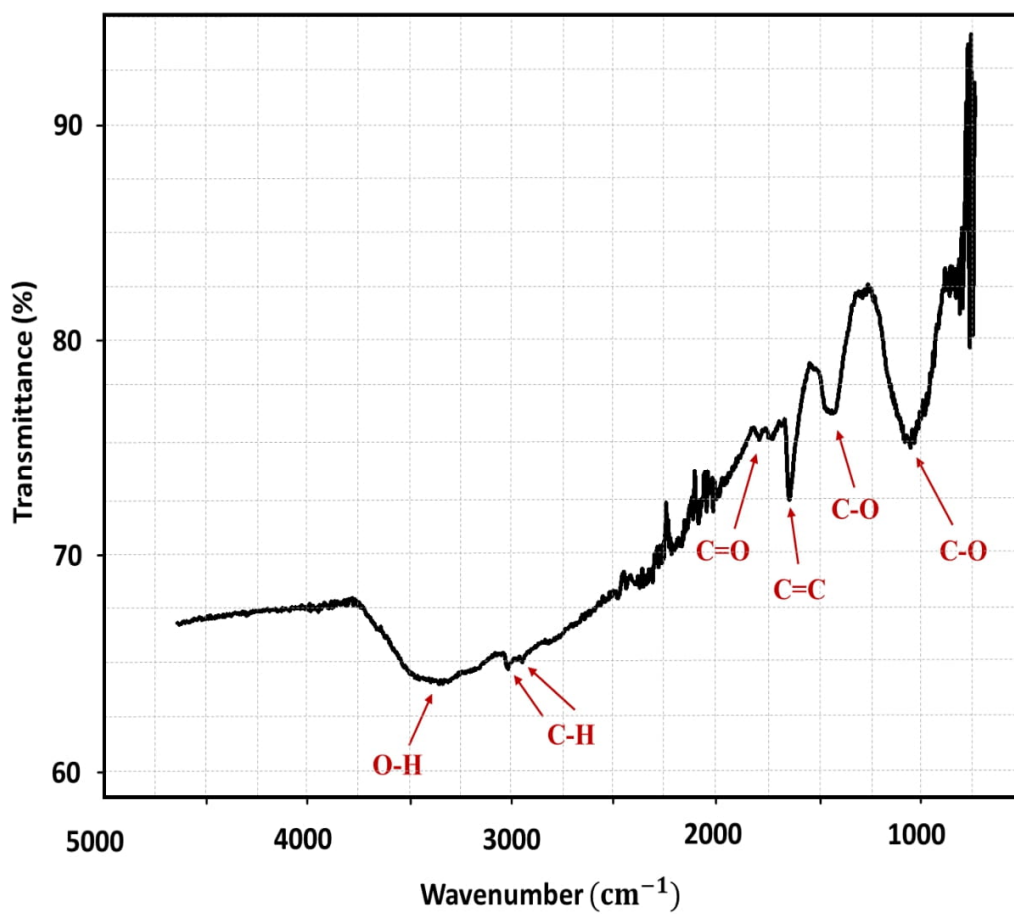


Figure S1. FTIR spectrum of 6h sonicated FLG that shows the presence of various oxygen-based functional groups on the surface/edge.

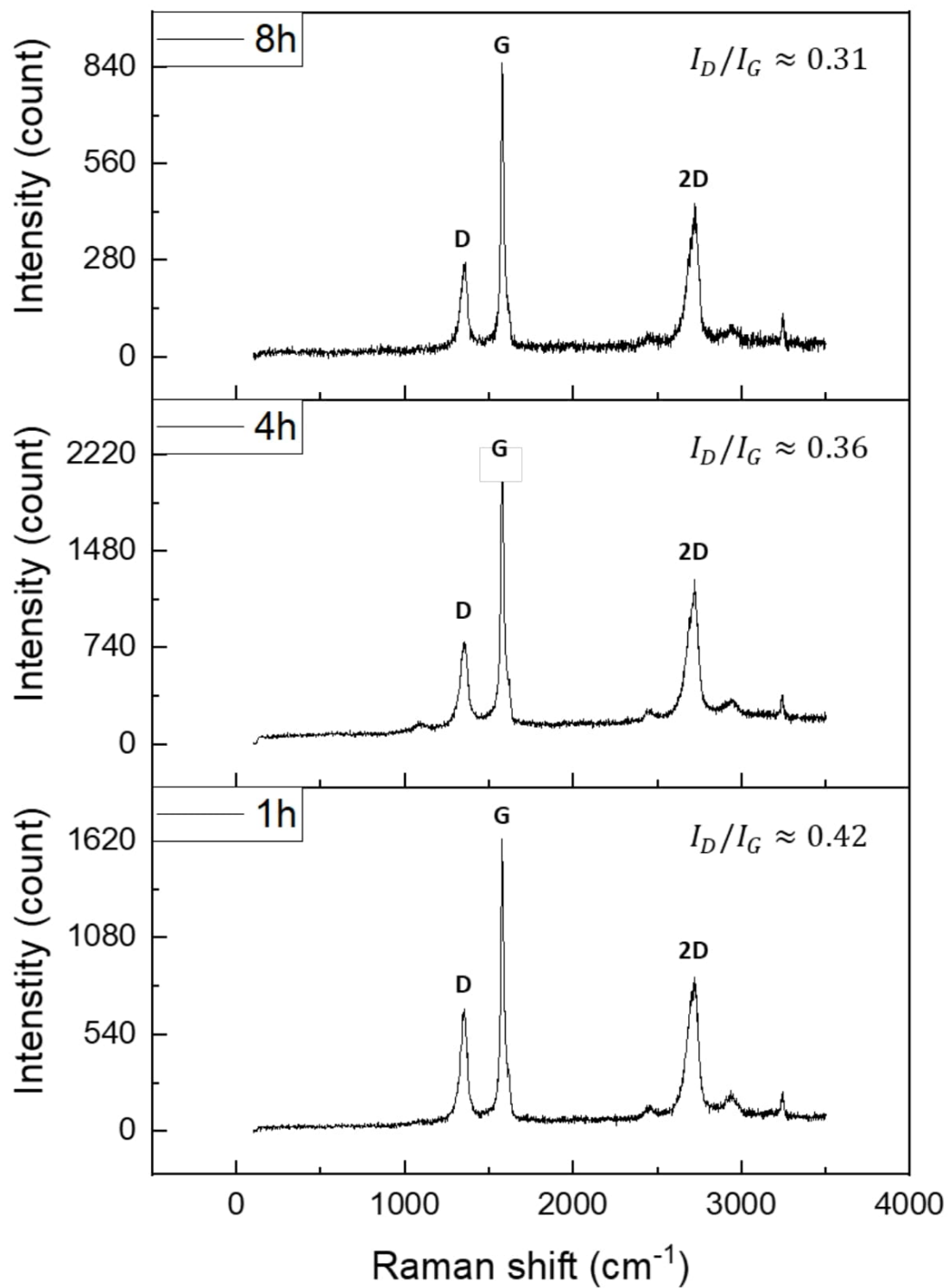


Figure S2. Raman of N_2 -annealed samples for 1h, 4h, and 8h

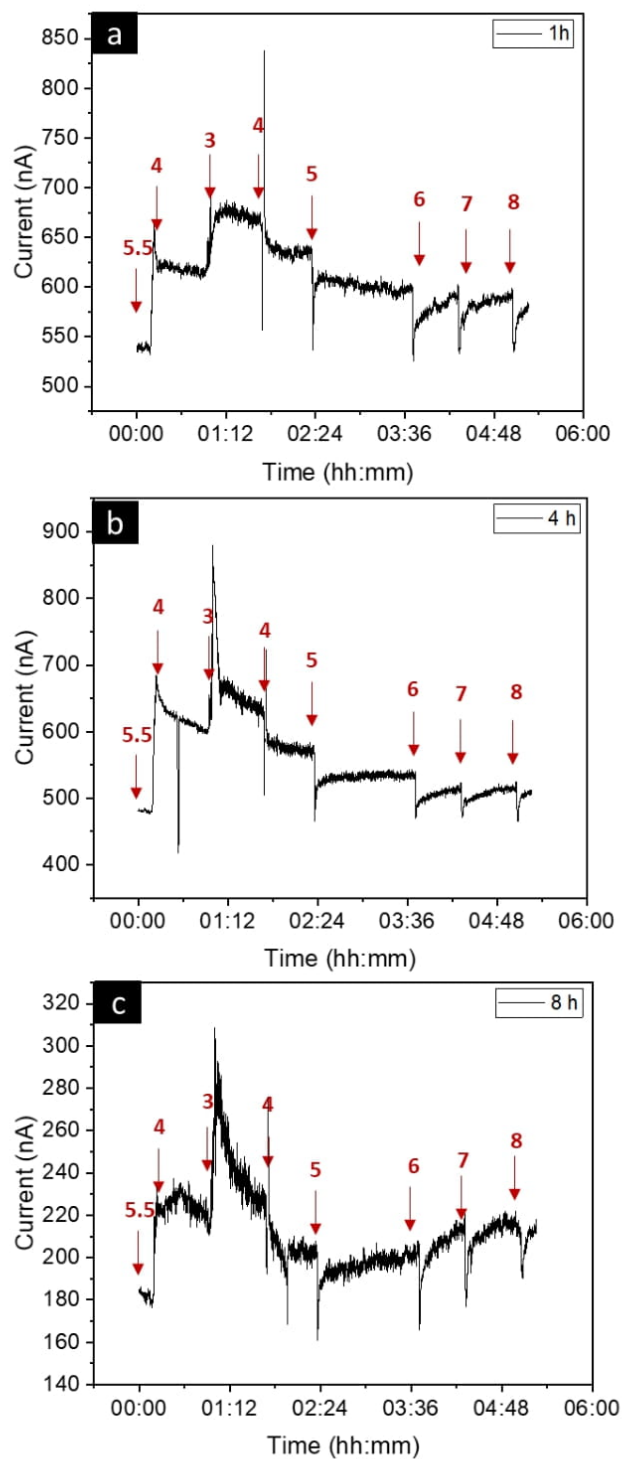
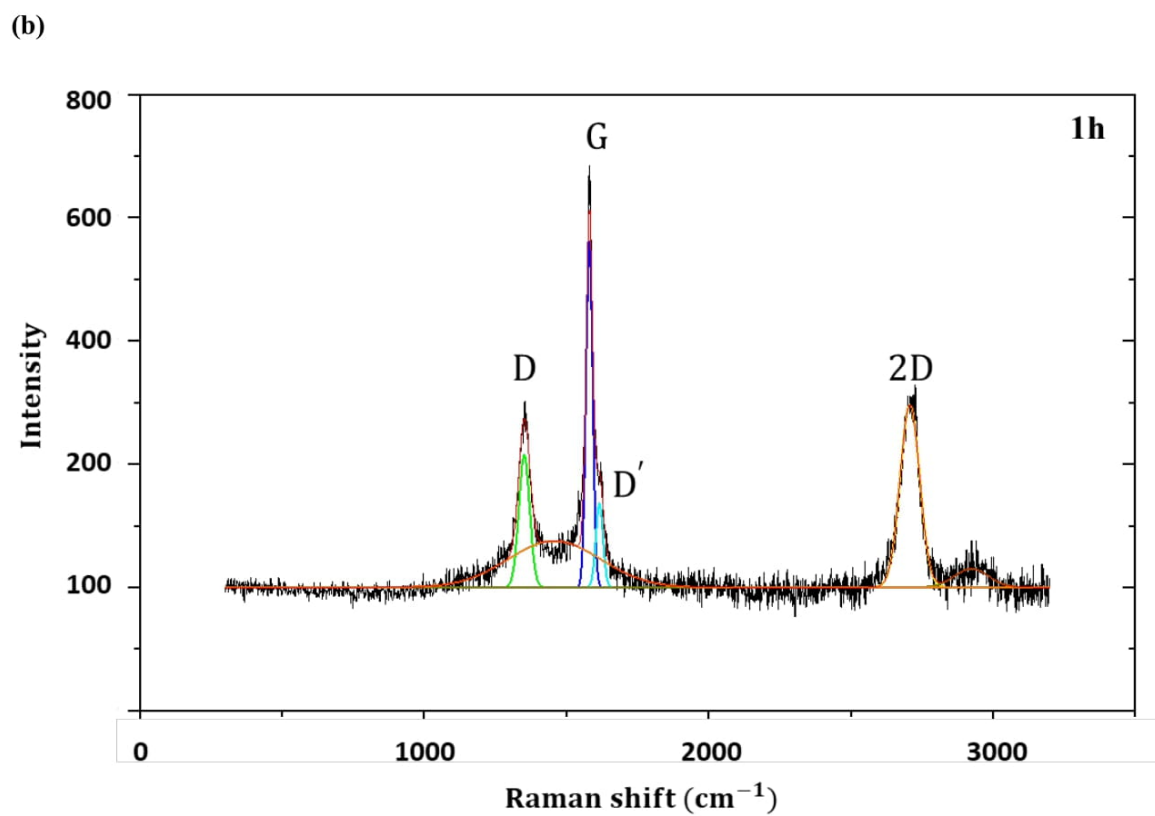
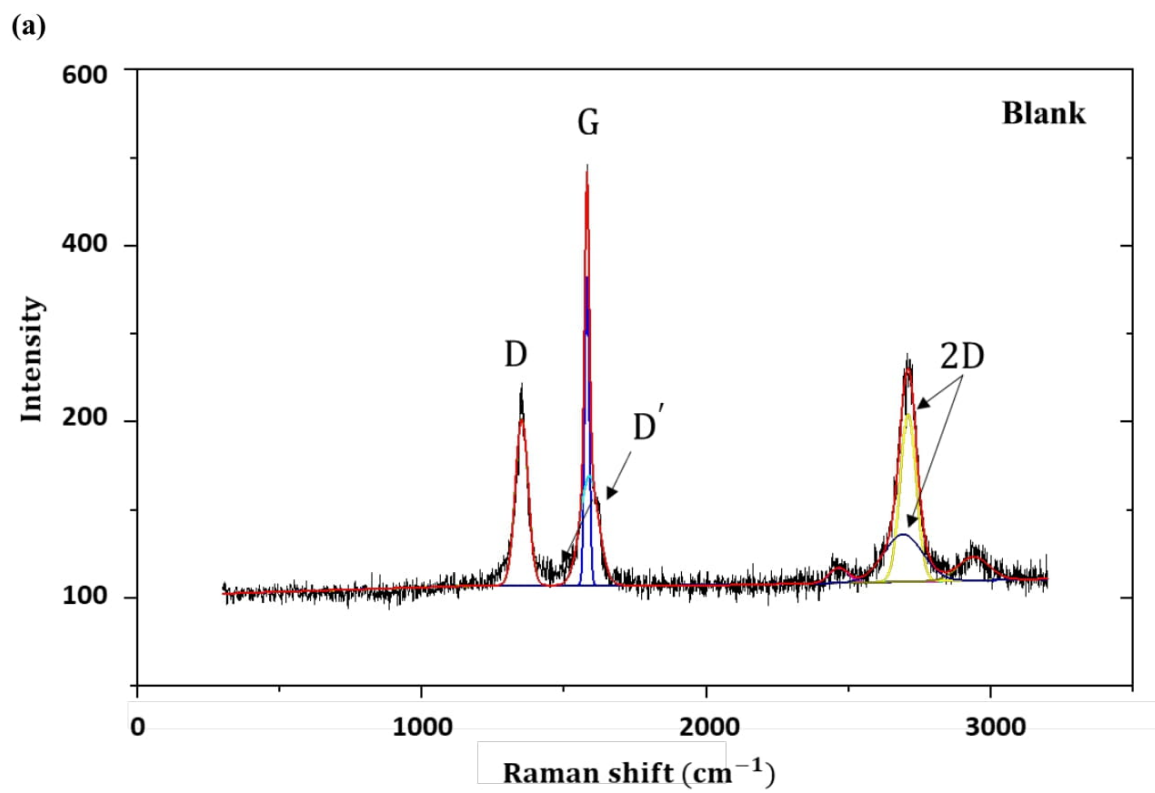
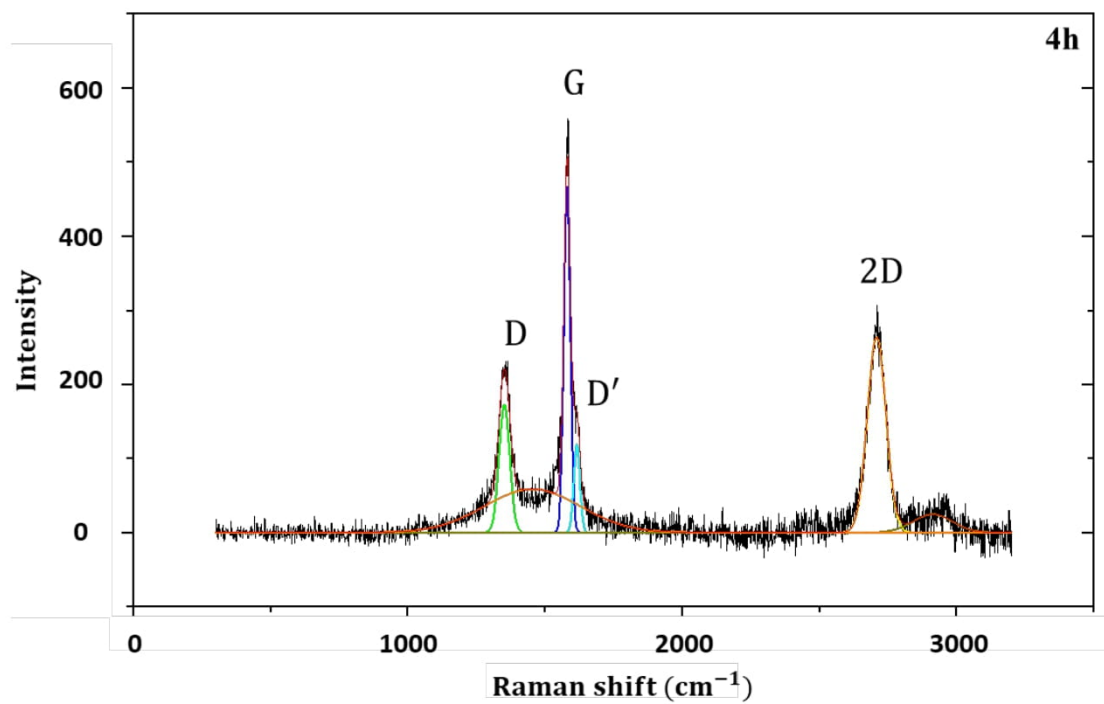


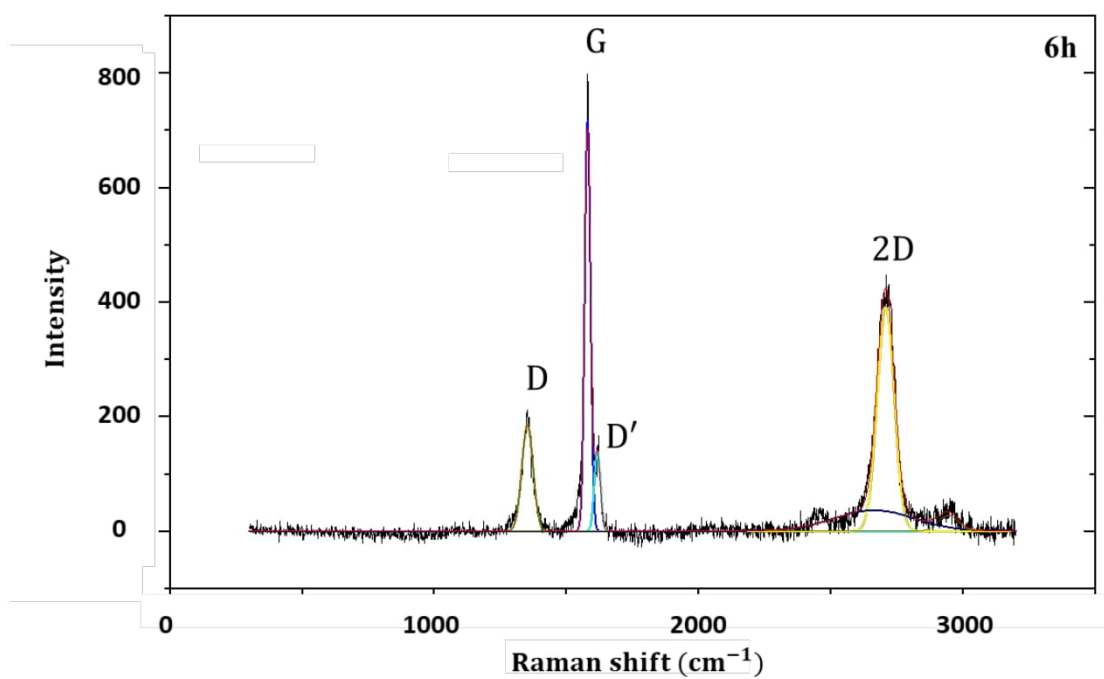
Figure S3



(c)



(d)



S6

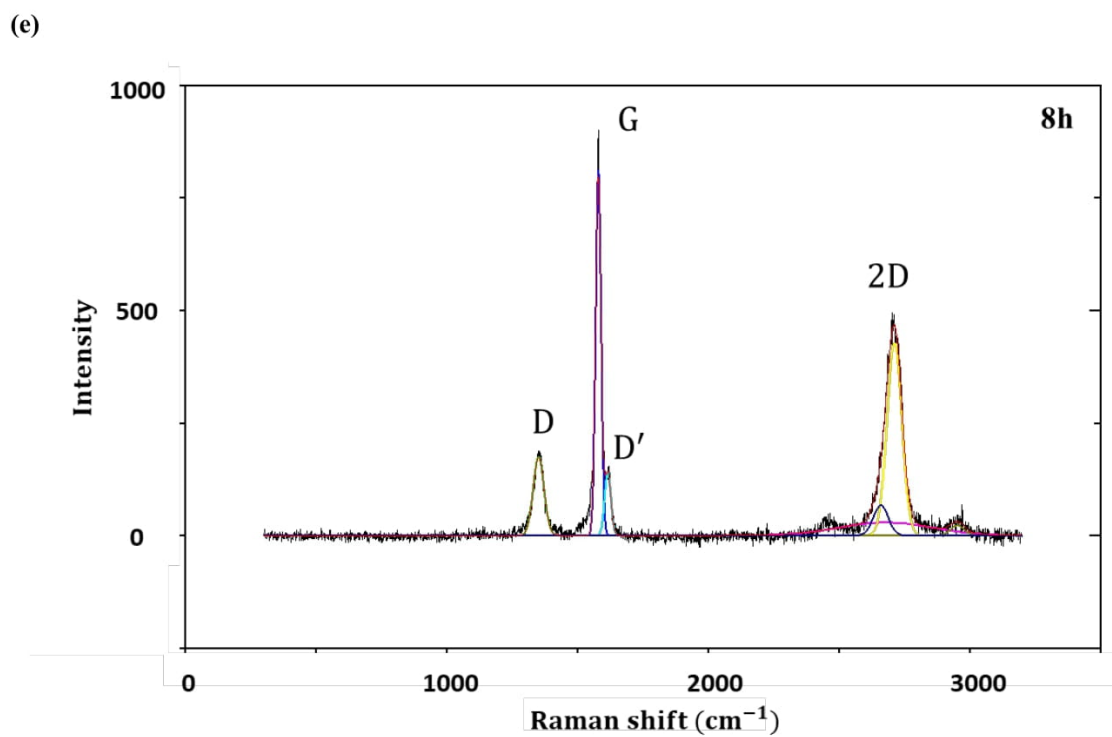


Figure S4. Examples of deconvoluted Raman spectra for (a) blank samples, and (b) 1 h, (c) 4 h, (d) 6 h and (e) 8 h N₂/H₂-annealed samples.

Table S1. Summary of information derived from deconvoluted Raman spectra.

Sample	I_D/I_G	$I_D/I_{D'}$	I_{2D}/I_G	$I_{D'}/I_G$
Blank 1	0.472976	2.049198	0.468519	0.23081
Blank 2	0.538445	1.519692	0.543327	0.354312
Blank 3	0.464551	2.080593	0.452524	0.223278
1h -1	0.381523	1.571434	0.52833	0.242786
1h- 2	0.483109	1.984856	0.579115	0.243397
1h- 3	0.370634	1.599196	0.400373	0.231763
4h-1	0.369217	1.44975	0.564955	0.254677
4h-3	0.37334	1.610875	0.505417	0.231762
4h-3	0.321505	1.574865	0.487186	0.204148
6h-1	0.270297	1.29791	0.542303	0.228255
6h-2	0.265671	1.355196	0.553105	0.196039
6h-3	0.253309	1.253483	0.561226	0.242084
8h-1	0.185154	1.213113	0.527567	0.193843
8h-2	0.151412	1.227409	0.527294	0.174687
8h-3	0.17972	1.328697	0.543947	0.19547

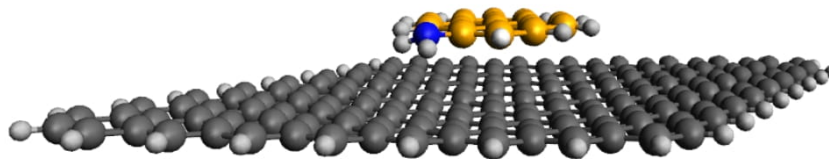


Figure S5. Visual depiction of 1-aminopyrene adsorbed onto an 8x8 graphene flake. Visualized using Avogadro.

Table S2. Adsorption energies and distances of Py- NH₂ , Py-OH, and Py-COOH in both protonated and deprotonated forms.

Molecule	Adsorption energy (kcal/mol)	Adsorption distance (Å)
Py-NH ₃ ⁺	-11.68	3.98
Py-NH ₂	-125.92	3.44
Py-OH	-159.55	3.43
Py-O ⁻	-247.81	3.91
Py-COOH	-214.13	3.39
Py-COO ⁻	-258.50	4.01

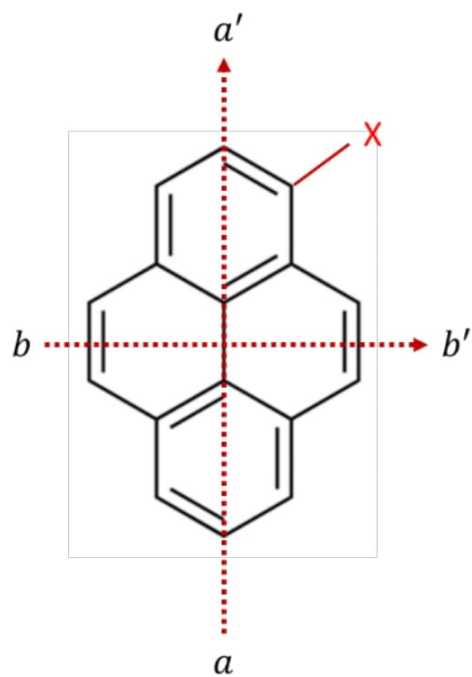


Figure S6. Schematic illustration of directional excitation in pyrene molecules

Table S3. Calculated UV/vis peak positions (oscillator strength in brackets).

Py-NH ₃ ⁺	Py-NH ₂	Py-OH	Py-O ⁻	Py-COOH	Py-COO ⁻
352.46 nm (0.3864)	347.92 nm (0.4129)	360.32 nm (0.3931)	420.74 nm (0.4027)	387.78 nm (0.49)	367.5 nm (0.3828)
334.01 nm (0.0043)	335.77 nm (0.0052)	340.74 nm (0.0386)	386.91 nm (0.0307)	346.47 nm (0.0367)	339.86 nm (0.0016)
287.11 nm (0.071)	292.48 nm (0.0002)	303.2 nm (0.0083)	350.64 nm (0.0898)	304.76 nm (0.013)	318.84 nm (0.0759)
277.35 nm (0.0358)	276.96 nm (0.3802)	278.9 nm (0.3201)	306.55 nm (0.0001)	287.09 nm (0.2727)	302.97 nm (0.0317)
274.25 nm (0.2815)	269.48 nm (0.0011)	268.07 nm (0.0005)	304.49 nm (0.0031)	279.68 nm (0.0549)	297.12 nm (0.0026)
257.48 nm (0.0017)	258.81 nm (0.0012)	265.95 nm (0.0119)	289.49 nm (0.1059)	266.65 nm (0.0078)	285.16 nm (0.035)
249.64 nm (0.0005)	252.26 nm (0.0006)	256.17 nm (0.017)	278.04 nm (0.0005)	248.72 nm (0.2734)	280.4 nm (0.2162)
240 nm (0.1629)	244.6 nm (0.0013)	253.41 nm (0.0004)	277.33 nm (0.1289)	241.85 nm (0.001)	269.93 nm (0.0003)
236.14 nm (0.8439)	241.49 nm (0.0306)	246.51 nm (0.0009)	272.07 nm (0.0012)	241.03 nm (0.111)	264.67 nm (0.0823)
230.84 nm (0.0001)	238.92 nm (0.0005)	240.15 nm (0.0386)	-	237.18 nm (0.3303)	260.92 nm (0.0107)
225.13 nm (0.0019)	238.47 nm (0.9869)	239.57 nm (0.7288)	-	230.94 nm (0.0454)	259.83 nm (0.0142)
-	-	233.57 nm (0.1998)	-	-	252.81 nm (0.0984)

Table S4. Calculated UV/vis triplet state positions.

Py-NH ₃ ⁺	Py-NH ₂	Py-OH	Py-O ⁻	Py-COOH	Py-COO ⁻
589.58 nm	586.08 nm	600.97 nm	655.57 nm	635.01 nm	598.77 nm
364.17 nm	369.14 nm	386.72 nm	463.25 nm	395.56 nm	373.27 nm
353.14 nm	352.67 nm	359.82 nm	409.15 nm	363.34 nm	359.28 nm
348.62 nm	345.46 nm	345.13 nm	371.52 nm	361.09 nm	355.11 nm
321.89 nm	323.17 nm	326.46 nm	339.15 nm	335.89 nm	341.97 nm
317.96 nm	320.61 nm	317.58 nm	335.51 nm	318.61 nm	322.58 nm
286.89 nm	285.77 nm	288.03 nm	333.06 nm	303.36 nm	315.75 nm
264.65 nm	273.6 nm	270.12 nm	310.26 nm	297.72 nm	313.38 nm
263.1 nm	266.47 nm	269.08 nm	306.78 nm	283.12 nm	299.33 nm
259.93 nm	265.27 nm	265.77 nm	304.52 nm	270.29 nm	288.78 nm
255.44 nm	261.38 nm	262.53 nm	297.37 nm	267.41 nm	275.51 nm
253.72 nm	259.65 nm	259.39 nm	293.03 nm	265.44 nm	268.33 nm

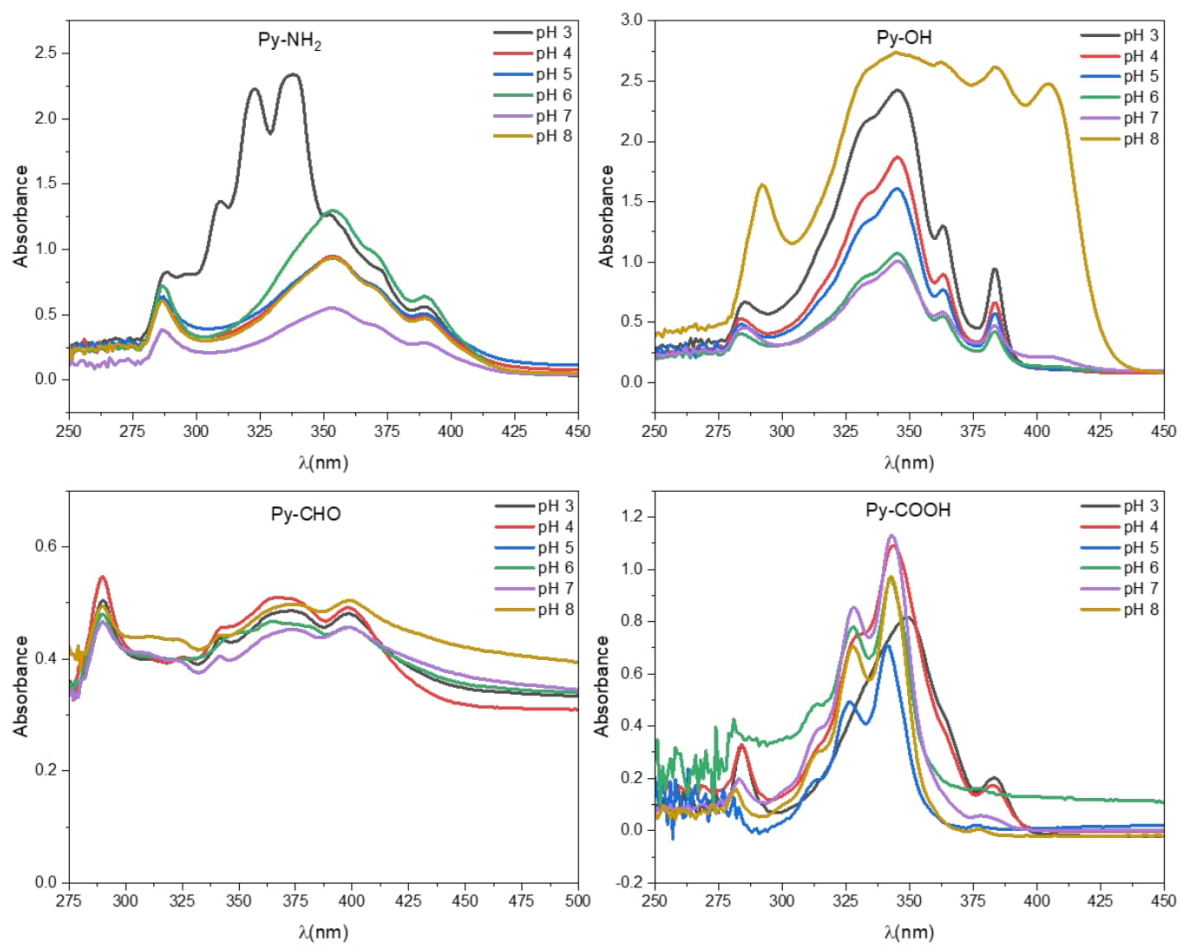


Figure S7. Absorption spectra of pyrene derivatives in pH 3-8

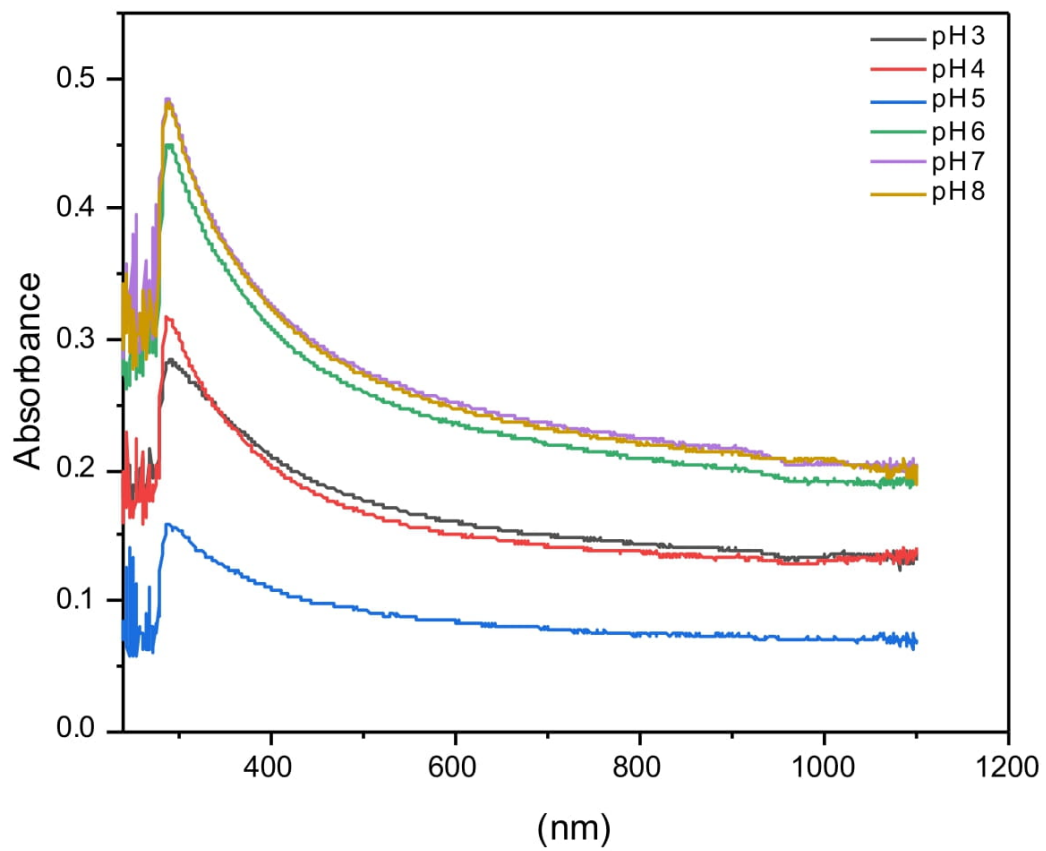


Figure S8. Absorption spectra of FLG in pH range of 3 to 8

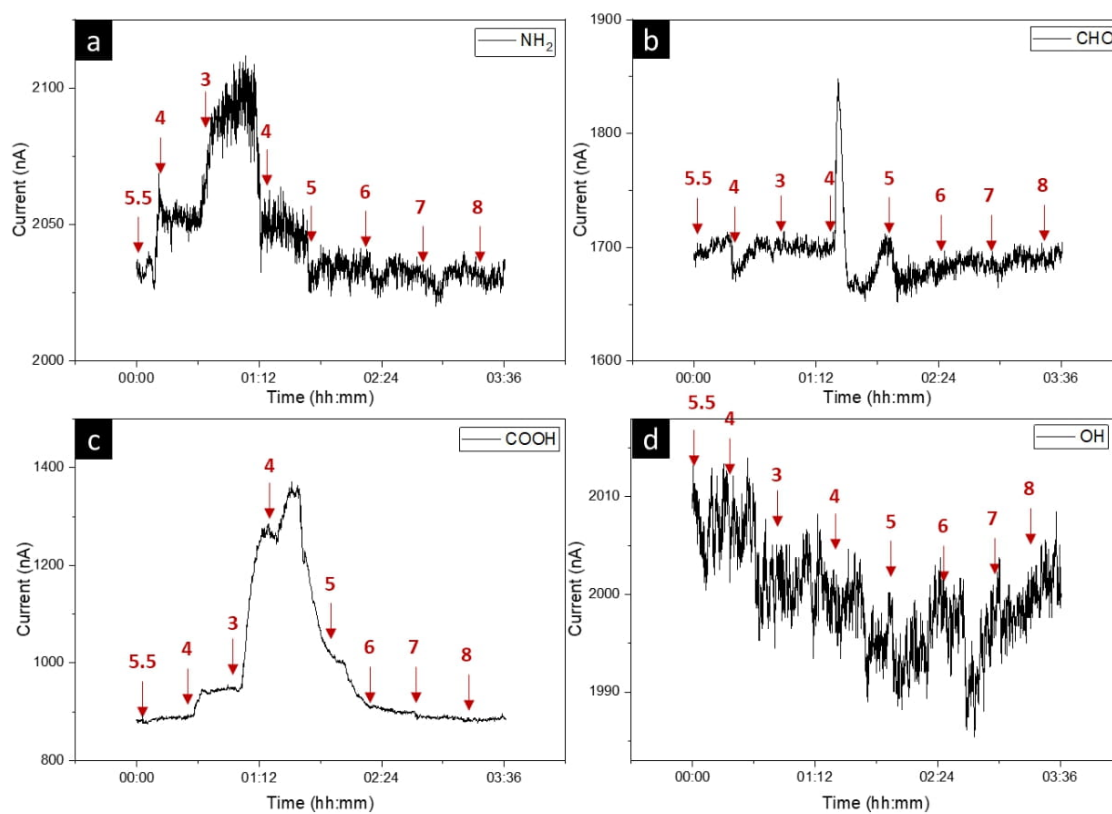


Figure S9. Calibration curves of PD functionalized graphene: a) Py-NH₂/FLG b) Py-CHO/FLG c) Py-OH/FLG d) Py-COOH/FLG

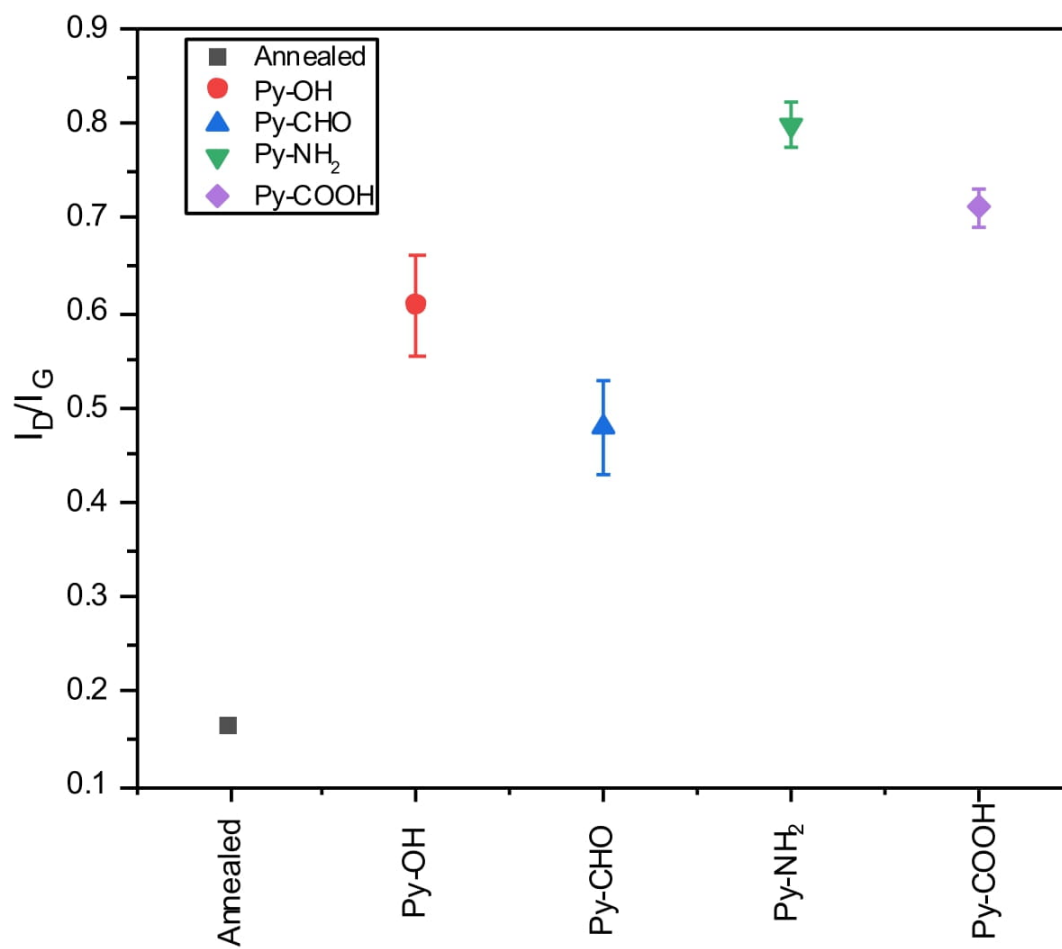


Figure S10. Plot of I_D/I_G ratio for pyrene derivative functionalized FLG compared to 8h N_2/H_2 annealed sample





Chapter 4 Defect Density-Dependent pH Response of Graphene Derivatives: Towards the Development of pH-Sensitive Graphene Oxide Devices

This chapter demonstrates that a highly pH-sensitive platform could be fabricated by adjusting graphene derivatives' type and defect density. From monolayer graphene to graphene oxides, various graphene derivatives were tested against pH, demonstrating a significant pH response upon the fabrication of graphene oxide-based sensors. Then, the surface functionalization was done using various concentrations of pyrene derivatives containing the pH-sensitive graphene groups, meaning carboxyl, amine, and hydroxyl, to explore the dominant role of defects. It was also shown that the graphene sensitivity could be numerically correlated to the density of each group. Later, it was found that deposition and post-treatment of graphene oxide could enhance their stability against water, leading to the development of highly pH-sensitive graphene oxide substrates.

Reprinted with permission from *Nanomaterials*, 2022, 12(11), 1801, Shayan Angizi, Xianxuan Huang, Lea Hong, Md Ali Akbar, P. Ravi Selvaganapathy, and Peter Kruse. DOI: 10.3390/nano12111801© 2022 MDPI

Article

Defect Density-Dependent pH Response of Graphene Derivatives: Towards the Development of pH-Sensitive Graphene Oxide Devices

 Shayan Angizi¹ , Xianxuan Huang¹, Lea Hong¹, Md Ali Akbar¹ , P. Ravi Selvaganapathy²  and Peter Kruse^{1,*} 

¹ Department of Chemistry and Chemical Biology, McMaster University, 1280 Main Street West, Hamilton, ON L8S 4M1, Canada; angizis@mcmaster.ca (S.A.); huangx87@mcmaster.ca (X.H.); hongl1@mcmaster.ca (L.H.); akbarm7@mcmaster.ca (M.A.A.)

² Department of Mechanical Engineering, McMaster University, 1280 Main Street West, Hamilton, ON L8S 4L7, Canada; selvaga@mcmaster.ca

* Correspondence: pkruse@mcmaster.ca

Abstract: In this study, we demonstrate that a highly pH-sensitive substrate could be fabricated by controlling the type and defect density of graphene derivatives. Nanomaterials from single-layer graphene resembling a defect-free structure to few-layer graphene and graphene oxide with high defect density were used to demonstrate the pH-sensing mechanisms of graphene. We show the presence of three competing mechanisms of pH sensitivity, including the availability of functional groups, the electrochemical double layer, and the ion trapping that determines the overall pH response. The graphene surface was selectively functionalized with hydroxyl, amine, and carboxyl groups to understand the role and density of the graphene pH-sensitive functional groups. Later, we establish the development of highly pH-sensitive graphene oxide by controlling its defect density. This research opens a new avenue for integrating micro–nano-sized pH sensors based on graphene derivatives into next-generation sensing platforms.

Keywords: pH; graphene; graphene oxide; defect; surface functionalization



Citation: Angizi, S.; Huang, X.; Hong, L.; Akbar, M.A.; Selvaganapathy, P.R.; Kruse, P. Defect Density-Dependent pH Response of Graphene Derivatives: Towards the Development of pH-Sensitive Graphene Oxide Devices. *Nanomaterials* **2022**, *12*, 1801. <https://doi.org/10.3390/nano12111801>

Academic Editor: Marco Cannas

Received: 30 April 2022

Accepted: 20 May 2022

Published: 25 May 2022

Publisher's Note: MDPI stays neutral with regard to jurisdictional claims in published maps and institutional affiliations.



Copyright: © 2022 by the authors. Licensee MDPI, Basel, Switzerland. This article is an open access article distributed under the terms and conditions of the Creative Commons Attribution (CC BY) license (<https://creativecommons.org/licenses/by/4.0/>).

1. Introduction

The pH measurement in an aqueous solution is a universal need and is widely utilized in various applications, from biology [1] to wastewater treatment [2]. The standard techniques for pH detections are often based on electrochemistry (potentiometry) using a porous glass electrode [3,4]. Later, the development of ion-selective membranes introduced a new category of sensing devices, such as field-effect transistors [5,6]. The ion-selective membranes transfer the charge to a conductive active layer under varying gate potentials [7]. Other pH detection methods, including conductometric [8,9] and optical [10,11], operate based on the pH sensitivity of an indicator dye, where adding an organic redox-active indicator is essential. Nevertheless, commercial pH measurements have a number of drawbacks. The porous glass electrodes require high maintenance and are prone to performance loss at low ionic strength or high temperature [12]. The ion-selective membranes are subject to degradation and loss of sensitivity over long-term operation [13,14]. The optical measurements require the introduction of undesirable chemical species in the reaction solution [15,16]. Therefore, developing reagent-free pH-sensitive platforms has remained a relevant topic.

Since the first successful isolation of monolayer graphene from graphite [17], there has been an increasing trend towards integrating these atomically thin structures into many sensing applications, including pH detection units. This broad range of graphene sensing applications is mainly due to three of its characteristics: superior conductivity,

high specific surface area, and modifiable surface chemistry [18–20]. Single-layer graphene (SLG) consists of an sp^2 -hybridized covalently bonded carbon network, while vertically stacked consecutive layers of graphene are held together by van der Waals forces [21]. Since the electronic properties of graphene greatly depend on the presence of delocalized π electrons, any minor disruption of the surface infinite symmetry causes changes in its electrical properties [22,23]. Therefore, defects involving sp^3 carbon atoms or in-plane lattice asymmetries play a vital role in determining graphene's ultimate electrical and chemical properties [24]. Accordingly, the defect engineering of graphene can lead to the generation of other graphene derivatives, such as graphene oxide (GO) and reduced graphene oxide (r-GO).

The sensing performance of graphene derivatives in contact with an aqueous environment is profoundly reliant on the electrolyte parameters, including pH, oxidation-reduction potential, ionic strength, dissolved oxygen, and temperature [25]. Therefore, the concept of pH sensors based on graphene derivatives can be fully developed only if the aqueous electrolyte's impact on graphene is entirely investigated. Moreover, the pH-sensing mechanism of graphene has been shown to be defect-dependent [26], but there is still no clarity on the role of defects in the pH response of graphene devices.

This lack of understanding originates because "ideal" defect-free graphene tends to be hydrophobic [23], making it challenging to elucidate the structure of the aqueous solution/graphene interface [27]. However, oxygen-based impurities enhance the surface local charges and decrease the liquid/surface contact angle [28–30]. Therefore, the defectivity level, type of defects, and their configurations (edge or plane) on graphene play a vital role in the graphene–solution interface. Despite a few studies exploring the possibility of developing a pH-sensing platform based on graphene derivatives [28,31–35], there is still a gap in understanding their response to pH at high defect levels. Thus far, there exist only a few reports on the application of GO in pH sensing, primarily due to three main limiting factors in the development of such devices: (i) the water dispersibility of the GO due to its hydrophilic nature and high negative zeta potential [36], (ii) its low surface conductance and semiconductive nature, (iii) the lack of understanding of the pH detection mechanisms of GO [37]. In 2020, potentiometric and chemiresistive measurements of hydrothermally reduced GO revealed potential sensitivities of 66 mV/pH (pH 2–12) and 44 mV/pH (pH 4–7), respectively. Accordingly, the reported working range of the chemiresistor was limited to acidic pH, and the higher pH sensitivities required a three-electrode design [38,39]. Although the presence of oxygen functional groups was shown to be responsible for such detection, no explanation for the limited linear range and mechanism has been proposed. In a different study, a sensitivity of 51 mV/pH was obtained for a pH of 2–10 using potentiometry [40] and FETs [41]. The authors successfully demonstrated the reversibility of the charge transfer on the GO surface upon exposure to pH. While the nature of the response has remained unknown, this study has pushed the boundaries toward mono- and diprotic acid potentiometric titration units based on GO.

Herein, we demonstrate the possibility of developing a pH-sensing platform based on various graphene derivatives, including single-layer graphene (SLG), few-layer graphene (FLG), and GO, focusing on the mechanisms by which each of these structures responds to pH. Furthermore, we examine the defect density-dependent pH response of graphene by varying the $-COOH$, $-OH$, and $-NH_2$ concentrations. The results fill the existing gap in understanding the GO pH detection mechanism and creates foundations for developing reagent-free GO pH chemiresistive sensors with a high sensitivity and reproducibility. The results of this study open up a new window into the development of graphene derivative-based pH sensing devices.

2. Materials and Methods

2.1. Single-Layer Graphene Transfer Process

The SLG coated with PMMA was purchased from Graphenea Inc. To fabricate the sensor, the PMMA/SLG/Cu samples were cut into 1 cm \times 1 cm squares and then placed

into 200 mL 0.1 M Ammonium persulfate (APS, purchased from VWR) to etch off the copper film. After about 30 min, the PMMA/SLG samples were transferred to 500 mL DI water to rinse off the remaining APS and transferred on a glass slide (VWR). The samples were first heated to 100 °C for 30 min and then annealed for 2 h at 600 °C under N₂ using a three-heat zone tube furnace (Lindberg Thermodyne 21100). The samples were then immersed in acetone overnight (16 h) to remove the PMMA. The annealing step is essential to achieve minimum PMMA residue on graphene.

2.2. Synthesis of FLG and Sensor Fabrication

Synthesis: The synthesis process of FLG has already been reported elsewhere [42]. Briefly, 40 mg of graphite powder (Alfa Aesar, Haverhill, MA, USA, 99.99%) is mixed with 4.5 mL and 10.5 mL of IPA and DI water, respectively. The mixture is then sonicated for 6 h using an Elmasonic P60H ultrasonic cleaner, 100% power; sweep mode at 37 kHz. Then, the products are centrifuged (Eppendorf MiniSpin Plus microcentrifuge) for 5 min at 14,000 rpm (13,149 × g). Afterward, the supernatant products are collected and centrifuged again for 15 min at the same speed. Lastly, the precipitated products are ordered and used for sensor fabrication.

Sensor fabrication: The frosted sides of the glass slides (VWR VistaVision) were initially rinsed with methanol (Fisher Scientific Canada, HPLC) and patterned by two parallel rectangles drawn by a 9B pencil (Figure 1a). Then, the FLG suspension was airbrushed (e NEO-Iwata CN Gravity Feed Dual Action Brush #N4500) using a nitrogen gas directly on the surface, preheated to 150 °C, until the resistance was measured in the range of 5–10 kΩ (Figure 1b). The copper tape was attached as sensor contacts to the pencil-drawn rectangle/airbrushed sample. To avoid direct exposure of copper tape to aqueous solutions, the contacts were covered by parafilm (Parafilm “M”, VWR). Increasing the temperature to 70 °C (above the melting point of parafilm) leads to a more uniform coverage (Figure 1c). An SEM image of an FLG film deposited for a sensor and the I-V curve characteristics of a typical device are shown in Figure 1d,e, respectively.

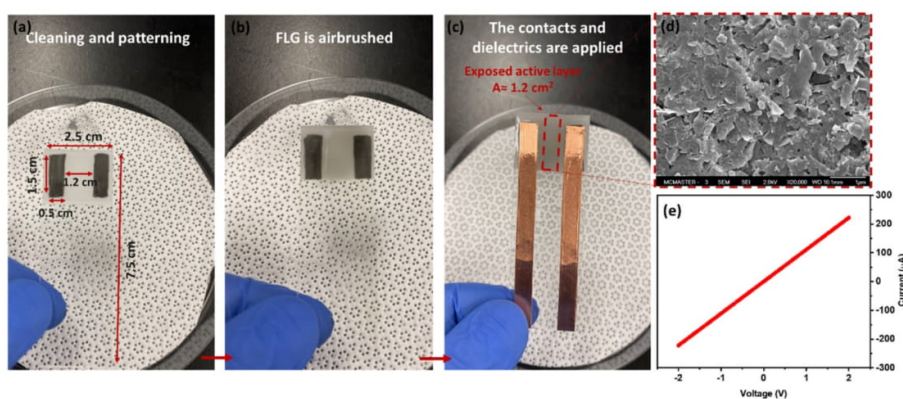


Figure 1. Sensor fabrication steps: (a) Cleaning and prepatterning with pencil-drawn contacts, (b) airbrushing FLG, and (c) attachment of Cu tape and dielectrics. (d) SEM image of the FLG airbrushed on the surface, (e) the I-V curve of the fabricated chemiresistive sensor indicating the ohmic device (sensor resistance was ~10 kΩ).

Annealing: The airbrushed samples were placed into a furnace under the flow of N₂/H₂ (95%/5%) and heated to 500 °C and 350 °C for FLG and GO, respectively. A temperature of 350 °C has been shown as a safe temperature to anneal GO without considerable thermal decompositions or mass loss [43]. The samples are left to cool down gradually overnight in an N₂ atmosphere.

Pyrene derivatives functionalization: Pyrene carboxylic acid (Py-COOH), 1-amino Pyrene (Py-NH₂), and 1-hydroxypyrene (Py-OH) were purchased from Sigma Aldrich and used without further purification. To dope the samples, the fabricated sensors were placed into solutions of the respective pyrene in acetonitrile overnight (~16 h). At the end, the functionalized sensors were rinsed with pure acetonitrile to remove any excess pyrene.

pH measurement experiment: In preparation for the experiments, the devices were initially placed into a 3.42 mM NaCl solution and left overnight to equilibrate with the environment. An initial ionic conductivity above 0.33 mS/cm (equivalent to 3.42 mM NaCl) minimizes possible interferences due to changes in ionic strength when adjusting pH using NaOH (99%-Caledon Laboratories Ltd., ACS reagent) or HCl (37.2%-Caledon Laboratories Ltd., Ahmedabad, India, ACS reagent). The pH of the solution was adjusted by drop-wise addition of NaOH (0.1 M) or HCl (0.1 M) into the system until the desired pH (pH 3 to 9) was achieved. The devices were kept at each pH for 30 min while the current was recorded at intervals of 1 data point every two seconds. The last 60 data points (two minutes) from each step were used for further analysis.

2.3. GO Preparation and SENSOR fabrication

The GO powder was purchased from Zentek Ltd (Canada). Initially, 40 mg of GO was dispersed in 15 mL of ultrapure water and sonicated for 1h. The products were airbrushed on a preheated substrate to 200 °C. If annealing was required, the samples were placed at 350 °C for 24 h under N₂/H₂ (95%/5%) reducing environment. Then, the copper tapes were attached and subsequently covered by parafilm as dielectric (as discussed in Section 2.2).

2.4. Characterization

A Renishaw inVia Raman spectrometer was used to characterize the defect level of the graphene film. A Renishaw 633 nm HeNe laser with 17 mW power output was focused through the 50× objective lens with a spot size of about 1.5 μm. The laser power used for few-layer graphene analysis was 50% to minimize the noise and 5% power for graphene oxide to avoid film damage. The range of the Raman region was from 500 to 3500 cm⁻¹ with a spectral resolution of 2 cm⁻¹. Spectra were recorded in at least two different spots for each sample to ensure reproducibility.

The XPS analyses were carried out with a Kratos AXIS Supra X-ray photoelectron spectrometer using a monochromatic Al K(α) source (15 mA, 15 kV). A charge neutralizer was used on all specimens. Survey scans were collected from an area of 300 × 700 μm² using a pass energy of 160 eV. High-resolution scans used a pass energy of 20 eV. All spectra were charge corrected to the mainline of C 1s (graphitic carbon, 284.5 eV). Spectra were analyzed using CasaXPS software (version 2.3.14).

3. Results and Discussions

3.1. pH Response of Bare Graphene

The response of bare graphene to pH was chosen as a starting point for understanding the impact of surface defectivity. Considering that most liquid-phase exfoliation methods to produce graphene derivatives, including ultrasonication, generate a high degree of defectivity (oxygen content between 10–15%), a defect-free (1–2%) CVD-grown SLG was used as a reference sample to obtain an insight into the response of pure graphene to pH. The SLG's low defectivity was confirmed by the XPS results, as shown in Figure 2. According to the high-resolution O 1s spectra, shown in Figure 2a, the peak at 533 eV is associated with the oxygen doubly bound to C, while the peak at 534.19 eV corresponds to oxygen in the SiO₂ substrate. The nature of oxygen-carbon bonds can be further analyzed using C 1s high-resolution spectra, as shown in Figure 2b. As seen, C-OH/C-O-C, and C=O peaks located at 286.50 and 287.90 eV are the dominant oxygen-based functional groups. The C=O is often interpreted as a result of graphene's ketone, aldehyde, and carboxyl groups [44]. The presence of C-OH indicates the formation of a primary or secondary alcohol and carboxyl groups, and the C-O-C implies the appearance of ether and epoxy

sites on the surface [45]. These results confirm that oxygen-based functional groups are inevitably formed on graphene during the synthesis or transfer process. In this case, the acetone treatment to eliminate the PMMA and subsequent multiple rounds of bathing in DI water could cause this oxidation. Moreover, the possibility of oxygen-containing contaminants (e.g., carboxylic acids, alcohols, aldehydes, etc.) from the environment cannot be neglected. Nevertheless, the O/C atomic ratio of the transferred SLG is calculated at ~ 0.05 , at the lower end of defect density. The atomic percentage of oxygen and carbon in SLG can be found in the XPS survey spectrum shown in Figure S1a.

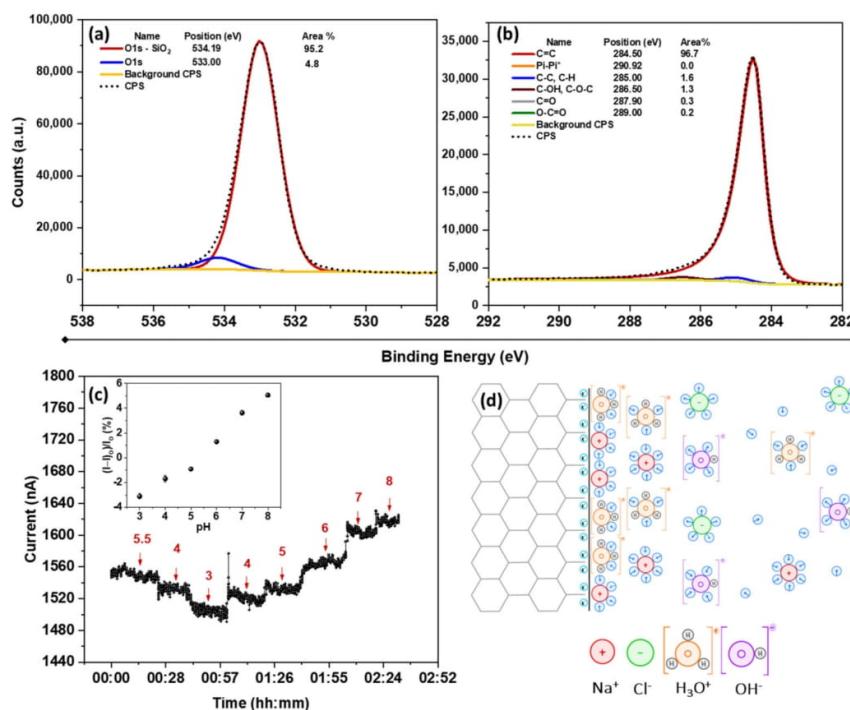


Figure 2. XPS high-resolution spectra of (a) O 1s and (b) C 1s of SLG, (c) pH response of SLG between pH 5.5–8 (the inset shows the corresponding calibration curve) with $I_0 = 1524$ nA, and (d) schematics illustration of the formation of EDL on graphene in acidic solution and its electrostatic gating charging.

The pH response of an SLG chemiresistive device is shown in Figure 2c. The starting pH (5.5) was determined by an equilibrium of the aqueous solution with ambient air, established overnight. Due to the partition of CO_2 from the ambient air into water, the pH of deionized water gradually equilibrates to 5.6, assuming 400 ppm of CO_2 in the air. According to Figure 2c, the current through the SLG is observed to decrease when the pH is reduced to 3, and conversely increased when the pH was raised. The low pH response can be explained by the electrostatic gating effect of $H_3O^+_{aq}$, which n-dopes the surface. Since the holes are the majority carrier in graphene due to the presence of electron-withdrawing oxygen atoms, n-doping the surface reduces the charge carriers in the chemiresistor and makes it more resistive. In contrast, electrostatic p-doping of OH^-_{aq} ions accumulated in the Stern layer increases the current at a high pH [26]. The schematic illustrations of the formation of the electrochemical double layer (EDL) in acidic solutions are shown in Figure 2d. It should be noted that the charge transfers through the formation of the EDL by H_3O^+ and OH^- are considered fully nonfaradaic. Therefore, the charges are electrostatically gated to the graphene surface. This mechanism is well-defined for SLG and is often deemed the typical graphene response to pH. This phenomenon has been studied

in other devices such as FETs [46,47] or Schottky diodes [25], demonstrating the decrease (increase) in Fermi energy upon exposure to a high (low) pH. However, the Fermi energy of SLG is prone to cross the Dirac point upon severe electrostatic doping [48,49]; therefore, it may not be a reliable system to further investigate the role of EDL and defects. Accordingly, the following parts of this research deploy FLG-based chemiresistive devices to explore the role of defects in pH sensitivity.

The transition from SLG to FLG requires a careful surface analysis, considering that a higher number of surface defects and functional groups are formed during the liquid-phase exfoliation method. The XPS survey spectrum of the synthesized FLG (Figure S1b) shows 13.9 at% of O and 79.5 at% of C. The O 1s high-resolution spectra (Figure 3a) show a peak at 532.4 eV attributed to trapped water and organic oxygen groups. The larger area of the peaks at 289.0 eV (O-C=O), 287.0 eV (C=O), and 286.5 eV (C-OH, C-O-C) in the C 1s high-resolution spectrum of the FLG compared to the SLG (Figure 3b) exhibit a higher oxygen content in the FLG lattice. Accordingly, the O/C ratio was calculated to be 0.24 by considering the areas of the C=C (284.5 eV) and O 1s (532.4 eV) features in the high-resolution spectra multiplied by their corresponding atomic percentages derived from the survey spectra. A summary of the oxygen-based functional groups in the SLG and FLG can be found in Table 1, demonstrating the greater defectivity of the FLG compared to SLG.

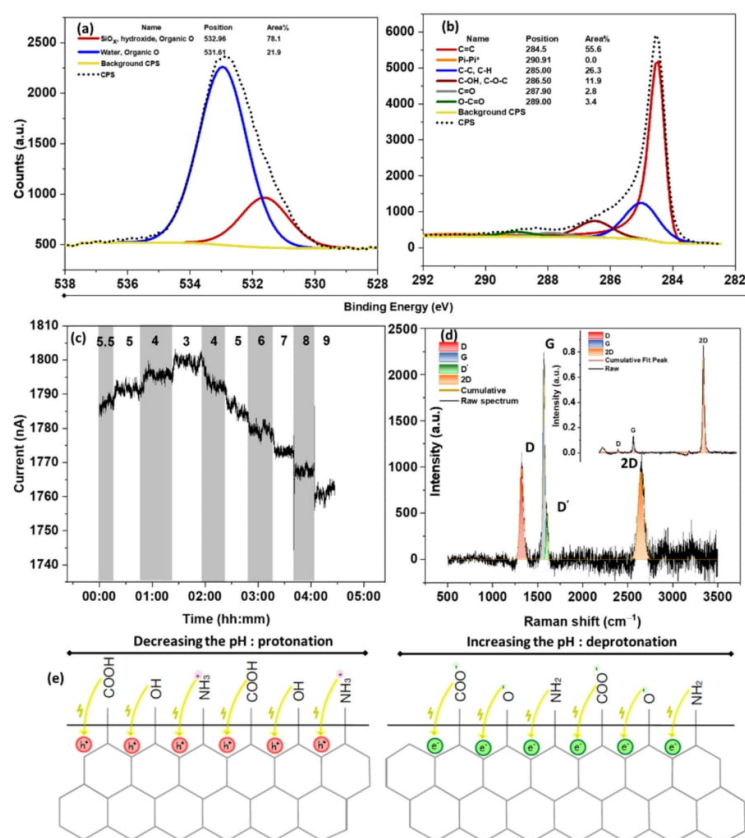


Figure 3. XPS high-resolution spectra of (a) O 1s and (b) C 1s of FLG, (c) pH response of FLG to pH 5.5–9 ($I_0 = 1788$ nA), (d) Raman of FLG deconvoluted to the main graphene characteristics of D, G, D', and 2D (inset shows the deconvoluted Raman spectrum of SLG), and (e) schematic illustration of defect-induced pH response of FLG through protonation/deprotonation of carboxyl, hydroxyl, and amine groups.

Table 1. Summary of the oxygen-containing groups obtained from XPS spectra of SLG and FLG.

	SLG			FLG		
	Area %	at% *	Ratio to C=C at%	Area %	at% *	Ratio to C=C at%
C=O	0.3	0.1119	0.003074	2.8	2.22	0.05
O-C=O	0.2	0.0746	0.002049	3.4	2.70	0.061
C-OH/O-C-O	1.3	0.4849	0.01332	11.9	9.46	0.214

* Atomic percentage is obtained by Area \times total atomic percentage.

To explore the impact of the enhanced defectivity on the pH response, the chemiresistive response of the FLG is shown in Figure 3c. As seen, the current response to the variation in pH is entirely reversed compared to the SLG (Figure 2c), indicating that the dominant pH response mechanism is different. This means that decreasing the pH reduces the current, while increasing the pH toward the basic solution increases n-doping. We have recently shown that the defect-induced pH response of graphene originates from the protonation/deprotonation of carboxyl and amine at a low pH and hydroxyl groups at a high pH [26]. For example, in carboxyl groups, upon decreasing the pH to 3 (below the $pK_a = 3.1$), the $-\text{COO}^-$ is protonated to $-\text{COOH}$, and the surface becomes p-doped. The same concept can be applied to the protonation of $-\text{NH}_2$ to $-\text{NH}_3^+$ and the protonation of $-\text{O}^-$ to $-\text{OH}$ at a pH around 3.7 and 8.2, respectively. Since this charge is transferred directly to the surface, the protonation causes p-doping, while deprotonation results in n-doping, giving an exact opposite behavior to the EDL-induced response. Apart from the defect-induced response, H_3O^+ ions have also been shown to enter the gaps between FLG flakes at a low pH. This proton injection in FLG can be confirmed by the blue shift of the 2D peak in the Raman spectra of FLG after the pH exposure (Figure S2). This result could be explained by the Faradaic charge transfer upon proton injection and p-doping of the graphene by lowering its Fermi energy [32,50]. This phenomenon becomes dominant when a porous structure is present [51] (e.g., porous graphitic electrodes in supercapacitors) [50]. Therefore, it is expected to observe a rise in conductance at low pH where H_3O^+ is present, mainly close to the surface. Accordingly, the main 2D peak of the FLG spectra (shown in Figure S2) shifts due to the lattice parameter modification by the stiffening/softening of the phonons–charge carrier interactions [52].

The defectivity level can also be estimated by Raman spectroscopy. The FLG (Figure 3d) and SLG (Figure 3d-inset) both exhibit the three main Raman characteristics of graphene, namely D, G, and 2D bands [53]. The D band stands for the presence of sp^3 -hybridized environments, generated mainly by defects. The G band, however, represents the sp^2 hybridization of the graphene lattice. Thus, the ratio of intensity (or area) of D to G qualitatively characterizes the defectivity level of the structure. Accordingly, the I_D/I_G of the SLG is calculated at 0.11, while the FLG shows 0.43, supporting the XPS results. These values can also be well-fitted to previously published reports that low defect density graphene (less than a cross-over point of $I_D/I_G \sim 0.35$) demonstrates positive pH sensitivity (Figure 2c, inset), while the higher I_D/I_G ratio results in inverted pH sensitivity. It should be mentioned that the positive and negative sensitivities are defined relative to the variation of the current with the pH. This cross-over is where the graphene will become pH insensitive. The schematic illustration of such a protonation/deprotonation mechanism can be seen in Figure 3e.

3.2. Selective Functionalization of Graphene

Knowing that the type and density of the defects in graphene derivatives determine their pH response, the development of a pH-sensitive device can be achieved by selective functionalization. For this purpose, noncovalently attached pyrene derivatives with various pH-sensitive functional groups were employed as a model system to resemble the graphene surface terminated with pH-sensitive groups [26]. The charge transfer upon

protonation/deprotonation of the functional groups is directly transduced to the FLG [46] via the interactions of the π -electron system of the pyrene ring with the FLG surface [54]. The maximum concentration of each pyrene derivative was chosen to give more than 90% surface coverage [55]. Moreover, the low pyrene solubility in water aids in the stability of the functionalization. However, to minimize the impact of the pre-existing defects of the FLG on pyrene functionalization, it is necessary to anneal the FLG samples under a reducing environment to eliminate the functionalities. The Raman spectra of the FLG before (Figure 3d) and after (Figure S3) annealing demonstrate the effective surface defect reduction, decreasing the I_D/I_G from 0.43 to 0.2. This surface defect reduction can be further confirmed by the pH response of the annealed samples (Figure S4). It is observed that the pH–current relationship is inverted compared to the bare (unannealed) FLG, rather more like the SLG (see Figure S5 for the calibration curve). This phenomenon demonstrates that the FLG has been annealed to a low defect state where the EDL response is dominant.

Figure 4 displays how the variation of carboxyl group concentration on graphene affects the pH response of a chemiresistive device. The sample exposed to 0.3 M Py-COOH (Figure 4a) demonstrates a selective response to the pH of around 3, giving a current change of $\sim 55\%$ ($-21.58\%/pH$). This response is considered significant compared to the other graphene devices, where the maximum response barely exceeds 20% (see Figures 2c and 3c). The low pH sensitivity of the device at a high pH could be due to two simultaneous factors: (i) the annealing before pyrene functionalization has successfully eliminated the responsive functional groups, or (ii) the pyrene molecules have passivated the existing groups and defects. Notably, the pH sensitivity of the device to a pH range of 3–4 decreases upon reduction of the pyrene concentration to 0.15 mM ($-12.31\%/pH$) and 0.1 mM ($-2.11\%/pH$), as shown in Figure 4b,c, respectively. With doping concentrations around 0.05 mM (Figure 4d), a pH-insensitive platform ($-0.2\%/pH$, Figure 4e, inset) is obtained, indicating the response due to carboxyl groups is balanced out by the response due to electrostatic gating by the EDL. The calibration curves representing the pH sensitivities are shown in Figure 4e. Although it is not easy to accurately measure the defect density of the -COOH group added to the surface, an estimate can be arrived at by making two assumptions: (i) the FLG film is flat with minimum surface roughness; (ii) a monolayer of molecules forms during functionalization. The last assumption has already been validated experimentally and can be considered realistic based on the selected concentrations in Table S1 [55]. Using these assumptions, and considering that each Py-COOH carries one carboxyl group, the approximate surface density of -COOH defects can be estimated:

$$\text{Surface density} = \frac{SC_{Rel}}{A_{Pyrene}}$$

where SC_{Rel} is the relative surface coverage of pyrene derivatives obtained from the literature [54,55], as shown in Table S1, and A_{Pyrene} is the area occupied by a single molecule of the respective pyrene derivative. The plot of the maximum pH response of the FLG as a function of the carboxyl group is shown in Figure 5a. Notably, the linear trend is not observed, and a carboxyl group density $\sim 5.36 \times 10^{13} \text{ cm}^{-2}$ is estimated to be where the EDL becomes dominant. The nonlinear dependence of the maximum response to the carboxyl group surface density confirms that the pH response is not exclusively determined by the functional group mechanism. It should also be noted that any sensing data above the maximum concentration of Py-COOH (0.3 mM) may not be valid due to exposure of the FLG to a concentrated solution that may contain dimers or stacked molecules, leading to an invalidation of the above-noted assumption that only a monolayer of molecules is formed [53,54]. The detailed information of the data shown in Figures 4e and 5 have been provided in Tables S2 and S3, respectively.

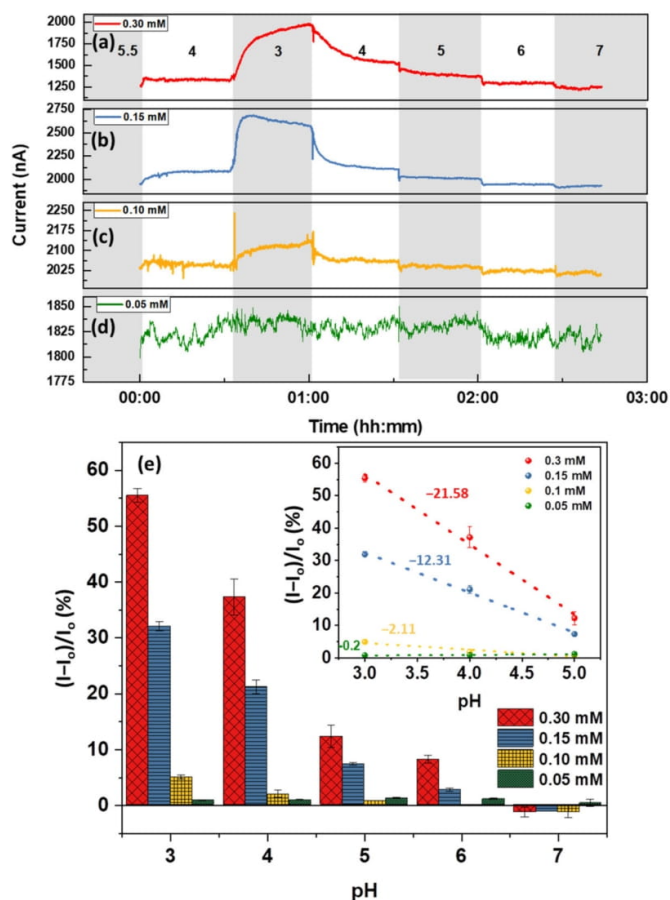


Figure 4. Sensing performance of 8 h annealed FLG functionalized by (a) 0.3 mM ($I_0 = 1274$ nA), (b) 0.15 mM ($I_0 = 1980$ nA), (c) 0.1 mM ($I_0 = 2052$ nA), and (d) 0.05 mM ($I_0 = 1812$ nA) of Py-COOH; (e) the calibration bar graph of the sensors demonstrating the highest pH response at around $-\text{COOH}$ pK_a (3.1). The error bars represent average \pm standard deviation of the last two minutes of the chemiresistive response (3 samples each).

Similar results can be obtained by using Py-NH₂, resembling amine groups of the FLG (see Figure 5b). The current increase at a pH of around 3–4 can be interpreted as the protonation of $-\text{NH}_2$ to $-\text{NH}_3^+$ and the p-doping of the surface. Remarkably, the highest concentration of Py-NH₂ (1.4 mM) does not lead to the maximum pH response of the surface (Figure 6a–d); this occurs at concentrations of around 0.7 mM, giving a maximum pH response of 6.8% (Figure 6e). Moreover, Figures 5b and 6e both reveal two phenomena: (i) 0.1 mM Py-NH₂, equivalent to a surface density of $\sim 5.35 \times 10^{13} \text{ cm}^{-2}$ for $-\text{NH}_2$ groups, is not sufficient to overcome the EDL response of the surface, so that a maximum negative response of $\sim -4.5\%$ is obtained; (ii) at 0.35 mM (equivalent to $1.5 \times 10^{14} \text{ cm}^{-2}$), a response of the device to both pH 3 and 4 is considerable, demonstrating that the lower surface coverage of Py-NH₂ may expose the leftover carboxyl group from the annealing process. It should be noted that the maximum response to pH drops from 3.1% to 2.7%, corresponding to 1.4 mM and 0.7 mM, respectively. Therefore, as expected, lower Py-NH₂ exposure leads to a lower response to a pH of 3. However, this trend is violated below 0.7 mM, equivalent to the surface density of $2.68 \times 10^{14} \text{ cm}^{-2}$. One possible mechanism for the lower pH response of the high amine concentration could be an amide formation reaction between $-\text{NH}_2$ and $-\text{COOH}$ of the surface. Upon these reactions, C in R-COOH is reduced to R-

CONH₂, n-doping the surface. This n-doping counteracts the p-doping of the protonation and leads to a lower response.

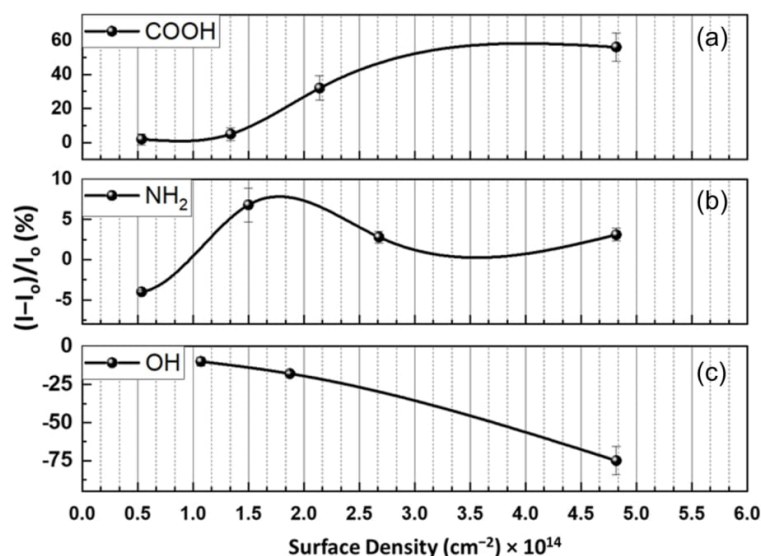


Figure 5. Variation of FLG pH sensitivity as a function of (a) carboxyl, (b) amine, and (c) hydroxyl defect densities. The error bars represent average \pm standard deviation of the last two minutes of the chemiresistive response (3 samples each).

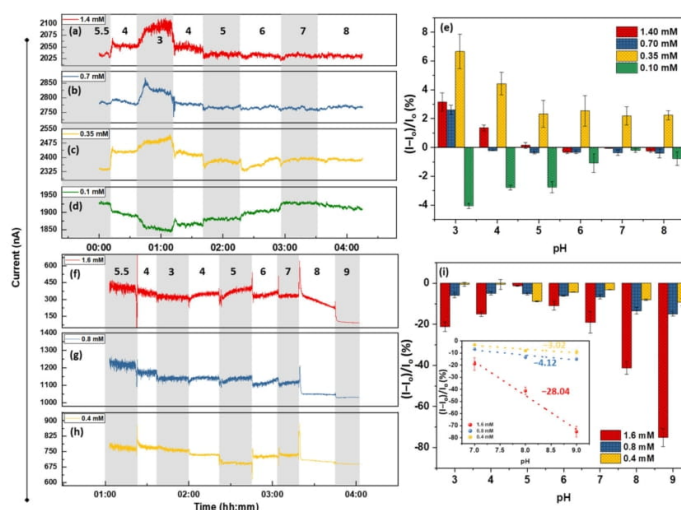


Figure 6. Sensing performance of 8 h annealed FLG functionalized by (a) 1.4 mM ($I_0 = 2035$ nA), (b) 0.7 mM ($I_0 = 2775$ nA), (c) 0.35 mM ($I_0 = 2330$ nA), and (d) 0.1 mM ($I_0 = 1927$ nA) of Py-NH₂. (e) Graph represents the calibration curve of the Py-NH₂-functionalized sensors. The sensing performance of 8 h annealed FLG functionalized with (f) 1.6 mM ($I_0 = 385$ nA), (g) 0.8 mM ($I_0 = 1220$ nA), and (h) 0.4 mM ($I_0 = 764$ nA) of Py-OH. (i) The calibration bar graph of the sensors demonstrating the maximum pH response at pH around -OH pKa (8.7). The error bars represent average \pm standard deviation of the last two minutes of the chemiresistive response (3 samples each).

The pH responses of the Py-OH-functionalized FLG at three different concentrations of 1.6, 0.8, and 0.4 mM are presented in Figure 6. The device pH response is dominated by the

protonation/deprotonation of the $-O^-/-OH$ groups at a high pH ($pK_a = 8.7$). Accordingly, the current drop at a pH of 9 of Figure 6f–h is due to this phenomenon. The corresponding calibration curves demonstrate that the device response to a pH of 7–9 is proportional to the $-OH$ concentration and the density, so that a pH of 7–9 and sensitivity of 1.6, 0.8, and 0.4 mM can be calculated for -28.04 , -4.12 , and $-3.02\%/pH$, respectively (Figure 6i, inset). Furthermore, the sensing behavior of the OH-functionalized FLG can be further analyzed: from a pH of 5.5 down to 3 and back up to 7, the device resembles the annealed FLG, while at a pH of 8 or above, it responds with OH groups. This manifestation reveals that even one sensor can respond differently at different pH ranges, depending on the dominant pH-sensing mechanisms. This result can be further confirmed by the significant impact of the high $-OH$ concentration on the pH response, leading to an almost -75% response to a pH of 9 when the surface defect density is $1.07 \times 10^{14} \text{ cm}^{-2}$ (Figure 5c). The detailed information of Figure 6e,i can be found in Tables S4 and S5, respectively.

3.3. pH Response of GO and Its Application towards the Development of GO-Based pH Sensors

Based on the discussion above, enhancing graphene defectivity leads to a more defect-induced response and higher sensitivity. Therefore, highly defective graphene derivatives such as GO, carrying various surface/edge functional groups, are expected to be a worthwhile platform to study. The Raman spectrum of the GO with overlapping D and G bands is shown in Figure S6, demonstrating a Raman spectrum consistent with the literature. The Lorentzian deconvolution of the spectrum reveals the presence of multiple subpeaks under the curves, demonstrating an I_D/I_G ratio of 1.74. The significant overlap of the D' and G bands are also due to the enhanced intervalley scattering in the high defect region. Even though the presence of D^{**} at 1479 cm^{-1} is often indicative of disordered carbons (amorphous), it could be due to the cumulative scattering of C=C stretching in sp^2 regions and the C-H wagging modes in a nanocrystalline diamond [56,57]. The higher defect density can enhance the GO pH sensitivity for aqueous solution applications. However, the stability of GO in water becomes an issue upon its exposure to aqueous solutions. The higher degree of local surface charges caused by functional groups decreases the GO water contact angle, increasing the GO dispersibility. The instability of GO-based chemiresistive device upon exposure to water can be seen in Figure 7a(1–3). Figure 7a(1) shows the airbrushed GO on the glass slide, and (b and c) display the same sensor after exposure to an aqueous solution after 30 and 60 min of exposure, respectively. This means that the delamination of the active layer of GO-based chemiresistors (Figure 7a(3)) limits their stability to less than 30 min. Moreover, the semiconductive nature of GO causes a high film resistance, which is impractical as a conductive active layer. Therefore, despite the remarkable properties of GO, it cannot be used as the active layer in a sensor in its pristine form.

To prevent disintegration, the GO samples were annealed at $350 \text{ }^\circ\text{C}$ under a reducing environment [43]. Exposure of GO to temperatures above $450 \text{ }^\circ\text{C}$ should either be done in vacuum systems or under a high flow of inert gas to avoid thermal decomposition [58]. This annealing treatment results in a visible color change from brown (Figure 7a(3)) to gray (Figure 7a(5–7)), indicating the successful reduction of the GO.

A comparison of the I_D/I_G ratio of pristine GO (Figure S6) with that of the 24 h annealed GO (Figure 7b) confirms an increase in surface sp^2 hybridization. However, due to the surface-insensitive nature of the Raman measurement, the obtained $I_D/I_G = 1.3$ (Figure 7b) indicates that a considerable number of defects still remain in the bulk. The low-temperature annealing of GO assists in the formation of a stable conductive GO film, while the intrinsic characteristics are preserved. It should be noted that the thermal annealing (reducing) of GO results in a more uniform and well-controlled product as compared to the chemically reduced GO [59]. Moreover, the $I_D/I_G = 1.3$ obtained from the 24 h-GO reveals that only a surface reduction has occurred, and the term reduced GO is not applied here.

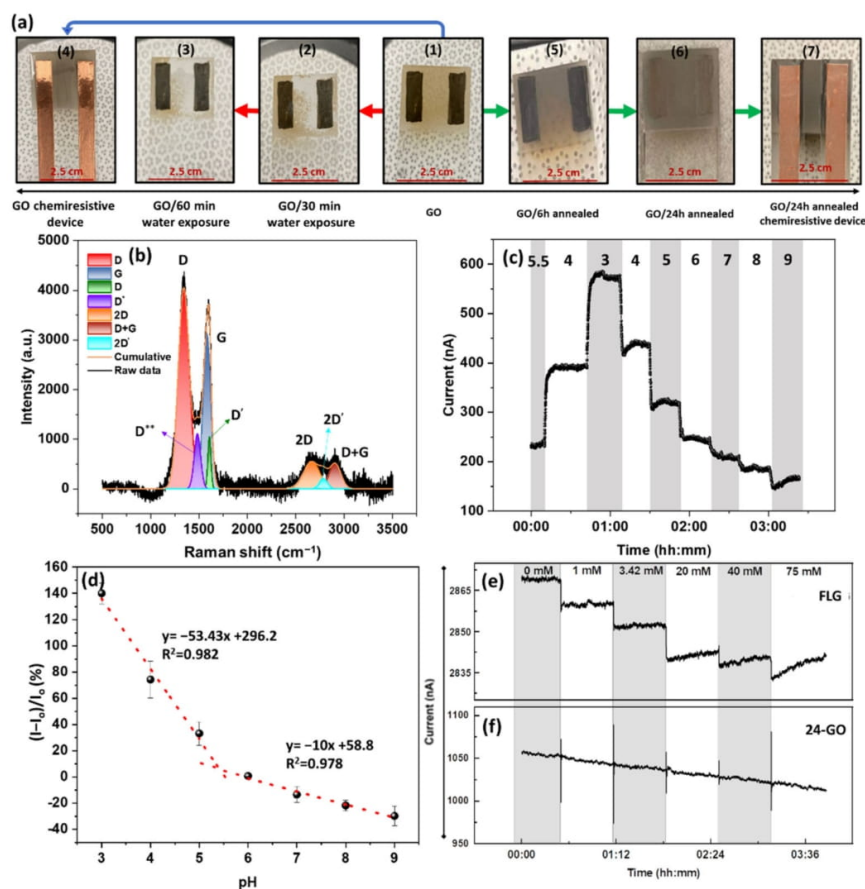


Figure 7. (a) The GO sensor fabrication: (1) Bare GO; (2) Bare GO exposed to the aqueous solution for 30 min; (3) Bare GO exposed to the aqueous solution for 6 min; (4) tTe GO chemiresistor without water exposure; (5) GO annealed for 6 h and (6) 26 h; (7) The 24 h annealed GO-based chemiresistor. (b) Deconvoluted Raman spectrum of 24 h-GO represents the presence of (from left to right): D, D*, G, D', 2D, 2D', D + G, and an I_D/I_G ratio of 1.3. (c) The pH response and (d) calibration curve of 24 h-GO (I₀ = 242 nA). The solution conductivity response of (e) FLG (I₀ = 2870 nA) and (f) 24 h-GO-based devices (I₀ = 1050 nA).

The chemiresistive pH response of the 24 h annealed GO (24 h-GO) is shown in Figure 7c. Notably, the stepwise variation of the current in the 24 h-GO resembles the FLG response; however, the magnitude of the response is much higher. According to the calibration curve shown in Figure 7d, a more than 140% change in the current is obtained by changing the pH from 5.5 to 3, leading to a total response of 175% from a pH from 3 to 9. In order to allow for a calculation of sensitivity despite the overall nonlinear response, the working performance of the device is divided into low (3–5) and high (6–9) pH ranges. The selection of these two regimes is not arbitrary. The low range is chosen based on the pH response of -COOH and -NH₂, while the latter is based on the pH response of -OH groups. Accordingly, the low range offers a sensitivity of -53.4%/pH. In contrast, the high range sensitivity is calculated as -10%/pH. This difference in sensitivity is due to the highly favorable formation of -COOH during the GO synthesis and the dominant response of the carboxyl groups. Notably, the initial formation of -OH upon the oxidation of graphene to GO could subsequently produce -COOH through the two-step oxidations of hydroxyl → aldehyde → carboxyl [60].

As one of the possible interferences for the pH measurement is the ionic strength of the solution, the performances of the FLG and the 24 h-GO were measured against the changing the solution conductivity. For this purpose, NaCl was used to adjust the solution conductivity, giving up to 7.25 mS/cm for 75 mM. As seen in Figure 7e, the addition of NaCl gives rise to a small stepwise reduction of the current in the FLG. The mechanism justifying this behavior originates from the formation of an EDL on the SLG or FLG due to the long-range arrangement of Na⁺ ions in the Stern layer. Therefore, the electrostatic gating charge screening is the primary mechanism, and the addition of Na⁺_{aq} induces negative charges in the FLG. In contrast, the addition of NaCl does not affect the current through the GO film, and a prolonged drift in current is observed (Figure 7f). The cause of this drift is unclear at this point but could be due to a number of reported effects, including interactions of sodium ions with the oxygen sites over time [61] or variations in the concentrations of dissolved gases (such as CO₂ or O₂) as a function of the ionic strength [62]. After drift correction, however, there is no discernible response of the devices to ionic strength. In fact, the EDL response is negligible compared to the high density of defects present in GO-based devices; therefore, they exhibit an inherent potential for the selective detection of pH.

4. Conclusions

We have reported the development of a highly pH-sensitive platform based on thermally annealed GO for next-generation sensing devices. To understand the sensing principle of the proposed platform, we established the pH detection mechanisms of the two most commonly used graphene derivatives (i.e., single-layer and few-layer graphene). The contrast in pH responses of the former as a defect-free model ($I_D/I_G \sim 0.1$, O/C ratio = 0.05), with the latter having a degree of defectivity ($I_D/I_G \sim 0.43$, O/C = 0.24), elucidates the importance of defects in pH-sensing graphene. Therefore, the selective functionalization of graphene using various pH-sensitive functional groups demonstrates graphene's defect density dependence on pH response. An approximate surface density of $4.82 \times 10^{14} \text{ cm}^{-2}$ of the carboxyl group on graphene leads to a 55% response with an $-21.58\%/pH$ sensitivity for a pH of 3–5. The exact same surface density of the -OH groups, however, results in a -75% change in the current, leading to a sensitivity of $-28.04\%/pH$ for a pH of 9–7. To develop a GO-based pH-sensitive platform, we demonstrated the importance of the surface reduction treatment at a relatively low temperature (350 °C) to enhance its durability for long-term operation while retaining its high defectivity. As a result, a pH-sensitive device with a maximum current change of 175% (from a pH of 3–9) was reported, giving the sensitivity of -53.43 and $-10\%/pH$ pertaining to the pH range of 3–5 and 6–9, respectively. The proposed platform demonstrates minimum interference with ionic conductivity due to the dominance of the defects and offers a reagent-free pH-sensitive substrate for future pH devices.

Supplementary Materials: The following supporting information can be downloaded at: <https://www.mdpi.com/article/10.3390/nano12111801/s1>, Figure S1: XPS survey spectra of Single layer graphene and few layer graphene; Figure S2: Raman spectra of few layer graphene before and after exposure to pH; Figure S3: Raman spectrum of 8h annealed few layer graphene; Figure S4: pH response of 8h annealed few layer graphene; Figure S5: calibration curve of the pH response of 8h annealed few layer graphene; Figure S6: the Lorentzian deconvolution of GO Raman spectrum; Table S1: Summary of information on Pyrene concentrations and their corresponding relative surface coverage obtained from literature; Table S2: average \pm Standard deviation of Py-COOH functionalized sensors to pH range 3-8 (3 sensors each); Table S3: average \pm standard deviation of maximum response of pyrene derivative functionalized sensors as a functional surface density (3 sensors each); Table S4: average \pm standard deviation of Py-NH₂ functionalized sensors to pH range 3-8 (3 sensors each); Table S5: average \pm standard deviation of Py-OH functionalized sensors to pH range 3-9 (3 sensors each) [63–65].

Author Contributions: S.A. wrote and prepared the manuscript for submission and was involved in planning the experiments; X.H. performed the experiments and measurements; L.H. performed the experiments and contributed to the discussions of the contents; M.A.A. contributed to the discussions

of the contents; P.R.S. contributed to the conceptualization, writing, and review; P.K. supervised the manuscript and contributed to conceptualization, methodology, writing, review, and editing. All authors have read and agreed to the published version of the manuscript.

Funding: The authors acknowledge financial support from the Natural Sciences and Engineering Research Council of Canada (NSERC) through the Discovery Grant Program (RGPIN06145-18).

Acknowledgments: The authors thank Doris Stevanovic from the Centre for Emerging Device Technologies (CEDT), McMaster University, for granting access to the furnace; Alex Adronov (McMaster) for giving access to a Raman spectrometer; Mark Biesinger (Surface Science Western) for the XPS operation and data analysis.

Conflicts of Interest: The authors declare no conflict of interest.

References

1. Casey, J.R.; Grinstein, S.; Orłowski, J. Sensors and Regulators of Intracellular PH. *Nat. Rev. Mol. Cell Biol.* **2009**, *11*, 50–61. [[CrossRef](#)] [[PubMed](#)]
2. Posadas, E.; del Morales, M.M.; Gomez, C.; Ación, F.G.; Muñoz, R. Influence of PH and CO₂ Source on the Performance of Microalgae-Based Secondary Domestic Wastewater Treatment in Outdoors Pilot Raceways. *Chem. Eng. J.* **2015**, *265*, 239–248. [[CrossRef](#)]
3. Kasi, V.; Sedaghat, S.; Alcaraz, A.; Kannan Maruthamuthu, M.; Heredia-Rivera, U.; Nejati, S.; Nguyen, J.; Rahimi, R. Low-Cost Flexible Glass-Based PH Sensor via Cold Atmospheric Plasma Deposition. *ACS Appl. Mater. Amp Interfaces* **2022**, *14*, 9697–9710. [[CrossRef](#)] [[PubMed](#)]
4. Wiora, A.; Wiora, J. Over One-Year Long-Term Laboratory Tests of PH Electrodes in Terms of Industrial Applications Checking Stabilities of Their Parameters and Their Influence on Uncertainties of Measurements. *Sensors* **2018**, *18*, 4102. [[CrossRef](#)] [[PubMed](#)]
5. Spijkman, M.-J.; Brondijk, J.J.; Geuns, T.C.T.; Smits, E.C.P.; Cramer, T.; Zerbetto, F.; Stoliar, P.; Biscarini, F.; Blom, P.W.M.; de Leeuw, D.M. Dual-Gate Organic Field-Effect Transistors as Potentiometric Sensors in Aqueous Solution. *Adv. Funct. Mater.* **2010**, *20*, 898–905. [[CrossRef](#)]
6. Bartic, C.; Palan, B.; Campitelli, A.; Borghs, G. Monitoring PH with Organic-Based Field-Effect Transistors. *Sens. Actuators B Chem.* **2002**, *83*, 115–122. [[CrossRef](#)]
7. Ghoneim, M.T.; Nguyen, A.; Dereje, N.; Huang, J.; Moore, G.C.; Murzynowski, P.J.; Dagdeviren, C. Recent Progress in Electrochemical PH-Sensing Materials and Configurations for Biomedical Applications. *Chem. Rev.* **2019**, *119*, 5248–5297. [[CrossRef](#)]
8. Chen, Y.; Mun, S.C.; Kim, J. A Wide Range Conductometric PH Sensor Made With Titanium Dioxide/Multiwall Carbon Nanotube/Cellulose Hybrid Nanocomposite. *IEEE Sens. J.* **2013**, *13*, 4157–4162. [[CrossRef](#)]
9. Avolio, R.; Grozdanov, A.; Avella, M.; Barton, J.; Cocca, M.; de Falco, F.; Dimitrov, A.T.; Errico, M.E.; Fanjul-Bolado, P.; Gentile, G.; et al. Review of PH Sensing Materials from Macro- to Nano-Scale: Recent Developments and Examples of Seawater Applications. *Crit. Rev. Environ. Sci. Technol.* **2022**, *52*, 979–1021. [[CrossRef](#)]
10. Magnusson, E.B.; Halldorsson, S.; Fleming, R.M.T.; Leosson, K. Real-Time Optical PH Measurement in a Standard Microfluidic Cell Culture System. *Biomed. Opt. Express* **2013**, *4*, 1749. [[CrossRef](#)]
11. Wencel, D.; Kaworek, A.; Abel, T.; Efremov, V.; Bradford, A.; Carthy, D.; Coady, G.; McMorro, R.C.N.; McDonagh, C. Optical Sensor for Real-Time PH Monitoring in Human Tissue. *Small* **2018**, *14*, 1803627. [[CrossRef](#)] [[PubMed](#)]
12. Goldcamp, M.J.; Conklin, A.; Nelson, K.; Marchetti, J.; Brashear, R.; Epure, E. Inexpensive and Disposable PH Electrodes. *J. Chem. Educ.* **2010**, *87*, 1262–1264. [[CrossRef](#)]
13. Takeshita, Y.; Martz, T.R.; Johnson, K.S.; Dickson, A.G. Characterization of an Ion Sensitive Field Effect Transistor and Chloride Ion Selective Electrodes for PH Measurements in Seawater. *Anal. Chem.* **2014**, *86*, 11189–11195. [[CrossRef](#)]
14. Shao, Y.; Ying, Y.; Ping, J. Recent Advances in Solid-Contact Ion-Selective Electrodes: Functional Materials, Transduction Mechanisms, and Development Trends. *Chem. Soc. Rev.* **2020**, *49*, 4405–4465. [[CrossRef](#)] [[PubMed](#)]
15. Vonau, W.; Guth, U. PH Monitoring: A Review. *J. Solid State Electrochem.* **2006**, *10*, 746–752. [[CrossRef](#)]
16. Kim, D.-M.; Cho, S.J.; Cho, C.-H.; Kim, K.B.; Kim, M.-Y.; Shim, Y.-B. Disposable All-Solid-State PH and Glucose Sensors Based on Conductive Polymer Covered Hierarchical AuZn Oxide. *Biosens. Bioelectron.* **2016**, *79*, 165–172. [[CrossRef](#)]
17. Novoselov, K.S.; Geim, A.K.; Morozov, S.V.; Jiang, D.; Zhang, Y.; Dubonos, S.V.; Grigorieva, I.V.; Firsov, A.A. Electric Field Effect in Atomically Thin Carbon Films. *Science* **2004**, *306*, 666–669. [[CrossRef](#)]
18. Novoselov, K.S.; Mishchenko, A.; Carvalho, A.; Castro Neto, A.H. 2D Materials and van Der Waals Heterostructures. *Science* **2016**, *353*. [[CrossRef](#)]
19. Angizi, S.; Akbar, M.A.; Darestani-Farahani, M.; Kruse, P. Review—Two-Dimensional Boron Carbon Nitride: A Comprehensive Review. *ECS J. Solid State Sci. Technol.* **2020**, *9*, 083004. [[CrossRef](#)]
20. Hatamie, A.; Rahmati, R.; Rezvani, E.; Angizi, S.; Simchi, A. Yttrium Hexacyanoferrate Microflowers on Freestanding Three-Dimensional Graphene Substrates for Ascorbic Acid Detection. *ACS Appl. Nano Mater.* **2019**, *2*, 2212–2221. [[CrossRef](#)]

21. Rezvani, E.; Hatamie, A.; Berahman, M.; Simchi, M.; Angizi, S.; Rahmati, R.; Kennedy, J.; Simchi, A. Synthesis, First-Principle Simulation, and Application of Three-Dimensional Ceria Nanoparticles/Graphene Nanocomposite for Non-Enzymatic Hydrogen Peroxide Detection. *J. Electrochem. Soc.* **2019**, *166*, H3167–H3174. [[CrossRef](#)]
22. Wehling, T.O.; Novoselov, K.S.; Morozov, S.V.; Vdovin, E.E.; Katsnelson, M.I.; Geim, A.K.; Lichtenstein, A.I. Molecular Doping of Graphene. *Nano Lett.* **2008**, *8*, 173–177. [[CrossRef](#)] [[PubMed](#)]
23. Zubiarraín-Laserna, A.; Angizi, S.; Akbar, M.A.; Divigalpitiya, R.; Selvaganapathy, P.R.; Kruse, P. Detection of Free Chlorine in Water Using Graphene-like Carbon Based Chemiresistive Sensors. *RSC Adv.* **2022**, *12*, 2485–2496. [[CrossRef](#)]
24. Castro Neto, A.H.; Guinea, F.; Peres, N.M.R.; Novoselov, K.S.; Geim, A.K. The Electronic Properties of Graphene. *Rev. Mod. Phys.* **2009**, *81*, 109–162. [[CrossRef](#)]
25. Angizi, S.; Selvaganapathy, P.R.; Kruse, P. Graphene-Silicon Schottky Devices for Operation in Aqueous Environments: Device Performance and Sensing Application. *Carbon* **2022**, *194*, 140–153. [[CrossRef](#)]
26. Angizi, S.; Yu, E.Y.C.; Dalmieda, J.; Saha, D.; Selvaganapathy, P.R.; Kruse, P. Defect Engineering of Graphene to Modulate pH Response of Graphene Devices. *Langmuir* **2021**, *37*, 12163–12178. [[CrossRef](#)] [[PubMed](#)]
27. Leenaerts, O.; Partoens, B.; Peeters, F.M. Water on Graphene: Hydrophobicity and Dipole Moment Using Density Functional Theory. *Phys. Rev. B* **2009**, *79*, 235440. [[CrossRef](#)]
28. Taherian, F.; Marcon, V.; van der Vegt, N.F.A.; Leroy, F. What Is the Contact Angle of Water on Graphene? *Langmuir* **2013**, *29*, 1457–1465. [[CrossRef](#)]
29. Angizi, S.; Hatamie, A.; Ghanbari, H.; Simchi, A. Mechanochemical Green Synthesis of Exfoliated Edge-Functionalized Boron Nitride Quantum Dots: Application to Vitamin C Sensing through Hybridization with Gold Electrodes. *ACS Appl. Mater. Interfaces* **2018**, *10*, 28819–28827. [[CrossRef](#)]
30. Angizi, S.; Shayeganfar, F.; Azar, M.H.; Simchi, A. Surface/Edge Functionalized Boron Nitride Quantum Dots: Spectroscopic Fingerprint of Bandgap Modification by Chemical Functionalization. *Ceram. Int.* **2020**, *46*, 978–985. [[CrossRef](#)]
31. Tehrani, Z.; Whelan, S.P.; Mostert, A.B.; Paulin, J.V.; Ali, M.M.; Ahmadi, E.D.; Graeff, C.F.O.; Guy, O.J.; Gethin, D.T. Printable and Flexible Graphene PH Sensors Utilising Thin Film Melanin for Physiological Applications. *2D Mater.* **2020**, *7*, 024008. [[CrossRef](#)]
32. Jung, S.-H.; Seo, Y.-M.; Gu, T.; Jang, W.; Kang, S.-G.; Hyeon, Y.; Hyun, S.-H.; Lee, J.-H.; Whang, D. Super-Nernstian PH Sensor Based on Anomalous Charge Transfer Doping of Defect-Engineered Graphene. *Nano Lett.* **2021**, *21*, 34–42. [[CrossRef](#)] [[PubMed](#)]
33. Salvo, P.; Melai, B.; Calisi, N.; Paoletti, C.; Bellagambi, F.; Kirchhain, A.; Trivella, M.G.; Fuoco, R.; di Francesco, F. Graphene-Based Devices for Measuring PH. *Sens. Actuators B Chem.* **2018**, *256*, 976–991. [[CrossRef](#)]
34. Vivaldi, F.; Bonini, A.; Melai, B.; Poma, N.; Kirchhain, A.; Santalucia, D.; Salvo, P.; Francesco, F. di A Graphene-Based pH Sensor on Paper for Human Plasma and Seawater. In *Proceedings of the 2019 41st Annual International Conference of the IEEE Engineering in Medicine and Biology Society (EMBC), Berlin, Germany, 23–27 July 2019*; IEEE: New York, NY, USA; pp. 1563–1566.
35. Sha, R.; Komori, K.; Badhulika, S. Amperometric PH Sensor Based on Graphene–Polyaniline Composite. *IEEE Sens. J.* **2017**, *17*, 5038–5043. [[CrossRef](#)]
36. Konkena, B.; Vasudevan, S. Understanding Aqueous Dispersibility of Graphene Oxide and Reduced Graphene Oxide through pK_a Measurements. *J. Phys. Chem. Lett.* **2012**, *3*, 867–872. [[CrossRef](#)] [[PubMed](#)]
37. Ito, J.; Nakamura, J.; Natori, A. Semiconducting Nature of the Oxygen-Adsorbed Graphene Sheet. *J. Appl. Phys.* **2008**, *103*, 113712. [[CrossRef](#)]
38. Chinnathambi, S.; Euverink, G.J.W. Hydrothermally Reduced Graphene Oxide as a Sensing Material for Electrically Transduced PH Sensors. *J. Electroanal. Chem.* **2021**, *895*, 115530. [[CrossRef](#)]
39. Kim, T.; Hong, S.; Yang, S. A Solid-State Thin-Film Ag/AgCl Reference Electrode Coated with Graphene Oxide and Its Use in a PH Sensor. *Sensors* **2015**, *15*, 6469–6482. [[CrossRef](#)]
40. Neupane, S.; Subedi, V.; Thapa, K.K.; Yadav, R.J.; Nakarmi, K.B.; Gupta, D.K.; Yadav, A.P. An Alternative pH Sensor: Graphene Oxide-Based Electrochemical Sensor. *Emergent Mater.* **2021**, *5*, 509–517. [[CrossRef](#)]
41. Sohn, I.-Y.; Kim, D.-J.; Jung, J.-H.; Yoon, O.J.; Nguyen Thanh, T.; Tran Quang, T.; Lee, N.-E. PH Sensing Characteristics and Biosensing Application of Solution-Gated Reduced Graphene Oxide Field-Effect Transistors. *Biosens. Bioelectron.* **2013**, *45*, 70–76. [[CrossRef](#)]
42. Dalmieda, J.; Zubiarraín-Laserna, A.; Ganepola, D.; Selvaganapathy, P.R.; Kruse, P. Chemiresistive Detection of Silver Ions in Aqueous Media. *Sens. Actuators B Chem.* **2021**, *328*, 129023. [[CrossRef](#)]
43. Sengupta, I.; Sharat Kumar, S.S.S.; Pal, S.K.; Chakraborty, S. Characterization of Structural Transformation of Graphene Oxide to Reduced Graphene Oxide during Thermal Annealing. *J. Mater. Res.* **2020**, *35*, 1197–1204. [[CrossRef](#)]
44. Gupta, B.; Kumar, N.; Panda, K.; Kanan, V.; Joshi, S.; Visoly-Fisher, I. Role of Oxygen Functional Groups in Reduced Graphene Oxide for Lubrication. *Sci. Rep.* **2017**, *7*, 45030. [[CrossRef](#)] [[PubMed](#)]
45. Kwan, Y.C.G.; Ng, G.M.; Huan, C.H.A. Identification of Functional Groups and Determination of Carboxyl Formation Temperature in Graphene Oxide Using the XPS O 1s Spectrum. *Thin Solid Film.* **2015**, *590*, 40–48. [[CrossRef](#)]
46. Achtyl, J.L.; Vlasiouk, I.V.; Fulvio, P.F.; Mahurin, S.M.; Dai, S.; Geiger, F.M. Free Energy Relationships in the Electrical Double Layer over Single-Layer Graphene. *J. Am. Chem. Soc.* **2013**, *135*, 979–981. [[CrossRef](#)]
47. Li, X.; Shi, J.; Pang, J.; Liu, W.; Liu, H.; Wang, X. Graphene Channel Liquid Container Field Effect Transistor as PH Sensor. *J. Nanomater.* **2014**, *2014*, 547139. [[CrossRef](#)]

48. He, H.; Kim, K.H.; Danilov, A.; Montemurro, D.; Yu, L.; Park, Y.W.; Lombardi, F.; Bauch, T.; Moth-Poulsen, K.; Iakimov, T.; et al. Uniform Doping of Graphene Close to the Dirac Point by Polymer-Assisted Assembly of Molecular Dopants. *Nat. Commun.* **2018**, *9*, 3956. [[CrossRef](#)]
49. Gierz, I.; Riedl, C.; Starke, U.; Ast, C.R.; Kern, K. Atomic Hole Doping of Graphene. *Nano Lett.* **2008**, *8*, 4603–4607. [[CrossRef](#)]
50. Kiani, M.J.; Ahmadi, M.T.; Karimi Feiz Abadi, H.; Rahmani, M.; Hashim, A.; Che harun, F.K. Analytical Modelling of Monolayer Graphene-Based Ion-Sensitive FET to PH Changes. *Nanoscale Res. Lett.* **2013**, *8*, 173. [[CrossRef](#)]
51. Zahed, M.A.; Barman, S.C.; Das, P.S.; Sharifuzzaman, M.; Yoon, H.S.; Yoon, S.H.; Park, J.Y. Highly Flexible and Conductive Poly (3, 4-Ethylene Dioxythiophene)-Poly (Styrene Sulfonate) Anchored 3-Dimensional Porous Graphene Network-Based Electrochemical Biosensor for Glucose and PH Detection in Human Perspiration. *Biosens. Bioelectron.* **2020**, *160*, 112220. [[CrossRef](#)]
52. Medina, H.; Lin, Y.-C.; Obergfell, D.; Chiu, P.-W. Tuning of Charge Densities in Graphene by Molecule Doping. *Adv. Funct. Mater.* **2011**, *21*, 2687–2692. [[CrossRef](#)]
53. Casiraghi, C.; Hartschuh, A.; Qian, H.; Piscanec, S.; Georgi, C.; Fasoli, A.; Novoselov, K.S.; Basko, D.M.; Ferrari, A.C. Raman Spectroscopy of Graphene Edges. *Nano Lett.* **2009**, *9*, 1433–1441. [[CrossRef](#)] [[PubMed](#)]
54. Osella, S.; Kiliszek, M.; Harputlu, E.; Unlu, C.G.; Ocakoglu, K.; Kargul, J.; Trzaskowski, B. Controlling the Charge Transfer Flow at the Graphene/Pyrene–Nitrilotriacetic Acid Interface. *J. Mater. Chem. C* **2018**, *6*, 5046–5054. [[CrossRef](#)]
55. Zhen, X.V.; Swanson, E.G.; Nelson, J.T.; Zhang, Y.; Su, Q.; Koester, S.J.; Bühlmann, P. Noncovalent Monolayer Modification of Graphene Using Pyrene and Cyclodextrin Receptors for Chemical Sensing. *ACS Appl. Nano Mater.* **2018**, *1*, 2718–2726. [[CrossRef](#)]
56. Tang, B.; Guoxin, H.; Gao, H. Raman Spectroscopic Characterization of Graphene. *Appl. Spectrosc. Rev.* **2010**, *45*, 369–407. [[CrossRef](#)]
57. Díez-Betriu, X.; Álvarez-García, S.; Botas, C.; Álvarez, P.; Sánchez-Marcos, J.; Prieto, C.; Menéndez, R.; de Andrés, A. Raman Spectroscopy for the Study of Reduction Mechanisms and Optimization of Conductivity in Graphene Oxide Thin Films. *J. Mater. Chem. C* **2013**, *1*, 6905. [[CrossRef](#)]
58. Sengupta, I.; Chakraborty, S.; Talukdar, M.; Pal, S.K.; Chakraborty, S. Thermal Reduction of Graphene Oxide: How Temperature Influences Purity. *J. Mater. Res.* **2018**, *33*, 4113–4122. [[CrossRef](#)]
59. Farah, S.; Farkas, A.; Madarász, J.; László, K. Comparison of Thermally and Chemically Reduced Graphene Oxides by Thermal Analysis and Raman Spectroscopy. *J. Therm. Anal. Calorim.* **2020**, *142*, 331–337. [[CrossRef](#)]
60. Vacchi, I.A.; Raya, J.; Bianco, A.; Ménard-Moyon, C. Controlled Derivatization of Hydroxyl Groups of Graphene Oxide in Mild Conditions. *2d Mater.* **2018**, *5*, 035037. [[CrossRef](#)]
61. Kwon, K.C.; Choi, K.S.; Kim, C.; Kim, S.Y. Role of Metal Cations in Alkali Metal Chloride Doped Graphene. *J. Phys. Chem. C* **2014**, *118*, 8187–8193. [[CrossRef](#)]
62. Sander, R. Compilation of Henry’s Law Constants (Version 4.0) for Water as Solvent. *Atmos. Chem. Phys.* **2015**, *15*, 4399–4981. [[CrossRef](#)]
63. Zhen, X.V.; Swanson, E.G.; Nelson, J.T.; Zhang, Y.; Su, Q.; Koester, S.J.; Bühlmann, P. Noncovalent Monolayer Modification of Graphene Using Pyrene and Cyclodextrin Receptors for Chemical Sensing. *ACS Appl. Nano Mat.* **2018**, *1*, 2718–2726. [[CrossRef](#)]
64. An, X.; Simmons, T.; Shah, R.; Wolfe, C.; Lewis, K.M.; Washington, M.; Nayak, S.K.; Talapatra, S.; Kar, S. Stable Aqueous Dispersions of Noncovalently Functionalized Graphene from Graphite and Their Multifunctional High-Performance Applications. *Nano Lett.* **2010**, *10*, 4295–4301. [[CrossRef](#)]
65. Georgakilas, V.; Otyepka, M.; Bourlinos, A.B.; Chandra, V.; Kim, N.; Kemp, K.C.; Hobza, P.; Zboril, R.; Kim, K.S. Functionalization of Graphene: Covalent and Non-Covalent Approaches, Derivatives and Applications. *Chem. Rev.* **2012**, *112*, 6156–6214. [[CrossRef](#)]

Defect density dependent pH response of graphene derivatives: towards the development of pH-sensitive graphene oxide devices

Shayan Angizi¹, Xianxuan Huang¹, Lea Hong¹, Md Ali Akbar¹, P. Ravi Selvaganapathy², Peter Kruse^{1, *}

¹ Department of Chemistry and Chemical Biology, McMaster University, 1280 Main Street West, Hamilton, Ontario L8S 4M1, Canada; angizis@mcmaster.ca

² Department of Mechanical Engineering, McMaster University, 1280 Main Street West, Hamilton, Ontario L8S 4L7, Canada.

Correspondence: pkruise@mcmaster.ca.

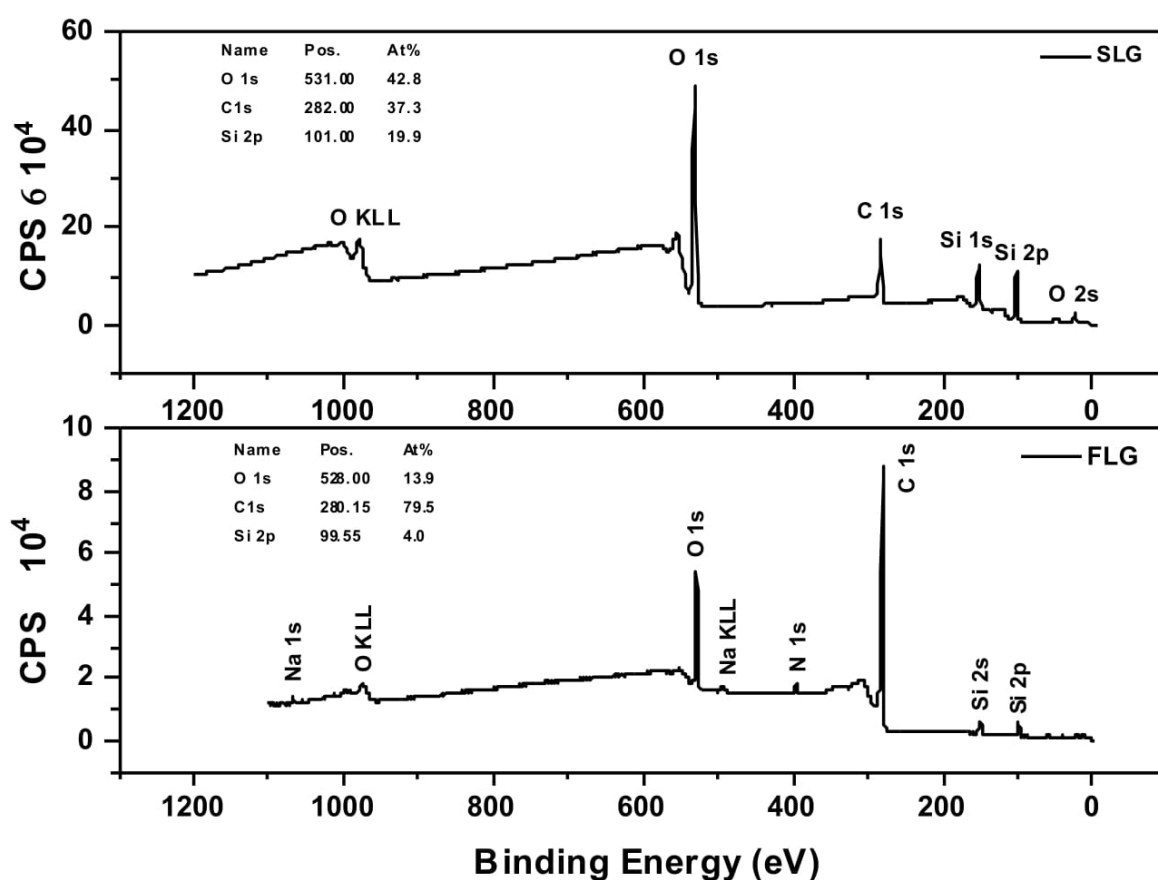


Figure S1. XPS survey spectra of a) SLG, b) FLG

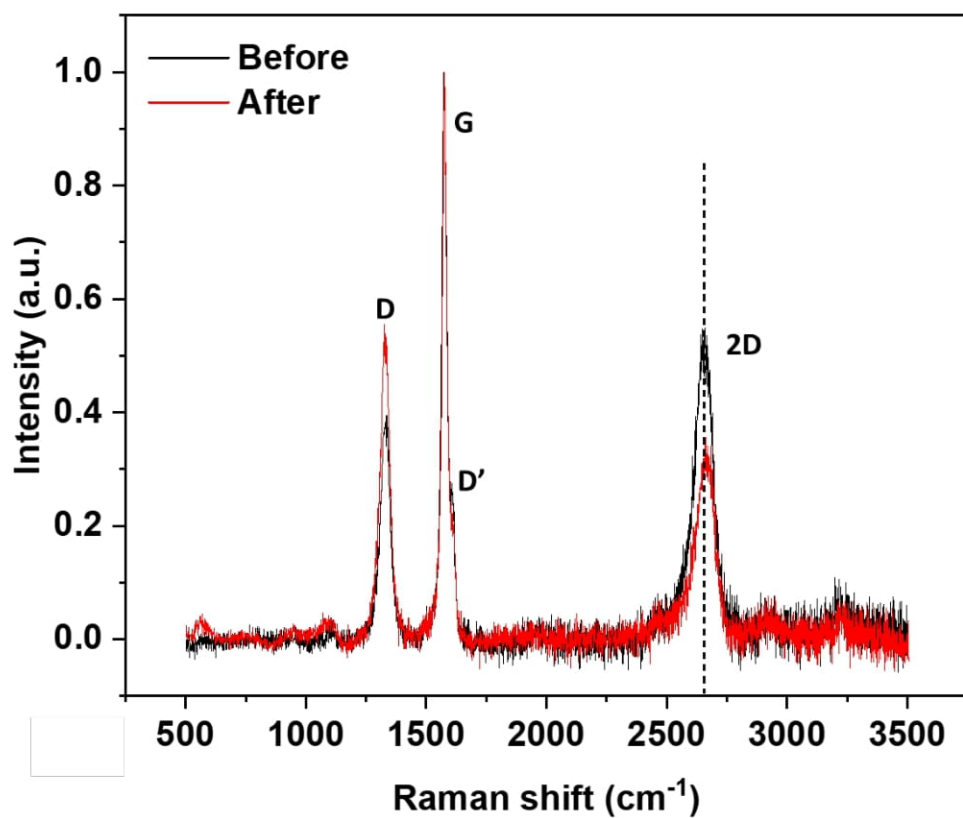


Figure S2. Raman spectra of FLG before and after exposure to pH

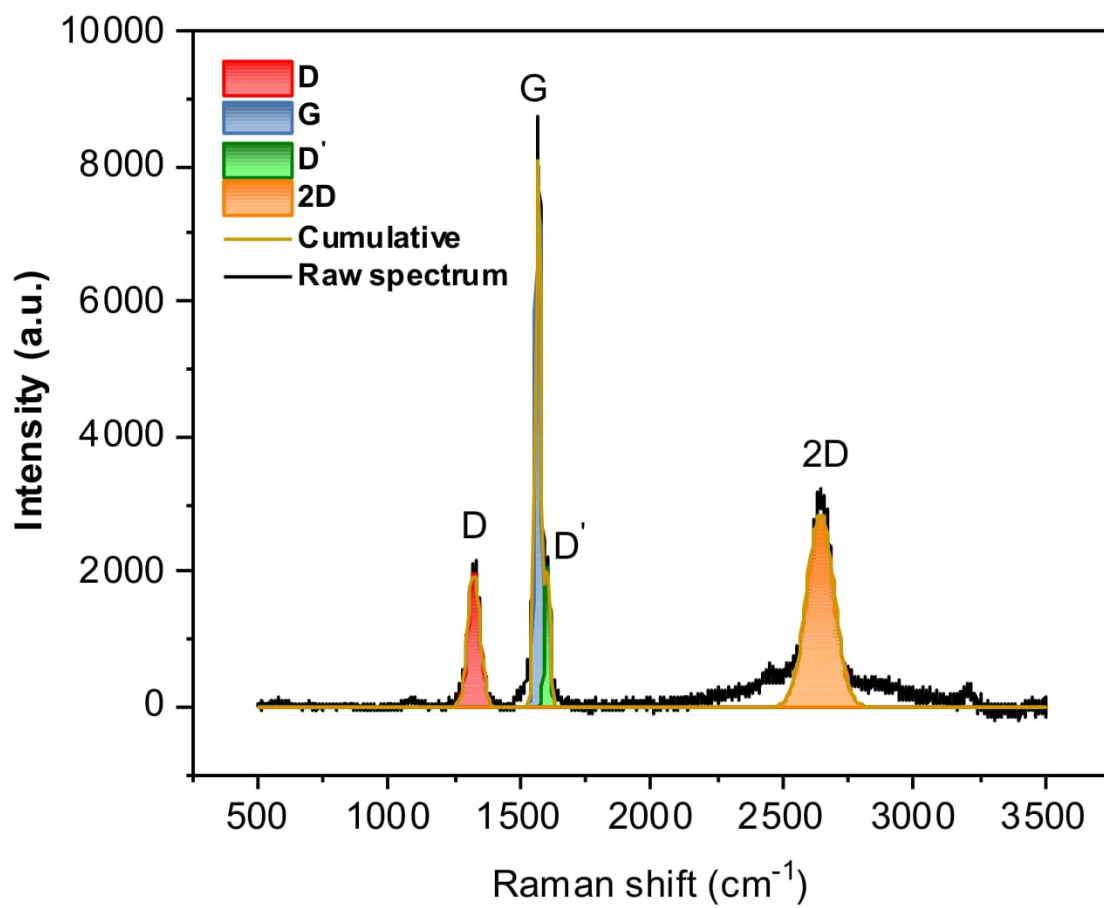


Figure S3. Raman spectrum of 8h annealed FLG

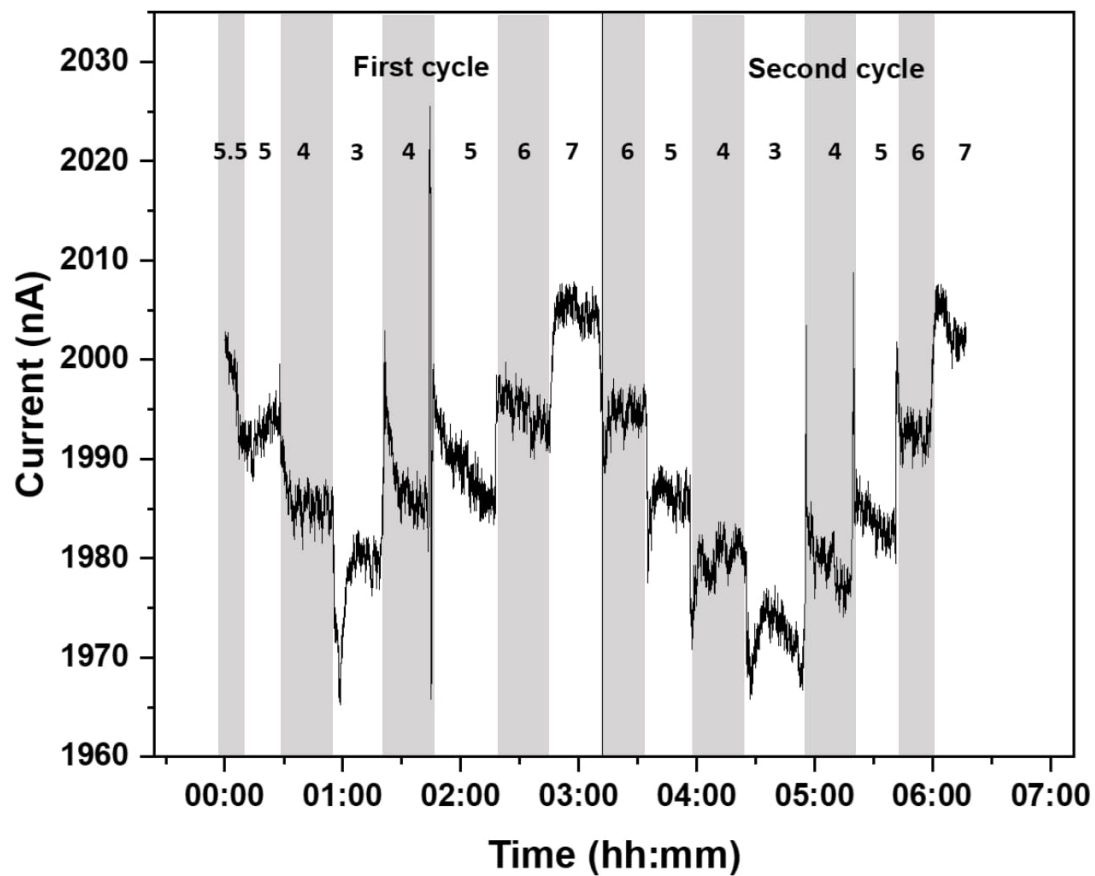


Figure S4. pH response of 8h annealed FLG

Table S1. Summary of information on Pyrene concentrations and their corresponding relative surface coverage obtained from literature [1–3]

	Pyrene derivatives concentration (mM)	Relative Surface coverage (%)	Surface density (#/cm ²)
Py-COOH	0.3	90	4.82×10^{14}
	0.15	40	2.14×10^{14}
	0.1	25	1.34×10^{14}
	0.05	10	5.35×10^{13}
Py-NH ₂	1.4	90	4.82×10^{14}
	0.7	50	2.68×10^{14}
	0.35	28	1.05×10^{14}
	0.1	10	5.35×10^{13}
Py-OH	1.6	90	4.82×10^{14}
	0.8	25	1.87×10^{14}
	0.4	20	1.07×10^{14}

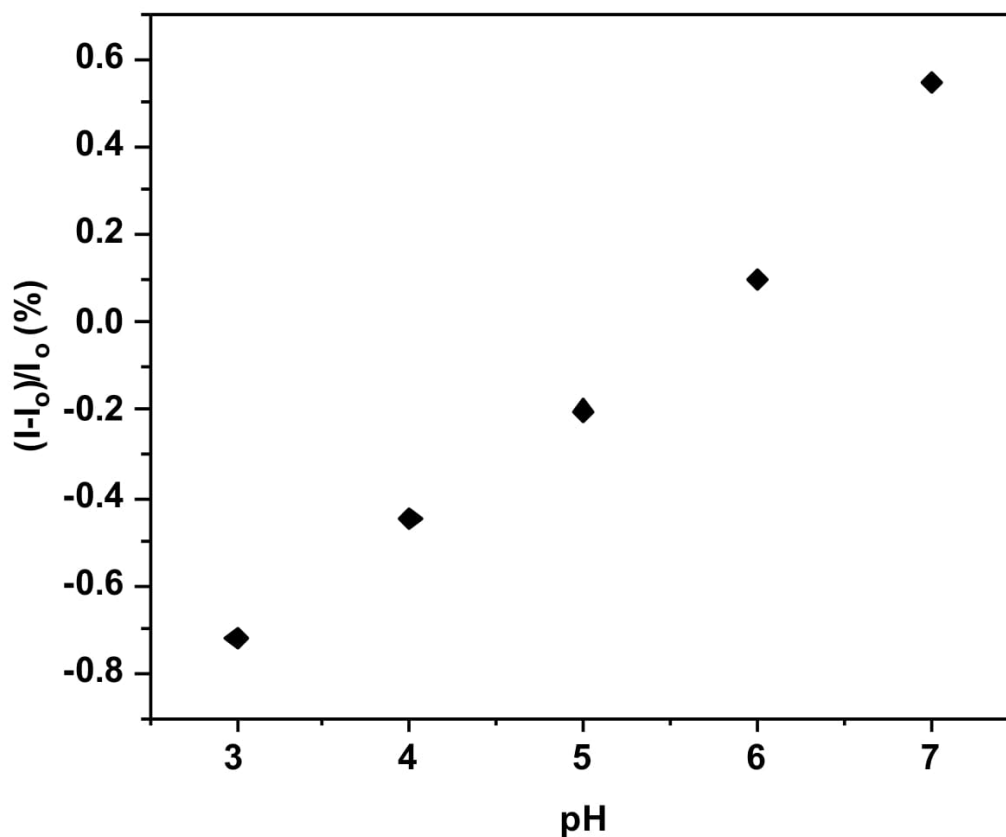


Figure S5. Calibration curve of the pH response of 8h annealed FLG

Table S2. Average \pm Standard deviation of Py-COOH functionalized sensors to pH range 3-8 (3 sensors each)

Concentration/pH	3	4	5	6	7
0.30 mM	55.6 \pm 1.21	37.2 \pm 3.2	12.27 \pm 2	8.09 \pm 0.7	-1.33 \pm 0.9
0.15 mM	31.96 \pm 0.84	21.12 \pm 1.26	7.33 \pm 0.24	2.68 \pm 0.3	-1.16 \pm 0.01
0.10 mM	4.92 \pm 0.4	1.9 \pm 0.62	0.69 \pm 0.02	0.02 \pm 0.003	1.3 \pm 1.1
0.05 mM	0.75 \pm 0.089	0.84 \pm 0.044	1.16 \pm 0.1	1.04 \pm 0.1	0.28 \pm 0.64

Table S3. Average \pm Standard deviation of Maximum response of pyrene derivative functionalized sensors as a functional surface density (3 sensors each).

-COOH		-NH ₂		-OH	
Surface density	Max. response	Surface density	Max. response	Surface density	Max. response
4.82E+14	56.1 \pm 8.31	4.82E+14	3.1 \pm 0.63	4.82E+14	-75.1 \pm 4.4
2.14E+14	32.4 \pm 7.21	2.68E+14	2.6 \pm 0.32	1.87E+14	-16.2 \pm 1.3
1.34E+14	5.1 \pm 3.79	1.50E+14	6.66 \pm 1.2	1.07E+14	-9.21 \pm 1.8
5.35E+13	2.05 \pm 3.26	5.35E+13	-4 \pm 0.19	-----	-----

Table S4. Average \pm Standard deviation of Py-NH₂ functionalized sensors to pH range 3-8 (3 sensors each).

Concentration/pH	3	4	5	6	7	8
1.4 mM	3.1 \pm 0.63	1.35 \pm 0.21	0.14 \pm 0.2	0.34 \pm 0.08	0.04 \pm 0.008	0.24 \pm 0.1
0.7 mM	2.6 \pm 0.32	0.21 \pm 0.023	0.36 \pm 0.091	0.32 \pm 0.1	0.36 \pm 0.2	0.39 \pm 0.32
0.35 mM	6.66 \pm 1.2	4.42 \pm 0.78	2.32 \pm 0.93	2.53 \pm 1.05	2.19 \pm 0.63	2.23 \pm 0.32
0.1 mM	-4.05 \pm 0.17	2.77 \pm 0.168	2.75 \pm 0.39	1.09 \pm 0.65	0.20 \pm 0.126	0.78 \pm 0.46

Table S5. Average \pm Standard deviation of Py-OH functionalized sensors to pH range 3-9 (3 sensors each).

Concentration /pH	3	4	5	6	7	8	9
1.6 mM	-21.21 \pm 2.3	-15 \pm 1.2	-1.21 \pm 0.2	-11 \pm 2.1	-19 \pm 5.2	-41.3 \pm 3.1	-75.1 \pm 4.4
0.8 mM	-5.9 \pm 1.2	-5 \pm 0.8	-5.2 \pm 0.61	-6.11 \pm 0.22	6.68 \pm 0.9	-13.3 \pm 1.6	-14.9 \pm 1.3
0.4 mM	-0.52 \pm 1	-0.53 \pm 2.4	-8.81 \pm 0.25	-4.34 \pm 0.11	-3.15 \pm 0.08	-8.02 \pm 0.42	-9.21 \pm 1.8

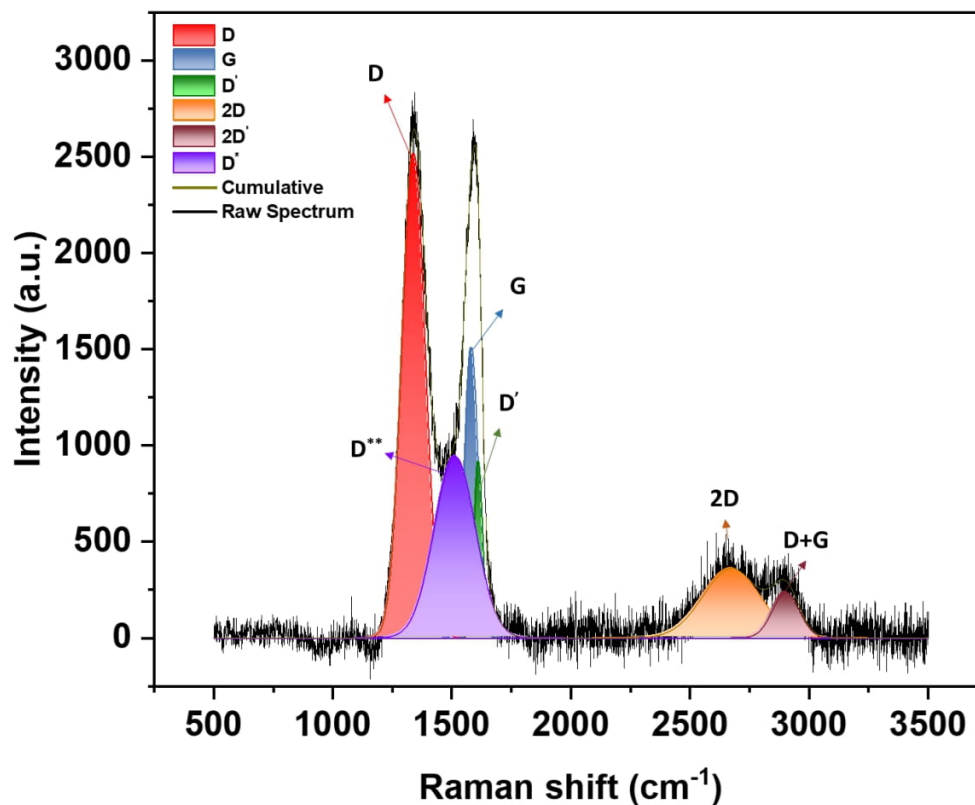


Figure S6. The Lorentzian deconvolution of GO Raman spectrum

References

1. Zhen, X. v.; Swanson, E.G.; Nelson, J.T.; Zhang, Y.; Su, Q.; Koester, S.J.; Bühlmann, P. Noncovalent Monolayer Modification of Graphene Using Pyrene and Cyclodextrin Receptors for Chemical Sensing. *ACS Applied Nano Materials* **2018**, *1*, 2718–2726, doi:10.1021/acsanm.8b00420.
2. An, X.; Simmons, T.; Shah, R.; Wolfe, C.; Lewis, K.M.; Washington, M.; Nayak, S.K.; Talapatra, S.; Kar, S. Stable Aqueous Dispersions of Noncovalently Functionalized Graphene from Graphite and Their Multifunctional High-Performance Applications. *Nano Letters* **2010**, *10*, 4295–4301, doi:10.1021/nl903557p.
3. Georgakilas, V.; Otyepka, M.; Bourlinos, A.B.; Chandra, V.; Kim, N.; Kemp, K.C.; Hobza, P.; Zboril, R.; Kim, K.S. Functionalization of Graphene: Covalent and Non-Covalent Approaches, Derivatives and Applications. *Chemical Reviews* **2012**, *112*, 6156–6214, doi:10.1021/cr3000412.

Chapter 5 Graphene versus Concentrated Electrolytes: An Experimental Study to Explore the Role of the Electrochemical Double Layer

Shayan Angizi¹, Lea Hong¹, Xianxuan Huang¹, P. Ravi Selvaganapathy², Peter Kruse^{1, *}

¹ Department of Chemistry and Chemical Biology, McMaster University, 1280 Main St. W. Hamilton, Ontario, Canada L8S 4M1

² Department of Mechanical Engineering, McMaster University, Hamilton, L8S 4M1, Canada

* Corresponding author. Tel. (905) 525-9140 (ext. 23480), e-mail: pkruise@mcmaster.ca

Abstract

Understanding the performance of graphene devices in contact with highly concentrated aqueous electrolytes is key to integrating graphene into next-generation devices operating in sea water environments, biosensors, and high-density energy production/storage units. Despite significant efforts toward interpreting the structure of the electrochemical double layer at high concentrations, the interface between graphene-based materials and concentrated aqueous solutions has remained vaguely described. In this study, we demonstrate the use of graphene-based chemiresistors as a technique to indirectly quantify the experimental Debye screening length of concentrated electrolytes. We report a breakdown of the Debye-Hückel theory in the proximity of graphene surfaces at lower concentrations (10-50 mM) than previously reported for other systems, depending on cation size, dissolved oxygen concentration, and degree of graphene defectivity.

5.1 Introduction

Graphene-based nanomaterials will be indispensable parts of next-generation sensors, microelectronics, and energy storage and conversion devices. Their rising importance is due to the outstanding properties of graphene, a low dimensional material with high specific surface area, high conductivity, low density, and ultra-high mechanical stability [1,2]. However, a considerable portion of graphene's popularity originates from the nature of its surface chemical bonds and suitable surface modifications [3,4]. The broad range of applications of graphene includes those in which graphene directly interacts with an aqueous solution (e.g., seawater

desalination [5,6], sensors [7,8], and supercapacitors [9,10]). Nevertheless, our understanding of graphene-aqueous electrolyte interactions is severely lacking and has not been sufficiently explored. On one side, the arrangement of ions and molecules of the electrolyte in the vicinity of the graphene is determined by the graphene's hydrophobicity. This ability to hydrogen bond and generate strong intermolecular interactions, often measured through water contact angle (WCA) measurements, is affected by the presence of surface local charges [11]. An ideal graphene lattice should be formed by sp^2 hybridized networks of carbon atoms, generating a highly symmetrical π -electron cloud. Hence, introducing common external dopants (e.g., molecular oxygen) or other functionalities (e.g., -OH, -COOH) disrupts the orbital symmetry and generates local polarities (defects). Therefore, the dipole orientations of water molecules and ions vary as the graphene chemistry changes [12].

Multiple solution parameters, including pH, oxidation-reduction potential, temperature, dissolved oxygen (DO), and, more importantly, ionic strength, influence the graphene properties simultaneously [13,14] through the interfacial electrochemical double layer (EDL). Therefore, the study of graphene-aqueous electrolyte interfaces requires well-controlled conditions where the co-influence of parameters is minimized. The EDL describes the arrangement of molecules and ions at the surface and indicates the distance from which the solid surface potential fades into the solution potential. Therefore, the extent of EDL and its impacts on graphene properties could be affected by the electrolytes' ionic strength [15]. Based on this, the ionic strength of the electrolyte that adjusts the thickness of EDL could be a powerful means to understand the impact of EDL on graphene, particularly at high concentrations.

Most graphene electrochemical devices require sufficient ionic strength of the electrolyte to provide cell conductance [16]. Also, the electrochemical currents are directed from one electrode to another through the solution. Therefore, the impact of EDL on the current passing

through (across) the graphene cannot be fully explored through electrochemical measurements, particularly at low ionic strength [17]. Moreover, despite the applied voltage independence of ideal EDL capacitance, the graphene electrode polarization is shown to be both frequency and voltage-dependent [18]. These facts highlight that understanding the EDL and ion configurations requires an alternative (or parallel) measurement method to monitor graphene behavior upon variation of EDL continuously.

The Debye-Hückel theory (D-H) is commonly used to postulate the relationship between the electrostatic screening length (λ_D) and the ionic strength of the solution as follows [19]:

$$\lambda_D = \sqrt{\frac{\epsilon_0 \epsilon_r k T}{2 I e^2}}$$

where ϵ_0 is the free space permittivity, ϵ_r is the solution permittivity, k is the Boltzmann's constant, T is the temperature (in Kelvin), and I represents the ionic strength [19]. The Debye length is also considered the characteristic decay length of the EDL forces proposed by the Poisson-Boltzmann (PB) theory. The PB theory assumes that the ions are non-polarizable point charges immersed in a continuous solution, meaning the ion-ion interactions are nearly zero. Accordingly, the λ_D calculation will only be valid in dilute solutions [20]. There have been multiple theories for concentrated electrolytes predicting the change in screening length; however, they are either invalid at practical electrolyte concentrations for the applications (~0.5-1 M), have ignored the role of substrates, or are not dedicated to the aqueous electrolytes. One of the recent studies revealed that the experimental screening length deviates from D-H theory at concentrations above 1 M for monovalent ions. This deviation was shown to increase with the increase in electrolyte concentration. Nevertheless, most experimental measurements of the screening length by using surface force measurement (SFM) or atomic force measurement (AFM) require complex equipment that may not be easily accessible. Moreover, there is no discussion of the role of the substrate in the deviation from ideality reported in the literature. The former issue originates from the complexity of confining an electrolyte between

two statically charged surfaces and changing the ionic concentrations while measuring the forces within nanometer distances [21]. The AFM investigation also comes with tip sensitivity (both materials and mode) to graphene topography and extreme substrate dependency of the results. Therefore, investigating the EDL should be done on free-standing graphene, which itself brings subsequent sophistication to the process [18]. The latter issue can be further classified into two arguments: i) majority of the techniques exploring the screening length of an electrolyte (i.e., SFM or SFG) are based on the substrates with static charges such as SiO₂[22]. Therefore, graphene derivatives with diverse conductivities have been less explored; ii) the impacts of graphene thickness, defect density and edge termination have been ignored in determining EDL composition in graphene devices [23,24].

In this study, we report the use of a simple graphene-based chemiresistive platform as an indirect tool for monitoring changes in the experimental screening lengths of concentrated aqueous solutions. With the help of electrochemical measurements, we propose a mechanism for the deviation of the screening length from the D-H theory at high concentrations. For this purpose, the roles of graphene defect density, cation size, and DO are explained in the formation of EDL, developing a complete picture of the mechanism.

5.2 Results and discussions

The structure of the EDL at the electrolyte/graphene interface depends on the defect density, surface charge, geometry, concentration, charge, and size of the ions in the electrolyte. The total capacitance resulting from the formation of EDL on graphene originates from the adsorption capacitance upon ion adsorption, Helmholtz Layer capacitance, and bulk capacitance. This means that the ion adsorption to the surface should be considered a separate capacitor parallel to where the Stern Layer containing both the inner and outer Helmholtz layer is located. [17–19] Therefore, prior to any experiments, understanding whether the ion adsorption could dope graphene chemically is vital. The Raman spectrum of FLG used in this

research (Figure 5.1.a, black spectrum) consists of the D, G and 2D bands at 1385, 1587, and 2580 cm^{-1} , respectively. The D band appears due to structural asymmetries caused by sp^3 hybridization in the graphene crystal, while the G band denotes the long-range ordered sp^2 hybridized network of carbon atoms [25]. The ratio of D to G intensities (or areas) indicates the defectivity of graphene [26]. Here, the I_D/I_G of the FLG is calculated as 0.33, indicating the existence of various defects such as oxygen atoms in the forms of diverse functional groups. The origin of these functional groups is mainly the sonication process through the direct interaction of graphene and solvents (IPA and H_2O) [27]. Therefore, electron-withdrawing oxygen atoms generate more holes as majority carriers and p-dope the graphene (see Section S1 in Supporting Information for the experimental procedure). Moreover, considering the difference in electronegativity between carbon and oxygen, oxygen dopants cause the negative zeta potential on the graphene surface exposed to aqueous electrolytes [28]. The rationale behind choosing FLG over monolayer graphene to study the EDL is its independence from substrate effect as well as modifiable defect density through synthesis process.

The impact of the ionic strength on the extent of the EDL (screening length) at the graphene/electrolyte interface can be investigated by measuring the response of the graphene chemiresistive device to the addition of salts to the aqueous electrolyte. However, since graphene/electrolyte interactions occur through two main pathways of electrostatic gating (known as capacitive charging) and charge transfer through redox reactions (known as pseudocapacitive charging), it is necessary to exclude charge transfer (chemical doping) effects during the experiments. Therefore, alkali chlorides (i.e., LiCl, NaCl, and KCl) were used to adjust the ionic strength since they dissociate into non-redox-active hydrated ions [29,30] (see Supporting Information Figure S1 for the measured ionic strengths of LiCl, NaCl, and KCl solution as a function of concentration)[31]. Therefore, we do not expect to observe chemical doping by the cations, which is confirmed by the Raman spectrum of graphene exposed to 0.1

M NaCl aqueous solution for two days, shown in Figure 5.1.a-red, compared to the blank graphene (Figure 5.1.a-black). The comparison of the band positions and intensities reveals that i) the G band is slightly shifted to higher Raman shifts, indicating the charged doped surface of graphene (n or p doping cannot be determined), ii) the redshift of the 2D band, demonstrating the hole-doping of graphene, and iii) a slightly higher I_D/I_G ratio for NaCl exposed graphene [29,30]. This shows that the graphene has slightly been p-doped by being in an aqueous electrolyte for a long time, and no trace of Na^+ doping (ion trapping or charge transfer) is observed. Nevertheless, the situation is different when 0.1 M NaCl is drop-cast on FLG and dried at 100 °C by forcing the ions to trap on and between graphene sheets. In this case, shown in Figure 5.1.b-red, a blueshift in the G band (from 2578 to 2573 cm^{-1}) is observed. This observation is in agreement with literature reports that ionic forms of metal with low ionization energy (e.g., Na^+ , K^+ , Ca^{2+}) can n-dope the graphene surface at a high concentration when directly applied [29]. Therefore, the response generated by the addition of both alkaline and alkaline earth ions are safe in regard to EDL measurement due to low charge transfer to graphene (chemical doping).

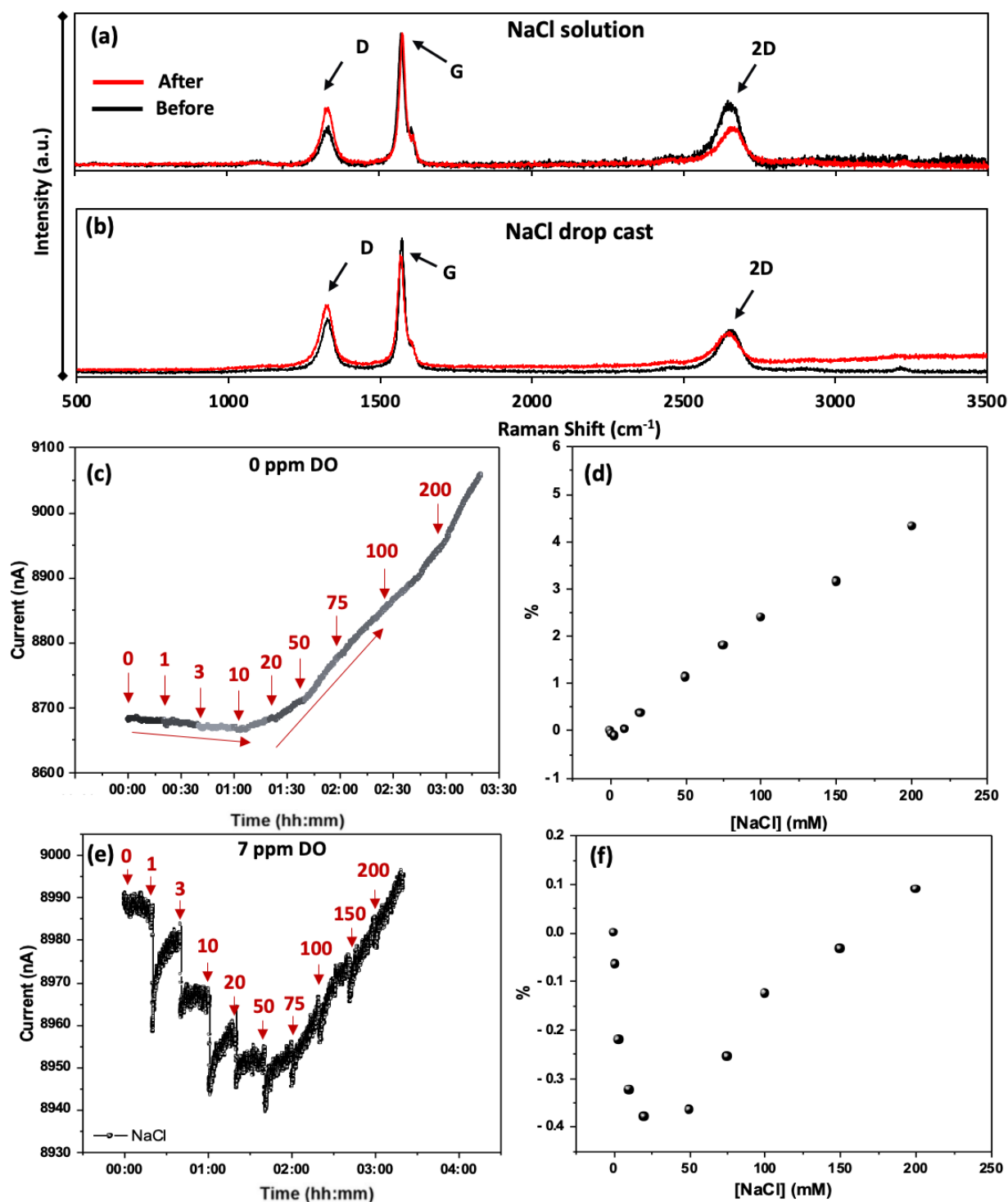


Figure 5.1. a) Raman spectra of FLG (black), FLG exposed to NaCl solution (Blue), and FLG with drop-cast 0.1 M NaCl (red), b) chemiresistive response of FLG to the addition of NaCl in 0 ppm DO solution. e) chemiresistive response and f) calibration curve of FLG to the addition of NaCl in the presence of DO (7 ppm).

Figure 5.1.c represents the chemiresistive response of the device to addition of NaCl. To ensure the dissolved gases and redox-active elements were minimized prior to the experiments, the

solution was purged continuously with dry $N_2(g)$, yielding nearly 0 ppm DO in the solution (Figure S2). As seen in Figure 5.1.c, addition of up to 10-20 mM NaCl reduces the current across the graphene chemiresistor. However, adding even more NaCl causes an unexpected increase in current, so the graphene response to salts is inverted. The former behavior in low concentrations follows the conventional EDL formation mechanism in graphene devices. By introducing the NaCl Na^+ and Cl^- hydrated ions are generated. Due to the presence of negatively charged oxygen atoms in functional groups of graphene, the Stern Layer is dominated by the Na^+ ions. Moreover, the underpotential deposition of alkali metals requires strong interactions between graphene and Na^+ to lower the energy needed for the electrodeposition. Therefore, it is unlikely to occur at such low applied potential (50 mV) in aqueous electrolytes and Na^+ ions maintain their solvation spheres and cannot directly adsorb onto the surface [32] (For the voltage-dependent EDL response of graphene, see Figure S3). Hence, these two layers of charges (Na being positive, graphene being negative, and water being dielectric) can be considered a standard capacitor. This means the formation of stern layers by Na^+ ions immobilizes electrons in the graphene; therefore, the chemiresistive current decreases. The level of n-doping increases as more NaCl is added to the solution, mainly due to the considerable reduction in theoretical Debye length (Figure S4).

The latter part of Figure 5.1.c (above 10-20 mM) is the result of deviation from ideal behavior, meaning from a particular concentration, λ_D increases as a function of salt concentration. In 2019, Gaddam and Ducker found this concentration around 1 M for NaCl, nearly independent of substrates[19]. These findings may be explained by the balance between ions' electrostatic double-layer forces with the van der Waals [33–35] and hydration interactions [36,37]. At low concentrations, ions can be considered separated; the local electric field on each ion is caused only by that ion. Therefore, the long-range double layer forces dominate, attracting ions to the charged surface of graphene. At higher concentrations, the deviation from the D-H theory's

condition alters the balance of forces. One theory proposes that the dominant Coulombic repulsive forces between similar ions ($\text{Na}^+\text{-Na}^+$) cause the EDL to expand and λ_D to increase [38,39]. Accordingly, the magnitude of EDL capacitive charge screening at the graphene surface decreases, leading to lower resistances (larger current). Some theoretical studies predict more complex surface structures, including overscreening of surface charge at the surface for low potentials and ion accumulation at interfaces where the surface potential is high. This substrate surface potential undergoes a “charge reversal” due to the non-electrostatic contributions of cation upon interactions with water. Early studies suggested that only divalent cations could result in a strongly correlated liquid at the surface while monovalent ions do not represent a charge reversal [40]. Nevertheless, this phenomenon was later observed for monovalent ions at concentrations around 1 M [22]. In contrast to the literature stating that no charge reversal occurs up to 0.15 M, we have seen this inversion at around 10 mM for Na^+ in the absence of DO (see Figure 5.1.d for the calibration curve). Hence, the role of the substrate’s surface chemistry needs to be considered. Another possibility could be a cross-over of the neutrality point of graphene’s band structure. As mentioned before, graphene is p-doped due to naturally found oxygen atoms, and charge screening of the stern layer induces electrons (n-doping). This means the graphene’s Fermi energy might pass the neutrality point, where electrons become the majority carriers. To test this hypothesis, we exposed the graphene to a series of experiments to ensure the charge type was the same. The graphene device was initially exposed to pH variation from 3 to 5 and down to 3, and the ionic experiment was conducted shortly after in the same solution. After one day of exposure to a highly concentrated salt solution (around 600 mM NaCl), graphene was exposed to the same pH experiment. As seen in Figure S5, the pH response of graphene is not changed but suppressed. The pH response of graphene with the Raman I_D/I_G ratio of 0.38 is believed to be due to the presence of pH-responsive functional groups of the surface namely carboxyl ($-\text{COOH}$), hydroxyl ($-\text{OH}$), amine

(-NH₂), and indirectly ketone (-CO-) and aldehydes (-CHO). Considering the p-doping nature of graphene, protonation of -COO⁻ to COOH at pH around its pK_a (3.74), the current increases. As seen, after exposure to salt for a day, the pH response remains the same, meaning the nature of the charge carriers has not changed.

The structure of the EDL formed by mono or divalent cations becomes more complex when DO is present. The graphene chemiresistive response to EDL in electrolyte equilibrating with air (7 ppm DO) (Figures 5.1.e and f) also shows the current inversion upon the addition of NaCl, however, at much higher concentrations (50-75 mM). This could be due to two simultaneous phenomena: i) direct absorption of DO and surface oxidation, and ii) charge neutralization that diminishes the electrostatic forces caused by Na⁺. The former is due to the redox activity of the DO toward withdrawing electrons from graphene. The latter must happen upon formation of the Stern layer by positively charged ions. These results can be confirmed by Electrochemical Impedance Spectroscopy (EIS) of graphene in the 0 and 7 ppm DO (Figure 5.2.c). Compared to when DO is present, N₂ purged solution exhibit lower charge transfer resistance (R_{ct}), smaller diffusion resistance, and slightly more ideal capacitive EDL characteristics (Figure S6). These indicate that the presence of DO may disrupt the long-range arrangement of Na⁺ ions and diminishes their capacitive charges to the graphene. Also, the possibility of the adsorbed DO to the surface should be considered. In this case, graphene surface charge may alter. However, since the DO adsorption on the surface is strongly ionic strength dependent (Figures 5.2.a-c), this can be said that change in FLG response to DO is due to the presence other ions in the Stern layer (here Na⁺ and Cl⁻). This hypothesis was also confirmed by testing the graphene response to DO at various ionic strengths. By equilibrating the graphene samples in NaCl electrolytes overnight, the device response against change in DO between 0 ppm (N₂ purged) and Air purged (11 ppm) was recorded. Figures 5.2.d and e show that the graphene device does not respond to changes in DO in 1- and 10 mM Na⁺. But the

introduction of DO causes a stepwise variation in current at 100 mM (Figure 5.2.f). Notably, upon purging the N_2 and dropping DO at 100 mM NaCl, the graphene is significantly influenced by the densification of the Stern layer and current drops, demonstrating the impact of DO contributions into EDL is stronger when Debye screening length is small.

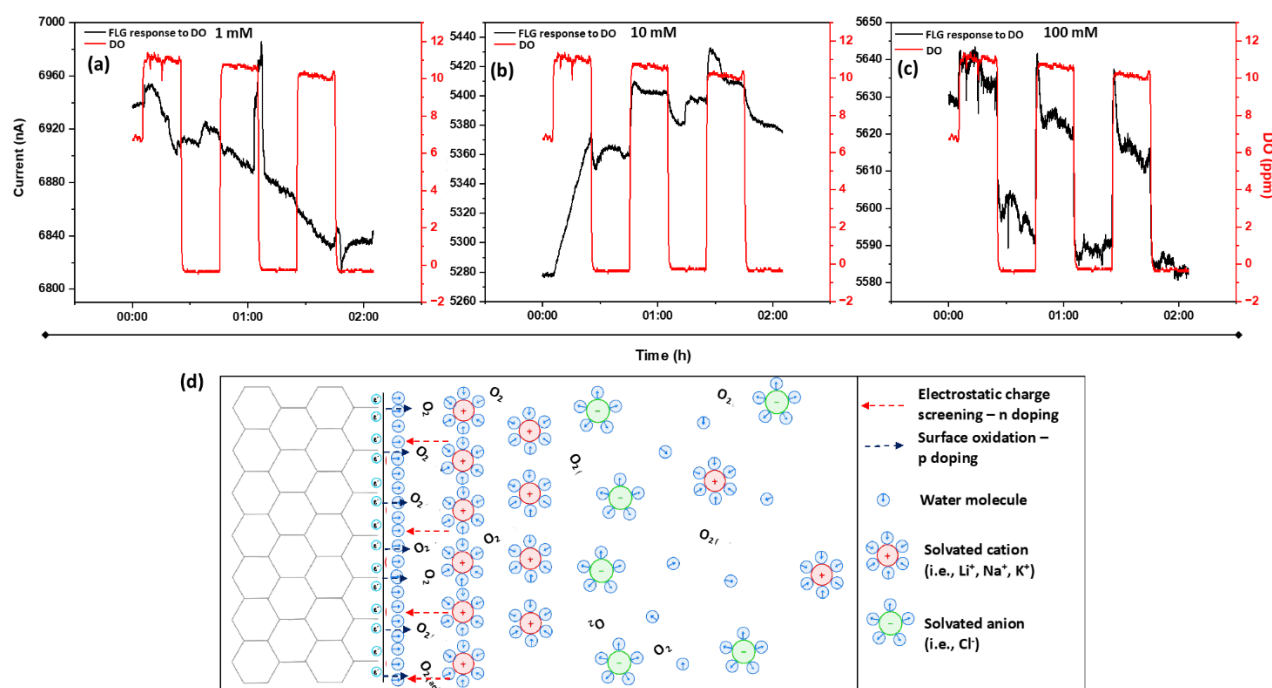


Figure 5.2. Chemiresistive response of graphene to variation of DO between 0 (N_2 purged) and 11 ppm (air purged) in a) 1 mM NaCl, b) 10 mM NaCl, c) 100 mM NaCl solutions, d) schematic illustration of EDL at graphene/electrolyte interface focusing on the role of DO.

As discussed above, the chemiresistive response of graphene demonstrates a current inversion upon increasing salt concentration, relatively similar to what has already been reported for the screening length of the solution. Notably, the plot of λ_D as a function of graphene sensor response (Figure 5.3.a- blue dots) revealed linear dependence in both regions. In fact, the slope of the fitted lines represents the dependence of sensor response to the screening length of EDL at low (black) and high (red) concentrations. Accordingly, two regions with slopes of 0.0286 and -0.454 can be obtained for NaCl (Figures S7.a and b). Also, since the deviation from ideality occurs at around 50-75 mM for NaCl, two responses could be considered for the concentration above 50-75 mM: i) experimentally measured sensor response ($\%_s$) obtained from the blue dots, ii) the theoretical response at high concentration in which λ_D is reduced continuously as a function of NaCl concentration ($\%_D$) and is obtained from the relationship between λ_D and sensor response at low concentrations. The difference between $\%_s$ and $\%_D$

indirectly represents the separation of experimental screening length (λ_s) from its theoretical value (λ_D).

The other term that needs to be defined is the ratio of ionic radius, a , and λ_D (a/λ_D). The a/λ_D ratio represents the concentration of the solution. When $a/\lambda_D \ll 1$, ionic radii are significantly smaller than the screening length, meaning the solution is dilute, and the surface potential of the ion drops into the solution before reaching the other ion. When $a/\lambda_D \geq 1$, the surface energy of the ions drops within the distance equal to or less than the ionic radius. Based on the literature, the $a/\lambda_D \approx 1$ is where the deviation from ideality occurs when the forces are measured using a surface force apparatus (SFA) technique at the surfaces without static charges [39]. By plotting the $\%_s - \%_D$ as a function of a/λ_D (Figure 5.3.b), this can be seen that up to 50 mM Na^+ , $\%_s - \%_D$ is nearly zero, meaning the theoretical and experimental screening lengths are almost the same. Nevertheless, at $a/\lambda_D \approx 0.06$, the $\%_s - \%_D$ starts to increase, confirming the screening length of EDL does not follow the D-H theory anymore.

The characterization of a/λ_D also draws attention toward the cation size-dependent response of graphene chemiresistive platform. Consider KCl as an alternative salt to NaCl with a similar anion: the λ_D can be assumed nearly the same for both salts at a particular concentration (the spectroscopically measured relative dielectric constants are almost the same for both Na^+ and K^+ [41,42]). However, careful considerations have revealed that dielectric constant at the interface (EDL) is nearly 10% less of that in bulk solution. This value can reach the permittivity saturation of water (6) when strong electric field (10^7 V/m) is present [23]. Therefore, upon increasing the concentration and reducing the λ_D , the one with a larger ionic radius will enter the non-ideal condition earlier due to the larger a/λ_D value. These assumptions can be confirmed by the chemiresistive response of graphene to LiCl and KCl compared to NaCl. As seen in Figure 5.3.c, adding Li does not lead to any current inversion up to 500 mM. This could be due to two simultaneous phenomena: i) the small size of Li^+ compared to λ_D requires considerably higher concentration to reach the current inversion zone (low a/λ_D), more than what is used here; ii) the Li^+ -intercalation or injection processes into graphene flakes upon the

addition of LiCl. This is a commonly observed phenomenon in applications where graphene-based materials are in contact with electrolytes containing Li^+ . Accordingly, upon Li^+ intercalation, the graphene is n-doped and the chemiresistive current decreases. Figures 5.3.d and e show the NaCl and KCl, respectively. A comparison of the curves shows that the current inversion for KCl happens at lower concentrations (10-20 mM) compared to NaCl (50-75 mM), demonstrating that the EDL response of graphene is cation size dependent. This can be re-confirmed by the faster rise of $\%_S - \%_D$ from 0 value in KCl compared to NaCl in Figure 5.3.b.

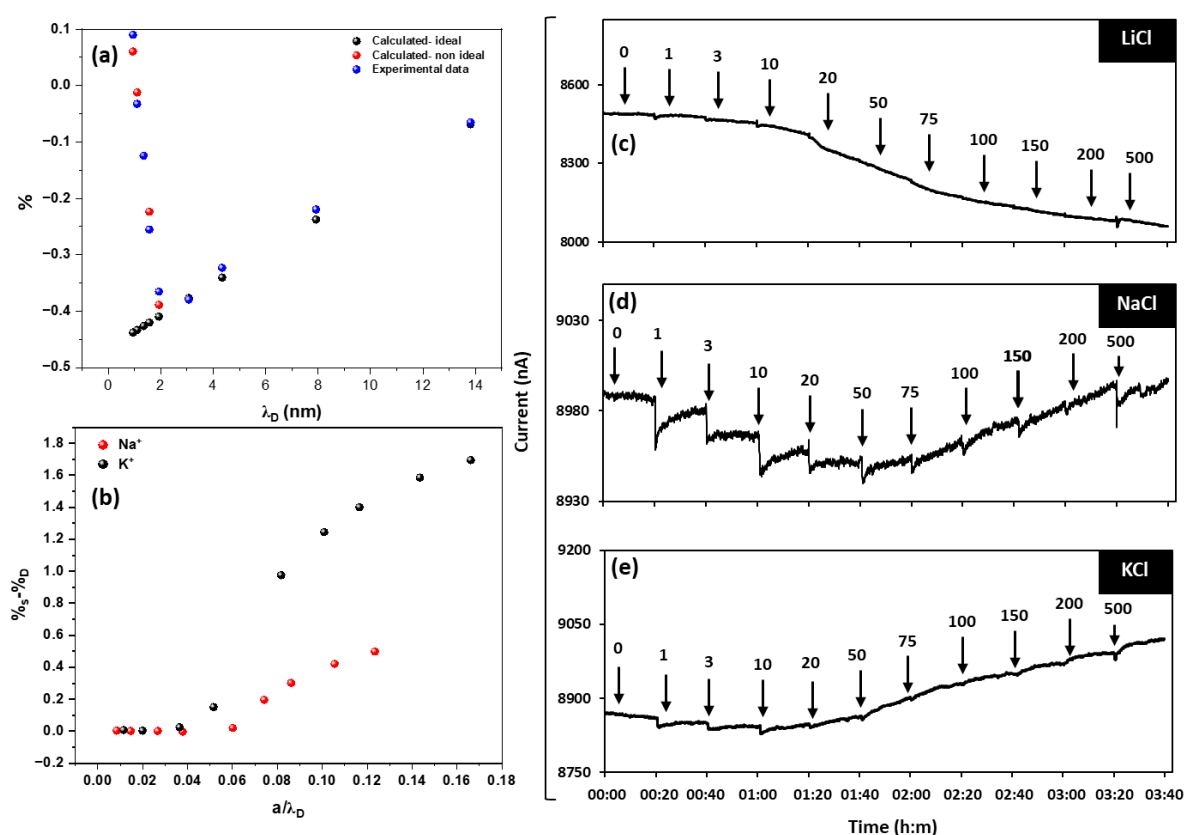


Figure 5.3. a) Graph of change in sensor response as a function of theoretical Debye screening length (blue) for two sections of ideal (black) and non-ideal (red) solutions. Chemiresistive sensing response of FLG to c) LiCl, d) NaCl, and e) KCl. (The insets show the corresponding calibration curves).

The graphene defectivity may also impact the arrangement of ions in the EDL. The presence of defects alters the graphene solution interactions. For example, according to **Figure S7.a**, the addition of NaCl causes the stepwise reduction in the chemiresistive current due to capacitive n-doping of graphene ($I_D/I_G = 0.33$) by the Na^+ ions. However, this scenario is not seen in

reduced graphene oxide for 12h (Figure S8.b), 9h (Figure S8.c) or 6 h (Figure S8.d), having I_D/I_G ratios of 1.11, 1.25 and 1.43, respectively. This observation is in agreement with our recent study on the competing roles of EDL and defect density in graphene during the interaction with the aqueous environment[12]. Accordingly, by increasing the defect density, three mechanisms may interrupt the formation and effect of EDL: i) formation of alkali metal complexes with oxygen atoms in surface functionalities, ii) dominant defect-induced interactions caused by the surface functionalities, and iii) discontinuity of the Stern layer [43]. The last phenomenon occurs primarily due to the greater surface charge of graphene caused by oxygen. Hence, interpretation of graphene surface defectivity is necessary to understand the impact of EDL, and the results of this research should be narrowed to graphene with an I_D/I_G range of 0.3-0.5, containing pH responsive oxygen based functional groups.

1- Conclusion

We have presented a systematic study of the performance of graphene devices exposed to concentrated aqueous electrolytes. The change in the current passing through the graphene thin film upon interaction with an aqueous electrolyte was shown to be a means to indirectly determine the experimental screening length of the solutions. An improved picture of EDL containing Stern layers, the diffuse layer, and the bulk solution, was illustrated, focusing on the role of DO at the graphene surface. It was demonstrated that the presence of cations in the Stern layer n-dopes the graphene through electrostatic charge screening, and these charges are neutralized by surface oxidation of DO. We also demonstrate that the current inversion of graphene devices upon adding NaCl is due to deviation from D-H prediction, and the experimental screening length increases as a function of salt concentration. This concentration was shown to be dependent on DO concentration, cation size, and defect density at the graphene surface. Accordingly, a lower DO, larger cation size, and lower defectivity cause the current

inversion to occur at lower concentrations. This study is a starting point for further exploration of the substrate-dependent experimental screening length of concentrated solutions.

Acknowledgments

The authors thank Doris Stevanovic from the Centre for Emerging Device Technologies (CEDT), McMaster University, for granting access to the furnace; Alex Adronov (McMaster) for giving access to a Raman spectrometer; Vinay Patel and Christopher Franko for their fruitful discussions on EIS measurements; Md. Ali Akbar and Mildred Tong for discussions on dissolved oxygen experiment and setup.

Reference

- [1] A. Ambrosi, C.K. Chua, A. Bonanni, M. Pumera, *Electrochemistry of Graphene and Related Materials*, *Chem Rev.* 114 (2014) 7150–7188. <https://doi.org/10.1021/cr500023c>.
- [2] V. Georgakilas, M. Otyepka, A.B. Bourlinos, V. Chandra, N. Kim, K.C. Kemp, P. Hobza, R. Zboril, K.S. Kim, *Functionalization of Graphene: Covalent and Non-Covalent Approaches, Derivatives and Applications*, *Chem Rev.* 112 (2012) 6156–6214. <https://doi.org/10.1021/cr3000412>.
- [3] Z.A. Jonoush, M. Farahani, M. Bohlouli, Z. Niknam, A. Golchin, S. Hatamie, M. Rezaei-Tavirani, M. Omid, H. Zali, *Surface Modification of Graphene and its Derivatives for Drug Delivery Systems*, *Mini Rev Org Chem.* 18 (2021) 78–92. <https://doi.org/10.2174/1570193X17999200507093954>.
- [4] W. Yu, L. Sisi, Y. Haiyan, L. Jie, *Progress in the functional modification of graphene/graphene oxide: a review*, *RSC Adv.* 10 (2020) 15328–15345. <https://doi.org/10.1039/D0RA01068E>.
- [5] X. Wang, G. Ou, N. Wang, H. Wu, *Graphene-based Recyclable Photo-Absorbers for High-Efficiency Seawater Desalination*, *ACS Appl Mater Interfaces.* 8 (2016) 9194–9199. <https://doi.org/10.1021/acsami.6b02071>.
- [6] K. Xu, B. Feng, C. Zhou, A. Huang, *Synthesis of highly stable graphene oxide membranes on polydopamine functionalized supports for seawater desalination*, *Chem Eng Sci.* 146 (2016) 159–165. <https://doi.org/10.1016/j.ces.2016.03.003>.
- [7] F. Vivaldi, A. Bonini, B. Melai, N. Poma, A. Kirchhain, D. Santalucia, P. Salvo, F. di Francesco, *A graphene-based pH sensor on paper for human plasma and seawater*, in: *2019 41st Annual International Conference of the IEEE Engineering in Medicine and Biology Society (EMBC)*, IEEE, 2019: pp. 1563–1566. <https://doi.org/10.1109/EMBC.2019.8856991>.
- [8] M. Zhou, Y. Zhai, S. Dong, *Electrochemical Sensing and Biosensing Platform Based on Chemically Reduced Graphene Oxide*, *Anal Chem.* 81 (2009) 5603–5613. <https://doi.org/10.1021/ac900136z>.
- [9] C. Liu, Z. Yu, D. Neff, A. Zhamu, B.Z. Jang, *Graphene-Based Supercapacitor with an Ultrahigh Energy Density*, *Nano Lett.* 10 (2010) 4863–4868. <https://doi.org/10.1021/nl102661q>.
- [10] P. Saikia, K. Dutta, A.K. Guha, S.K. Dolui, P. Barman, L.J. Borthakur, *High-performance aqueous electrolyte based supercapacitor of carboxylic acid functionalized*

carbon-nanotubes and graphene nano composite, *Mater Chem Phys.* 258 (2021) 123786. <https://doi.org/10.1016/j.matchemphys.2020.123786>.

[11] S.S. Kwon, J. Choi, M. Heiranian, Y. Kim, W.J. Chang, P.M. Knapp, M.C. Wang, J.M. Kim, N.R. Aluru, W. il Park, S. Nam, Electrical Double Layer of Supported Atomically Thin Materials, *Nano Lett.* 19 (2019) 4588–4593. <https://doi.org/10.1021/acs.nanolett.9b01563>.

[12] S. Angizi, X. Huang, L. Hong, M.A. Akbar, P.R. Selvaganapathy, P. Kruse, Defect Density-Dependent pH Response of Graphene Derivatives: Towards the Development of pH-Sensitive Graphene Oxide Devices, *Nanomaterials.* 12 (2022) 1801. <https://doi.org/10.3390/nano12111801>.

[13] S. Angizi, P.R. Selvaganapathy, P. Kruse, Graphene-silicon Schottky devices for operation in aqueous environments: Device performance and sensing application, *Carbon N Y.* 194 (2022) 140–153. <https://doi.org/10.1016/j.carbon.2022.03.052>.

[14] A. Zubiarrain-Laserna, S. Angizi, M.A. Akbar, R. Divigalpitiya, P.R. Selvaganapathy, P. Kruse, Detection of free chlorine in water using graphene-like carbon based chemiresistive sensors, *RSC Adv.* 12 (2022) 2485–2496. <https://doi.org/10.1039/D1RA08264G>.

[15] H. Yang, X. Zhang, J. Yang, Z. Bo, M. Hu, J. Yan, K. Cen, Molecular Origin of Electric Double-Layer Capacitance at Multilayer Graphene Edges, *J Phys Chem Lett.* 8 (2017) 153–160. <https://doi.org/10.1021/acs.jpcclett.6b02659>.

[16] R. Simon, S. Chakraborty, K.S. Darshini, N.L. Mary, Electrolyte dependent performance of graphene–mixed metal oxide composites for enhanced supercapacitor applications, *SN Appl Sci.* 2 (2020) 1898. <https://doi.org/10.1007/s42452-020-03708-9>.

[17] P. Kruse, Review on water quality sensors, *J Phys D Appl Phys.* 51 (2018) 203002. <https://doi.org/10.1088/1361-6463/aabb93>.

[18] L.A. Jurado, R.M. Espinosa-Marzal, Insight into the Electrical Double Layer of an Ionic Liquid on Graphene, *Sci Rep.* 7 (2017) 4225. <https://doi.org/10.1038/s41598-017-04576-x>.

[19] P. Gaddam, W. Ducker, Electrostatic Screening Length in Concentrated Salt Solutions, *Langmuir.* 35 (2019) 5719–5727. <https://doi.org/10.1021/acs.langmuir.9b00375>.

[20] J. Forsman, A Simple Correlation-Corrected Poisson–Boltzmann Theory, *J Phys Chem B.* 108 (2004) 9236–9245. <https://doi.org/10.1021/jp049571u>.

[21] C.D. van Engers, N.E.A. Cousens, V. Babenko, J. Britton, B. Zappone, N. Grobert, S. Perkin, Direct Measurement of the Surface Energy of Graphene, *Nano Lett.* 17 (2017) 3815–3821. <https://doi.org/10.1021/acs.nanolett.7b01181>.

[22] P. Gaddam, W. Ducker, Electrostatic Screening Length in Concentrated Salt Solutions, *Langmuir.* 35 (2019) 5719–5727. <https://doi.org/10.1021/acs.langmuir.9b00375>.

[23] M. Khademi, D.P.J. Barz, Structure of the Electrical Double Layer Revisited: Electrode Capacitance in Aqueous Solutions, *Langmuir.* 36 (2020) 4250–4260. <https://doi.org/10.1021/acs.langmuir.0c00024>.

[24] A.M. Smith, A.A. Lee, S. Perkin, The Electrostatic Screening Length in Concentrated Electrolytes Increases with Concentration, *J Phys Chem Lett.* 7 (2016) 2157–2163. <https://doi.org/10.1021/acs.jpcclett.6b00867>.

[25] A.C. Ferrari, D.M. Basko, Raman spectroscopy as a versatile tool for studying the properties of graphene, *Nat Nanotechnol.* 8 (2013) 235–246. <https://doi.org/10.1038/nnano.2013.46>.

[26] A. Eckmann, A. Felten, A. Mishchenko, L. Britnell, R. Krupke, K.S. Novoselov, C. Casiraghi, Probing the Nature of Defects in Graphene by Raman Spectroscopy, *Nano Lett.* 12 (2012) 3925–3930. <https://doi.org/10.1021/nl300901a>.

[27] U. Halim, C.R. Zheng, Y. Chen, Z. Lin, S. Jiang, R. Cheng, Y. Huang, X. Duan, A rational design of cosolvent exfoliation of layered materials by directly probing liquid–solid interaction, *Nat Commun.* 4 (2013) 2213. <https://doi.org/10.1038/ncomms3213>.

- [28] Y.J. Shin, Y. Wang, H. Huang, G. Kalon, A.T.S. Wee, Z. Shen, C.S. Bhatia, H. Yang, Surface-Energy Engineering of Graphene, *Langmuir*. 26 (2010) 3798–3802. <https://doi.org/10.1021/la100231u>.
- [29] K.C. Kwon, K.S. Choi, C. Kim, S.Y. Kim, Role of Metal Cations in Alkali Metal Chloride Doped Graphene, *The Journal of Physical Chemistry C*. 118 (2014) 8187–8193. <https://doi.org/10.1021/jp500646e>.
- [30] K.C. Kwon, K.S. Choi, B.J. Kim, J.-L. Lee, S.Y. Kim, Work-Function Decrease of Graphene Sheet Using Alkali Metal Carbonates, *The Journal of Physical Chemistry C*. 116 (2012) 26586–26591. <https://doi.org/10.1021/jp3069927>.
- [31] H.W. Nesbitt, Activity coefficients of ions in alkali and alkaline-earth chloride dominated waters including seawater, *Chem Geol*. 43 (1984) 127–142. [https://doi.org/10.1016/0009-2541\(84\)90143-8](https://doi.org/10.1016/0009-2541(84)90143-8).
- [32] V. Sudha, M. v. Sangaranarayanan, Underpotential Deposition of Metals: Structural and Thermodynamic Considerations, *J Phys Chem B*. 106 (2002) 2699–2707. <https://doi.org/10.1021/jp013544b>.
- [33] R.G. Horn, J.N. Israelachvili, Direct measurement of forces due to solvent structure, *Chem Phys Lett*. 71 (1980) 192–194. [https://doi.org/10.1016/0009-2614\(80\)80144-8](https://doi.org/10.1016/0009-2614(80)80144-8).
- [34] J.N. Israelachvili, R.M. Pashley, Molecular layering of water at surfaces and origin of repulsive hydration forces, *Nature*. 306 (1983) 249–250. <https://doi.org/10.1038/306249a0>.
- [35] H.-W. Cheng, P. Stock, B. Moeremans, T. Baimpos, X. Banquy, F.U. Renner, M. Valtiner, Characterizing the Influence of Water on Charging and Layering at Electrified Ionic-Liquid/Solid Interfaces, *Adv Mater Interfaces*. 2 (2015) 1500159. <https://doi.org/10.1002/admi.201500159>.
- [36] W.A. Ducker, T.J. Senden, R.M. Pashley, Direct measurement of colloidal forces using an atomic force microscope, *Nature*. 353 (1991) 239–241. <https://doi.org/10.1038/353239a0>.
- [37] R.M. Pashley, DLVO and hydration forces between mica surfaces in Li⁺, Na⁺, K⁺, and Cs⁺ electrolyte solutions: A correlation of double-layer and hydration forces with surface cation exchange properties, *J Colloid Interface Sci*. 83 (1981) 531–546. [https://doi.org/10.1016/0021-9797\(81\)90348-9](https://doi.org/10.1016/0021-9797(81)90348-9).
- [38] M. McEldrew, Z.A.H. Goodwin, A.A. Kornyshev, M.Z. Bazant, Theory of the Double Layer in Water-in-Salt Electrolytes, *J Phys Chem Lett*. 9 (2018) 5840–5846. <https://doi.org/10.1021/acs.jpcclett.8b02543>.
- [39] A.A. Lee, C.S. Perez-Martinez, A.M. Smith, S. Perkin, Scaling Analysis of the Screening Length in Concentrated Electrolytes, *Phys Rev Lett*. 119 (2017) 026002. <https://doi.org/10.1103/PhysRevLett.119.026002>.
- [40] F.H.J. van der Heyden, D. Stein, K. Besteman, S.G. Lemay, C. Dekker, Charge Inversion at High Ionic Strength Studied by Streaming Currents, *Phys Rev Lett*. 96 (2006) 224502. <https://doi.org/10.1103/PhysRevLett.96.224502>.
- [41] R. Buchner, G.T. Hefter, P.M. May, Dielectric Relaxation of Aqueous NaCl Solutions, *J Phys Chem A*. 103 (1999) 1–9. <https://doi.org/10.1021/jp982977k>.
- [42] T. Chen, G. Hefter, R. Buchner, Dielectric Spectroscopy of Aqueous Solutions of KCl and CsCl, *J Phys Chem A*. 107 (2003) 4025–4031. <https://doi.org/10.1021/jp026429p>.
- [43] S. Angizi, E. Yu, J. Dalmieda, D. Saha, P.R. Selvaganapathy, P. Kruse, Defect Engineering of Graphene to Modulate pH Response of Graphene Devices, *Langmuir*. 37 (n.d.) 12163–12178. <https://doi.org/10.1021/acs.langmuir.1c02088>.

Supporting Information

Graphene versus Concentrated Electrolyte: An Experimental Study to Explore the Role of the Electrochemical Double Layer

Shayan Angizi¹, Lea Hong¹, Xianxuan Huang¹, P. Ravi Selvaganapathy², Peter Kruse^{1,*}

¹ Department of Chemistry and Chemical Biology, McMaster University, 1280 Main St. W. Hamilton, Ontario, Canada L8S 4M1

² Department of Mechanical Engineering, McMaster University, Hamilton, L8S 4M1, Canada

* Corresponding author. Tel. (905) 525-9140 (ext. 23480), e-mail: pkruise@mcmaster.ca

Section S1- Device fabrication and characterization

S 1.1 Materials

Graphite powder (99.99%) was purchased from Sigma Aldrich. Glass slides were bought from VWR. Isopropanol (99.99%) was purchased from VWR. Ultrapure water with a resistance of 18.2 M Ω cm was obtained from a Millipore Simplicity UV water purifier system. Sodium chloride (99.99%) and Lithium chloride were purchased from VWR. Potassium chloride was purchased from Caledon Laboratories Ltd). Sodium hydroxide (99%) and hydrochloric acids (37.2%, HPCL 99.99%) were used to regulate the pH in the experiments if necessary. Graphene oxide was provided from ZEN Graphene Solutions Ltd, containing 33% oxygen atoms in graphene structure.

S 1.2 Device fabrication and experimental procedure

The fabrication procedure of a chemiresistive sensor based on a few layers of graphene (FLG) has been reported in detail elsewhere ¹³. Briefly, 40 mg of graphite powder mixed with H₂O: IPA (10.5:4.5 mL) are sonicated for 6h in a bath sonicator (Elmasonic P60H ultrasonic cleaner) at 37 kHz and 30 °C. Then, the suspension is centrifuged twice by using an Eppendorf MiniSpin

Plus microcentrifuge, once at 14,000 rpm (13,140 g) for 5 minutes, the supernatant is separated, then centrifuged at 14,000 rpm (13,140 g) for 15 minutes, and the sedimented flakes are kept for the sensor fabrication.

To fabricate the chemiresistive sensors, the glass slides were rinsed with methanol and dried with N₂ (g) to eliminate the surface contaminations. Then, the slides are pre-patterned with two rectangles of 9B pencil to reduce the contact resistance between the active layer and electrodes. The glass slides are heated up to 100 °C, and the FLG is spray-coated on the surface uniformly until the average surface resistance reaches ~ 5 kΩ. Subsequently, the copper tape is attached on both sides of the FLG film, covering the pencil-drawn rectangle. Lastly, parafilm (M) is used to mask the contacts to avoid direct contact with electrodes and solution. To ensure the sealing quality of the parafilm, the substrate should be heated to 70 °C.

S 1.3 Characterizations

The Raman spectroscopy was done using a Renishaw inVia instrument in the range of 500–3500 cm⁻¹ with a spectral resolution of 2 cm⁻¹. The 633 nm laser was focused using a 50× objective lens on the sample. The laser power was set to 1 % to avoid surface damage during the analysis. The spectra were taken from three spots on each sample to ensure data reproducibility.

The UV-Visible spectra of FLG in the presence of salts were obtained by placing 1 mL of solution (0.3 mL of salt solution with the desired concentration in 0.7 mL FLG/ethanol/DI water suspension) into a quartz cuvette in an Orion Aquamate 8000 spectrophotometer over a range from 250 to 600 nm.

For chemiresistive measurements, an eDAQ EPU452 Quad Multifunction isoPod was used to measure the sensing behavior sensors. The channel type for chemiresistive sensing was set to the biosensor, with an applied voltage of 50 mV. A conductivity probe (cell constant K=1.057) was calibrated by using 0.1 mM KCl solution (12.64 mS.cm⁻¹) for 30 minutes. The pH electrode

used in the experiments was calibrated with pH 4 and 7 calibration solutions before the experiments.

The electrochemical measurements were performed using a three-electrode configuration on an EC301 electrochemical workstation (Palmsens). The electrolyte was purged with dry N₂ (g) for 40 minutes to eliminate the dissolved O₂ prior to electrochemical measurements. Similarly, to enhance the dissolved O₂ content, air was purged for 40 minutes. EIS measurements were conducted in the frequency range of 1MHz to 10 KHz with AC and DC potentials of 10 and 5 mV, respectively. In each case, FLG and graphite were used as working and counter electrodes with a Ag/AgCl reference electrode.

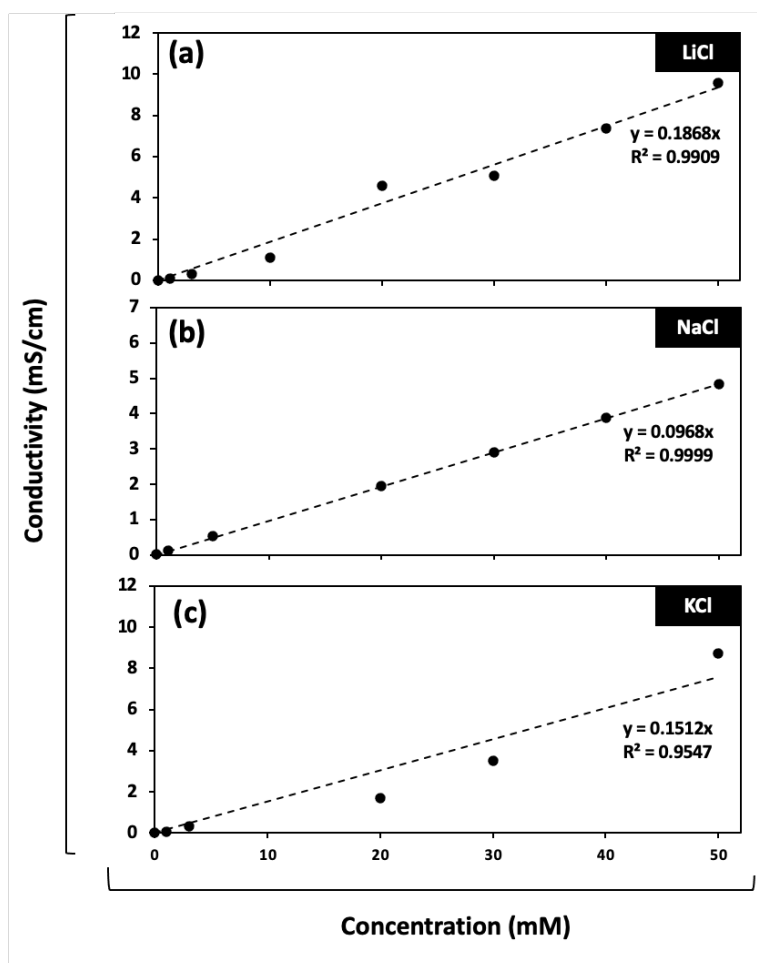


Figure S1 (Figure 5.4). Change in the ionic conductivity of the a) LiCl, b) NaCl, and c) KCl solution as a function of concentration.

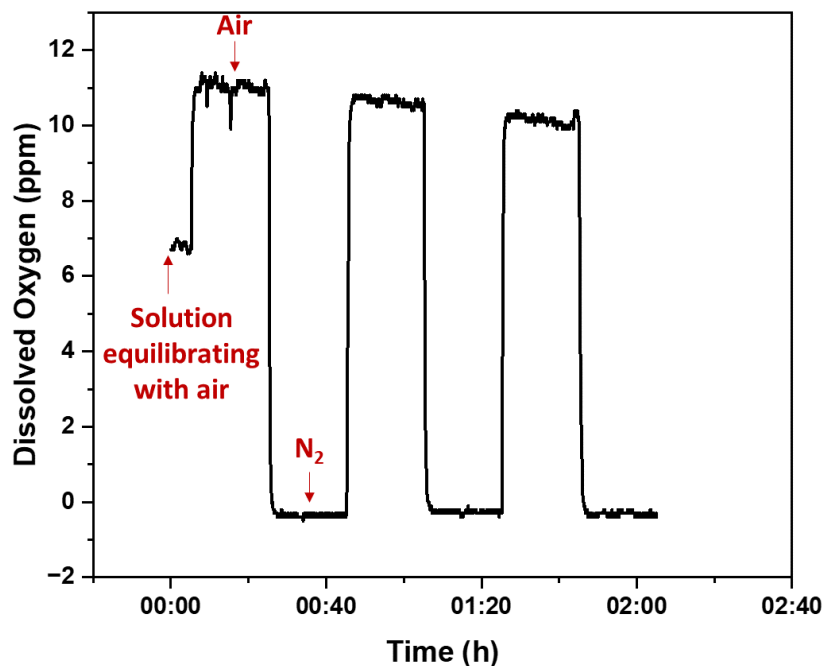


Figure S2 (Figure 5.5). Variation of dissolved oxygen in a solution equilibrating with air upon purging N₂ and air

Section S2 – Applied voltage-dependent EDL response

Since the formation of EDL at the graphene/electrolyte depends on the applied potential across the graphene, we tested four potentials of 10, 50, 100 and 500 mV to the chemiresistive device. We measured the response against the addition of NaCl. As seen in Figure S3, higher voltage causes a larger signal-to-noise ratio and lower noises. However, sensor-to-sensor variation was increased considerably so that the standard deviation at 500 mV was measured at more than 35%, while this value is less than 1% for 10 mV. Therefore, it is safe to say the high potential is not a reliable environment to operate due to approaching the water hydrolysis potential (i.e., 1.2 V).

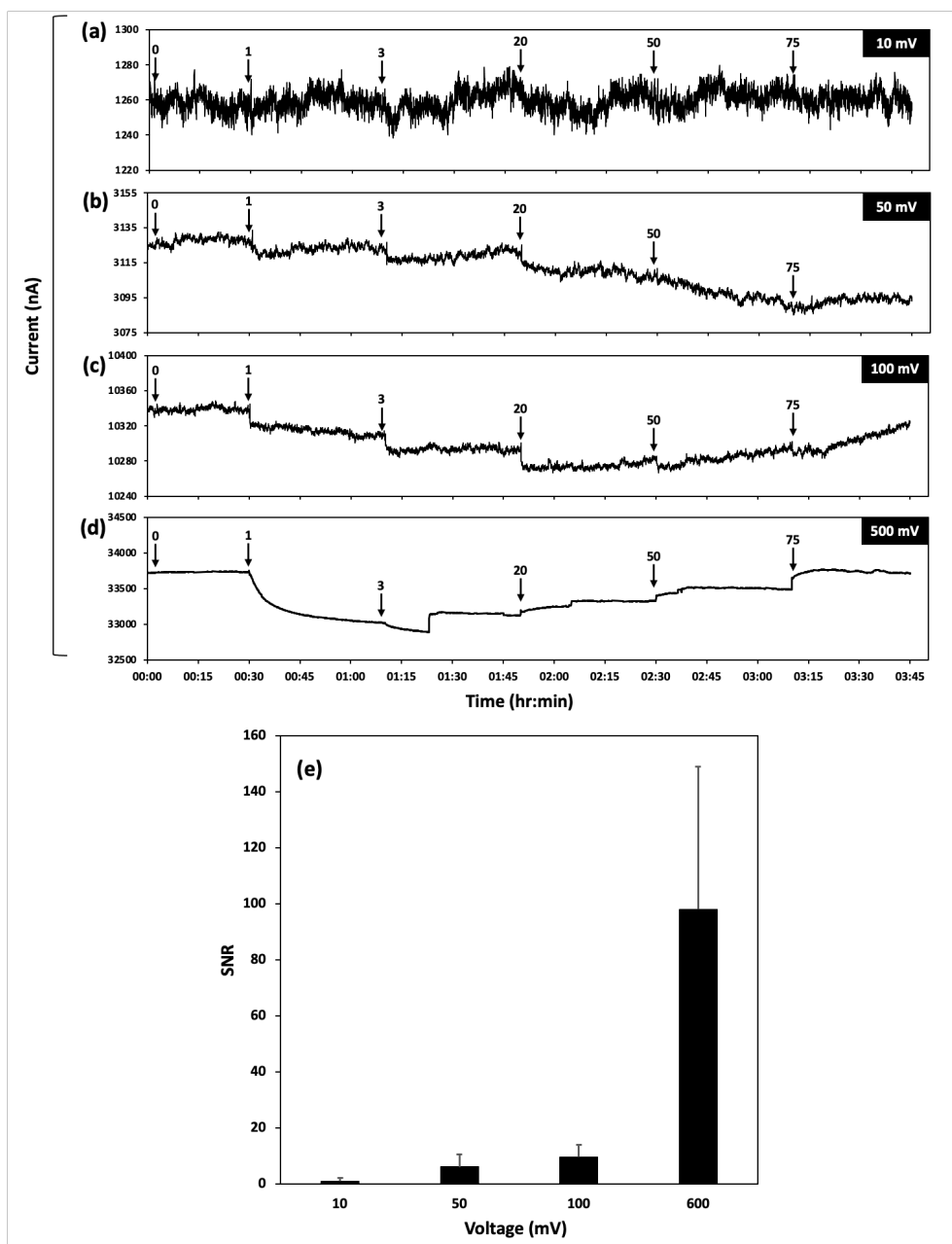


Figure S3 (Figure 5.6). Voltage-dependent response graphene chemiresistive device in a) 10 mV, b) 50 mV, c) 100 mV, and d) 500 mV applied potential, d) signal-to-noise ratio of the sensors operate at each voltage with the $n=6$.

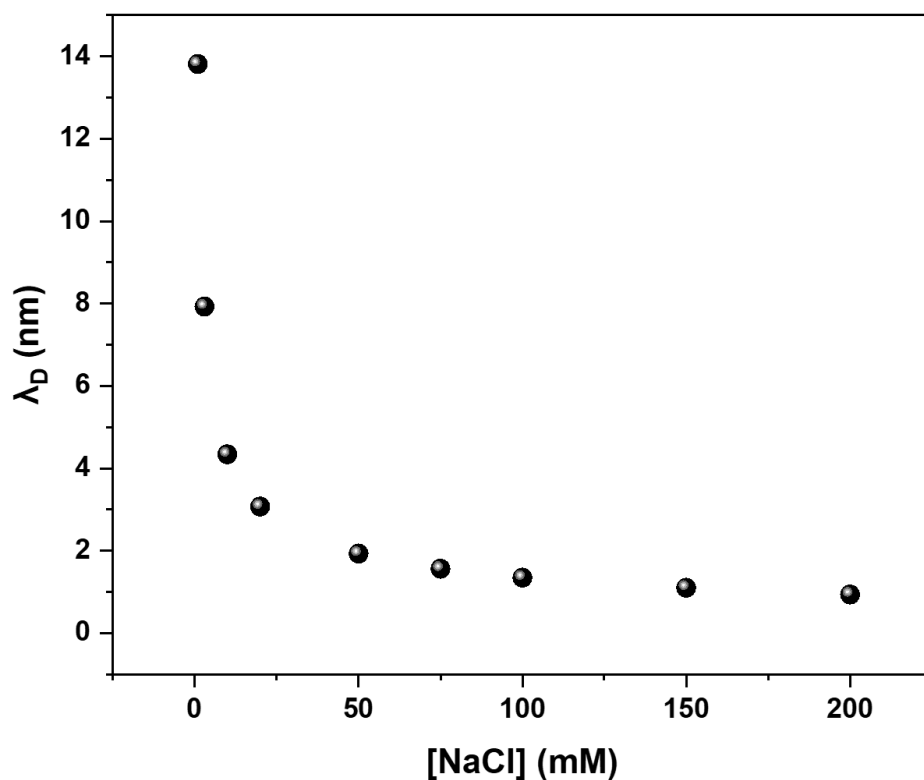


Figure S4 (Figure 5.7). Change in theoretical Debye screening length of the solution as a function of NaCl concentration

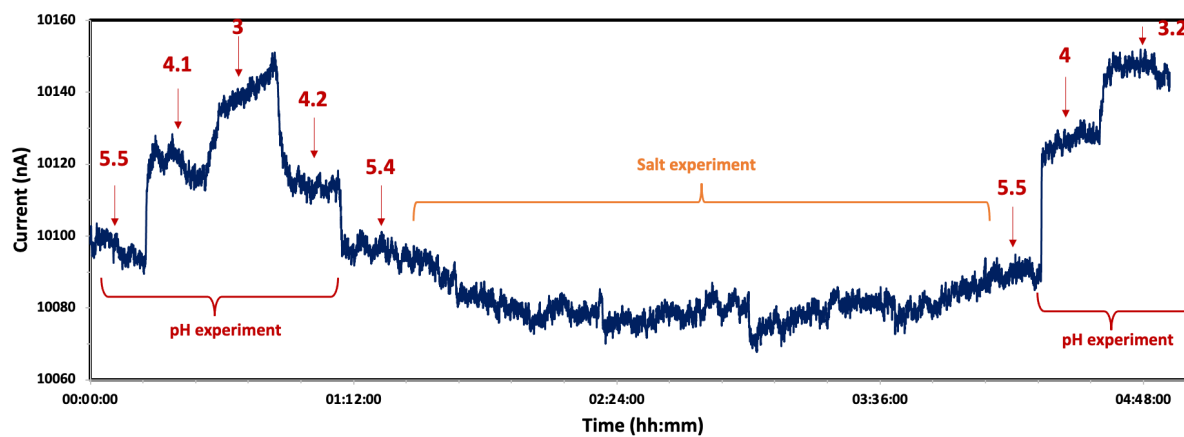


Figure S5 (Figure 5.8). pH response of graphene to pH 3-5 before and after the exposure to highly concentrated NaCl solution (0-600 mM).

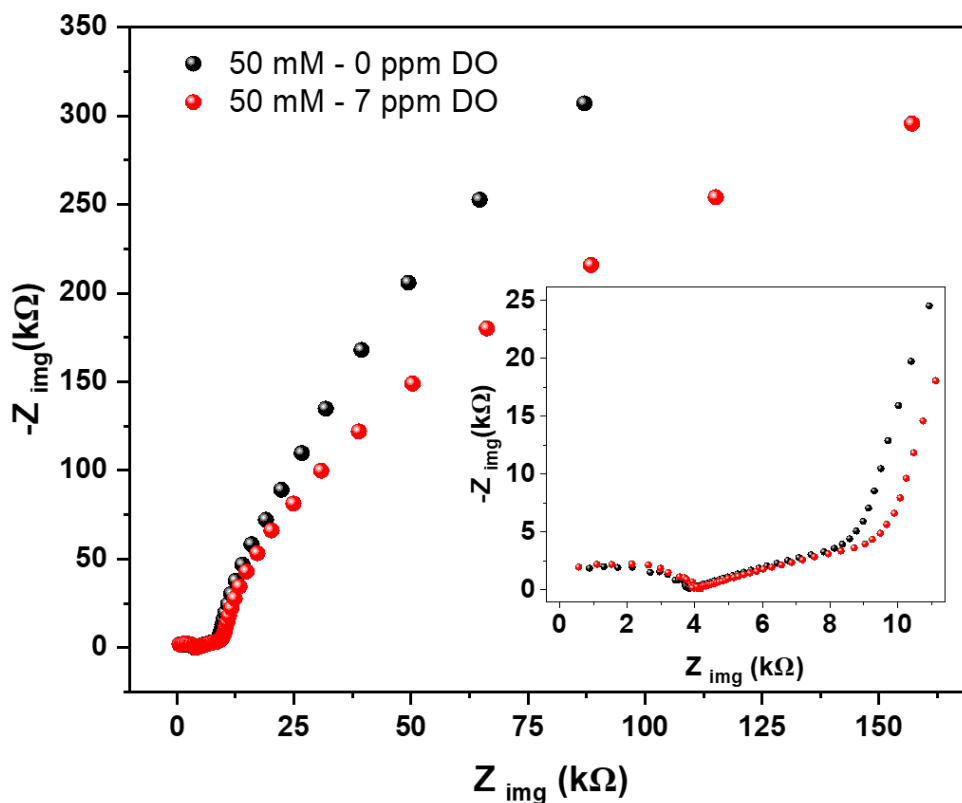


Figure S6 (Figure 5.9) Nyquist plots of FLG chemiresistive sensor in 50 mM NaCl in 0 and 7 ppm dissolved O_2 .

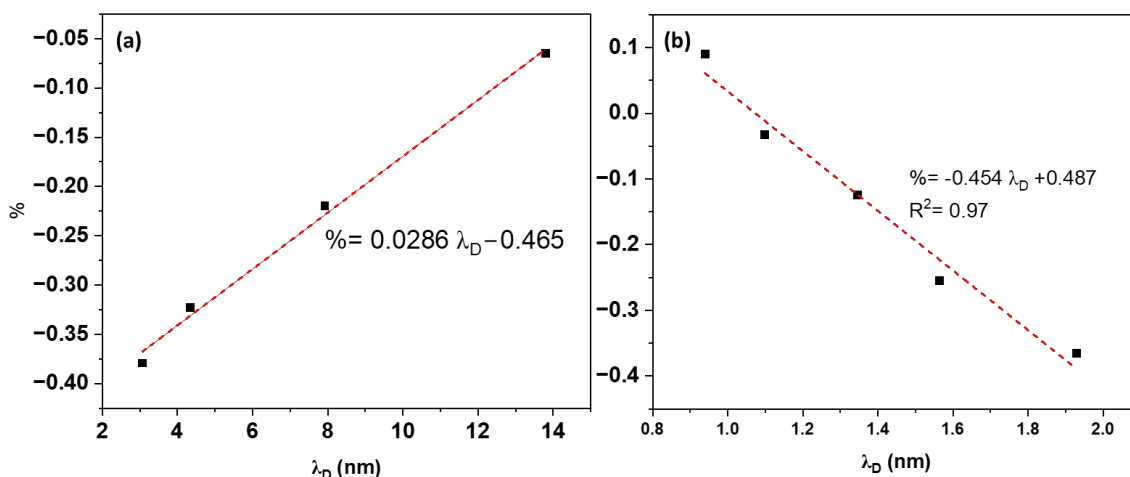


Figure S7 (Figure 5.10). The linear slopes of chemiresistive response as a function of screening length for a) low range and b) high concentration regions.

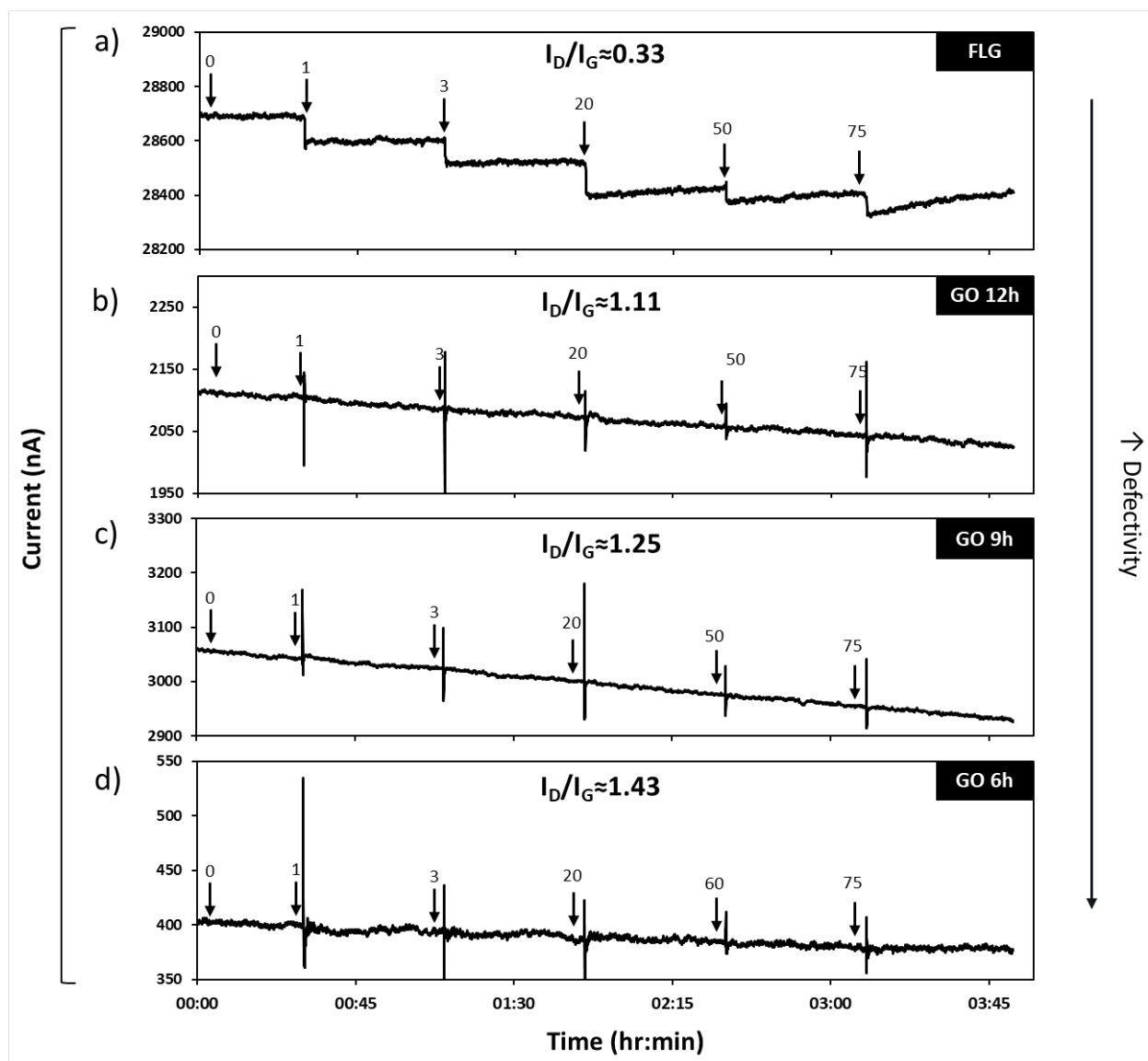


Figure S8 (Figure 5.11). Defect density-dependent EDL response of graphene surface exposed to NaCl solution for a) graphene, reduced GO for b) 12 h, c) 9h, and d) 6h under N_2/H_2 environment at 350 °C

Reference

- (1) Yavari, F.; Koratkar, N. Graphene-Based Chemical Sensors. *J. Phys. Chem. Lett.* **2012**, *3* (13), 1746–1753. <https://doi.org/10.1021/jz300358t>.
- (2) Zang, X. Graphene-Based Flexible Energy Storage Devices. In *Graphene*; Elsevier, 2018; pp 175–199. <https://doi.org/10.1016/B978-0-12-812651-6.00007-0>.
- (3) Guo, S.; Dong, S. Graphene and Its Derivative-Based Sensing Materials for Analytical Devices. *J. Mater. Chem.* **2011**, *21* (46), 18503. <https://doi.org/10.1039/c1jm13228h>.

- (4) Varghese, S.; Varghese, S.; Swaminathan, S.; Singh, K.; Mittal, V. Two-Dimensional Materials for Sensing: Graphene and Beyond. *Electronics* **2015**, *4* (3), 651–687. <https://doi.org/10.3390/electronics4030651>.
- (5) Choi, J. H.; Lee, J.; Byeon, M.; Hong, T. E.; Park, H.; Lee, C. Y. Graphene-Based Gas Sensors with High Sensitivity and Minimal Sensor-to-Sensor Variation. *ACS Appl. Nano Mater.* **2020**, *3* (3), 2257–2265. <https://doi.org/10.1021/acsanm.9b02378>.
- (6) Zubiarrain-Laserna, A.; Kruse, P. Review—Graphene-Based Water Quality Sensors. *J. Electrochem. Soc.* **2020**, *167* (3), 037539. <https://doi.org/10.1149/1945-7111/ab67a5>.
- (7) Peña-Bahamonde, J.; Nguyen, H. N.; Fanourakis, S. K.; Rodrigues, D. F. Recent Advances in Graphene-Based Biosensor Technology with Applications in Life Sciences. *J. Nanobiotechnology* **2018**, *16* (1), 75. <https://doi.org/10.1186/s12951-018-0400-z>.
- (8) Melios, C.; Giusca, C. E.; Panchal, V.; Kazakova, O. Water on Graphene: Review of Recent Progress. *2D Mater.* **2018**, *5* (2), 022001. <https://doi.org/10.1088/2053-1583/aa9ea9>.
- (9) Jurado, L. A.; Espinosa-Marzal, R. M. Insight into the Electrical Double Layer of an Ionic Liquid on Graphene. *Sci. Rep.* **2017**, *7* (1), 4225. <https://doi.org/10.1038/s41598-017-04576-x>.
- (10) Leonardi, S. G.; Aloisio, D.; Latino, M.; Donato, N.; Neri, G. Dissolved Oxygen Sensor Based on Reduced Graphene Oxide; 2014; pp 89–93. https://doi.org/10.1007/978-3-319-00684-0_17.
- (11) Pak, A. J.; Paek, E.; Hwang, G. S. Impact of Graphene Edges on Enhancing the Performance of Electrochemical Double Layer Capacitors. *J. Phys. Chem. C* **2014**, *118* (38), 21770–21777. <https://doi.org/10.1021/jp504458z>.
- (12) Angizi, S.; Selvaganapathy, P. R.; Kruse, P. Graphene-Silicon Schottky Devices for

Operation in Aqueous Environments: Device Performance and Sensing Application.

Carbon N. Y. **2022**, *194*, 140–153. <https://doi.org/10.1016/j.carbon.2022.03.052>.

- (13) Angizi, S.; Yu, E. Y. C.; Dalmieda, J.; Saha, D.; Selvaganapathy, P. R.; Kruse, P. Defect Engineering of Graphene to Modulate PH Response of Graphene Devices. *Langmuir* **2021**, *37* (41), 12163–12178. <https://doi.org/10.1021/acs.langmuir.1c02088>.

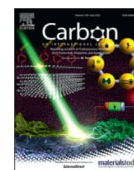
Chapter 6 Graphene-Silicon Schottky Devices for Operation in Aqueous Environments: Device Performance and Sensing Application

The aim of this chapter is to better understand the interaction between graphene and aqueous electrolytes by developing a graphene/n-type silicon Schottky junction. This was the first ever study on utilizing the Schottky junction in an aqueous electrolyte. Therefore, in addition to fully characterizing the bare junction properties, variation of graphene properties upon exposure to multiple water parameters such as pH, ORP and ionic strength were investigated. To expand the applicability of this diode sensor design in an aqueous environment, the graphene surface was functionalized via non-covalent functionalization using 1-aminopyrene. Then, it was used for the detection of free chlorine - a common disinfectant for drinking water - to elucidate the sensing capabilities of this new platform. The device demonstrated up to 80% change in series resistance (4% change in Schottky barrier height) of the functionalized device upon exposure to 1 ppm free chlorine. In contrast, the unfunctionalized device only shows a 17% response. The results of this study will provide a new approach to developing highly sensitive detection methods for analytes.



Contents lists available at ScienceDirect

Carbon

journal homepage: www.elsevier.com/locate/carbon

Graphene-silicon Schottky devices for operation in aqueous environments: Device performance and sensing application

Shayan Angizi^a, P. Ravi Selvaganapathy^b, Peter Kruse^{a,*}

^a Department of Chemistry and Chemical Biology, McMaster University, 1280 Main St. W. Hamilton, Ontario, Canada, L8S 4M1

^b Department of Mechanical Engineering, McMaster University, Hamilton, L8S 4M1, Canada



ARTICLE INFO

Article history:

Received 20 December 2021
Received in revised form
14 February 2022
Accepted 20 March 2022
Available online 23 March 2022

Keywords:

Graphene
Schottky junction
Surface functionalization
Chemical sensor
Free chlorine
Water quality sensor

ABSTRACT

Graphene/silicon Schottky diodes have recently been of heightened interest due to their high sensitivity towards surface chemical modifications. Here we demonstrate the operation of a graphene/n-type silicon Schottky junction in aqueous media, quantifying the impacts of the ionic strength, oxidation-reduction potential, and pH of an aqueous solution on diode characteristics. The roles of the electrical double layer and the surface functional groups of graphene in determining the graphene/silicon junction response to changes in the aqueous environment were investigated. The application of this diode sensor design was demonstrated in an aqueous environment by the introduction of functional groups to the graphene surface via non-covalent functionalization (here with 1-aminopyrene). Free chlorine - a common disinfectant for drinking water - is used to illustrate the sensing capabilities of this new platform, demonstrating up to 80% change in series resistance (4% change in Schottky barrier height) of the functionalized device upon exposure to 1 ppm free chlorine, while the unfunctionalized device only shows a 17% response. The results achieved in this study will open up new opportunities for highly sensitive detection of (bio)analytes using graphene/silicon diode devices in aqueous environments, beyond their conventional gas sensing applications.

© 2022 Elsevier Ltd. All rights reserved.

1. Introduction

The fabrication and characterization of well-defined graphene samples in 2004 [1] enabled its massive incorporation into a variety of applications such as optoelectronic devices [2], energy storage [3] and electrochemical sensors [4,5]. Its unique cone-shaped electronic band structure, superb electrical conductivity, high charge carrier mobility and tuneability of surface chemistry are highly beneficial in sensing applications [6,7], from simple cost-effective layouts such as chemiresistors [8,9] to more complex geometries such as Schottky diodes or field-effect transistors (FETs). The development of graphene-silicon heterojunctions (G/Si) has provided researchers with a unique platform for the accurate understanding and manipulation of graphene's electronic properties. Unlike chemiresistive platforms where Ohm's law dictates the change in graphene resistance [10], the current rectification at the interface of graphene/Si (lightly doped n-type or p-type), resembles diode characteristics [11]. This current rectification, resulting from

the formation of a Schottky barrier at the interface, is due to the built-in potential against charge transport from graphene to Si [12]. Since the Fermi level of graphene (4.6–4.7 eV) is located in the bandgap of Si, both p-type and n-type Si can form a Schottky junction with graphene [13]. A p-type Si has been shown to form a higher Schottky barrier (Φ_{SB}) compared to n-type Si (0.61–0.78 eV and 0.52–0.73 eV for p-Si and n-Si, respectively) [14].

The concept of a Schottky junction between graphite and a semiconductor was first introduced in 2009 [15], when Highly Ordered Pyrolytic Graphite (HOPG) was added on top of three different semiconductive substrates of Si, GaAs, and 4H-SiC. Since the outmost surface of HOPG touching the substrates can be considered as a monolayer of graphene, it was accurately predicted that a graphene/semiconductor device should exhibit diode characteristics [15]. However, since the band structure of graphene is thickness-dependent, the results needed further verification. Later, incorporation of few-layer exfoliated graphene on Si [11,12], bilayer [14] and monolayer graphene on the various substrate including n-type [16,17] and p-type Si [18,19], GaN [20], GaAs [20], CdS [21], MoS₂ [22], other 2D materials [6,23,24], expanded the application of graphene/semiconductor-based

* Corresponding author.

E-mail address: pkruise@mcmaster.ca (P. Kruse).

<https://doi.org/10.1016/j.carbon.2022.03.052>

0008-6223/© 2022 Elsevier Ltd. All rights reserved.

Schottky diodes to various areas of photodetectors, photovoltaics, and chemical sensors [25–27].

Thus far, G/Si Schottky diodes have been proposed for applications in gas sensing, demonstrating high sensitivity for the detection of numerous gaseous species such as H_2S [28], NH_3 [28], or H_2 [28]. The rectifying behavior of the G/Si junction provides researchers with two possible detection regimes: 1) forward bias at which the series resistance (R_s) of the device is dominant [29,30], and 2) reverse bias at which the saturation current is limited by the formation of a Schottky barrier ϕ_{SB} [31,32]. A Schottky barrier is a potential seen by graphene charge carriers when moving to silicon due to the difference in graphene work function and silicon electron affinity. This allows researchers to identify possible interactions by monitoring the variation of R_s or ϕ_{SB} . However, despite the great inherent sensing potential of this platform, very few attempts have been made to explore sensing in liquid media [13,30,33,34]. This is mainly due to the simultaneous impacts of multiple environmental parameters on graphene surface chemistry and the complication of data interpretation. In 2013, Kim et al. [30] successfully fabricated a monolayer G/Si diode sensor and exposed it to various liquids and gases. They demonstrated that upon exposure of graphene to electron-acceptor molecules, the ϕ_{SB} of the device increases (decreases) for n-Si (p-Si). Also, the R_s of the device drops (rises) for n-Si (p-Si) upon exposure to electron acceptors. Surface charge doping of graphene by molecules can therefore modulate the Fermi energy (E_F) of graphene and the electronic properties of the device. However, their droplet sensor geometry to test neat organic liquids is not practical for continuous measurements or other applications [30]. Similarly, Noroozi and Abdi [33] reported a considerable variation of the saturation current in G/n-Si by exposing it to the electron-donating protein Bovine Serum Albumin (BSA) under UV light. Incident UV photons generate electron-hole pairs, enhancing the saturation current by injecting the generated holes into the graphene. This enables reverse bias sensing measurement, which will reduce the energy consumption of the system. With the addition of BSA as an electron donor, the overall series resistance of the diode decreased. Moreover, the addition of BSA changed the absorption of the solution, decreasing the incident light. Therefore, they observed a dramatic reduction in saturation current by increasing the BSA. They reported sensitivities as high as 0.5 A M^{-1} with a detection limit of 0.25 nM [33]. However, the impact of environmental parameters such as pH, ionic strength, temperature, and surface modifications in the presence of aqueous solution was not discussed.

Here we demonstrate that G/n-Si Schottky diode devices can also meaningfully operate in aqueous environments. We elucidate the impact of pH of the solution, ionic strength, and oxidation-reduction potentials on the performance of the Schottky diode. Furthermore, to demonstrate the possibility of quantitatively and selectively sensing analytes in aqueous solutions, a monolayer of 1-aminopyrene (AP) was adsorbed onto the graphene layer to enhance the sensitivity and selectivity against free chlorine, a commonly used disinfectant for drinking water. Our systematic exploration of the impact of different parameters on device performance lays the foundation for widespread applications of G/Si Schottky diodes as chemical or biosensors in aqueous environments.

2. Device fabrication

A lightly doped n-Si wafer (Fig. 1a) was rinsed and sonicated several times in acetone, isopropanol, water, and isopropanol for 15 min each and dried by $\text{N}_2(\text{g})$. This needs to be done with much care since the presence of contamination can severely impact the performance of the device. Then the wafer was transferred into a

wet-oxidation tube furnace (Lindberg, model STF55666C-1) for in-situ formation of SiO_2 ($\sim 200 \text{ nm}$) at $1000 \text{ }^\circ\text{C}$ for 30 min (Fig. 1b). The heating cycle of the furnace was as follows: 15 K min^{-1} ramp from 25 to $400 \text{ }^\circ\text{C}$, hold for 30 min at $300 \text{ }^\circ\text{C}$; 15 K min^{-1} ramp from 400 to $800 \text{ }^\circ\text{C}$ and hold at $800 \text{ }^\circ\text{C}$ for 30 min. Then the samples are ramped up to $900 \text{ }^\circ\text{C}$ and $1000 \text{ }^\circ\text{C}$ and held for 30 min at each step. A 200 nm SiO_2 was formed after 30 min at $1000 \text{ }^\circ\text{C}$. A gradual increase in temperature is required to avoid the formation of microcracks in the Si substrate. Then the Si/ SiO_2 samples were cooled down gradually overnight. The samples were directly etched using an ammonium fluoride/hydrofluoric acid (4:1) buffer (Sigma Aldrich) to pattern the desired area of SiO_2 (Fig. 1c). The samples were then rinsed in DI water and transferred to a sputtering machine (Torr DC/RF). A 20 nm Ti and 200 nm of Au were sputtered as contacts onto the desired areas using pre-patterned Kapton tape (Uline, S-11731) (Fig. 1d). The graphene was transferred to the etched SiO_2 area and heated to $100 \text{ }^\circ\text{C}$ for 30 min followed by $50 \text{ }^\circ\text{C}$ for 6 h (Fig. 1e). The heating enhances the graphene adhesion to the surface by gradual evaporation of water between graphene and substrate. The sample annealing after hot acetone treatment was done at $600 \text{ }^\circ\text{C}$ in a three-heat zone Lindberg Thermodyne 21100 tube furnace purged with Ar/H_2 (95%/5%, purchased from Praxair Inc.). To control the flow of the analyte solutions, a poly dimethyl siloxane (PDMS) channel was added on top of the device (Fig. 1f). To dope the devices with 1-aminopyrene, they were exposed to a 1.4 mM ethanolic solution overnight. The devices were then thoroughly rinsed with ethanol to remove away any excess molecules or any possible dimers or trimers on the graphene layer [33].

Experiments started by flowing DI water over the G/Si junction overnight in order to attain equilibrium and avoid abrupt changes in current. The platform has a 2 cm long PDMS channel so that the solution can interact with the graphene without reaching the gold contacts. The desired analyte solution is prepared in a bowl containing 800 mL DI water. Then, the solution is moved through the channel over the graphene devices using a two-channel peristaltic pump (Masterflex® L/S® Digital Miniflex Pump Systems from ColeParmer) with a flow rate of 0.2 mL/min . After interacting with the graphene devices, the solution leaves the channel and is collected in a waste container. Current-time graphs were then recorded continuously while the devices are exposed to various environments. To normalize the current by the surface area of the transferred graphene, the current density (J) - voltage curves were taken once the device response had stabilized (approximately after 30 min). Each experiment involved two sensors used in parallel per condition. Data from three experiments was combined into each calibration curve, ensuring reproducibility of the data over at least six devices per condition. Detailed information about materials and characterization techniques that were used in this paper has been provided in the Supplementary Material, sections S1 and S2, respectively.

3. Results and discussions

3.1. Device performance

Since the electronic structure of a Schottky junction is affected by structural defects, the performance of a G/n-Si Schottky diode strongly depends on the quality of the transferred graphene. A Raman spectrum of graphene on SiO_2 is shown in Fig. 2a, representing the main Raman characteristic features of graphene. Given that the modulation of electron transport by defects, edges, and doping impacts the position and intensity of the Raman peaks, the surface phonon scattering of graphene depends on its electronic properties [33]. The G band located at 1590 cm^{-1} is due to the high-frequency E_{2g} phonon at Γ , representing a primary in-plane

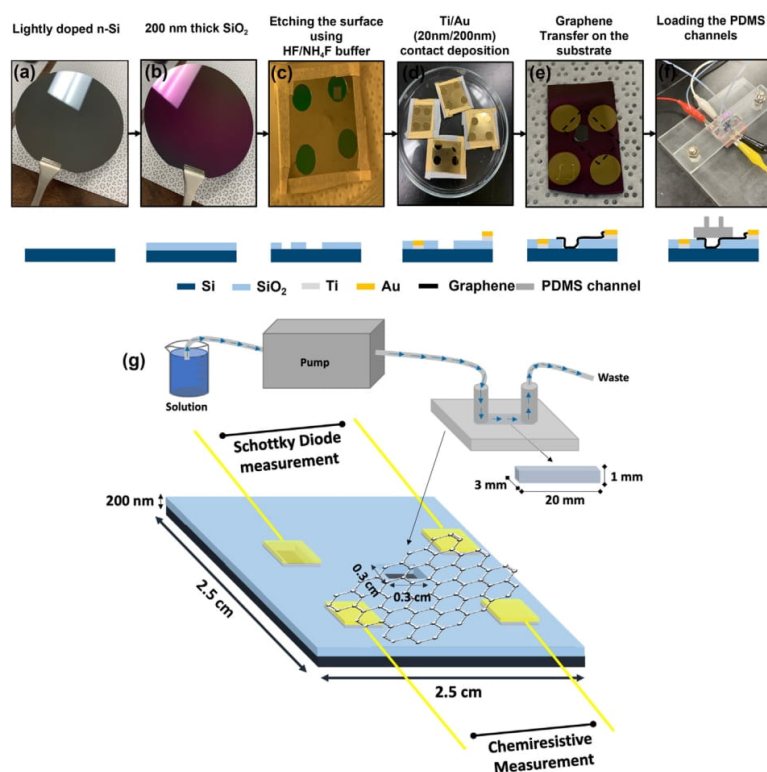


Fig. 1. a-f) Device fabrication process, g) schematic illustration of the proposed platform indicating the thickness and lateral dimensions.

vibrational mode of the sp^2 hybridized lattice configuration [35]. The peak at 1350 cm^{-1} (D band) is due to the presence of asymmetry in the graphene lattice [35]. As seen in Fig. 2a, the graphene monolayer has a very low-intensity first-order D peak due to high crystal symmetry. The ratio of intensities of D to G bands (I_D/I_G) is often utilized to quantify the defectivity level of the graphene so that as the defect density increases, the ratio of I_D/I_G increases (in the low defect density region). As seen in Fig. S1, incomplete removal of PMMA from the graphene transfer causes a considerable D peak to arise at around 1342 cm^{-1} . Hence the transfer process of graphene is extremely important to maintain the graphene's inherent electrical characteristics, particularly the surface sensitivity and high mobility. The D' band at 1620 cm^{-1} (appears as a shoulder of the G band) is due to electrons being scattered in the K–K direction (intervalley) [36]. The 2D peaks, labelled at 2680 cm^{-1} , are generated by a two-photon mode transition in the graphene lattice. Generally, monolayer graphene has an I_{2D}/I_G ratio of ~ 2 – 2.9 . However, the substrate-mediated enhancement of the Raman features of graphene causes a significant change in this ratio so that graphene on Si/SiO₂ may exhibit a ratio of 7–9 with a peak width of $\sim 35\text{ cm}^{-1}$, as previously reported [37,38].

Generally, oxygen-based functional groups are known to exist on transferred graphene due to the transfer process, storage conditions, and exposure to air [39]. Hence, graphene is intrinsically p-doped. From the atomic ratios in the survey XPS spectrum of the transferred graphene, as well as the high-resolution O 1s spectrum, shown in Fig. 2 b, we can calculate a 0.05 O to C atomic ratio in the graphene. The ratio is obtained by considering that 4.8% of the total oxygen atoms (O 1s peak at 534.19 eV) are bonded to aromatic

carbon, compared to 96.8% of the total carbon assigned to C=C (the total atomic percentages of C, O are 37.3% and 42.8%, respectively). Consistent with the C 1s high-resolution spectrum (Fig. 2c), the oxygen may be bonded to the graphene lattice as C–OH and C–O–C (286.5 eV), C=O (287.9 eV), and O–C=O (289 eV) [40]. The C–C, C–H peak at 285 eV will in part be due to the PMMA residual left on the surface during the transfer process [41,42].

Scanning Electron Microscopy (SEM) images (Fig. 2d and e) show the graphene monolayer after transfer onto SiO₂. The inevitably formed wrinkles or folded layers provide contrast as dark lines. The dry transfer of graphene leads to a continuous layer of graphene, even across the etched step. The G/Si interface creates a Schottky barrier due to the difference in graphene work function and the electron affinity of the n-Si substrate. Therefore, the device made by this junction exhibits current rectification with a rectification factor (r) of 64, evidenced by the J–V curve shown in Fig. 2 f. Since the carrier transport is controlled by the G/Si interface, the J–V behavior of the diode can be well described using the thermionic theory [29]:

$$J = J_s \left[\exp\left(\frac{qV_D}{\eta k_B T}\right) - 1 \right] \quad (1)$$

where J_s is the saturation current density, q is the electron charge, V_D is the applied voltage, k_B is the Boltzmann constant, T is the temperature and the η is the ideality factor. The ideality factor indicates how far the diode is from the ideal condition ($\eta = 1$) [30]. This theory posits that the current at the junction is dominated by the emission of thermally excited carriers (electrons or holes) over

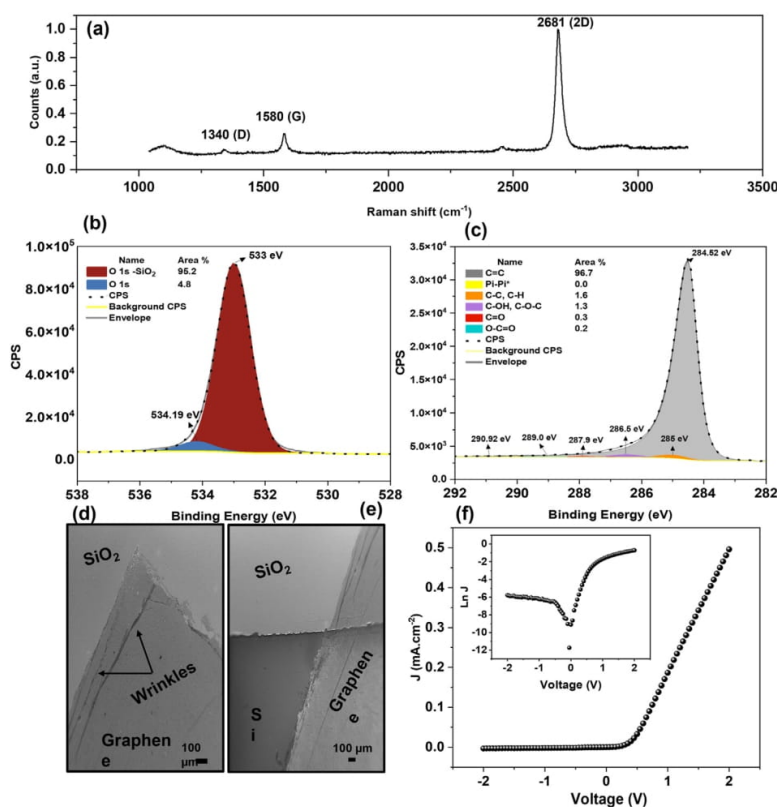


Fig. 2. a) Raman spectrum of monolayer graphene transferred on SiO_2 . XPS high resolution spectra of b) O 1s and c) C 1s for transferred graphene. FESEM images of transferred graphene on d) SiO_2 and e) interface of Si and SiO_2 indicating the continuity of the film, f) J-V curves of the G/n-Si device.

the existing barrier (built-in potential, Φ_{bi}) [13]. In a real device, deviation from ideality will increase at higher currents due to R_s [14], the series resistance which includes all resistances of the contacts, bulk metal and bulk semiconductor. It diminishes the effective voltage at the G/Si interface so that eq. (1) can be rewritten as [13]:

$$J = J_s \left[\exp\left(\frac{q \cdot (V - R_s I)}{\eta k_B T}\right) - 1 \right] \quad (2)$$

where $V - R_s I$ is defined as effective voltage (V_{eff}). The saturation current density, J_s , can be expressed as:

$$J_s = AA^* \exp\left(-\frac{q\Phi_{SB}}{k_B T}\right) \quad (3)$$

where Φ_{SB} is the Schottky barrier potential in eV and A^* is the Richardson's constant ($112 \text{ A cm}^{-2} \text{ K}^{-2}$ for n-type Si and $32 \text{ A cm}^{-2} \text{ K}^{-2}$ for p-type Si), and T is the temperature (in Kelvin). As seen in eq. (3), the magnitude of J_s is exponentially dependent on Φ_{SB} and therefore a slight modulation of Φ_{SB} causes a considerable change in J_s . The detailed mathematical approaches to obtain R_s , Φ_{SB} and η are presented in the Supplementary Material, Section S3).

Moreover, unlike an ideal diode, the J_s of the G/n-Si junction is not constant and varies depending on the applied reverse bias (Fig. 2f, inset). This is largely due to the voltage-dependent Fermi energy (E_f) of graphene, by which the magnitude of Φ_{SB} changes

due to the applied bias. Accordingly, adjusting the bias voltage to more negative values (with respect to graphene) causes the E_f to shift towards the Dirac point, decreasing the Φ_{SB} and therefore, enhancing the J_s [34,43]. In fact, the much lower density of states in graphene compared to its conductive alternatives leads to a strong bias dependence of the position of its Fermi level [43]. On the other side, the instant formation of native SiO_2 (with thicknesses between 1 nm–10 nm) on the etched Si introduces both acceptor and donor-type surface states on Si [44]. Nevertheless, the native oxide layer is often tunneled by thermionic currents while at higher oxide thicknesses, the presence of surface states on SiO_2 may pin the graphene E_f [45].

3.2. Impact of aqueous solution parameters

3.2.1. Effect of solution conductivity and ionic strength

The structure of an aqueous solution at the surface of graphene is known to depend on surface properties such as defect density, roughness, and edge configurations [46,47]. Ideal graphene with an infinite symmetry of sp^2 hybridization is considered to be a hydrophobic structure repelling the water [48]. However, the existence of local polarities such as defects brings the water closer to the surface and therefore, impacts of capacitive electrostatic gating effects enhance considerably. Nevertheless, the structure of water at the surface of graphene is still a controversial topic [49]. The formation of the EDL becomes important when the ionic strength of

the solution increases. To evaluate how the ionic strength may affect the electronic band structure and sensing performance of G/Si, we performed a series of experiments in which the ionic conductivity of the solution is increased stepwise by the addition of NaCl. The chosen concentrations of NaCl were 0, 0.17, 0.85, 3.42 and 8.55 mM corresponding to 0, 10, 50, 200, and 500 ppm, respectively. The chosen concentration range of NaCl provides a wide range of solution conductivity, from nearly $0.055 \mu\text{S cm}^{-1}$ in DI water to $0.8231 \text{ mS cm}^{-1}$ for 8.55 mM NaCl (see Fig. S2). The given range of NaCl concentration encompasses common applications in drinking water (with average solution conductivities of 0.2–0.8 mS/cm) [50] while still preserving the validity of the ideal solution approximation. Therefore, the activity coefficients of both monovalent ions (Na^+_{aq} and Cl^-_{aq}) remain above 0.95.

As expected, the J-V characteristics of the diode vary considerably with the increasing ionic strength of the solution. In particular, the overall R_s of the diode rises at a forward bias. Accordingly, increasing the concentration of NaCl to 8.55 mM can cause up to 257% change in R_s of the diode (Fig. 3a). In contrast, higher ionic strength increases the saturation current at any given reverse bias, resulting from a reduction of Φ_{SB} of the diode (Fig. 3a, inset). It is observed that the change in Φ_{SB} follows an exponential decay function, giving a higher change when Φ_{SB} is larger. In fact, since Φ_{SB} is determined by the difference in electron affinity of the silicon and the Fermi energy of graphene, at a constant dopant level of Si, the Φ_{SB} reduction is controlled by Fermi pinning at a high doping level [29]. Also, it should be noted that the measured Φ_{SB} is already less than the theoretical value (0.74 eV) due to the Schottky barrier lowering mechanism [13]. Therefore, further reduction in Φ_{SB} (by doping the graphene) is not thermodynamically favorable at the G/Si junction interface. Here, the change in R_s and Φ_{SB} behavior can be explained by a two-step mechanism: 1) adsorption of cations (e.g.,

Na^+) on the surface of graphene (which contains oxygen-based functional groups) to form the Inner Helmholtz Layer (IHL), subsequently causing the assembly of anions (e.g., Cl^-) in the Outer Helmholtz Layer (OHL); 2) electrostatic gating by the generated EDL attracts excess electrons to the graphene surface. Here, graphene (–) and IHL (+) can be modeled as the plates of a capacitor, causing a static charge separation across an infinitely thin dielectric [51] (Fig. 3b). Given that the graphene starts out being p-doped, the charge carrier density is diminished by the accumulation of excess negative charges, therefore resulting of an increase of R_s of the device. In contrast, Φ_{SB} decreases since the E_f shifts towards the Dirac point. Therefore, the ionic strength of the solution will heavily affect the device performance of a G/n-Si Schottky diode. It is important to note that the calculation of Φ_{SB} is done at 0 V where no bias is applied on the surface. Therefore, the formation of the EDL is governed by the chemistry of the surface.

The charge screening due to electrostatic gating can be discussed using Debye-Hückel theory. The electric field created by an ion in the electrolyte changes the solid surface potential by the formation of a compact layer of immobile ions in the vicinity of the surface [52]. Moreover, independent interactions of ions in an electrolyte induce an electric field with the charge screening length of [53]:

$$\lambda_D = \sqrt{\frac{\epsilon_0 \epsilon_r k_B T}{2Ie^2}} \quad (4)$$

where ϵ_0 is the vacuum permittivity ($8.85 \times 10^{-12} \text{ F m}^{-1}$), ϵ_r is the permittivity of the solution, k_B is the Boltzmann constant ($1.38 \times 10^{-23} \text{ J K}^{-1}$), T is the temperature (in Kelvin), e is the electron charge ($1.6 \times 10^{-19} \text{ C}$), I is the ionic strength. The ionic strength of an aqueous solution is defined as $I = \frac{1}{2} \sum c_i z_i^2$ where c_i

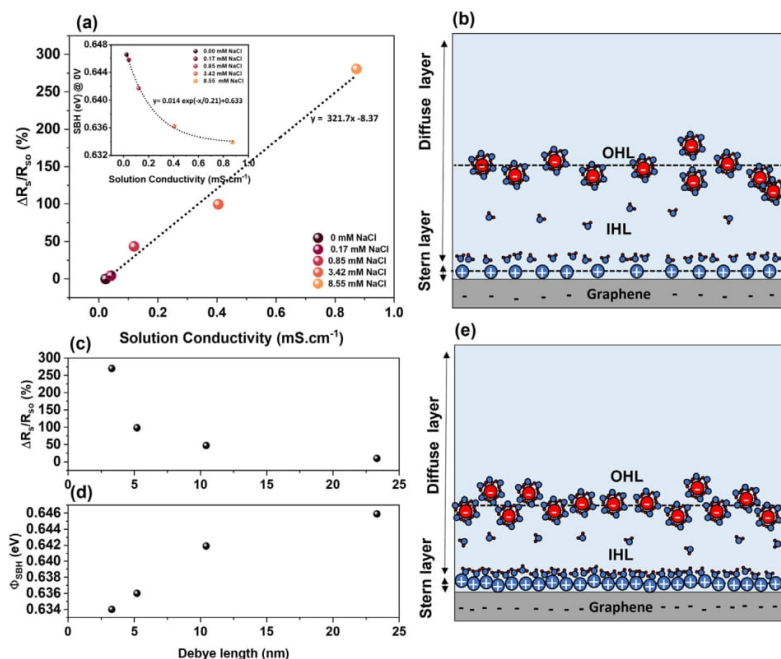


Fig. 3. a) Variation of G/n-Si R_s by exposure to various concentrations of NaCl (the inset shows changes in Φ_{SBH} with solution conductivity, i.e., ionic strength), b) The schematic illustration of the EDL and charge doping of the graphene surface by the inner Helmholtz layer. The variation of c) R_s and d) Φ_{SB} as a function of Debye length shows the impact of changes in the EDL on surface characteristics, e) The schematic representation of EDL at high ionic strength. An increase of ionic strength reduces the screening length (Debye length).

and z_i are the concentrations and charges of the different ions, respectively [53]. As per equation (4), the Debye length λ_D is inversely proportional to the square root of the ionic strength of the solution.

According to equation (4), an increase in ionic strength causes a reduction in the Debye length of an aqueous solution, thus reducing charge screening length. The calculated Debye length of a 50 ppm NaCl solution is ~ 24 nm while this value drops to ~ 3 nm for 500 ppm NaCl, thus intensifying the impact of EDL on both R_s and ϕ_{SB} . Notably, a 175% change in R_s results from a reduction of the Debye length from 5 nm to 3 nm (Fig. 3c), while the change in R_s for a Debye length reduction from 25 to 5 nm is only 98%. At the same time, ϕ_{SB} is lowered as the Debye length is reduced (Fig. 3d). The schematic illustration of an EDL resulting from a high ionic strength aqueous solution is shown in Fig. 3e. As seen, the IHL is concentrated in Na^+ ions and is closer to the surface. Hence, the mean charge screening length decreases, leading to higher surface n-doping. Therefore, changes in the ionic strength of the solution (and hence the structure of the EDL) have a considerable impact on the modulation of the charge carrier density in graphene.

3.2.2. Effect of pH

To obtain a full insight into the operation of a G/Si Schottky junction in an aqueous solution, the general pH response of graphene devices should be well understood. As seen in Fig. 4a, increasing the pH causes a reduction in the R_s while lower pH results in a higher R_s . The mechanism by which graphene perceives the pH variation has been subject to debate due to the existence of competing mechanisms by which the graphene surface responds to pH [54]. It has recently been shown that a (near) defect-free graphene surface tends to repel the water molecules due to its hydrophobicity, resulting in a very low susceptibility to pH variations (and any other ionic interactions) [55]. However, the presence of "external" chemical species in graphene introduces polar defect sites which favor stronger interactions with the aqueous phase and the formation of an EDL [56]. The defect density of graphene thus determines the overall pH response. At low pH, the accumulation of $\text{H}_3\text{O}^+_{\text{aq}}$ ions close to the graphene's surface (in the IHL) causes surface charge doping with electrons. This accumulation is often due to the presence of negatively charged oxygen-containing functional groups on the graphene surface. Therefore, this n-doping causes an increase in device R_s and decreases the ϕ_{SB} . In contrast, accumulation of OH^-_{aq} in the IHL (or reduction in $\text{H}_3\text{O}^+_{\text{aq}}$) causes p-doping and consequently a lower R_s and a higher ϕ_{SB} [57]. Nevertheless, since the dominant pathway for modulation of the

surface current is through electrostatic charging, the overall variations of R_s (Fig. 4b) and ϕ_{SB} (Fig. 4b, inset) do not exceed $\sim 20\%$ and 1% for the pH range of 3–8, respectively. However, according to the XPS results shown in Fig. 2c, the presence of pH-sensitive functional groups on graphene (including carboxyl and hydroxyl groups) cannot be ignored. We have recently shown that the deprotonation of carboxyl groups (and amine groups if present) near their pK_a value of 3.41 induces extra electrons to the surface [54]. Similarly, hydroxyl groups ($-\text{OH}$) at high pH values close to their pK_a of 8.51 undergo protonation, thus hole-doping the surface. This protonation/deprotonation of functional groups enhances responses due to defects and will provide an opposite sign response compared to the capacitive charge screening by the EDL [58]. This can be seen in the change in ϕ_{SB} (Fig. 4b, inset). From pH 3 to 4, the ϕ_{SB} does not change considerably, meaning the deprotonation of $-\text{COOH}$ to $-\text{COO}^-$ on the surface balances the p-doping caused by EDL. Analogous behavior is seen at pH 6–8 for the deprotonation of $-\text{OH}$ to $-\text{O}^-$. Hence, the balance between the two competing mechanisms of pH-sensitive groups and electrostatic gating effects will determine the net response of graphene to pH variation. At low defect density – as is the case for the G/n-Si Schottky devices presented here – the EDL-induced gating effect will dominate, meaning that the acidic and basic solutions dope the surface with electrons and holes through electrostatic interactions, respectively. In contrast, a higher defect density, particularly of pH-sensitive groups, would result in the dominance of direct charge transfer upon protonation/deprotonation of the groups. Since these two mechanisms provide opposite responses to the surface, they will balance each other out at a certain cross-over point. At this point the surface would be pH-insensitive, providing a chance to develop pH-insensitive graphene-based devices. A variation in pH, therefore, affects the junction performance through both EDL and defect-induced mechanisms. Special attention must be devoted to understanding the impact of pH in graphene devices.

3.2.3. Effect of oxidation-reduction potential (ORP)

The ORP of a solution describes its average ability to act as an oxidant in a redox reaction as a result of the presence of an ensemble of dissolved redox-active species. These species will also be present in the EDL and act as n-dopants (reducing agents) or p-dopants (oxidants) at the graphene surface. Therefore, the performance of the G/Si junction in an aqueous environment will be strongly impacted by the ORP. The ORP of natural water is often dominated by the presence of dissolved oxygen (DO) [50]. In order to prevent pathogen growth in drinking water, however, the ORP is

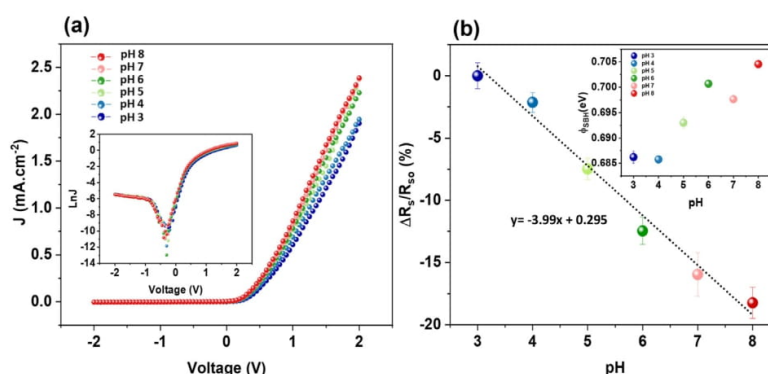
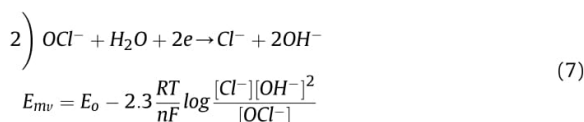
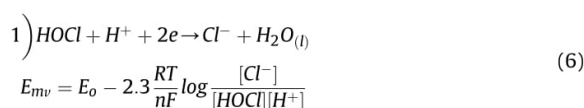


Fig. 4. a) J-V curves of a G/n-Si Schottky diode upon exposure to pH 3–8 (inset illustrates the corresponding semi-logarithmic graph), b) change in series resistance and ϕ_{SB} (inset) of the device as the results of pH.

often artificially increased by the addition of a disinfectant. Free chlorine, a commonly used disinfectant for drinking water, can be employed to evaluate the impact of solution ORP on the performance G/n-Si junctions. In practice, the ORP of a solution is measured as the potential difference between a platinum working electrode and a reference electrode and is governed by the Nernst equation as [59]:

$$E_{mv} = E_o - 2.3026 \frac{RT}{nF} \log \frac{[\text{reducer}]^r}{[\text{oxidizer}]^o} \quad (5)$$

where E_{mv} , E_o , R , T , n , and F are the actual redox potential, standard redox potential, gas constant, temperature, number of electrons transferred during the reaction, and Faraday constant, respectively. Depending on solution pH, the term free chlorine encompassed Cl_2 , HOCl_{aq} and OCl^-_{aq} . Above pH 5, the presence of HOCl_{aq} and OCl^-_{aq} as oxidizers in pH-dependent equilibria can be written as:



Accordingly, free chlorine at pH 5 will consist of 99.71% HOCl and 0.29% OCl^- , whereas at pH 9.5 OCl^- is dominant at 99% [60]. Below pH 5, the equilibrium starts shifting towards Cl_2 as the active species, limited in concentration by its solubility. Since we use a dilute sodium hypochlorite solution as a source of free chlorine, and HOCl is a weak acid, the addition of up to 1 ppm free chlorine increases the pH from 5.5 to 6.4 (Fig. S3) according to:

$$K_a = \frac{[\text{OCl}^-][\text{H}^+]}{[\text{HOCl}]}, pK_a = 7.25 \text{ at } 25^\circ\text{C} \quad (8)$$

Over the entire observed pH range, HOCl is the dominant free chlorine species, with only small amounts of OCl^- present. Nevertheless, the impact of pH during the ORP measurements cannot be neglected since according to equations (6) and (7), an increase in $[\text{H}^+]$ (decreasing the pH) results in a higher ORP. Therefore, this pH response may constructively or destructively overlap the actual device response to ORP, affecting the accuracy of the measurement.

As seen in Fig. 5a, exposing a G/n-Si junction to increasing free chlorine concentrations (see Fig. S4a for the relationship between free chlorine concentration and ORP), causes an increase in the forward bias current of the device. The variation of R_s with ORP is shown in Fig. S4b, indicating that R_s varies with ORP due to the addition of free chlorine.

The R_s of the device changes from 11.2 to 8.1 k Ω , corresponding to 0 ppm and 1 ppm concentration of free chlorine, respectively (Figure S5a). To calculate the response of a Schottky diode to ORP, the following equation is used:

$$\text{Response (\%)} = \frac{(R_s - R_{s0 \text{ ppm}})}{R_{s0 \text{ ppm}}} \times 100 \quad (10)$$

where R_s is the series resistance at a given free chlorine concentration, with 0 ppm serving as a baseline. As seen in Fig. 5b, the overall reduction in R_s can be up to -17% . This enhancement in

current density (or reduction in R_s) is mainly due to the oxidizing (i.e., electron-withdrawing) characteristics of the solution at a high ORP value, resulting in the induction of holes. Since the graphene has already been p-doped, the overall R_s across the film and junction decreases. Accordingly, the hole doping of graphene should shift the E_f away from the Dirac point, leading to a higher value of Φ_{SB} (at 0 V). However, this trend is not observed in the Schottky device, showing that in addition to the ORP of the solution other environmental parameters (including pH and ionic strength) also affect the Φ_{SB} variation (the H-J graphs of devices to obtain Φ_{SB} are shown in Figure S5b). According to Fig. 4b our G/n-Si device will show a nearly -8% change in R_s (increase in Φ_{SB} from 0.694 to 0.698 eV) as a result of the expected pH change from 5.5 to 6.4. This confirms that a part of the response to free chlorine is due to the change in pH. Moreover, the addition of free chlorine to DI water increases the ionic strength of the solution. Therefore, the change in R_s and Φ_{SB} is in part due to the electrostatic gating effect and reduction of λ_D . As seen in Fig. 5c, the addition of 1 ppm free chlorine to DI water causes a nearly 18% change in solution conductivity, while the change is less than 1% when 3.42 mM NaCl is present. Therefore, this is necessary to maintain the solution conductivity above a certain value (0.40 mS cm^{-1}) to minimize the impact of ionic strength on device response. However, a significant increase of the ionic strength will suppress the response to ORP due to the domination of electrostatic gating of EDL over the surface oxidation by free chlorine. As seen in Fig. 5d increasing the ionic strength reduces the device response at a particular concentration (here 0.5 ppm free chlorine, 797 mV ORP at pH 5.9). The overall reduction of the G/n-Si response upon addition of 8.55 mM NaCl is calculated to be $\sim 75\%$. This demonstrates that the ORP interaction with the surface is strongly dependent on the p-doping of graphene through charge screening of free chlorine.

3.3. Application as a sensor by introducing selectivity through chemical functionalization

Up to this point, we have quantified how G/n-Si Schottky junctions immersed in aqueous media respond to changes in their environment. These junctions can be utilized in sensing applications if a selective response to a single parameter can be obtained while minimizing interferences. Even though blank G/n-Si devices can detect changes in free chlorine concentration, they exhibit a non-specific response to a range of parameters including solution ORP, pH and ionic strength. Therefore, they cannot be used to selectively detect free chlorine. A selective response can be achieved by surface functionalization with moieties that undergo selective chemical interactions [10,61,62]. Here we demonstrate that the functionalization of a G/n-Si diode with 1-aminopyrene (AP) can enhance both sensitivity and selectivity towards the detection of free chlorine. The pyrene rings can anchor the AP to the graphene surface, providing a stable functionalization, while amine groups provide selectivity toward free chlorine.

The Raman spectrum of AP is shown in Fig. 6a (bottom spectrum), including the distinct features of the pyrene ring systems at 1621, 1595, 1406, 1220 and 1187 cm^{-1} . In general, pyrene peaks in the range of 1650-1500 cm^{-1} are assigned to C–C stretching modes mixed with the in-plane vibration of C–H (right dashed box). The peaks at 1406 cm^{-1} (middle box) and 1220 cm^{-1} (left box) originate from C–C stretching coupled with ring-breathing vibrations and C–H in-plane bending vibrations, respectively. The peak at 1187 cm^{-1} is assigned to N–H stretching vibrations of amine groups [63].

The simultaneous presence of Raman features typical for both graphene and AP in the spectrum of AP-graphene (Fig. 6a, top spectrum), confirms the successful functionalization of graphene.

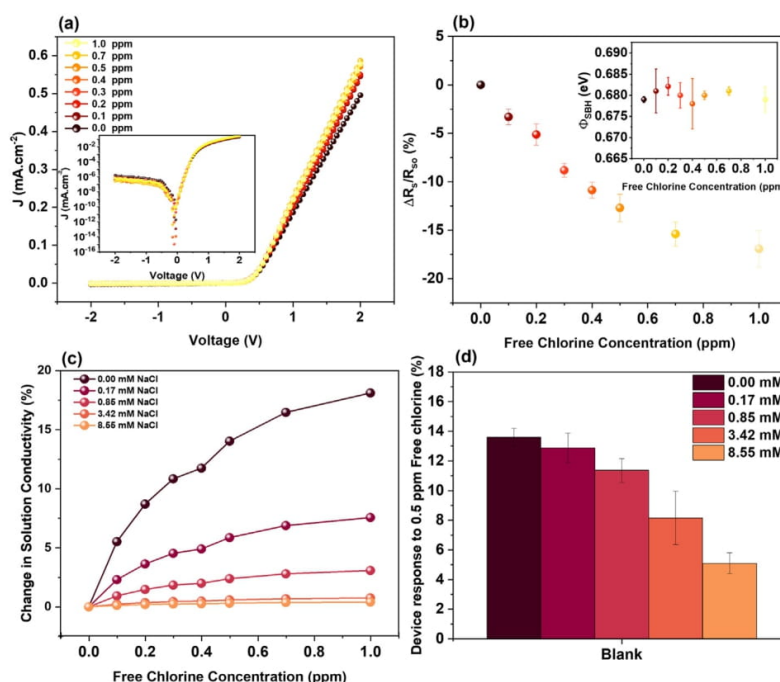


Fig. 5. a) J-V curves of G/n-Si exposed to various concentrations of free chlorine. b) obtained device response by the change in resistance upon increasing the free chlorine concentration (inset shows the change in ϕ_{SB}). c) Graph represents the change in solution conductivity by addition of free chlorine at different NaCl background concentrations, d) change in ORP response of G/n-Si junction (blank) as a function of the ionic strength of the solution.

As seen in the top spectrum, the higher intensity of the peak at 1593 cm^{-1} compared to bare AP (Fig. 6a bottom spectrum) indicates the presence of newly emerging vibrations perpendicular to the surfaces of pyrene and graphene (due to π - π interactions). Moreover, the G band of graphene overlaps with the AP peak at 1593 cm^{-1} , causing a selective enhancement of in-plane vibrations of sp^2 -hybridized C-C bonds. Hence, graphene functionalization with pyrene derivatives through π - π interactions decreases the delocalization of π electrons and charge-dopes the surface.

The J-V curves of AP/G/n-Si upon exposure to water are shown in Figs. S6 and S7. R_s is found to increase once the AP/graphene starts interacting with the DI water. Moreover, similar to the blank G/n-Si (Figure S7a), the AP/G/n-Si shows a slightly higher J_s in aqueous solution compared to the dry state (Figure S7b). These changes are due to the instant formation of an electrical double layer (EDL) on the surface and the pH response of the surface. From the J-V curves of AP-G/n-Si (Fig. S6) and their semi-logarithmic graphs (Fig. S6, inset) upon exposure to free chlorine it can be found that R_s is reduced dramatically compared to the blank device, demonstrating that the surface sensitivity towards free chlorine is enhanced. As seen in Fig. 6b, the R_s of the AP-functionalized sensor changes by nearly -80% upon exposure to 1 ppm free chlorine. In contrast, R_s of the blank sensor only changes by -17% under the same conditions (Fig. 5b, calculated values for R_s and ϕ_{SB} in Figures S8a and b). ϕ_{SB} of the AP-doped device (Fig. 6c) also increases by almost 3% upon addition of 1 ppm free chlorine.

One possible mechanism for the response in AP-G/n-Si is due to the chlorination of the amine group of the AP. In fact, multiple steps of amine ($-NH_2$) oxidation to monochloramine ($-NHCl$) and dichloramine ($-NCl_2$) may offer a promising pathway to sense free chlorine. X-ray photoelectron spectroscopy (XPS) was used to

evaluate this hypothesis. High-resolution Cl 2p spectra of AP-doped graphene before exposure to free chlorine reveal two peaks at 200.18 and 201.78 eV corresponding to Cl $2p_{1/2}$ C-Cl and Cl $2p_{3/2}$ C-Cl, respectively (Fig. 6d) [64]. The presence of organic chlorine on graphene has already been detected by exposing the graphene to chlorine gas in graphene-based gas sensors. However, it has been suggested in the literature that the appearance of two new peaks at 198.78 eV (Cl $2p_{3/2}$ chloride) and (200.38 eV Cl $2p_{3/2}$ chloride) is due to chlorine that is covalently bound to the amine nitrogen of the pyrene ($-N-Cl$) (Fig. 6e) [65–67]. Further evidence of chlorination can be observed in N 1s spectra. The peak located at 402.02 eV can be assigned to the protonated form of amine (Fig. 6f and g) [68]. However, it has been assigned to the formation of $-NH-Cl$ bonds elsewhere [65]. To obtain an insight into the formation of chloramine, we found that the atomic ratio of Cl (associated with amine chlorination, not organic chloride) to N (amine) changes from 0 to 0.21 as a result of the free chlorine treatment. This means that more than 20% of the amine N is chlorinated by free chlorine. The lack of evidence for the formation of dichloramine implies that free chlorine detection occurs through one-step chloramination, and dichloramine is unlikely to form. This can be confirmed by the pH dependence of chloramine species as well. As suggested in the literature [69], the formation of dichloramine is more likely at low pH values (pH 3–4) whereas here the addition of hypochlorite to the solution increases the pH from 5.5 to 6.4. Hence, dichloramine will not be thermodynamically stable at high pH.

To understand the variation of ϕ_{SB} in blank and doped conditions, Fig. 7 schematically represents how ϕ_{SB} varies with free chlorine concentration. The simultaneous influence of multiple effects on bare sensors causes the fluctuations of ϕ_{SB} with high error bars as shown in Fig. 5b, inset. Variations in the ionic strength

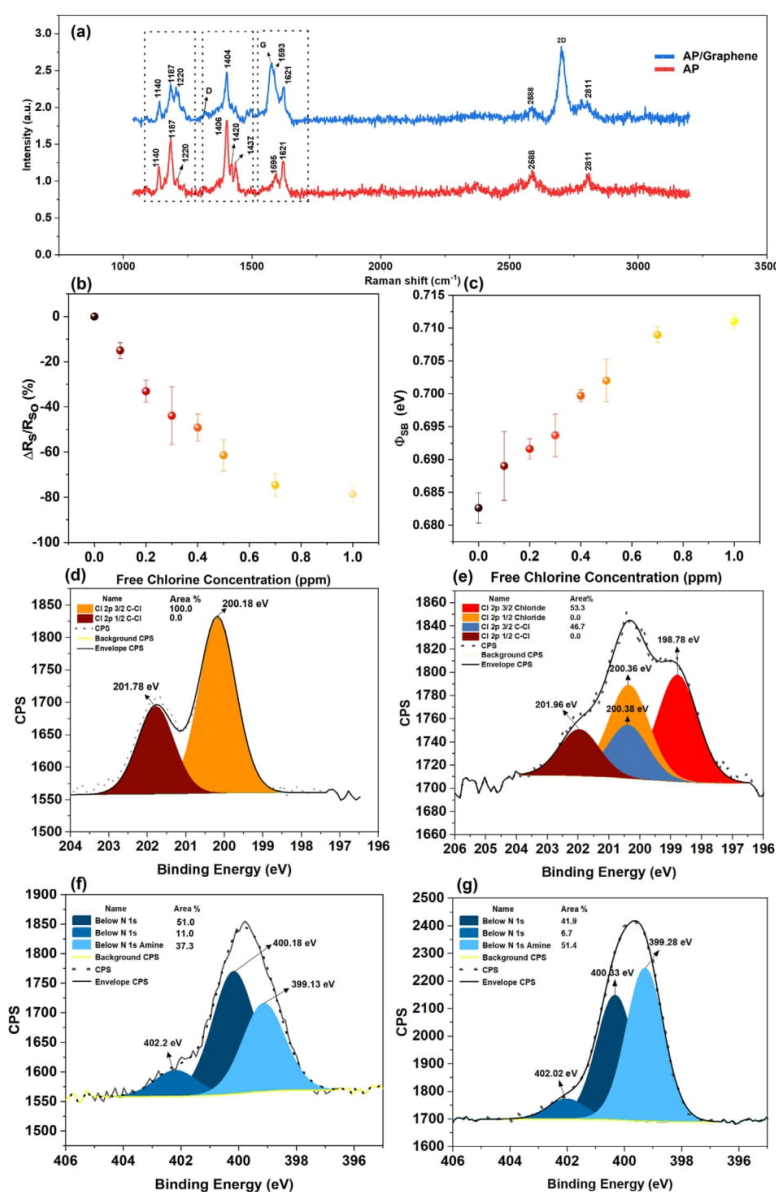


Fig. 6. a) Raman spectra of 1-aminopyrene (bottom) and 1-aminopyrene doped graphene (top), extracted b) R_s and c) Φ_{SBH} variation of devices at given free chlorine concentrations, Cl 2p high-resolution XPS spectra of AP/G/n-Si d) before and e) after exposure to free chlorine. N 1s high-resolution XPS spectra of AP/G/n-Si f) before and g) after exposure to free chlorine

of the solution, as well as electrostatic gating effects of non-faradic hydronium ($\text{H}_3\text{O}^+_{\text{aq}}$) and hydroxide (OH^-_{aq}) ions, may impact the charge doping of graphene oppositely [70]. Therefore, since the addition of free chlorine (a salt of a weak acid (HOCl) and a strong base (NaOH)) increases the pH and the conductivity of the solution in addition to the interactions of free chlorine with graphene [71], the variation of Φ_{SB} may not follow a clear trend (Fig. 5b, inset). The comparison of the responses of blank and AP-doped devices to 0.5 ppm free chlorine is shown in Fig. S9. As explained before, the ORP response of blank devices is strongly affected by ionic strength

(~75% reduction in device response from DI water to 500 ppm NaCl) while covalent interactions are dominant in AP/G/n-Si and less affected by changes in the EDL.

In contrast, the AP-functionalized sensor exhibits an up to 4% increase in Φ_{SB} upon exposure to 1 ppm free chlorine (Fig. 6c) due to AP selectively forming a chloramine species, as discussed in the XPS results. The charge transfer upon oxidation of the amine groups directly impacts the electronic structure of the graphene sheet due to close π - π interactions with the pyrene rings. Hence, band bending due to the band alignment at the G/n-Si interface becomes

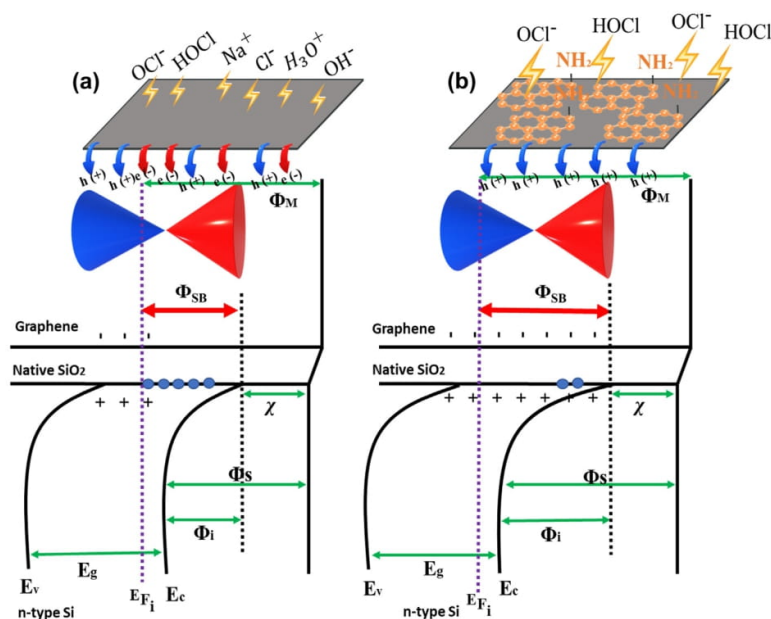


Fig. 7. Schematic illustration of the mechanism by which the electronic band structures of G/n-Si are modulated upon addition of free chlorine on a) blank and b) AP-doped sensors. The electronic structure highlights the conduction band (E_c), valence band (E_v), and Fermi energy (E_f) of the n-Si in contact with graphene. The position of E_f (purple dashed line) represents the p-doped nature of the graphene. Φ_M , Φ_S , Φ_i , and χ are indicative of graphene work function, Si work function, the built-in potential of the junction, and electron affinity of Si, respectively.

more extreme, providing a higher built-in potential against electron transport at the conduction band edge of Si. These enhanced internal electric forces increase Φ_{SB} and widen the depletion region into the bulk Si (shown by positive and negative signs). Therefore, a higher degree of rectification is expected in doped sensors compared to blank sensors. The degree of rectification (rectification factor r) is obtained by the ratio of currents at \pm voltage of the flat band region (V_{FB}) [34]. The flat band region is where the R_s is dominant, and the semi-logarithmic J-V curve deviates from the initial straight behavior. In our proposed sensors, V_{FB} is predicted to be ± 0.4 V so that the variation of r can be plotted as in Fig. S10. As presented, the doped sensor demonstrates a considerably higher r at any free chlorine concentration, and it is enhanced as the free chlorine concentration increases.

3.4. Interference studies

To further evaluate the sensing capability of this platform, we studied interferences due to commonly present anions and cations, other oxidants, and pH variations. The anionic interferences were measured for 2.5 ppm HPO_4^{2-} , 250 ppm SO_4^{2-} , 25 ppm NO_3^- , 43.5 ppm Cl^- (in addition to the 121.25 ppm background), 11.2 ppm HCO_3^- , and compared to 0.5 ppm free chlorine (Fig. 8a - left side). The concentration of each ion was chosen based on maximum guideline values or concentrations usually found in drinking water [72,73]. As seen, the response originating from free chlorine is higher (for both blank and doped sensors) compared to other analytes, which is due to the strong oxidizing nature of free chlorine. However, the doped sensor demonstrates nearly -60% response while the blank offers only -13% response to 0.5 ppm free chlorine. This compares with less than 4% response to HPO_4^{2-} , SO_4^{2-} , and NO_3^- . However, the addition of Cl^- and HCO_3^- causes blank sensor responses of 5% and 7%, respectively. Common cationic

interferences also result in considerably lower responses (less than 4% for K^+ (4.2 ppm), Mg^+ (7.1 ppm) and Ca^+ (12.3 ppm)) compared to free chlorine (Fig. 8a - right side). However, the addition of Na^+ leads to a 7.5% response in the blank sensor. We believe this could be due to the enhanced ionic strength of the solution through the addition of 27.5 ppm Na^+ in addition to the existing Na^+ background (78.66 ppm or 3.42 mM). Moreover, as seen in Fig. 8b, the sensors still show a substantial response upon exposure to other common disinfectants (with the same concentration as free chlorine, 9.53 μM or 0.5 ppm). Exposure to MnO_4^- caused -33 and -21% changes in R_s for blank and doped, respectively. This could be due to the strong oxidizing nature of MnO_4^- and/or the direct oxidation of the surface. The fact that both sensors respond to MnO_4^- highlights the fact that the ORP response is rather strong, even in doped sensors, due to the accessible surface area of graphene to oxidants. It is also worth pointing out that the AP doped sensors show a lesser response to permanganate and peroxide, but a higher response to free chlorine, due to the AP layer interfering with the non-specific ORP response.

Variations in pH also impact the sensor response. The results in Fig. 4 show that a blank G/n-Si device gave an approximate pH sensitivity of -3.99%/pH. For AP/G/n-Si, however, the presence of amine groups on pyrene rings anchored to graphene provides pH-sensitive sites on the surface so that their protonation/deprotonation has the potential to dominate the pH responsivity. As seen in Fig. S11 corresponding to AP-doped graphene, except at pH 3, the rest of the J-V curves overlap at both forward and reverse currents. The UV-visible spectra of AP molecules at different pH are shown in Fig. S12, demonstrating that the protonation/deprotonation of AP occurs at low pH around 3–4. At high pH values, three prominent absorption peaks at around 288, 353 and 390 nm are the main characteristics of AP [52]. At pH 3, new peaks at 338, 323 and 309 nm arise from the presence of the protonated form of the

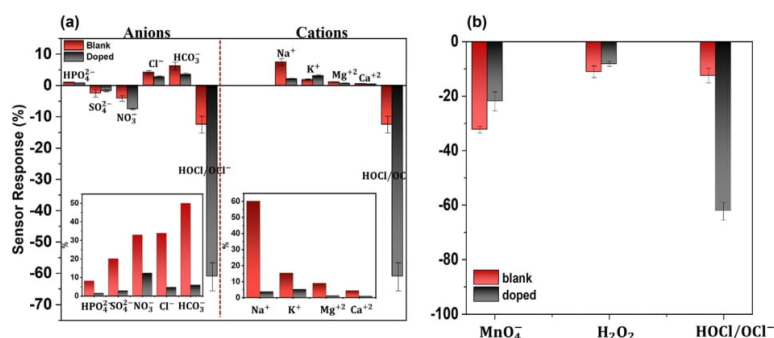


Fig. 8. a) Anionic interference (on the left side of dashed line) study by addition of 2.5 ppm HPO_4^{2-} , 250 ppm SO_4^{2-} , 25 ppm NO_3^- , 43.5 ppm Cl^- , 11.2 ppm HCO_3^- , and 0.5 ppm free chlorine (the inset shows the relative sensor response of anions to free chlorine response). b) cations interference test (on the right side of the dashed line) by addition of 4.2 ppm K^+ , 7.1 ppm Mg^{2+} , and 12.3 ppm Ca^{2+} (inset shows the relative sensor response of cations to free chlorine response), b) oxidant interference study at pH 5.6 by addition of 1.34 μM of each oxidant (0.5 ppm HOCl = 9.53 μM)

molecule. The theoretically calculated $\text{pK}_a = 4.13$ of AP molecules attached on a sheet of graphene ($8 \times 8 \text{ cm}^2$) is consistent with the UV–visible data, confirming that the majority of protonation/deprotonation occurs around pH 3–4 [54,74].

As the pH increases from 3 to 8, conversion of pyrene- NH_3^+ to Py- NH_2 induces electrons to the surface and therefore, the overall R_s increases (Fig. S13) while Φ_{SB} drops (Fig. S13, inset). These two regimes can be observed in Fig. S13 where the change from pH 3 to 5 causes a rise in R_s while R_s decreases in the range of pH 5–8. Moreover, the maximum pH response of AP-graphene does not exceed 9% while more than 7% change is associated with the change of pH from 3 to 4. Therefore, this pH insensitivity at pH above 5 makes it possible to perform sensing measurements independent of the pH response. In contrast, the blank sensor has a 10% response to variation of pH between 5 and 8.

3.5. Comparison with chemiresistive platforms

The nature of the response in a Schottky diode is different compared to FETs or chemiresistive platforms. In the latter, Ohm's law dictates a linear dependence of current and voltage while the gate potential modulates the surface resistance through the electrostatic gating effect. During the operation of a FET at zero gate voltage, it effectively works as a chemiresistor. To compare the performance of a chemiresistive design with the Schottky diode geometry, our device design allows simultaneous operation in both modes. The chemiresistive measurements of blank graphene and AP/graphene upon exposure to 0.7 ppm free chlorine (shown in Figures S14a and b, respectively), reveal the stepwise reduction of resistance upon addition of free chlorine. Due to the slower kinetics of the chloramination reaction, the AP/graphene device responds

more slowly to free chlorine compared to the sharp ORP response of bare graphene. Nevertheless, the doped device exhibits a nearly 2 times higher sensitivity (–15% and –7.2% response to 0.7 ppm free chlorine, respectively) (Figure S14c). Comparing these results with corresponding Schottky diode measurements shown in Fig. S15 demonstrates a nearly 5.5 times higher sensitivity for the AP-G/n-Si device compared to the G/n-Si device and the chemiresistive geometry.

The different performances of these two sensing geometries originate from the nature of the change in R_s . Among the contributions of contacts, bulk metal, and bulk semiconductor resistances to the overall R_s , the contacts can be considered unchanged since they are removed from any sensing interactions by a thick dielectric cover. In a chemiresistive geometry, the change in R_s of the graphene between the contacts determines the sensitivity. However, in a Schottky junction, in addition to the contributions of the contacts and the graphene sheet, there is also a contribution of the junction resistance to R_s , which plays a decisive role in determining the sensitivity. Therefore, the difference in responses in Schottky diode geometry and chemiresistive geometry originates from the Schottky barrier formed at the interface of Si and graphene. The exponential dependence of R_s on Φ_{SB} means that the small change in Φ_{SB} changes R_s of the junction considerably, making the junction sensitive to small variations. The Schottky junctions' response follows a linear range of 0.01–0.7 ppm, a LOD of 3.1 ppb (59 nM) and a sensitivity of 10.2 ppm^{-1} ($0.53 \mu\text{M}^{-1}$).

A comparison of G/n-Si junction sensing performance with other reported designs has been provided in Table 1. As seen, the LOD of the proposed G/n-Si Schottky junction platform is lower than most published electrochemical designs and FETs. This indicates that the G/n-Si junction provides excellent sensitivity for

Table 1
Comparison of solid-state free chlorine sensors in the literature with this research.

Sensing principle	Conductive layer	Selective species	Linear range [ppm]	LOD [ppb]	Ref
Potentiometry	Stainless steel vs. Pt	–	1–10	–	[75]
Amperometry	Pencil trace	Graphite	7–500	6600	[76]
	Glassy carbon	Prussian Blue	0.009–10	9	[77]
	Glassy carbon	Polydopamine at GO	0.7–16	3	[78]
	Pencil graphite	Carbamate	0.4–6	400	[79]
	Graphene	Graphene	0.07–0.7	7	[80]
Chemiresistive	Pencil trace	Oligoanilines	0.06–60	–	[81]
	Pencil trace	Oligoanilines	0.1–60	–	[71]
	CNTs	Oligoanilines	0.06–60	–	[61]
	CNTs	CNTs	0.03–8	–	[82]
Schottky Diode	G/n-Si	AP	0.01–0.7	3	This work

GO = Graphene oxide; GLC = Graphene like carbon, PCAT = phenyl-capped aniline tetramers; CNTs = carbon nanotubes; AP = 1-Aminopyrene.

the detection of analyte without the need for gate or reference electrode, offering a robust and perhaps simpler fabrication design. Although the working range of the device goes as low as 10 ppb free chlorine, it starts saturating at lower concentrations (0.7 ppm) compared to other conventional methods. Therefore, the sensor is of the highest benefit in applications where high sensitivity is required, such as disinfectant removal by filtration devices at the point of use.

4. Conclusion

We demonstrate the use of a G/n-Si Schottky platform in aqueous environments, report the impact of solution parameters on their performance, and elucidate the working principle of these devices in water. The impact of ionic strength of the solution was demonstrated to be significant (up to 257% change in R_s) due to the instant formation of an EDL on the graphene surface and capacitive screening of charges. The presence of oxygen-containing functional groups or contaminations provides negative surface charges and therefore, the IHL on graphene is expected to be formed by cations from the solution. As an increase in ionic strength causes the reduction of the Debye length and more n-doping of the surface, a higher ionic strength causes a more compact EDL and intensification of charge doping. Moreover, the solution pH also impacts R_s and Φ_{SB} . At low (high) pH, the accumulation of $H_3O^+_{aq}$ (OH^-_{aq}) ions in EDL causes n-doping (p-doping) of graphene and a decrease (increase) in the R_s of the junction. The ORP of the solution was also found to influence the performance of the device so that higher ORP may lead to oxidization of the graphene surface. The ORP of the solution was controlled by the addition of free chlorine.

To demonstrate the sensing capabilities and the possibility of surface modification of this platform, we modified the graphene surface with 1-aminopyrene to provide a sensitive and selective area for the detection of free chlorine. The sensing measurements reveal up to 80% change in R_s upon exposure to 1 ppm free chlorine in AP/G/n-Si samples, giving almost 5.5 times higher sensitivity than bare graphene sensors. Moreover, we demonstrate that the protonation/deprotonation of amine groups on the graphene dominates the pH response of doped graphene at low pH while the surface becomes pH-insensitive at higher pH. This is mainly due to the opposite signs of responses originating in surface EDL induce response and defect protonation/deprotonation.

Associated content

Detailed information on experimental sections, X-ray photoelectron spectroscopy (XPS), Raman spectra of the graphene, mathematical approach to obtain the series resistance and Schottky barrier height of the diode, impacts of free chlorine concentration on conductivity, variation of conductivity by addition of NaCl, and spectroscopic analysis of AP are provided in the Supplementary Material.

CRediT authorship contribution statement

Shayan Angizi: Methodology, Investigation, Writing – original draft. **P. Ravi Selvaganapathy:** Conceptualization, Writing – review & editing. **Peter Kruse:** Supervision, Conceptualization, Methodology, Writing – review & editing.

Declaration of competing interest

The authors declare that they have no known competing financial interests or personal relationships that could have appeared to influence the work reported in this paper.

Acknowledgment

The authors thank Doris Stevanovic from the Centre for Emerging Device Technologies (CEDT), McMaster University for granting access to the cleanroom; Dr. Alex Adronov (McMaster) for granting access to a Raman spectrometer; Chris Butcher in the Center for Canadian Electron Microscopy (CCEM), McMaster University for help with SEM, Dr. Mark Biesinger (Surface Science Western) for the XPS operation and data analysis, Dr. Chang Xu for granting access to Silicon oxidation furnace, Md. Ali Akbar for fruitful discussions on ORP measurement and free chlorine detection.

The authors acknowledge financial support from the Natural Sciences and Engineering Research Council of Canada (NSERC) through the Discovery Grant Program and a Canada First Research Excellence Fund project “Global Water Futures.”

Appendix A. Supplementary data

Supplementary data to this article can be found online at <https://doi.org/10.1016/j.carbon.2022.03.052>.

References

- [1] I.V. Grigorieva, A.A. Firsov, K.S. Novoselov, A.K. Geim, S.V. Morozov, D. Jiang, Y. Zhang, S.V. Dubonos, K.S. Novoselov, Electric field effect in atomically thin carbon films, 80-, *Science* 306 (2016) 666–669, <https://doi.org/10.1126/science.1102896>.
- [2] J. Wang, X. Mu, M. Sun, T. Mu, Optoelectronic properties and applications of graphene-based hybrid nanomaterials and van der Waals heterostructures, *Appl. Mater. Today*. 16 (2019) 1–20, <https://doi.org/10.1016/j.apmt.2019.03.006>.
- [3] A.G. Olabi, M.A. Abdelkareem, T. Wilberforce, E.T. Sayed, Application of graphene in energy storage device – a review, *Renew. Sustain. Energy Rev.* 135 (2021), 110026, <https://doi.org/10.1016/j.rser.2020.110026>.
- [4] A. Hatamie, R. Rahmati, E. Rezvani, S. Angizi, A. Simchi, Yttrium hexacyanoferrate microflowers on freestanding three-dimensional graphene substrates for ascorbic acid detection, *ACS Appl. Nano Mater.* 2 (2019) 2212–2221, <https://doi.org/10.1021/acsnan.9b00167>.
- [5] A. Ambrosi, C.K. Chua, A. Bonanni, M. Pumera, Electrochemistry of graphene and related materials, *Chem. Rev.* 114 (2014) 7150–7188, <https://doi.org/10.1021/cr500023c>.
- [6] E. Rezvani, A. Hatamie, M. Berahman, M. Simchi, S. Angizi, R. Rahmati, J. Kennedy, A. Simchi, Synthesis, first-principle simulation, and application of three-dimensional ceria nanoparticles/graphene nanocomposite for non-enzymatic hydrogen peroxide detection, *J. Electrochem. Soc.* 166 (2019) H3167–H3174, <https://doi.org/10.1149/2.0191905jes>.
- [7] T.T. Tung, M.J. Nine, M. Krebsz, T. Pasinszki, C.J. Coghlan, D.N.H. Tran, D. Losic, Recent advances in sensing applications of graphene assemblies and their composites, *Adv. Funct. Mater.* 27 (2017), 1702891, <https://doi.org/10.1002/adfm.201702891>.
- [8] A. Zubiarrain-Laserna, P. Kruse, Review—graphene-based water quality sensors, *J. Electrochem. Soc.* 167 (2020), 037539, <https://doi.org/10.1149/1945-7111/ab67a5>.
- [9] F.-L. Meng, Z. Guo, X.-J. Huang, Graphene-based hybrids for chemiresistive gas sensors, *TrAC Trends Anal. Chem.* 68 (2015) 37–47, <https://doi.org/10.1016/j.trac.2015.02.008>.
- [10] J. Dalmieda, A. Zubiarrain-Laserna, D. Ganepola, P.R. Selvaganapathy, P. Kruse, Chemiresistive detection of silver ions in aqueous media, *Sensor. Actuator. B Chem.* 328 (2021), 129023, <https://doi.org/10.1016/j.snb.2020.129023>.
- [11] M. Mohammed, Z. Li, J. Cui, T. Chen, Junction investigation of graphene/silicon Schottky diodes, *Nanoscale Res. Lett.* 7 (2012) 302, <https://doi.org/10.1186/1556-276X-7-302>.
- [12] X. Li, H. Zhu, K. Wang, A. Cao, J. Wei, C. Li, Y. Jia, Z. Li, X. Li, D. Wu, Graphene-on-silicon Schottky junction solar cells, *Adv. Mater.* 22 (2010) 2743–2748, <https://doi.org/10.1002/adma.200904383>.
- [13] A. Di Bartolomeo, Graphene Schottky diodes: an experimental review of the rectifying graphene/semiconductor heterojunction, *Phys. Rep.* 606 (2016) 1–58, <https://doi.org/10.1016/j.physrep.2015.10.003>.
- [14] C.-C. Chen, M. Aykol, C.-C. Chang, A.F.J. Levi, S.B. Cronin, Graphene-silicon Schottky diodes, *Nano Lett* 11 (2011) 1863–1867, <https://doi.org/10.1021/nl104364c>.
- [15] S. Tongay, T. Schumann, A.F. Hebard, Graphite based Schottky diodes formed on Si, GaAs, and 4H-SiC substrates, *Appl. Phys. Lett.* 95 (2009), 222103, <https://doi.org/10.1063/1.3268788>.
- [16] S. Parui, R. Ruitter, P.J. Zomer, M. Wojtaszek, B.J. van Wees, T. Banerjee, Temperature dependent transport characteristics of graphene/n-Si diodes, *J. Appl.*

- biocidal materials, *J. Chem. Theor. Comput.* 2 (2006) 879–884, <https://doi.org/10.1021/ct060007s>.
- [68] C.S.R. Vusa, M. Venkatesan, S. Berchmans, P. Arumugam, Tactical tuning of the surface and interfacial properties of graphene: a Versatile and rational electrochemical approach, *Sci. Rep.* 7 (2017) 8354, <https://doi.org/10.1038/s41598-017-08627-1>.
- [69] N.R. Ward, R.L. Wolfe, B.H. Olson, Effect of pH, application technique, and chlorine-to-nitrogen ratio on disinfectant activity of inorganic chloramines with pure culture bacteria, *Appl. Environ. Microbiol.* 48 (1984) 508–514, <https://doi.org/10.1128/aem.48.3.508-514.1984>.
- [70] B. Maily-Giacchetti, A. Hsu, H. Wang, V. Vinciguerra, F. Pappalardo, L. Occhipinti, E. Guidetti, S. Coffa, J. Kong, T. Palacios, pH sensing properties of graphene solution-gated field-effect transistors, *J. Appl. Phys.* 114 (2013), 084505, <https://doi.org/10.1063/1.4819219>.
- [71] A. Mohtasebi, A.D. Broomfield, T. Chowdhury, P.R. Selvaganapathy, P. Kruse, Reagent-free quantification of aqueous free chlorine via electrical readout of colorimetrically functionalized pencil lines, *ACS Appl. Mater. Interfaces* 9 (2017) 20748–20761, <https://doi.org/10.1021/acsami.7b03968>.
- [72] Health Canada, Guidelines for Canadian Drinking Water Quality- Summary Table, Water and Air Quality Bureau, Healthy Environments and Consumer Safety Branch, 2020, Ottawa, Ontario.
- [73] City of Toronto, Drinking Water Analysis Summary, Toronto, 2020.
- [74] M. Sato, A. Harata, Y. Hatano, T. Ogawa, T. Kaieda, K. Ohmukai, H. Kawazumi, Acid–Base equilibrium constants and distribution coefficients of aminopyrene between the surface and bulk of liquid water as studied by a laser two-photon ionization technique, *J. Phys. Chem. B* 108 (2004) 12111–12115, <https://doi.org/10.1021/jp0491616>.
- [75] N. Kato, N. Hirano, S. Okazaki, S. Matsushita, T. Gomei, Development of an all-solid-state residual chlorine sensor for tap water quality monitoring, *Sensor. Actuator. B Chem.* 248 (2017) 1037–1044, <https://doi.org/10.1016/j.snb.2017.03.089>.
- [76] J. Islam, H. Shao, M.M.R. Badal, K.M. Razeed, M. Jamal, Pencil graphite as electrode platform for free chlorine sensors and energy storage devices, *PLoS One* 16 (2021), e0248142, <https://doi.org/10.1371/journal.pone.0248142>.
- [77] P. Salazar, M. Martín, F.J. García-García, J.L. González-Mora, A.R. González-Elípe, A novel and improved surfactant-modified Prussian Blue electrode for amperometric detection of free chlorine in water, *Sensor. Actuator. B Chem.* 213 (2015) 116–123, <https://doi.org/10.1016/j.snb.2015.02.092>.
- [78] D.R. Kumar, S. Kesavan, T.T. Nguyen, J. Hwang, C. Lamiel, J.-J. Shim, Polydopamine@electrochemically reduced graphene oxide-modified electrode for electrochemical detection of free-chlorine, *Sensor. Actuator. B Chem.* 240 (2017) 818–828, <https://doi.org/10.1016/j.snb.2016.09.025>.
- [79] S. Pan, M.J. Deen, R. Ghosh, Low-cost graphite-based free chlorine sensor, *Anal. Chem.* 87 (2015) 10734–10737, <https://doi.org/10.1021/acs.analchem.5b03164>.
- [80] C. Xiong, T. Zhang, D. Wang, Y. Lin, H. Qu, W. Chen, L. Luo, Y. Wang, L. Zheng, L. Fu, Highly sensitive solution-gated graphene transistor based sensor for continuous and real-time detection of free chlorine, *Anal. Chim. Acta* 1033 (2018) 65–72, <https://doi.org/10.1016/j.aca.2018.06.041>.
- [81] E. Hoque, L.H.H. Hsu, A. Aryasomayajula, P.R. Selvaganapathy, P. Kruse, Pencil-drawn chemiresistive sensor for free chlorine in water, *IEEE Sensors Lett* 1 (2017) 1–4, <https://doi.org/10.1109/ISENS.2017.2722958>.
- [82] L. Yang, M. Li, Y. Qu, Z. Dong, W.J. Li, Carbon nanotube-sensor-integrated microfluidic platform for real-time chemical concentration detection, *Electrophoresis* 30 (2009) 3198–3205, <https://doi.org/10.1002/elps.200900126>.

Graphene-Silicon Schottky Devices for Operation in Aqueous Environments: Device Performance and Sensing Application

Shayan Angizi¹, P. Ravi Selvaganapathy², Peter Kruse^{1,*}

¹ Department of Chemistry and Chemical Biology, McMaster University, 1280 Main St. W. Hamilton, Ontario Canada L8S 4M1

² Department of Mechanical Engineering, McMaster University, Hamilton, L8S 4M1, Canada

* Corresponding author. Tel. (905) 525-9140 (ext. 23480), e-mail: pkruse@mcmaster.ca

S1 Materials and Methods

The lightly doped n-type Si wafers ($n_d \sim 5 \times 10^{15} \text{ cm}^{-3}$, phosphorous) were purchased from Virginia Semiconductor. The monolayer graphene covered by PMMA was bought from Graphenea. Ammonium persulfate (APS) was purchased from WVR. Sodium hydroxide (99%) and hydrochloric acid (37%) used to adjust the pH were purchased from Caledon Laboratories Ltd. Sodium chloride used to control the solution ionic conductivity was purchased from Caledon Laboratories Ltd. 1- amino pyrene (99%) and calcium chloride (99%) were purchased from Sigma Aldrich. Sodium phosphate (dibasic, anhydrous) was purchased from Baker Chemical Co. Sodium sulfate and magnesium chloride were supplied from Fisher Scientific. Potassium chloride (ACS grade, PX1405-1) and sodium bicarbonate (ACS grade, 99%, SX0320-1) were purchased from EMD. Ammonium fluoride hydrofluoric acid known as buffered oxide etch (BOE) 4:1 (HF: NH_4F =20%:80%) was purchased from Sigma Aldrich. Ultrapure water used for the experiments ($18.2 \text{ M}\Omega \cdot \text{cm}$) was obtained from a Millipore Simplicity UV water purifier system. Sodium hypochlorite solution (reagent grade, 10 – 15%) was used as a source of free chlorine. All chemical reagents were analytical grade and were used as purchased unless stated.

The free chlorine concentration was measured using the Hach Pocket Colorimeter™ II kit through addition of N, N-diethyl-p-phenylenediamine and measurement of optical absorption. The results were also checked with the obtained values from a UV-Visible spectrometer to ensure accuracy.

S2 Characterization

A Raman spectrometer (Renishaw inVia) was used to analyze the transferred graphene on Si and SiO_2 in the range of $300\text{--}3500 \text{ cm}^{-1}$ with a spectral resolution of 3 cm^{-1} . A $50\times$ objective lens was

used to focus the 514 nm laser on the sample through an aperture for a spot size of about 1 μm . The optimum laser power was chosen to be 1% to avoid the local burning of carbon. Each sample was characterized in three different spots to ensure reproducibility.

The SEM images were taken on a JEOL JSM7000F microscope at 20 kV.

XPS spectra were taken using a Kratos AXIS Supra X-ray photoelectron spectrometer. XPS survey spectra were obtained from an area of approximately $300 \times 700 \mu\text{m}^2$ by using a pass energy of 160 eV. XPS high-resolution spectra were recorded from an area of approximately $300 \times 700 \mu\text{m}^2$ by using a pass energy of 20 eV. The survey and high-resolution spectra of C 1s, O 1s, N 1s, and Cl 2p were recorded.

The UV-Visible spectra of 1-aminopyrene were obtained by placing 2 mL of solution (0.3 mL of 1.4 mM 1-aminopyrene/ethanol in 1.7 mL DI water) into a quartz cuvette and measuring in an Orion Aquamate 8000 spectrophotometer over a range from 250 to 600 nm.

For electrochemical and chemiresistive measurements, a four-channel eDAQ EPU452 Quad Multifunction isoPod was connected to the electrodes. The channel type for chemiresistive sensing was set to the biosensor, with an applied voltage of 100 mV. An ORP electrode, a pH electrode, and a conductivity electrode (all purchased from eDAQ Inc.) were calibrated and connected to channel types of ISE, ISE, and conductivity, respectively. The pH electrode was calibrated with pH 4 and pH 7 calibration solutions before the experiments. The ORP electrode was kept in calibration solution and washed several times to avoid introducing contamination to the experiment. The conductivity electrode was calibrated in 0.1 mM KCl solution ($12.64 \text{ mS}\cdot\text{cm}^{-1}$) for 30 minutes, giving a cell constant (k) of 1.038 A. A Keithley source meter (2450) was used for diode measurements. In the sweep function, the voltage range was set to -2 to +2 V with decimal of 10 mV.

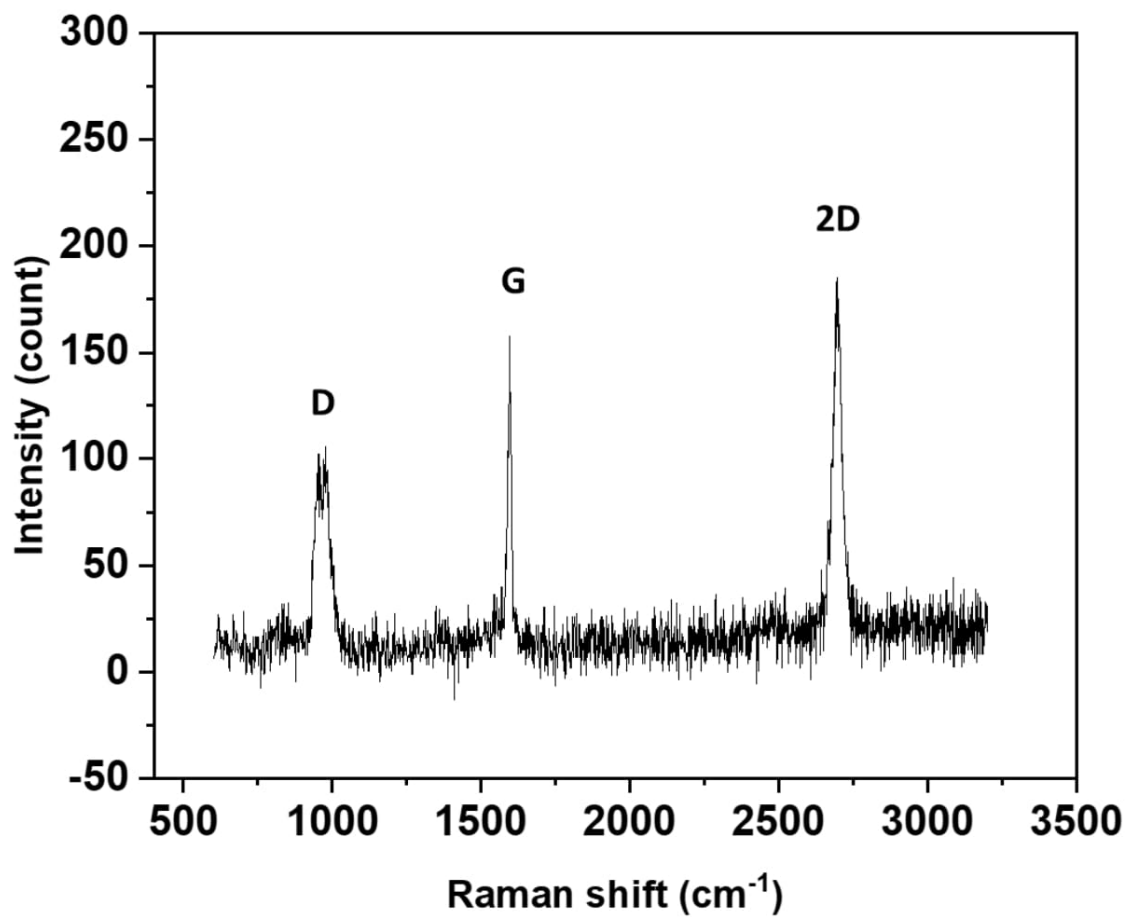


Figure S1. Raman spectrum of Graphene before PMMA removal.

S3 Procedure for calculating R_s , η , and Φ_{SB}

To calculate the diode parameter, we start with thermionic theory as equation S1[1,2]:

$$J = J_s \left[\exp\left(\frac{q(V_D - (R_s I))}{\eta k_B T}\right) - 1 \right] \quad \text{eq. S1}$$

Where the saturation current is defined as:

$$J_s = AA^* \exp\left(-\frac{q\Phi_{SB}}{k_B T}\right) \quad \text{eq. S2}$$

by isolating V in equation S1, equation S3 will be generated:

$$V = \frac{\eta k_B T}{q} \ln\left(\frac{J}{J_s}\right) + JAR_s \quad \text{eq. S3}$$

by differentiation equation of equation S3, we can obtain:

$$\frac{dV}{dJ} = \frac{\eta k_B T}{q} \cdot \frac{1}{J} + AR_s \quad \text{eq. S4}$$

So, plotting $\frac{dV}{dJ}$ vs. $\frac{1}{J}$ will provide us with a linear zone in which slope and Y-intercepts, η and R_s can be calculated [1]. This can be similarly done in semi-logarithmic format of equation S4:

$$\frac{dV}{d(\ln J)} = \frac{\eta k_B T}{q} + JAR_s$$

At this point, by plotting $\frac{dV}{d \ln J}$ vs. J , R_s and η can be obtained from the slope and y-intercept of the linear sections, respectively.

To obtain Φ_{SB} , isolation of V from thermionic theory will give [3,4]:

$$V = JAR_s + \eta\Phi_{SB} + \frac{\eta k_B T}{q} \ln\left(\frac{J}{A^* T^2}\right) \quad \text{eq. S5}$$

So, by defining the new term of H (J)

$$H(J) \equiv V - \frac{\eta k_B T}{q} \ln\left(\frac{J}{A^* T^2}\right) \quad \text{eq. S6}$$

$$H(J) \equiv R_s A J + \eta\Phi_{SB} \quad \text{eq. S7}$$

So, plotting H vs. J will give us a linear zone having the slope and Y-intercepts of η and Φ_{SB} respectively.

It should be noted that the fitting techniques to obtain the slope and Y-intercepts are extremely sensitive to the data scattering, the linearity of the graphs. One simple method to obtain the values of η and R_s was to fit a line to the linear sections of semilogarithmic J-V curves of the sensor for $V > 3KT$. However, since the dominance of R_s occurs at high forward biases, the obtained values have a considerable deviation from actual values. Therefore, the calculation of R_s range should be limited in the range of $V = 3KT$ and the flat band voltage (a voltage at which the semi-logarithmic J-V curve deviates from the initial straight behavior).

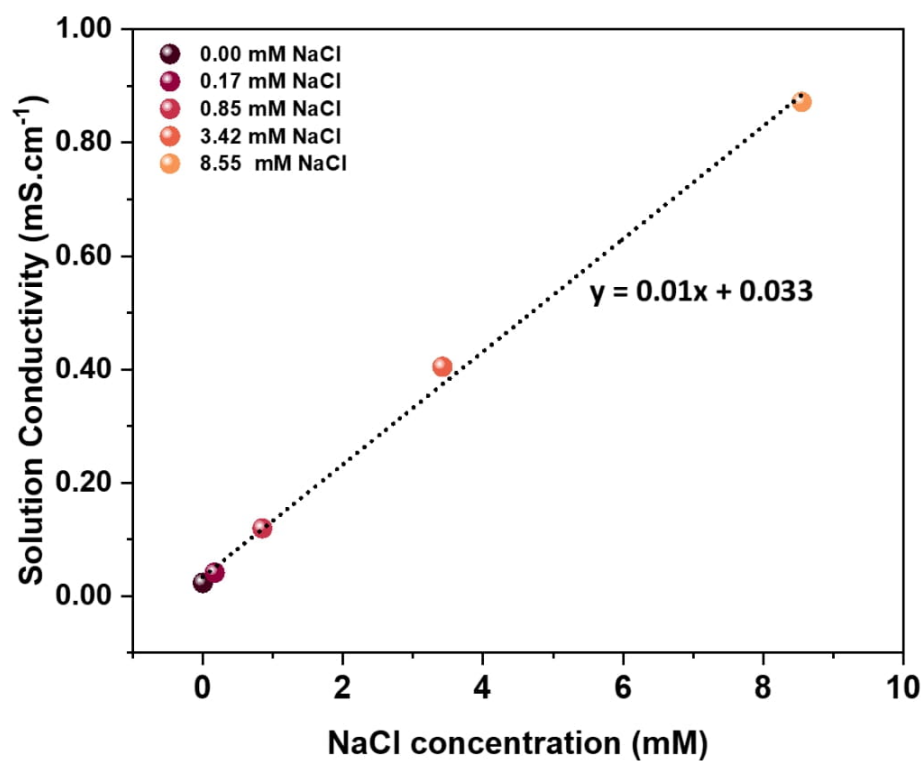


Figure S2. Plot of solution conductivity (mS.cm⁻¹) of an aqueous solution upon addition of NaCl.

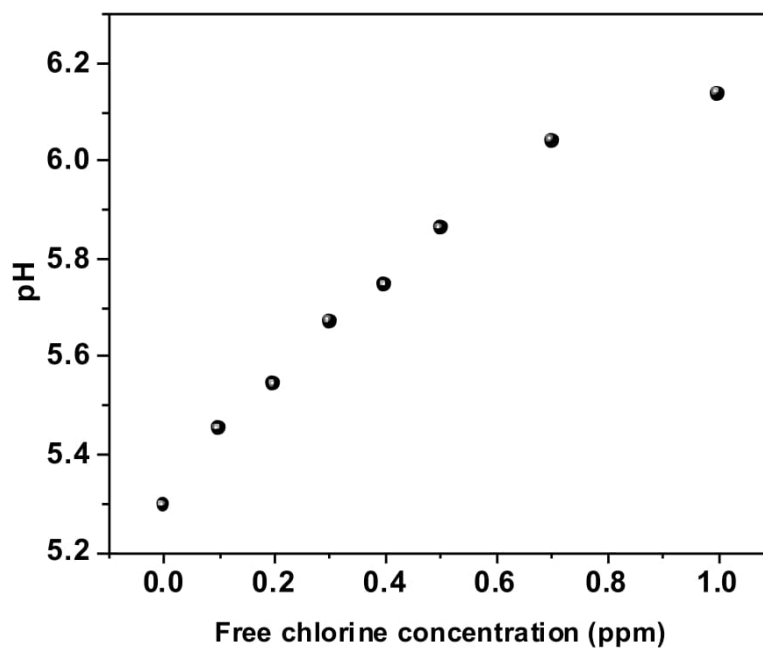


Figure S3. Change in pH of solution upon addition of free chlorine.

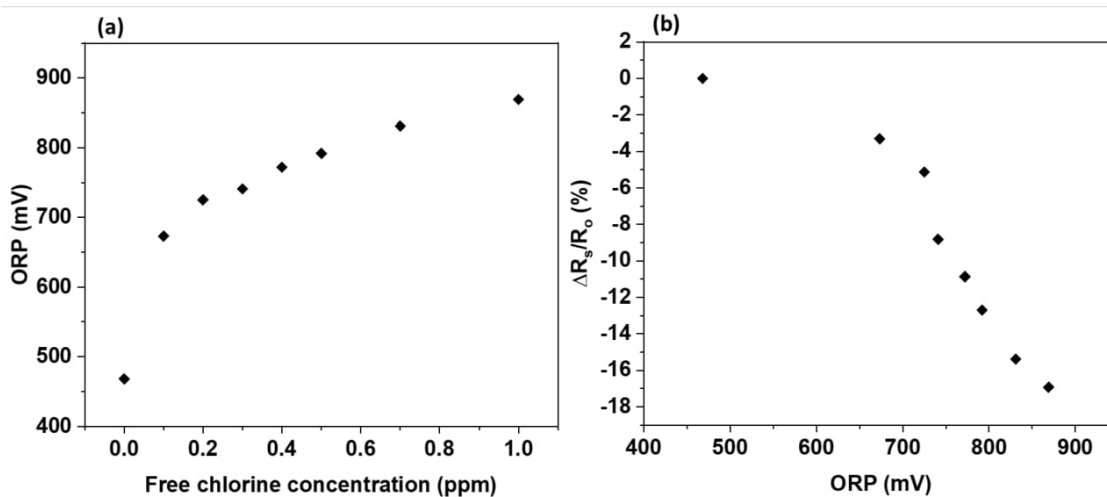


Figure S4. a) plot of oxidation reduction potential of the solution by addition of free chlorine b) change in the device series resistance with increasing the ORP values.

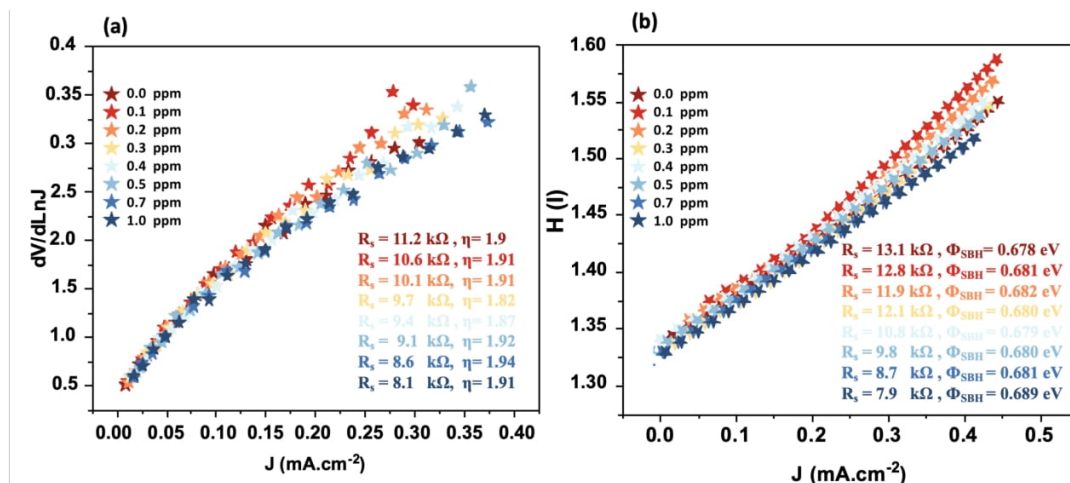


Figure S5. a) $dV/d\ln J$ vs. J graphs for the blank device at forward bias, demonstrating the validity of the used circuit model, b) the H vs. J graphs of the blank device, revealing the linearity of the fitted lines with less than 10% offset from the model.

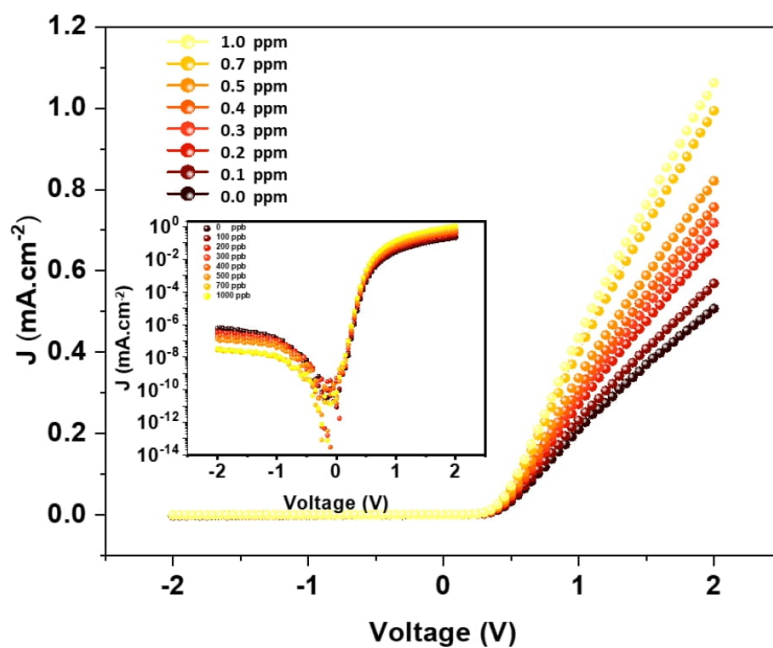


Figure S6. J-V curves of AP-G/Si upon exposure to free chlorine concentrations

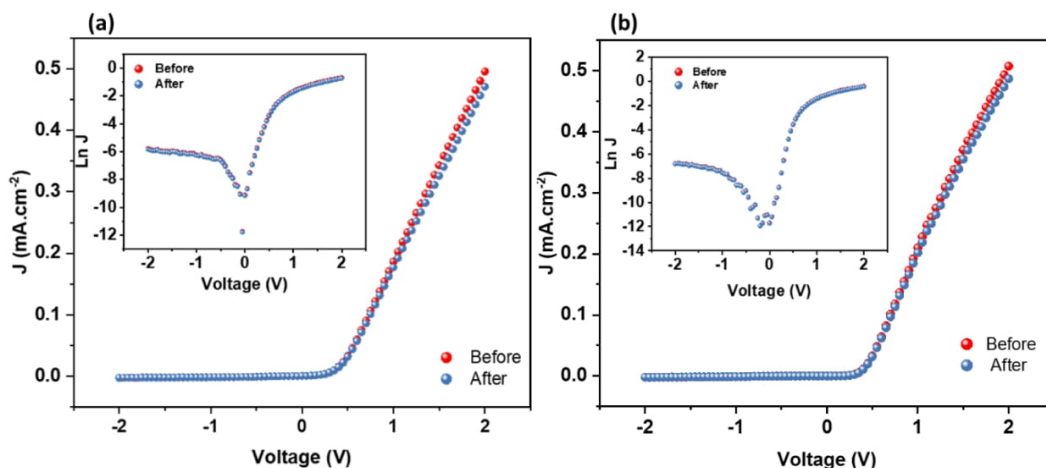


Figure S7. J-V curves of a) G/n-Si and b) AP/G/n-Si devices before and after exposure to water (the insets show the corresponding semi-logarithmic J-V curves)

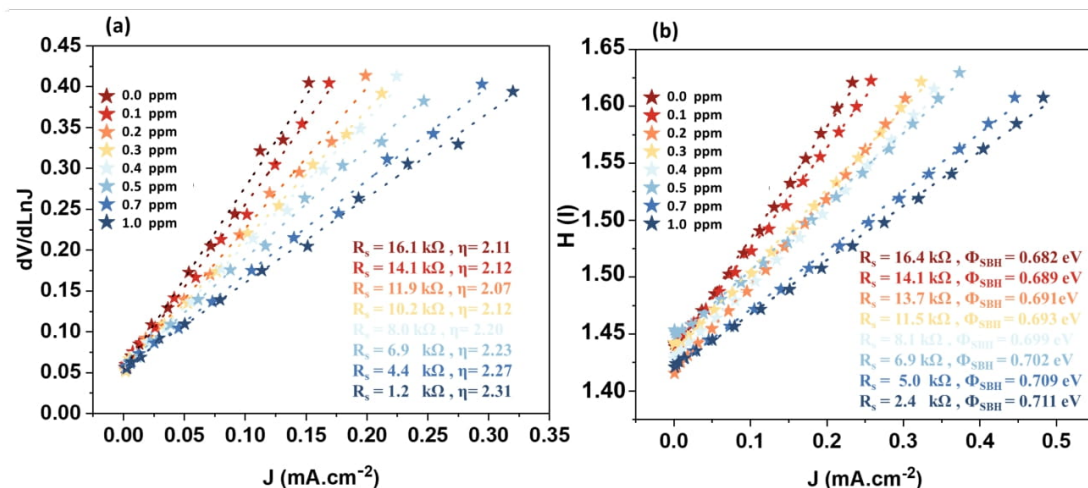


Figure S8. a) $dV/d\ln J$ vs. J graphs for AP/G/n-Si at forward bias, demonstrating the validity of the used circuit model, b) the H vs. J graphs of AP/G/n-Si device, revealing the linearity of the fitted lines with less than 10% offset from the model.

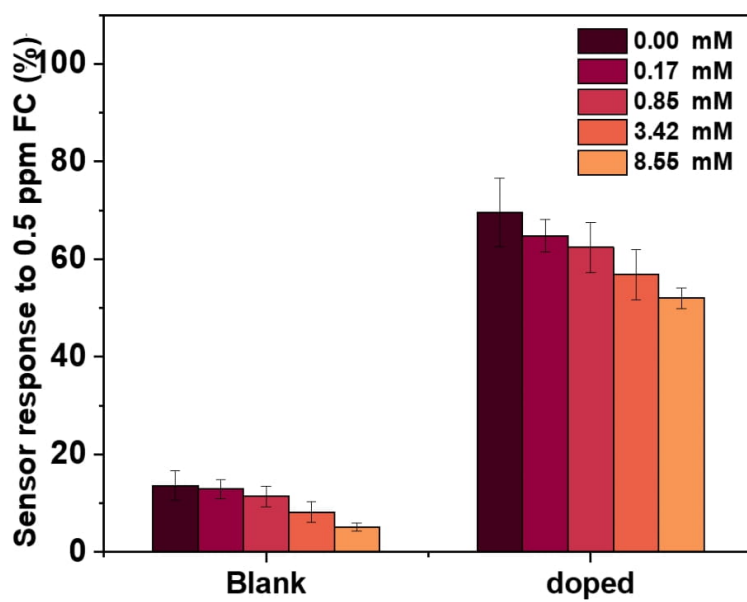


Figure S9. Blank and AP doped device performances upon addition of NaCl at different concentrations.

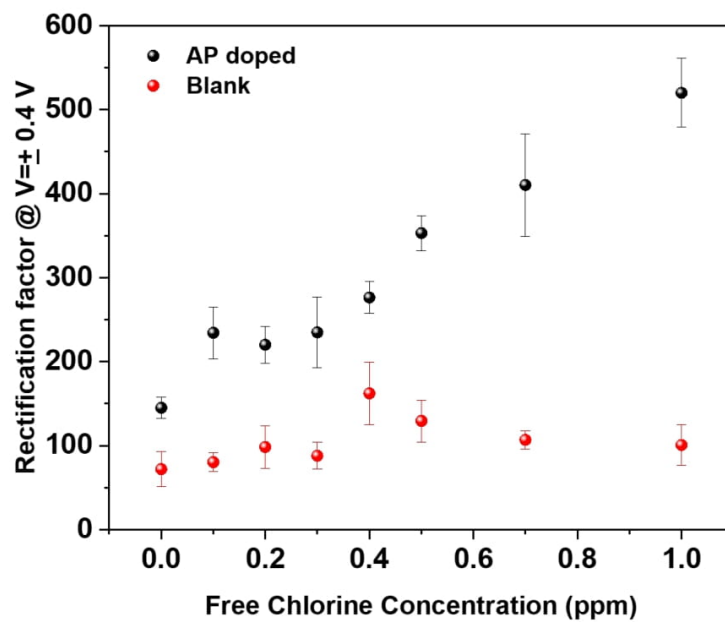


Figure S10. Variation of rectification factors for blank (black-top) and doped (red-bottom) devices at different free chlorine concentrations.

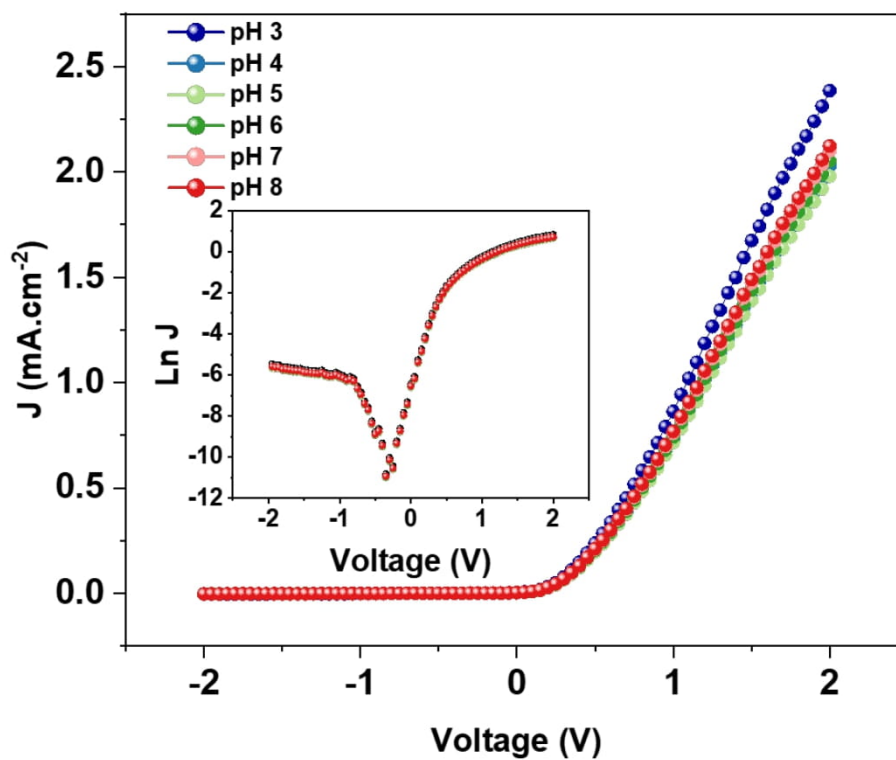


Figure S11. J-V curves of AP-doped device upon variation of pH from 3 to 8 (the insets represent the corresponding semilogarithmic curves).

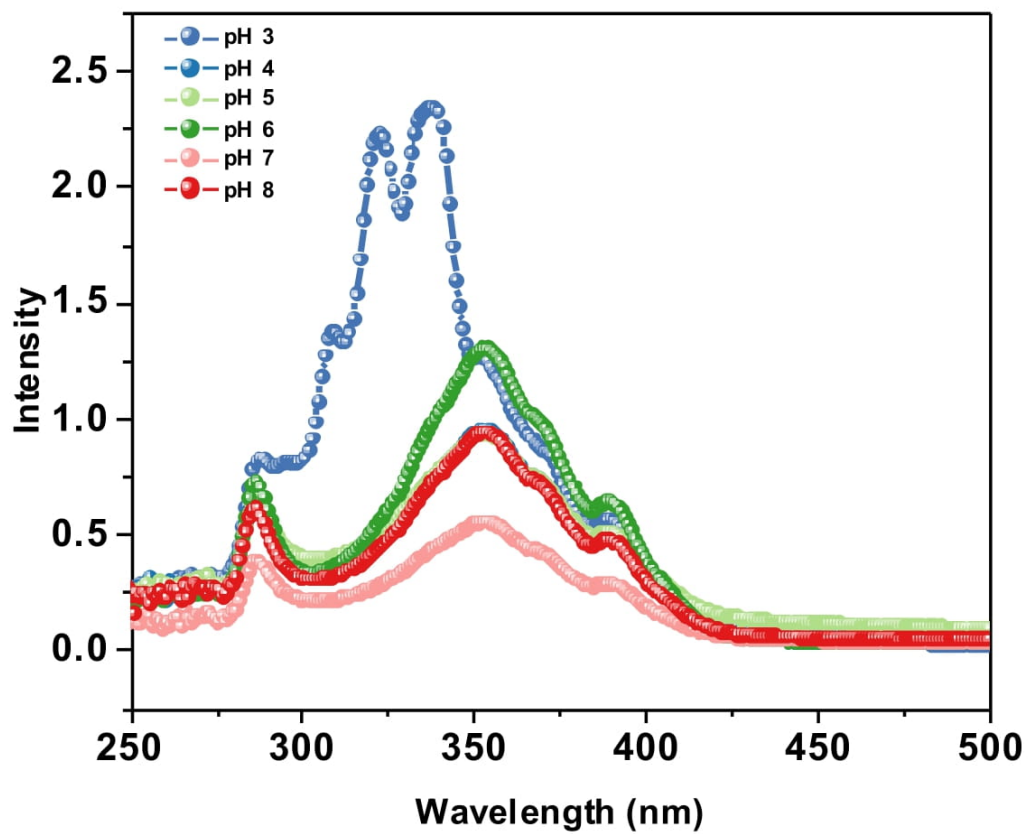


Figure S12. UV-vis absorption spectra of 1-aminopyrene molecules at pH 3-8.

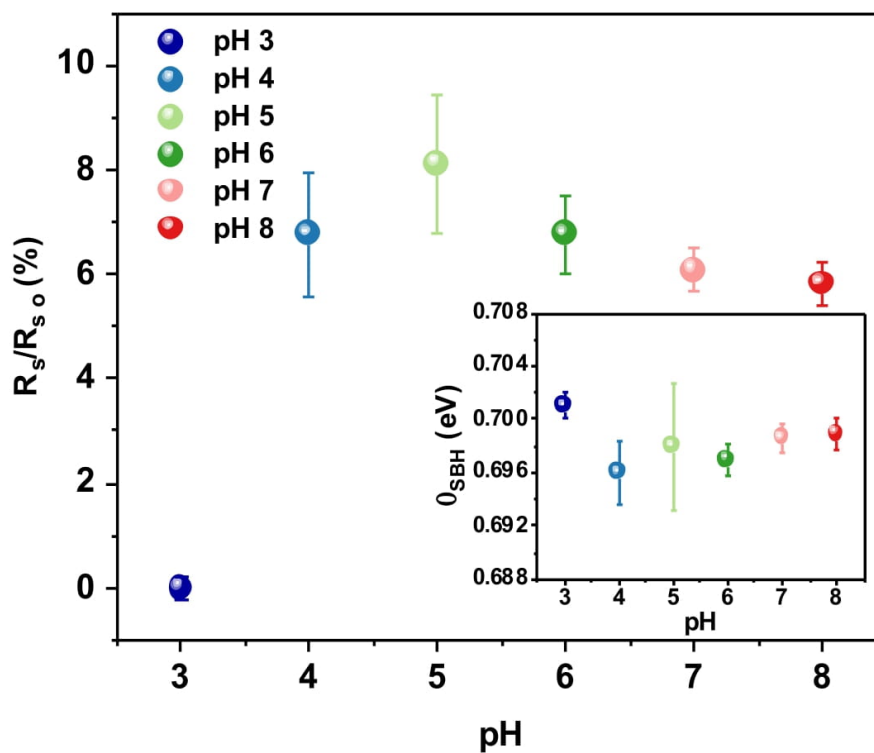


Figure S13. Change in R_s and Φ_{SBH} (inset) of the 1-aminopyrene doped devices upon exposure to pH 3-8.

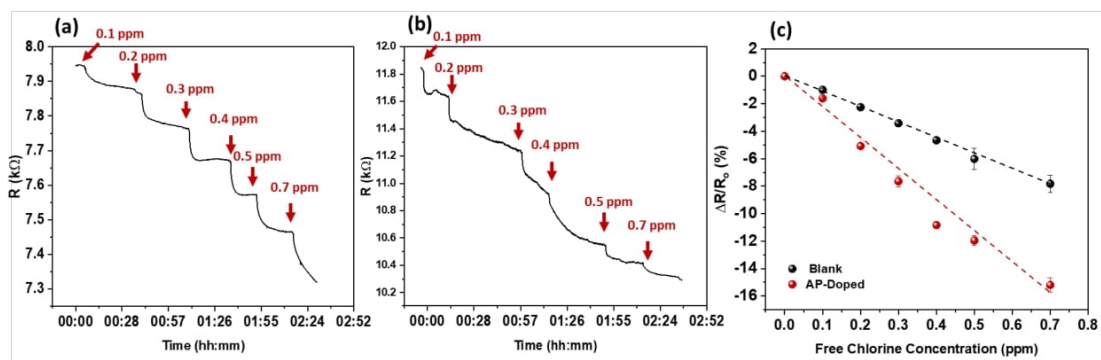


Figure S14. Real-time chemiresistive measurements of a) blank b) AP-doped sensors upon exposure to free chlorine, c) calibration curves of the sensors.

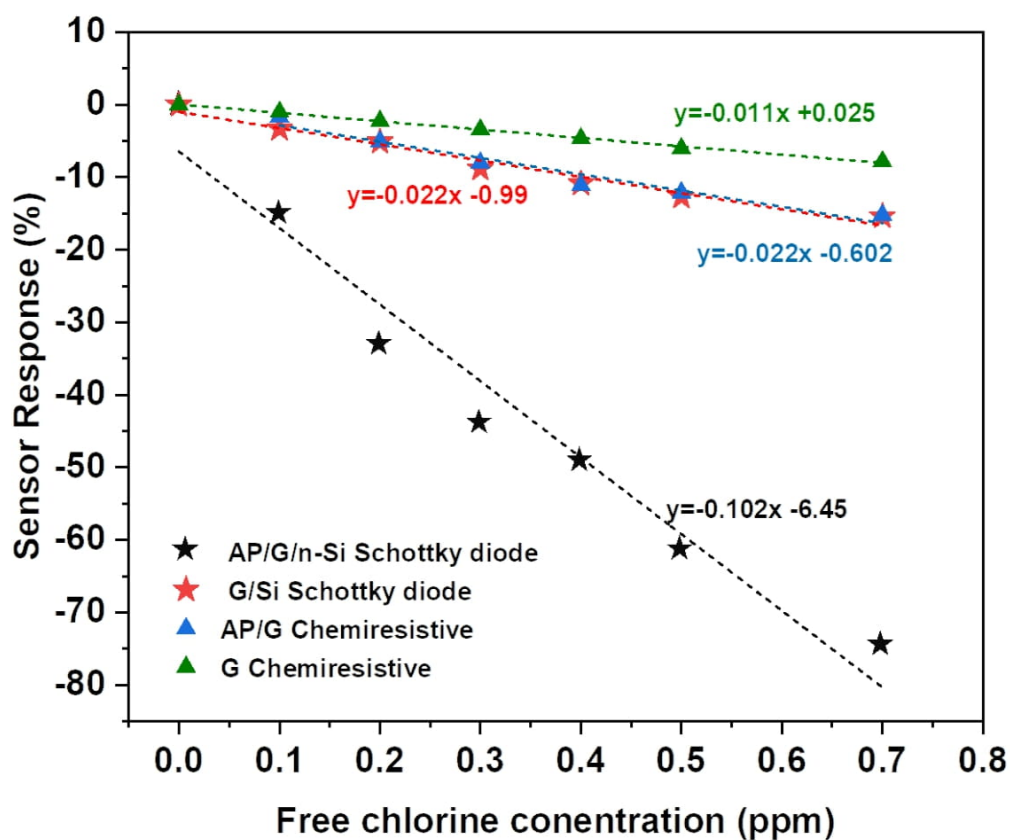


Figure S15. Comparison of blank and AP-doped G/n-Si Schottky diode and chemiresistive responses to free chlorine under same conditions.

References

- [1] Kim H-Y, Lee K, McEvoy N, Yim C, Duesberg GS. Chemically Modulated Graphene Diodes. *Nano Lett* 2013;13:2182–8. <https://doi.org/10.1021/nl400674k>.
- [2] Nouchi R. Extraction of the Schottky parameters in metal- semiconductor-metal diodes from a single current- voltage measurement n.d.:1–16.
- [3] Fattah A, Khatami S. Selective H₂S Gas Sensing With a Graphene/n-Si Schottky Diode. *IEEE Sens J* 2014;14:4104–8. <https://doi.org/10.1109/JSEN.2014.2334064>.
- [4] Fattah A, Khatami S, Mayorga-Martinez CC. Graphene / Silicon Heterojunction Schottky Diode for Vapors Sensing Using Impedance Spectroscopy 2014:4193–9. <https://doi.org/10.1002/sml.201400691>.



Product Datasheet

Graphenea Monolayer Graphene film on Cu with PMMA

Graphene Film

Growth Method	CVD synthesis
Transfer Method	Clean transfer method
Quality Control	Optical Microscopy & Raman checked
Appearance (Color)	Transparent
Transparency	>97%
Appearance (Form)	Film
Coverage	>95%
Number of graphene layers	1
Thickness (theoretical)	0.345 nm
AFM Thickness (air @RT)	<1nm
Electron Mobility on SiO ₂ /Si	≈1500 cm ² /V·s
Sheet Resistance on SiO ₂ /Si (Van der Pauw)	450±40 Ohms/sq. (1cm x 1cm)
Sheet Resistance PEN (Van der Pauw)	750±50 Ohms/sq. (1cm x 1cm)
Sheet Resistance Quartz (Van der Pauw)	360±50 Ohms/sq. (1cm x 1cm)
Grain size	Up to 20 μm

Substrates

Cu foil

Thickness	18 μm
Roughness	80 nm

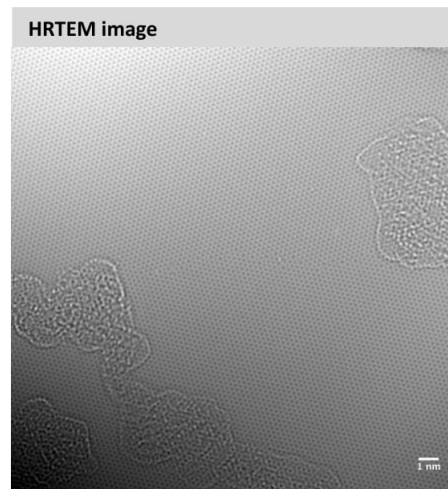
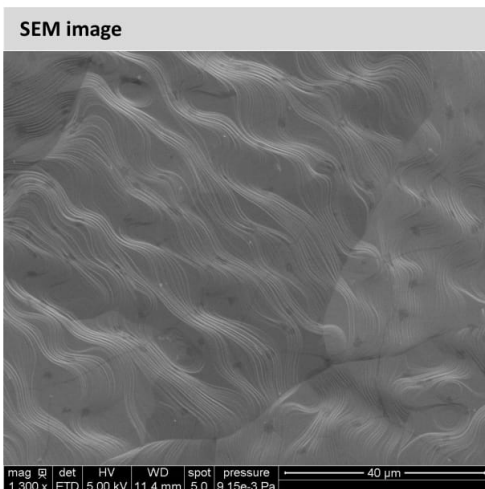
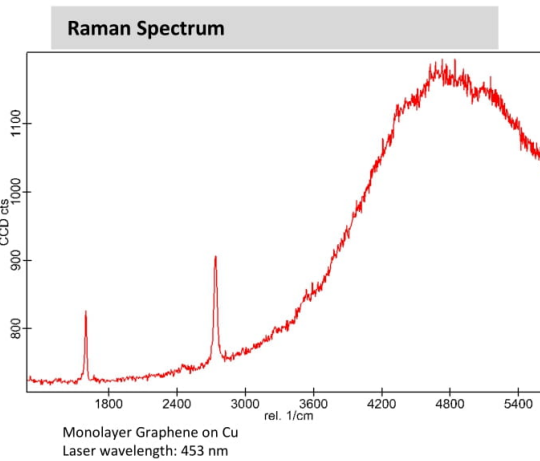
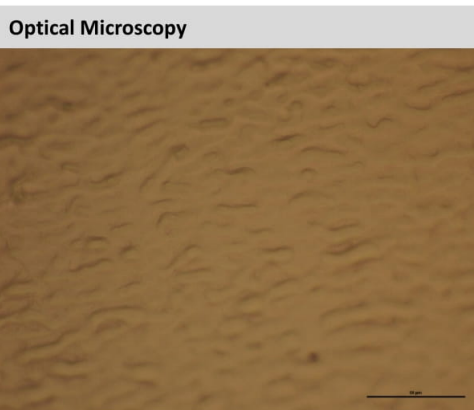
PMMA Coating

Thickness	60 nm
PMMA Model	495K, A2

Note: Pretreated for easier bottom layer removal

- Recommended use of the product up to 3 months

www.graphenea.com



Chapter 7 Conclusions and Outlook

In this thesis, the interfacial interactions between graphene and aqueous electrolytes are investigated with a focus on the role of environmental parameters such as pH, ORP, DO and ionic strength. This is accomplished by monitoring the reactions through output electrical signals from solid-state water quality sensors. First, graphene, as electrical transducing films of the devices, is exposed to the change in pH, ORP, and ionic strength. Then upon interaction with surroundings, the interfacial interactions are explored through the device signal.

The 3rd chapter of the thesis aims to address some of the existing ambiguities in the literature on the pH sensing mechanism of graphene devices. By fabricating graphene samples with a wide range of defectivity, it was shown that the pH response of graphene is defect dependent. Also, functionalizing the graphene by using pyrene derivatives with various pH-sensitive functional groups was shown as a great study model to investigate the pH responsivity of graphene devices. The main findings of the 3rd chapter of the thesis can be summarized as follows:

- Demonstration and optimization of graphene thermal reduction processes to reduce its defectivity level. The optimizations are done in N₂ (without reducing agent) and N₂/H₂ (95/5-with reducing agent). The former was shown inefficient in reducing the defectivity below I_D/I_G values of 0.36, while the latter demonstrated a ratio as low as 0.15 during only 6 hrs of annealing.
- For extracting the relevant information regarding defectivity, Gaussian and Lorentzian Raman spectra deconvolution processes were used. Lorentzian offered a better accuracy for first-order peak deconvolution. Accordingly, intensity of the D, D', and G bands are reported based on the deconvoluted spectra.
- Illustrating a comprehensive plot on how graphene pH sensitivity varies by the change of defectivity. The graph shows two main regions: the high defect region (above I_D/I_G

=0.35) demonstrates an inverse relationship between change in the chemiresistive current and pH. In this region, increasing the defectivity enhances the sensitivity. In low defect region (below $I_D/I_G = 0.35$), reducing the defectivity increases the sensitivity to a certain value. Considerable reduction in defectivity, however, reduces the sensitivity due to the dominance of graphene hydrophobicity.

- The mechanism justifying the sensing mechanism in low defectivity region is shown to be the dominance of electrostatic gating effect of ions in EDL. Upon addition of an acid, accumulation of H_3O^+ ions in the vicinity of graphene generates a field effect that immobilizes opposite charges (electrons) in graphene. Therefore, it is expected to observe that reducing the pH decreases the graphene current.
- The mechanism explaining the high defectivity region is shown to be protonation-deprotonation of pH sensitive oxygen containing functional groups, namely $-COOH$, $-OH$ and $-NH_2$. Upon reducing the pH below 4, $-COO^-$ group of the surface are protonated to $-COOH$ and the surface is p-doped. Similarly, increasing the pH above 8 deprotonates $-OH$ to $-O^-$; therefore, graphene is n-doped.
- Pyrene derivatives containing graphene's functional groups (Py- NH_2 , Py- OH , Py- $COOH$, and Py- CHO) are used to functionalize the annealed graphene to explore the pH response of each group.
- A general roadmap for pH sensitivity of graphene is presented. Although the results are specifically for the FLG synthesized by sonication method in the presence of IPA and H_2O , the concept can be generalized to other graphene synthesis methods and defectivity. Hence, predictions on how the plot would change by various defects are also given.

In the 4th chapter, we focused on the pH sensing mechanism of graphene derivatives, including SLG, FLG and GO. Also, we showed how pH response of graphene depends on the type and

density of each functional group. Finally, optimization of GO thermal reduction processes resulted in the development of stable GO devices in an aqueous solution. The results of this study could assist researchers to understand how various graphene nanomorphologies respond to the change in pH and open new avenues for manufacturing GO based pH-sensitive platforms. The main findings of chapter 4 can be summarized as follows:

- Successful transfer of a SLG by using a wet chemical technique followed by chemiresistive sensor fabrication. In this method, Cu substrate is etched off using APS, then the graphene is rinsed with water and methanol. Then suspended graphene film is transferred onto desire substrate, followed by hot acetone treatment and thermal annealing process.
- Finding the numerical relationships between the functional groups' defect density and pH sensitivity of graphene. Pyrene derivatives are used to create graphene surfaces with selective functional groups. The results reveal that larger contents of in-plane -COOH results in ~ 55% change in current when pH is changed from 5.5 to 3. A similar observation was shown for NH₂ and OH at low and high pH ranges, respectively.
- GO chemiresistive device was fabricated through solvent chemistry and optimization of deposition parameters.
- GO chemiresistive stability in water was enhanced by optimization of the thermal annealing process. The temperature and duration of 350 °C and 24 hr are found to result in reduced GO with slightly reduced I_D/I_G compared to GO, while the film conductivity enhances to 5-10.
- Proposing a reduced GO base pH sensing platform by demonstrating its pH sensitivity. The proposed device responds to pH change from 3-9 by 175% change in chemiresistive current.

In the 5th chapter, we focused on the performance of graphene devices in contact with concentrated aqueous electrolytes. We demonstrate the use of graphene-based chemiresistors as a technique to indirectly quantify the experimental Debye screening length of concentrated electrolytes. We report a breakdown of the Debye-Hückel theory in the proximity of a graphene surface at a lower concentration (10-50 mM) than previously reported for other systems, depending on the cation size, dissolved oxygen concentration, and degree of graphene defectivity. The key findings of this research are:

- Demonstration of possible interactions between Na^+ ions and graphene surface. Graphene exposure to concentrated NaCl solution does not result in Na^+ doping. While drop casting NaCl could result in chemical doping. Therefore, change in the current upon exposure to alkaline salt solutions could be due to EDL.
- Demonstration of mechanisms through which graphene is influenced by ions at the surface. We used Grahame's theoretical model for EDL and predicted the change in graphene response upon exposure to LiCl, NaCl, and KCl solutions.
- The presence of positively charged ions (Li^+ , Na^+ and K^+) in the proximity of graphene is confirmed by n-doping the graphene through the electrostatic gating effect.
- The impact of DO on graphene properties is enhanced by increasing solution ionic strength. Therefore, DO should be considered in EDL composition and is responsible for neutralizing the impact of Na^+ ions.
- Graphene current decreases by the addition of salt concentration; however, it starts to rise again at higher concentration. The mechanism justifying this behavior is anticipated as surface charge reversal due to the formation of strongly correlated liquids at the surface and the balance between the van der Waals forces forming the EDL and Coulombic repulsive forces between two ions with similar charges.

- The current inversion was found to be cation-size dependent, demonstrating a current inversion at a lower concentration for K^+ than Na^+ .
- The current inversion is found to be DO-dependent, revealing a faster inversion when DO is absent.
- The current inversion phenomenon is also shown to be defect dependent. GO and reduced GO with large defectivity do not show a response to Na addition due to the dominance of defect induced response.

Finally, in the 6th chapter, we strive to demonstrate the practical application of the obtained knowledge on the interfacial interaction between graphene and aqueous electrolytes. For this purpose, a novel platform containing chemiresistive and Schottky diodes was fabricated. The sensitivity of the Schottky junction's properties to environment was used to explore the interactions. Free chlorine, as the primary disinfectant of water, is chosen as the model study here. Its addition to water is shown to increase the pH, ORP, and ionic strength at once; therefore, its sensitive and selective detection occurs only if the graphene interactions with environmental parameters are understood properly. The key findings of this study are as follows:

- Development of a novel platform by SLG and n-Si that operates in both modes of chemiresistor and Schottky diode simultaneously.
- Demonstration of G/n-Si junction properties in bare and wet conditions. We showed operation of such junction in the presence of water is possible.
- Interpretation of junction response to the change in pH. Upon using the previously discussed mechanism of pH, the impact of EDL on graphene was demonstrated by adjusting the pH. Accordingly, nearly 18% response is reported for such system for the pH change from

- Demonstration of the junction response to the change in ionic strength. It was shown that junction R_s increases nearly 257% upon exposure to only 8.55 mM NaCl compared to DI water.
- Demonstration of the junction response to the ORP change in the solution. For this purpose, the bare surface of graphene is exposed to free chlorine, and graphene response to the change in ORP of the solution is measured.
- Surface functionalization of graphene with 1-amino pyrene molecules and its application for free chlorine detection. The AP molecule showed selective detection of free chlorine with minimum interference with cations, anions, and other disinfectants.
- The Schottky device revealed nearly 5 times higher sensitivity compared to the chemiresistor, demonstrating a LOD and sensitivity of 59 nM and $0.53\mu\text{M}^{-1}$, respectively, for free chlorine detection.

As demonstrated in this thesis, understanding graphene - aqueous electrolytes interfacial interactions are still in the early stages of research. Here in, some of the future research avenues to explore are introduced.

1- Exploring the interfacial interactions

a) understanding the relationship between graphene wettability and its interfacial interactions:

We have shown that graphene/electrolyte interactions strongly depend on graphene defectivity. However, the impact of types of defects, their positions, graphene size, thickness, and substrates has not been fully explored. Hence, a careful analysis of parameters affecting graphene wettability is required to obtain a universal insight into the degree of interactions. In the next step, a correlation of graphene wettability with pH, ORP and ionic strength of the solution could be obtained.

b) Advanced electrochemical characterizations of EDL at high concentrations:

We demonstrated that ion arrangements at the graphene/electrolyte interface are determined by graphene surface charges. We also showed that graphene device responses to ionic strength is comprised of two sections: low and high. In this project, advanced electrochemical measurements could be used for better interpretation of the ion arrangements. Techniques such as EIS could elucidate equivalent circuit assigned to the interface, demonstrating the sectional and total capacitances. Moreover, SGFET could also be used to modulate the EDL forces through applying gate voltage. Accordingly, a better understanding of how graphene electronic properties change upon exposure to salt.

c) Development of Graphene/Si Schottky diode FETs to explore the interfacial interactions

In this project, by the addition of a back gate or solution gate electrode to the configuration of the G/n-Si junction, the Φ_{SB} can also be modulated through the gate voltage. This means the device sensitivity towards interactions could be enhanced more since carrier mobility and density in each reaction can be modulated through the gate electrode.

2) Towards Development of water quality sensing platforms

a) Development of pH sensors based on graphene oxide:

We reported the development of a pH-sensitive platform based on reduced graphene oxide. However, its selectivity towards pH was never tested. Therefore, surface functionalization or application of ion-selective membranes could enhance the selectivity of this system, producing pH sensors that can be integrated into small electronics.

b) Application of graphene/Schottky FETs for the sensitive detection of other water analytes:

Taking advantage of the sensitivity of G/Si Schottky junctions, it can be used for the detection of other water parameters such as Pb^+ . Since the low concentration of Pb^{2+} could result in

severe health issues, particularly in children, G/Si Schottky junctions could be a platform for such detection.